

# Development of neutron detector for use in radiation protection

Thèse de doctorat de l'Université ParisSaclay  
préparée à l'université Paris Sud

École doctorale n°576 particules hadrons énergie et noyau :  
instrumentation, imagerie, cosmos et simulation (Pheniics)  
Spécialité de doctorat: Physique des accélérateurs

Thèse présentée et soutenue à Paris, le 24 juin 2019, par

**Nesrine Dinar**

Composition du Jury :

**Marie-Hélène Schune**

Directrice de Recherche, CNRS LAL

Présidente

**Frank Gunsing**

Chercheur CEA

Rapporteur

**Didier Lacour**

Directeur de Recherche, CNRS LPHNE

Rapporteur

**Pierre Barrillon**

Ingénieur de Recherche, CNRS CPPM

Examineur

**Patrick Puzo**

Professeur Université Paris Sud

Directeur de thèse

**Marco Silari**

Physicien, CERN

Co-Directeur de thèse



# Remerciements

Je remercie chaleureusement toutes les personnes qui m'ont aidé pendant l'élaboration de ma thèse et notamment mes superviseurs Marco Silari et Patrick Puzo, pour leur intérêt et leur soutien, leur grande disponibilité et leurs nombreux conseils durant la rédaction de ma thèse (j'en profite Marco, puisque ce n'est pas un article scientifique pour faire de longues phrases !). Une pensée particulière pour vous Patrick qui vous êtes rendu disponible pour discuter des avancements de ma thèse (même si cela voulait dire le dimanche !). Merci pour la liberté que vous m'avez donné pour gérer mes expériences.

Merci aux Professeurs. Alberto Fazzi et Vicenzo Varoli pour leur expertise en électronique et leur grande disponibilité. Vous n'avez pas compté vos heures pour m'aider à développer un système de lecture efficace et je vous en suis extrêmement reconnaissante.

Merci Pierre Carbonez, pour m'avoir fait suffisamment confiance pour effectuer mes nombreuses mesures au laboratoire, même pendant les week-ends.

J'adresse tous mes remerciements à Monsieur Didier Lacour, directeur de recherche au CNRS LPHNE, ainsi qu'à Monsieur Frank Gunsing, chercheur au CEA, de l'honneur qu'ils m'ont fait en acceptant d'être rapporteurs de cette thèse.

J'exprime ma gratitude à Madame Marie-Helene Schune, directrice de recherche au CNRS LAL et à Monsieur Pierre Barillon, ingénieur de recherche au CNRS CPPM, qui ont bien voulu être examinateurs.

Ce travail de thèse n'aurait jamais pu aboutir sans le travail considérable de celui que je considère comme 'le couteau suisse' de notre section, Damiano Celeste. Je te remercie pour ton soutien quotidien indéfectible et ton enthousiasme contagieux à l'égard de mes travaux comme de la vie en général. Notre couple a grandi en même temps que mon projet scientifique, le premier servant de socle solide à l'épanouissement du second.

Au terme de ce parcours, je remercie enfin celles et ceux qui me sont chers et que j'ai quelque peu délaissés ces derniers mois pour achever cette thèse. Leurs attentions et encouragements m'ont accompagnée tout au long de ces années. Mes remerciements vont ainsi à ma famille et mes amis qui, avec cette question récurrente, « quand est-ce que tu la soutiens cette thèse? », bien qu'angoissante en période fréquente de doutes, m'ont permis de ne jamais dévier de mon objectif final.

CERN, Genève, le 20 juin 2019

## RESUME DE LA THESE :

### DEVELOPPEMENT DE DETECTEURS DE NEUTRON POUR L'UTILISATION EN RADIOPROTECTION

La première partie de cette étude a consisté à tester les performances de plusieurs détecteurs de neutrons habituellement utilisés pour la radioprotection des accélérateurs de particules à haute énergie. La comparaison a été réalisée au CERF, un champ unique qui simule le spectre neutronique rencontré à proximité d'accélérateurs à haute énergie et à des altitudes de vols commerciaux. Avant d'être utilisés à la CERF, les détecteurs ont été caractérisés et étalonnés dans le laboratoire du CERN. Une attention particulière a été accordée au détecteur de référence, le LINUS, qui a été testé pour la première fois lors d'une campagne aérienne à Prague. La campagne a permis de comprendre le comportement des différents détecteurs et de quantifier leurs sur/sous-estimations par rapport à la fonction d'équivalent de dose ambiante de référence. Ces données expérimentales ont servi de référence à la nouvelle simulation FLUKA réalisée en 2017. Ce travail visait à caractériser correctement le champ de rayonnement neutronique afin de démarrer le processus d'accréditation en tant que champ de référence.

La deuxième partie de cette thèse portait sur l'exploration d'un détecteur à neutrons rapides destiné à un nouvel appareil de mesure (appelé B-RAD) capable de fonctionner en présence d'un champ magnétique puissant (par exemple dans les zones expérimentales du LHC). Le CLYC a été choisi comme candidat potentiel pour la détection neutronique en raison de ses propriétés prometteuses, telles que sa capacité à discriminer les rayons gamma des neutrons rapides et sa résolution énergétique. De petits scintillateurs CLYC étaient déjà utilisés, mais associés au PMT. Cependant, le choix de SiPM était justifié par des exigences cruciales: insensibilité aux champs magnétiques externes, compacité extrême, dispositif mécanique léger et robuste. Cette thèse évalue les performances d'un large cylindre CLYC couplé à une matrice SiPM et compare les résultats à ceux des PMT. L'uniformité du SiPM a été étudiée à travers des mesures de la tension de polarisation, du gain, de l'efficacité de la détection photo en mesurant chaque réponse de pixel. La sensibilité à la température du système CLYC + SiPM a été testée de  $-10\text{ }^{\circ}\text{C}$  à  $+40\text{ }^{\circ}\text{C}$ . Une variation de 10% de la position du pic a été constatée. Le système est linéaire jusqu'à  $1\text{ mSv/h}$ . Une variation 20% du taux de comptage a été observée entre les irradiations avant et latérale ( $0\text{ }^{\circ}$  et  $90\text{ }^{\circ}$ ). La résolution en énergie gamma du système CLYC + SiPM était de 5,6%, ce qui est meilleur que le CLYC + PMT (Bialkalide). Cette résolution énergétique est comparable à la résolution intrinsèque du cristal LaBr ( $4,6\%$  avec la même configuration électronique). La capacité du CLYC + SiPM à discriminer les signaux gamma et neutroniques était la partie la plus difficile lorsqu'il s'agissait de traiter avec un aussi grand réseau, car la capacité totale augmentait avec le nombre de pixels. L'extraction des constantes de temps de décroissance de scintillation les plus rapides du cristal et le raccourcissement du temps de chute du signal sans couper la réponse du cristal ont été effectués par un processus électronique (compensation RC). Un excellent FOM de 2,03 a été trouvé approchant les résultats obtenus avec le PMT. Le raccourcissement des signaux permet d'augmenter la plage de linéarité et la fréquence de l'événement auquel le CLYC est sensible. L'efficacité des neutrons rapides a été simulée avec MCNP et les résultats ont été validés expérimentalement ( $0,8\%$ ). Cette efficacité et la longue durée de mesure qui en découle pourraient constituer le facteur limitant pour une application en tant que sonde portative ( $0,2\text{ coups par seconde}$  pour un débit de dose de  $1\text{ uSv/h}$ ). Cependant, le CLYC pourrait servir de détecteur fixe pour surveiller les débits de dose gamma et neutroniques sur les lieux de travail, qui pourraient entraîner une exposition indésirable du personnel (installations nucléaires, surveillance du personnel, environnement...).

# Contents

<b>INTRODUCTION</b>	<b>13</b>
<b>CHAPTER 1 BACKGROUND AND LITERATURE REVIEW</b>	<b>14</b>
<b>1.1 INTERACTION OF GAMMA RAYS WITH MATTER</b>	<b>14</b>
<b>1.2 INTERACTION OF NEUTRONS WITH MATTER</b>	<b>15</b>
1.2.1 FAST NEUTRONS	16
1.2.2 SLOW NEUTRONS	17
<b>1.3 NEUTRON DETECTION</b>	<b>18</b>
1.3.1 SLOW NEUTRON DETECTORS	18
1.3.2 FAST NEUTRON DETECTORS	21
<b>1.4 RADIATION PROTECTION QUANTITIES</b>	<b>27</b>
1.4.1 BASIC PHYSICAL QUANTITIES	27
1.4.2 PROTECTION QUANTITIES	27
1.4.3 OPERATIONAL QUANTITIES	29
<b>REFERENCES</b>	<b>31</b>
<b>CHAPTER 2 NEUTRON INSTRUMENTATION AND CERN IRRADIATION FACILITIES</b>	<b>32</b>
<b>2.1 NEUTRON INSTRUMENTATION</b>	<b>32</b>
2.1.1 BSS	32
2.1.2 LINUS	33
2.1.3 LB6411	34
2.1.4 WENDI	34
2.1.5 LUPIN	35
2.1.6 PRESCILA	35
<b>2.2 CERN IRRADIATION FACILITIES</b>	<b>36</b>
2.2.1 THE CERN CALIBRATION LABORATORY (CALLAB)	36
2.2.2 THE CERN-EU HIGH-ENERGY REFERENCE FIELD FACILITY (CERF)	37
<b>REFERENCES</b>	<b>40</b>
<b>CHAPTER 3 PERFORMANCE INTERCOMPARISON OF CONVENTIONAL NEUTRON DETECTORS</b>	<b>41</b>
<b>3.1 CHARACTERIZATION OF DETECTORS</b>	<b>41</b>
3.1.1 DETECTOR CALIBRATION	41
3.1.2 MEASUREMENT WITH AMBe NEUTRON SOURCE	43
3.1.3 LINUS REFERENCE DETECTOR AT CERF	45
<b>3.2 MEASUREMENT AT CERF</b>	<b>51</b>
3.2.1 NEUTRON SPECTRAL FLUENCE AND $H^*(10)$ MEASUREMENTS	51
3.2.2 COMPARISON OF THE EXPECTED AND MEASURED $H^*(10)$	63
<b>3.3 MODIFIED BSS</b>	<b>69</b>
3.3.1 RESPONSE TO THERMAL NEUTRONS	71
3.3.2 RESPONSE TO HIGH ENERGY NEUTRONS	71
<b>3.4 CONCLUSION</b>	<b>74</b>
<b>REFERENCES</b>	<b>75</b>



<b>APPENDIX A</b>	<b>76</b>
<hr/>	
<b>CHAPTER 4 INVESTIGATION OF THE ELECTRONIC READOUT FOR THE CLYC SCINTILLATOR</b>	<b>78</b>
<b>4.1 CLYC SCINTILLATOR</b>	<b>78</b>
<b>4.2 PMT CHARACTERIZATION</b>	<b>79</b>
4.2.1 PLATEAU CHARACTERISTIC	79
4.2.2 ENERGY RESOLUTION OF CLYC COUPLED WITH PMTs	80
<b>4.3 SiPM CHARACTERIZATION</b>	<b>82</b>
4.3.1 I-V CHARACTERIZATION	83
4.3.2 COMPARISON WITH ARRAYC-30035-16P-PCB COUPLED WITH LABr <sub>3</sub>	86
4.3.4 ENERGY RESOLUTION OF CLYC COUPLED WITH ARRAYJ-30035-64P-PCB	88
4.3.5 TEMPERATURE SENSITIVITY OF THE SYSTEM CLYC+ARRAYJ-30035-64P-PCB	89
4.3.6 UNIFORMITY	92
<b>4.4 ELECTRONIC PROBE PROTOTYPE</b>	<b>102</b>
4.4.1 CHARACTERIZATION AT POLIMI	102
4.4.2 ELECTRONIC DESIGN	109
<b>4.5 CONCLUSIONS</b>	<b>116</b>
<b>REFERENCES</b>	<b>117</b>
<hr/>	
<b>APPENDIX B</b>	<b>118</b>
<hr/>	
<b>CHAPTER 5 EVALUATION OF THE PERFORMANCE OF THE CLYC SCINTILLATOR</b>	<b>121</b>
<b>5.1 PULSE SHAPE DISCRIMINATION</b>	<b>121</b>
5.1.1 CHARGE INTEGRATION METHOD	121
5.1.2 PSD WITH CLYC + PMT R6231-100	122
5.1.3 PSD WITH CLYC + SiPM ARRAY J-30035-64P-PCB	126
<b>5.2 SCINTILLATION DECAY TIMES</b>	<b>134</b>
5.2.2 SCINTILLATION MECHANISMS	135
5.2.3 DECAY TIMES	136
<b>5.3 RESPONSE LINEARITY</b>	<b>140</b>
<b>5.4 ANGULAR DEPENDENCE</b>	<b>143</b>
<b>5.5 FAST NEUTRON EFFICIENCY</b>	<b>145</b>
<b>REFERENCES</b>	<b>147</b>
<hr/>	
<b>CHAPTER 6 NEW MATERIALS AS PERSPECTIVE</b>	<b>148</b>
<b>6.1 EJ-276 PLASTIC SCINTILLATOR</b>	<b>148</b>
<b>6.2 STILBENE SCINTILLATOR</b>	<b>150</b>
<b>REFERENCES</b>	<b>152</b>
<hr/>	
<b>CONCLUSIONS</b>	<b>155</b>
<hr/>	

## List of Figures

<i>Figure 1.1 The relative importance of the three major interaction mechanisms of gamma rays with matter. The lines shows the values of Z and energy for which the two neighbouring effects are equal [].</i>	14
<i>Figure 1.2 Summary of neutron interaction with matter [2].</i>	16
<i>Figure 1.3 Pulse height spectrum of <math>^3\text{He}</math> proportional counter [].</i>	19
<i>Figure 1.4 Cross section for <math>^3\text{He}</math>, <math>^{10}\text{B}</math> and <math>^6\text{Li}</math> for increasing neutron energy. All cross sections show a <math>1/v</math> energy dependence [].</i>	20
<i>Figure 1.5 Geometry of Stanlio (on the left) and Ollio (on the right).</i>	22
<i>Figure 1.6 Cross section of neutron-capture reactions on <math>^{35}\text{Cl}</math> [].</i>	24
<i>Figure 1.7 Energy levels of an organic molecule with <math>\pi</math> structure [].</i>	26
<i>Figure 1.8 Distribution and equation of radiation weighting factor for neutrons according to their energy [11].</i>	28
<i>Figure 1.9. Fluence-to-dose equivalent conversion coefficient for neutron energies from 1 meV to 10 GeV, provided by ICRP 74 [].</i>	30
<i>Figure 1:10. Summary of the radiation protection quantities and their relation.</i>	30
<i>Figure 2.1 The BSS consisting of five polyethylene spheres and two polyethylene/lead spheres (Stanlio and Ollio). The filler pieces fitting around the proportional counter and the aluminium supports are also shown.</i>	32
<i>Figure 2.2 BSS fluence responses as a function of the impinging neutron energy, as calculated via FLUKA simulations [].</i>	33
<i>Figure 2.3 The extended-range rem counter LINUS.</i>	33
<i>Figure 2.4 Energy response function of the LINUS, WENDI, LUPIN and LB6411 together with the ICRP 74 fluence-to-ambient dose equivalent conversion coefficients.</i>	34
<i>Figure 2.5 Berthold LB6411.</i>	34
<i>Figure 2.6 Scheme and photograph of the Thermo Scientific WENDI.</i>	35
<i>Figure 2.7 Scheme and photograph of the ELSE Nuclear LUPIN-BF, dimensions in centimetres.</i>	35
<i>Figure 2.8 An exploded view of the PRESCILA neutron rem counter (left) and its response function compared to the response of WENDI (right).</i>	36
<i>Figure 2.9 Top view of the calibration hall with the four irradiators and of irradiation room 1 with the photon irradiator [].</i>	37
<i>Figure 2.10 Cross sectional view of the CERF facility.</i>	38
<i>Figure 2.11 The reference grid with the 16 exposure locations used on the concrete roof shield.</i>	39
<i>Figure 2.12 Neutron spectral fluence obtained with FLUKA for position IT7 (red), CT7 (blue) and CS4 (green). The statistical uncertainty on the fluence values is generally below 1%.</i>	39
<i>Figure 3.1 Detector calibration factor in nSv/count measured at the CALLAB (blue) and given by the manufacturer (red).</i>	43
<i>Figure 3.2 Neutron spectral fluence obtained with the AmBe source in the RP calibration laboratory, measured with the BSS and compared with the guess spectrum. The uncertainties are not shown for clarity.</i>	44
<i>Figure 3.3 <math>H^*(10)</math> in <math>\mu\text{Sv/h}</math> from AmBe source measured with BSS, WENDI, LINUS, PRESCILA and the reference detector SmartREM at the CALLAB. The expected value from the folding between the response function and the FLUKA spectrum are also given for the WENDI and LINUS.</i>	45
<i>Figure 3.4 Experimental set up of the LINUS in the CALLAB (CERN).</i>	46
<i>Figure 3.5 Pulse height spectrum from noise (electronic and gamma) data.</i>	47
<i>Figure 3.6 Pulse-height spectra at two different MCA thresholds.</i>	47
<i>Figure 3.7 Counts variation as function of voltage applied. The yellow square located between 810 V and 900 V corresponds to the plateau region of the LINUS.</i>	49
<i>Figure 3.8 Flight position according to the GPS.</i>	50
<i>Figure 3.9 Photo of LINUS during the aircraft campaign.</i>	50
<i>Figure 3.10 LINUS <math>H^*(10)</math> as function of time and flight level.</i>	51
<i>Figure 3.11 Neutron spectral fluences obtained for position CT7, compared with the guess spectrum. The two unfolded spectra are nearly undistinguishable. The uncertainties are not shown for clarity.</i>	53
<i>Figure 3.12 <math>H^*(10)</math> in nSv per IC count of WENDI, LUPIN, LB6411, LINUS and FLUKA on the CT positions.</i>	55
<i>Figure 3.13 <math>H^*(10)</math> ratios between WENDI, LUPIN, LB6411, LINUS and FLUKA on the CT positions.</i>	55
<i>Figure 3.14. <math>H^*(10)</math> ratios between PRESCILA and FLUKA on the CT.</i>	56

<i>Figure 3.15 Experimental set-up of the measurements performed with the WENDI rem counter in the CS positions.</i>	57
<i>Figure 3.16 Neutron spectral fluences obtained for position CS4, compared with the guess spectrum. The two unfolded spectra are nearly undistinguishable. The uncertainties are not shown for clarity.</i>	58
<i>Figure 3.17 <math>H^*(10)</math> in nSv per IC count measured with LINUS, WENDI, BSS, LB6411, LUPIN and calculated with FLUKA on the CS positions.</i>	59
<i>Figure 3.18 <math>H^*(10)</math> ratios between WENDI, LUPIN, LB6411, LINUS and FLUKA on the CS positions.</i>	59
<i>Figure 3.19 Neutron spectral fluence obtained for position IT7, compared with the guess spectrum. The three spectra are nearly undistinguishable. The uncertainties are not shown for clarity.</i>	61
<i>Figure 3.20 <math>H^*(10)</math> in nSv per IC count measured by LINUS, WENDI, LUPIN, LB6411, BSS and calculated with FLUKA on IT.</i>	62
<i>Figure 3.21 <math>H^*(10)</math> ratios between WENDI, LUPIN, LB6411, LINUS and FLUKA on the IT.</i>	62
<i>Figure 3.22 <math>H^*(10)</math> ratios between PRESCILA and FLUKA on the IT.</i>	63
<i>Figure 3.23 <math>H^*(10)</math> in nSv per IC count measured and expected with LINUS on CT positions.</i>	64
<i>Figure 3.24 <math>H^*(10)</math> in nSv per IC count measured and expected with WENDI on CT positions.</i>	64
<i>Figure 3.25 <math>H^*(10)</math> in nSv per IC count measured and expected with LINUS on CS positions.</i>	65
<i>Figure 3.26 <math>H^*(10)</math> in nSv per IC count measured and expected with WENDI on CS positions.</i>	65
<i>Figure 3.27 <math>H^*(10)</math> in nSv per IC count measured and expected with LINUS on IT positions.</i>	66
<i>Figure 3.28 <math>H^*(10)</math> in nSv per IC count measured and expected with WENDI on IT.</i>	66
<i>Figure 3.29 CERN BSS response functions, together with an example spectrum of a high-energy stray neutron field (CS4, CERF).</i>	69
<i>Figure 3.30 The relative readings of the BSS as a function of sphere.</i>	70
<i>Figure 3.31 Calimero and its response function as calculated with FLUKA. The response function of the bare detector is shown for comparison.</i>	71
<i>Figure 3.32 Response functions of Stanlio and Stanlio-2, as calculated via FLUKA. The response functions of Ollio and the 233 mm sphere are also plotted for comparison.</i>	72
<i>Figure 3.33 Proton synchrotron neutron spectra obtained with MAXED for the usual 7-sphere configuration of the BSS (in red) and with the additional Calimero (in blue). The FLUKA spectrum is given as comparison (in red).</i>	73
<i>Figure 3.34 CERF CS4 neutron spectra obtained with MAXED for the different BSS configurations and the two FLUKA guess spectra for comparison. See text for details on the various BSS configurations.</i>	74
<i>Figure 4.1 The CLYC scintillator used for the measurements.</i>	79
<i>Figure 4.2 Plateau characteristic measurement for the SBA PMT R6231-100.</i>	80
<i>Figure 4.3 <math>^{137}\text{Cs}</math> spectrum and energy resolution obtained with the CLYC and the PMT BA R580.</i>	81
<i>Figure 4.4 <math>^{241}\text{Am}</math> and <math>^{137}\text{Cs}</math> spectra and energy resolution obtained with the CLYC and the PMT SBA R6231-100.</i>	81
<i>Figure 4.5 Quantum efficiency versus wavelength of the different technologies of PMT (Ultra Bialkali, Super Bialkali and Bialkali). In green the mean peak scintillation wavelength of CLYC [4].</i>	82
<i>Figure 4.6 SiPM array SensL J-30035-64P-PCB with its breakout board.</i>	83
<i>Figure 4.7 I-V curves for the 1<sup>st</sup> set of data (pixels 1 to 16).</i>	84
<i>Figure 4.8 I-V curves for the 2<sup>nd</sup> set of data (pixels 17 to 32).</i>	84
<i>Figure 4.9 I-V curves for the 3<sup>rd</sup> set of data (pixels 33 to 48).</i>	85
<i>Figure 4.10 I-V curves for the 4<sup>th</sup> set of data (pixels 49 to 64).</i>	85
<i>Figure 4.11 Frequency histogram of the <math>V_{\text{BD}}</math> distribution in the array.</i>	86
<i>Figure 4.12 The ArrayC-30035-16P by SensL and the breakout board on the left and the 15 <math>\emptyset</math> x 15 mm <math>\text{LaBr}_3</math> crystal on the right.</i>	87
<i>Figure 4.13 <math>^{137}\text{Cs}</math> spectra and energy resolution at 662 keV. The blue spectrum represents the system <math>\text{LaBr}_3</math> (15mm) + 4x4 ArrayC-30035-16P. The energy resolution of the 662 keV peak is 7.2%. The red curve represents the system <math>\text{LaBr}_3</math> (1 inch) + 8x8 ArrayJ-30035-64P-PCB. An energy resolution of 4.6% was obtained for the 662 keV peak.</i>	87
<i>Figure 4.14 <math>^{241}\text{Am}</math>, <math>^{137}\text{Cs}</math> and <math>^{60}\text{Co}</math> spectra and energy resolutions obtained with the <math>\text{LaBr}_3</math>, the 8x8 ArrayJ-30035-64P-PCB (A) and the energy-channel calibration (B).</i>	88
<i>Figure 4.15 <math>^{241}\text{Am}</math>, <math>^{137}\text{Cs}</math> and <math>^{60}\text{Co}</math> spectra, and energy resolutions obtained with the CLYC coupled with the 8x8 ArrayJ-30035-64P-PCB (A) and the energy-channel calibration (B).</i>	90
<i>Figure 4.16 The 662 keV photopeak channel position of the system CLYC+ ArrayJ-30035-64P-PCB as a function of temperature from -10 °C to +40 °C.</i>	91
<i>Figure 4.17 The energy resolution of the system CLYC+ArrayJ-30035-64P-PCB as a function of temperature from -10 °C to +40 °C. Data refer to the 662 keV photopeak.</i>	91

Figure 4:18 Variation of peak centroid as a function of temperature from -10 °C to +40 °C. The blue points represent the measured peak centroids with the system CLYC+ArrayJ-30035-64P-PCB. The red points are the theoretical peak centroids calculated from the response of SiPM ArrayJ-30035-64P-PCB only.....	92
Figure 4.19 Layout of the experimental set-up []. .....	93
Figure 4.20 Picture of the experimental set-up. ....	94
Figure 4.21 PDE ratio of the HAMAMATSU (S13360-3050PE) used for the calibration with and without nozzle. ...	95
Figure 4.22 Single photoelectron spectrum recorded for one pixel of the SiPM array J-30035-64P. Each peak corresponds to a certain number of photoelectrons (pe). The highlighted area corresponds to the number of pedestal events. ....	97
Figure 4.23 Dark noise spectrum recorded for one pixel of the SiPM array J-30035-64P.....	97
Figure 4.24 Number of photoelectrons before (blue curve) and after dark correction (red curve) for one pixel of the SiPM array J-30035-64P.....	98
Figure 4.25 PDE before (blue curve) and after dark correction (red curve) for one pixel of the SiPM array J-30035-64P.....	98
Figure 4.26 Gain versus bias voltage for one pixel. ....	99
Figure 4.27 Breakdown voltage distribution per pixel at 28.5 V.....	100
Figure 4.28 Gain distribution per pixel at 28.5 V.....	100
Figure 4.29 Photoelectron number ( $N_{pe}$ ) distribution per pixel at 28.5 V. ....	101
Figure 4.30 Photodetection efficiency (PDE) distribution per pixel at 28.5 V. ....	101
Figure 4.31 The measurement setup employed at POLIMI. ....	103
Figure 4.32 Schematic of the standard and fast outputs. ....	103
Figure 4.33 STD output (Ch. 1, yellow) with 50 $\Omega$ and fast output (Ch. 2, green) with 50 $\Omega$ .....	104
Figure 4.34 STD output (Ch. 1, yellow) with 50/3 $\Omega$ and fast output (Ch. 2, green) with 50 $\Omega$ .....	104
Figure 4.35 STD output with (blue) and without (red) connection of fast output.....	105
Figure 4.36 STD output connected to balun transformer with $R_{load}=50 \Omega$ (red) and $R_{load}=12.5 \Omega$ .....	105
Figure 4.37 Signal from single APD avalanche in the SiPM array.....	106
Figure 4.38 $^{137}\text{Cs}$ signal from $\text{LaBr}_3$ coupled with the SiPM array with $R_{load}=3.6 \Omega$ and Gain = 9.9. ....	107
Figure 4.39 $^{137}\text{Cs}$ signal from $\text{LaBr}_3$ coupled with the SiPM array with $R_{load}=3.6 \Omega$ and Gain = 9.9, with pole-zero compensation with $RC=1 \mu\text{s}$ (a), 930 ns (b) and 500 ns (c). ....	108
Figure 4.40 $^{241}\text{Am}$ signal from the EJ-404 coupled with the SiPM array with $R_{load}=10 \Omega$ , Gain = 9.9 and pole zero compensation at 500 ns.....	108
Figure 4.41 $^{137}\text{Cs}$ signal from CLYC coupled with the SiPM array with $R_{load}=10 \Omega$ , Gain = 9.9 and p-z compensation at 500 ns. ....	109
Figure 4.42 The CLYC coupled with the SiPM and the electronic board. 1, 2, 3 and 4 are the SiPM, the amplifier, the pole zero and the shaper outputs, respectively. ....	112
Figure 4.43 Measurement setup.....	112
Figure 4.44 : Picture of the STD output with 10 $\Omega$ .....	113
Figure 4.45 Amplifier output with 50 $\Omega$ termination.....	113
Figure 4.46 Pole zero output with 50 $\Omega$ termination.....	114
Figure 4.47 Zoom of pole zero output with 50 $\Omega$ termination.....	114
Figure 4.48 Waveform from CLYC coupled with SiPM before (green) and after (blue) pole zero cancellation. ...	115
Figure 4.49 Shaper output.....	115
Figure 4.50 $^{137}\text{Cs}$ signal from CLYC coupled with the SiPM array with shaping time $ST=330 \text{ ns}$ (on the left) and $ST=1 \mu\text{s}$ (on the right).....	116
Figure 5.1 $^{60}\text{Co}$ and $^{137}\text{Cs}$ spectra (upper figures) and the energy-charge calibration curve (bottom figure).....	123
Figure 5.2 100 PMT output signals from the oscilloscope .....	124
Figure 5.3 The output signals from the oscilloscope after normalization to their peak.....	124
Figure 5.4 FOM versus prompt window time. The best FOM is found at 70 ns. ....	125
Figure 5.5 Two dimension PSD plot for the best configuration (prompt window = 70 ns). The blue box identifies gamma events while the red one corresponds to neutron events.....	125
Figure 5.6 The standard output signals from the oscilloscope on the left and the same signals after normalization to the maximal amplitude and smoothing filter on the right. ....	126
Figure 5.7: The peak to tail algorithm principle. ....	127
Figure 5.8 The PSD results with two different integration tails from 10-15 $\mu\text{s}$ and from 15-20 $\mu\text{s}$ . ....	127
Figure 5.9: (a) Equivalent circuit of a GM-APD (APD operating in Geiger mode) (b) Time evolution of the avalanche current signal and the voltage across a Geiger-mode diode. ....	128

<i>Figure 5.10 The fast output signals from the oscilloscope</i> .....	130
<i>Figure 5.11 The fast output signals from the oscilloscope after the Savitzky–Golay smooth filter. The internal plot is a zoom of the first 100 ns of the plot.</i> .....	130
<i>Figure 5.12 FOM versus delayed windows time for different prompt windows. The best configuration for an optimized FOM of 1.64 is 150 ns-600 ns.</i> .....	131
<i>Figure 5.13 two dimension PSD plot. The blue box are gamma events while the red box corresponds to neutron events.</i> .....	131
<i>Figure 5.14 Projection of PSD axis. Two Gaussians are separated.</i> .....	132
<i>Figure 5.15 output signals from the oscilloscope.</i> .....	132
<i>Figure 5.16 FOM versus delayed window time for different prompt windows. The best configuration for an optimized FOM of 2.03 is 90 ns -1 <math>\mu</math>s.</i> .....	133
<i>Figure 5.17 two dimension PSD plot for the best configuration (prompt window =90 ns, delayed window = 1 <math>\mu</math>s). The blue box are gamma events while the red box corresponds to neutron events.</i> .....	134
<i>Figure 5.18 Projection of PSD ratio on the axis. The two Gaussians are well separated.</i> .....	134
<i>Figure 5.19 X-ray excited emission spectra of pure Cs<sub>2</sub>LiYCl<sub>6</sub> (solid line), Cs<sub>2</sub>LiYCl<sub>6</sub>: Ce (dashed line), recorded at room temperature. The inset displays the same spectra plotted with a logarithmic axis. The emission intensity of the crystals was normalized at 300 nm.</i> .....	136
<i>Figure 5.20 Neutron and gamma standard pulses.</i> .....	137
<i>Figure 5.21 Gamma standard pulse.</i> .....	137
<i>Figure 5.22 Neutron standard pulse.</i> .....	138
<i>Figure 5.23 Neutron signals with PMT (red) and SiPM (blue).</i> .....	140
<i>Figure 5.24 Gamma signals with PMT (red) and SiPM (blue).</i> .....	140
<i>Figure 5.25 <sup>137</sup>Cs (blue) and <sup>60</sup>Co (orange) spectra obtained with the CLYC + PMT.</i> .....	142
<i>Figure 5.26 <sup>137</sup>Cs (blue) and <sup>60</sup>Co (orange) spectra obtained with the CLYC + SiPM.</i> .....	142
<i>Figure 5.27 Count rate as a function of dose rate obtained with the SiPM (blue) and PMT (black) at the energy threshold of 330 keV. The red line represents the linear fit to the PMT data.</i> .....	143
<i>Figure 5.28 Schematic of the irradiation set-up for determining the angular response of the CLYC.</i> .....	143
<i>Figure 5.29 Directional response of the CLYC to a <sup>137</sup>Cs source.</i> .....	144
<i>Figure 5.30 Directional response of the CLYC to an AmBe source.</i> .....	144
<i>Figure 5.31 Screen view of the MCNP geometry.</i> .....	145
<i>Figure 5.32 ISO 8529-2 recommended <sup>241</sup>Am-Be neutron spectrum [14].</i> .....	146
<i>Figure 6.1 The EJ-276 output signals from the oscilloscope after normalization to their peak.</i> .....	149
<i>Figure 6.2 FOM versus delayed window time for different prompt windows. The best configuration for an optimized FOM of 1.40 is 200 ns -1.5 <math>\mu</math>s.</i> .....	149
<i>Figure 6.3 two dimension PSD plot for the best configuration (prompt window =200 ns, delayed window = 1.5 <math>\mu</math>s). The blue box are gamma events while the red box corresponds to neutron events.</i> .....	150
<i>Figure 6.4 FOM versus delayed window time for different prompt windows. The best configuration for an optimized FOM of 1.51 is 1.5 <math>\mu</math>s -4 <math>\mu</math>s.</i> .....	151
<i>Figure 6.5 Two dimension PSD plot for the best configuration (prompt window =1.5 <math>\mu</math>s, delayed window = 4 <math>\mu</math>s). The blue box are gamma events while the red box corresponds to neutron events.</i> .....	151

## List of Tables

<i>Table 1:1 Classification of neutron in function of the energy ranges. []</i> .....	16
<i>Table 1.2 Absorption reaction of nuclear reaction of interest for slow neutron detection[]</i> .....	18
<i>Table 1.3 Moderating powers and ratios of selected materials</i> .....	21
<i>Table 1.4 Recommended radiation weighting factors from ICRP 103 (2007) []</i> .....	28
<i>Table 1.5 Tissue weighting factors (ICRP 2007) [11]</i> .....	28
<i>Table 3.1 Parameters used to determine the calibration factor of the LINUS in nSv/ct</i> .....	42
<i>Table 3.2 Parameters used to determine the calibration factor of the WENDI in nSv/ct</i> .....	42
<i>Table 3.3 Parameters used to determine the calibration factor of the LUPIN in nSv/ct</i> .....	42
<i>Table 3.4 Parameters used to determine the calibration factor of the PRESCILA in nSv/ct</i> .....	42
<i>Table 3.5 Measured and expected H*(10) in the AmBe source neutrons of the RP calibration laboratory. The expected value is obtained from the simulation spectrum (FLUKA)</i> .....	43
<i>Table 3.6 – Counts integrated by the SCA (LINUS SCA) and the MCA (LINUS MCA)</i> .....	48
<i>Table 3.7 LINUS results at flight level and for the entire flight</i> .....	51
<i>Table 3.8 Measurement positions in the CERF runs 2015, 2016 and 2017</i> .....	52
<i>Table 3.9 Data obtained with the BSS in position CS4, CT7 and IT7 normalised to the number of particles impinging on the target</i> .....	53
<i>Table 3.10 Neutron H*(10) in nSv per IC count measured by the different detectors and simulated by FLUKA in the CT positions. The H*(10) obtained from the unfolded BSS spectrum in CT7 is also shown. The BSS value is the average of the MAXED and GRAVEL values</i> .....	54
<i>Table 3.11 PRESCILA Neutron Rem Meter energy response: response per unit ambient dose equivalent [H*(10)] relative to both bare <sup>252</sup>Cf and <sup>241</sup>AmBe Calibrations</i> .....	56
<i>Table 3.12 Neutron H*(10) in nSv per IC count measured with the different detectors and simulated by FLUKA in the CS positions. The H*(10) obtained from the unfolded BSS spectrum in CS4 is also shown. The BSS value is the average of the MAXED and GRAVEL values</i> .....	58
<i>Table 3.13 Repartition of H*(10) in nSv per IC count on IT7, CT7 and CS4</i> .....	60
<i>Table 3.14 Neutron H*(10) in nSv per IC count measured with the different detectors and simulated by FLUKA in the IT positions. The H*(10) obtained from the unfolded BSS spectrum in IT7 is also shown. The BSS value is the average of the MAXED and GRAVEL values</i> .....	61
<i>Table 3.15 Relative contribution of H*(10) in percentage according to the spectral component</i> .....	67
<i>Table 3.16 Repartition of H*(10) in nSv per IC count according to the spectral component</i> .....	68
<i>Table 3.17 Ratio measured H*(10) /FLUKA H*(10) according to the spectral component</i> .....	68
<i>Table 5.1 Measured decay times for gamma and neutron induced CLYC emission at room temperature</i> .....	139
<i>Table 5.2 CLYC emission decay times from the literature at room temperature</i> .....	139
<i>Table 5.3 Rise and fall times for CLYC</i> .....	139
<i>Table 6.1 Properties of the CLYC, the STILBENE and the EJ-276 plastic scintillators</i> .....	152

# Introduction

Around high-energy particle accelerators and nuclear reactors, stray radiation fields are comprised of neutrons, photons and charged particles. However, behind thick shielding, the neutron component is the top contributor to the ambient dose equivalent ( $H^*(10)$ ) and its energy can range from thermal energy up to several GeV. In radiation protection, there is growing concern for neutron dosimetry. The studies after the Hiroshima and Nagasaki tragedies shows the need to revise upward the estimation of the neutron contribution to health effect. Therefore ICRP 60 publication introduced new, increased quality factors and lowered the annual dose limits for radiation workers, thereby putting new demands on the performance of personal neutron dosimeters.

A correct monitoring of the  $H^*(10)$  is essential to ensure the compliance with the radiological area classification. Radiation protection instrumentation usually employed to monitor the neutron  $H^*(10)$  have responses functions attempting to reproduce the ICRP74 fluence-to-ambient dose equivalent conversion coefficients. Unfortunately, an exact replication is not fully possible and therefore these instruments can underestimate or overestimate some components of the neutron energy spectrum, resulting in a wrong estimation of the  $H^*(10)$ . The behaviour of each instrument can be assessed in simulated workplace reference fields and intercomparison with similar instruments can help the choice of the proper instrument according to the radiation fields to be measured.

In the past decades, the advancement of radiation detection technologies has been outstanding. Helium-3 gaseous detectors were considered as the gold standard. Recent discovery and development of novel radiation detection materials are beginning to challenge this standard. New materials, such as the elpasolite  $Cs_2LiYCl_7:Ce^{3+}$  (CLYC), offer the ability to perform gamma-ray spectroscopy with an energy resolution better than that of NaI, to detect and perform fast neutron spectroscopy, and be able to discriminate gamma and neutron particle in a single scintillator. Scintillators are typically coupled to photomultiplier tubes (PMTs) as readout. However, recent development in the electronic readout lead to the choice of solid state (silicon) photomultipliers (SiPMs) for building a small size neutron probe, extremely compact, light and robust.

This thesis will therefore be organised in the following 6-chapter structure. General methodology of neutron detection as well as the definition of the radiation protection quantities are given in chapter 1. The chapter 2 presents the working principle of conventional detectors used in radiation protection and the two installations where most of the measurements were performed: the CERN calibration laboratory (CALLAB) and the CERN-EU high energy reference field facility (CERF).

The 3<sup>rd</sup> part of the thesis presents an intercomparison at CERF, a workplace reference field that simulates the neutron spectrum encountered in the proximity of high-energy accelerators and at commercial flight altitudes, with a range of instruments usually employed at high energy particle accelerators. Before being used at CERF, the detectors were characterized and calibrated in the CALLAB. Particular attention was given to the reference detector of the CERF field, the LINUS that was tested for the first time in an aircraft campaign in Prague. The CERF intercomparison campaign allowed to understand the behaviour of the different detector and quantify their over/underestimations with respect to the reference ambient dose equivalent function. Moreover, these experimental data were used to benchmark the new FLUKA simulation performed in 2017. This work aimed at properly characterizing the neutron radiation field in order to start the facility accreditation process as reference workplace field.

The chapter 3 and 4 are based on the investigation of a fast neutron detector for a novel radiation survey meter (called B-RAD) able to operate in the presence of a strong magnetic field, to be used for radiation surveys e.g. in the LHC experimental areas. The new prototype is based on a CLYC scintillator coupled with a large SiPM array. The design and the development of an electronic board as well as the characterization of the SiPM performance compared to the PMT are discussed in the chapter 4. The performance of the prototype detector in term of neutron/gamma discrimination capabilities, linearity, efficiency are detailed in chapter 5. The scintillation mechanism and the decay times when coupling the CLYC with the PMT and the SiPM are intercompared to better understand the SiPM effect on the system. Finally the chapter 6 discussed two new materials: the stilbene and the EJ-276. Despite the fact that the spectroscopy is not possible without intensive unfolding methods with these scintillators, they have a higher fast neutron efficiency compare to the CLYC.

# Chapter 1 Background and literature review

This chapter discusses the main principle of slow and fast neutron detection, based on material and nuclear interactions of interest. Since neutrons always produces secondary gamma rays by interacting either with detector materials or with surrounding materials, the gamma interaction with matter are briefly developed. In addition an overview of the common detection methods for slow and fast neutron are presented. Finally the system of radiation protection quantites is described. These informations are pertinent for understanding the science and the engineering behind the development of neutron detectors.

## 1.1 Interaction of gamma rays with matter

Gamma rays are photons and have no electric charge and no rest mass. The interaction of gamma rays leads to the partial or total transfer of their energy to electrons. As a result, the photon either disappears or is scattered with a significant angle. These sudden processes contrast with the continuous slowing down of heavy charged particles or electrons through subsequent interactions. The electrons produced during an interaction with the detector allows the gamma detection.

There are three important mechanisms from the point of view of radiation protection: Photoelectric absorption, Compton scattering and Pair production. The relative importance of these effects depends on the atomic density of the material ( $Z$ ) and on the energy of the photon (Figure 1.1).

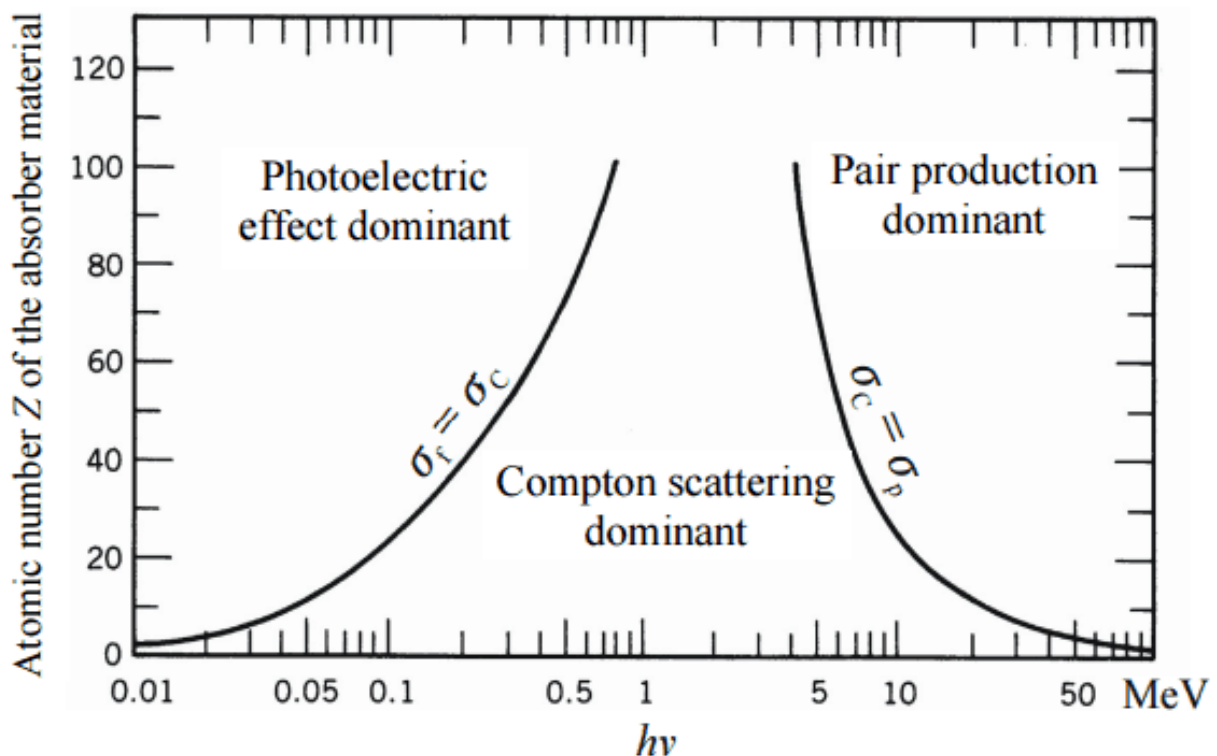


Figure 1.1 The relative importance of the three major interaction mechanisms of gamma rays with matter. The lines shows the values of  $Z$  and energy  $h\nu$  for which the two neighbouring effects are equal [1].



- Photoelectric absorption

A photon undergoes an interaction with an absorber atom; it loses all its energy and disappears. An electron, called photoelectron, is ejected from the atom from one of its shells. The photoelectron appears with an energy equal to the difference between the incident photon energy and the binding energy of the photoelectron in its shell. In addition, the vacancy created by the photoelectron is quickly filled by electron rearrangement. Thus, the binding energy is liberated in the form of X-ray or Auger electron. The total electron energy, however, will always be equal to the initial photon energy involved and will appear as a peak in spectrum measurement. This effect is dominant at low energy gamma rays and enhanced with increasing  $Z$  of the material.

- Compton scattering

In this process, the photon transfers a portion of its energy to the electron and is then deflected with an angle  $\theta$  from its original direction. Depending on the scattering angles, the energy transfer to the electron varies from 0 to a large fraction of the gamma ray energy. The energy of the scattered gamma ray is reduced from the initial value and the direction of propagation is changed as described by the equation 1.1 below:

$$hv' = \frac{hv}{1 + \frac{hv}{m_0c^2}(1 - \cos \theta)} \quad \text{and} \quad E_e = hv - hv' \quad (1.1)$$

where  $hv$  is the energy of the incident gamma ray,  $hv'$  is the energy of the scattered gamma ray,  $m_0$  is the rest mass of the electron,  $c$  is the velocity of light, and  $\theta$  is the angle at which the gamma ray is scattered.  $E_e$  is the Compton electron energy, which is equal to the difference between the energy of the photon before and after the interaction. For a grazing angle  $\theta \approx 0$ , the energy of the Compton electron is minimal while for a head-on collision ( $\theta \approx \pi$ ) it is maximal. In spectroscopy, the Compton is represented as a continuum of energy between 0 and the Compton edge ( $\theta \approx \pi$ ). The Compton effect is the predominant at intermediate gamma energies.

- Pair production

A photon with energy exceeding twice the rest mass energy of an electron (1.022 MeV) may also interact in the field of a nucleus to produce an electron-positron pair. The photon disappears, with the excess energy shared between the electron and positron. The positron eventually meets another electron and annihilates, producing a pair of approximately back-to-back 511 keV gamma rays. In the spectrum, this process corresponds to the double escape peak or single escape peak, depending on geometry and density and the material.

## 1.2 Interaction of neutrons with matter

Similar to the photon, the neutron lacks an electric charge, and therefore it is not subject to Coulomb interactions with electrons and nuclei in matter. A neutron will penetrate in matter until it undergoes a strong interaction with a nucleus. This hadronic interaction has a very short range, which means that the neutrons have to pass close to a nucleus for an interaction to occur. Because of the small size of the nucleus in relation to the atom, neutrons have a low probability of interaction and can therefore travel considerable distances in matter.

When a neutron interacts with an atomic nucleus, the neutron can be scattered (deflected or slowed down) or captured (absorbed). The relative probability or cross section of the various types of neutron interactions changes dramatically with the neutron energy. A summary of the different neutron interaction is presented in Figure 1.2. Different classifications exist, an example of one is given in Table 1.1. However, it is generally considered that that the neutrons are ‘slow’ when they have a kinetic energy of less than 0.5 eV (cadmium cut-off energy<sup>1</sup>) and ‘fast’ when they have energy higher than this value.

---

<sup>1</sup> It is the energy value taken as a boundary between the low energy neutron that are absorbed by a cadmium sheet and the higher energy neutrons that are not absorbed.

Table 1:1 Classification of neutron in function of the energy ranges. [2].

Category	Energy
Thermal	< 0.1 eV
Epithermal	0.1 - 10 eV
Intermediate	10 eV - 100 keV
Fast	100 keV - 100 MeV
High-energy	> 100 MeV

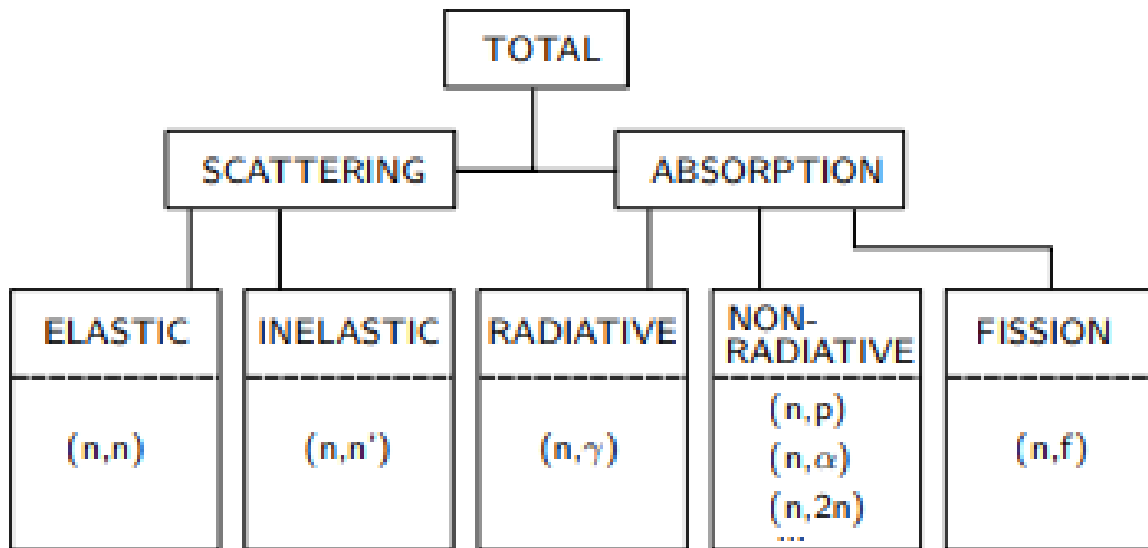


Figure 1.2 Summary of neutron interaction with matter [2].

### 1.2.1 Fast neutrons

The probability of most capture reactions potentially exploitable by a detector drops-off rapidly with increasing neutron energy. However, the importance of scattering becomes greater because of the amount of energy that can be transferred in one collision. Fast neutrons mainly interact by scattering. According to the neutron energy, two types of scattering reactions can occur: elastic (<10 MeV) and inelastic (>10 MeV).

- Elastic scattering

In an elastic scattering process between an incident neutron and a target nucleus, neutrons are scattered by light nuclei, transferring a portion of their kinetic energy to the target nucleus, resulting in a recoil nucleus. This process is particularly important because it can occur for any neutron energy without threshold. In addition, the elastic scattering is responsible for the moderation of fast neutrons. Indeed, for incoming neutrons with nonrelativistic kinetic energy ( $E_n \ll 1$  GeV), conservation of momentum and energy in the laboratory coordinate system gives the following relation (1.2) for the energy of the recoil nucleus:

$$E_r = E_n \frac{4A}{(1+A)^2} (\cos^2 \theta) \quad (1.2)$$

where  $A$  is the mass of the target nucleus (neutron mass if the target is a proton),  $E_n$  the incoming neutron kinetic energy,  $E_r$  the recoil nucleus kinetic energy and  $\theta$  its scattering angle.

From equation 1.2, two conclusions can be drawn:

-When the neutron is deflected only slightly, the recoil is emitted almost perpendicular to the incoming neutron direction and the recoil energy is near zero. At the other extreme, a head-on collision of the incoming neutron with the target nucleus will lead to a recoil in the same direction.

- To slow down the velocity of the neutron with the fewest number of collisions, a light target nucleus (small A) should be used. The greatest average energy transfer occurs with a neutron-proton collision:  $E_r = E_n/2$ . Thus, the most hydrogenated materials used to moderate neutrons are water, paraffin and polyethylene.

- Inelastic scattering

In an inelastic scattering process, the incident neutron enters the nucleus for a brief period and forms a compound nucleus. The compound nucleus will then emit a neutron and a gamma ray photon, and thus will be reverting to the target nucleus. The direction of the emitted neutron is more or less random. A distinction between the elastic and inelastic scattering is that elastic scattering can occur at any neutron energy while the inelastic process requires excitation of the nucleus and is most probable for fast neutrons (via threshold reactions).

- Spallation (n, xn)

This reaction occurs when an energetic incident neutron ( $> 100$  MeV) interacts with a heavy target nucleus. This results in emission of a number of neutrons represented by 'x'. If two neutrons are emitted, it is then (n, 2n) reaction.

### 1.2.2 Slow neutrons

In an absorption reaction, neutrons are absorbed by the nucleus, and as a result can release a significant amount of energy into that nucleus. The combined neutron + nucleus system, referred to as a compound nucleus, is often in an excited state and can go back to ground state through a number of different pathways.

- Radiative capture (n,  $\gamma$ )

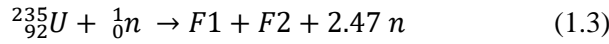
It is a nuclear reaction in which a target nucleus absorbs a neutron and then emits a cascade of gamma rays. The target nucleus and the product nucleus are isotopes of the same element. The heavier isotope that results may be radioactive, so that neutron capture, which occurs with almost any nucleus, is a common way of producing radioactive isotopes. Neutron capture is also named *neutron-gamma*, or ( $n, \gamma$ ), reaction from the bombarding particle and the emitted particle and sometimes called *neutron radiative capture* because of the prompt emission of only electromagnetic radiation. It is the most probable nuclear reaction for thermal neutrons. Among the natural elements, boron, cadmium, and gadolinium are the best absorbers of slow neutrons by the capture process.

- Transmutation (n, p) or (n,  $\alpha$ )

The compound nucleus can de-excite emitting a charged particle either a proton or an  $\alpha$ . As the remaining nucleus is different from the incident nucleus, this process allows the transformation of an element to another. This process can also be called *non-radiative capture*.

- Fission

When a neutron interacts with a heavy nucleus ( $Z \geq 92$  for thermal neutrons), the compound nucleus may usually split into two daughter nuclei of lighter mass (fragments). This process always releases one or more fast neutrons that in turn, can trigger other fissions in a self-sustained nuclear chain reaction. Controlled chain reactions are usually used in nuclear reactors for research and power generation. Only a few nuclides can fission with thermal neutrons. Among them, there is only one naturally occurring fissile nuclide:  $^{235}\text{U}$ . The following reaction 1.3 takes place:



where F1 and F2 indicate the two fission fragments. The energy liberated in a neutron fission reaction is of great importance and is commonly called Q-value. The Q-value is equal to 207 MeV, which is extremely large compared with those of the previous reactions. The total energy produced in this reaction is distributed to both neutrons and fission products; in particular, about 168 MeV is the typical kinetic energy of the two fragments. The cross sections of  ${}^{233}\text{U}$  and of isotopes  ${}^{239}\text{Pu}$  and  ${}^{241}\text{Pu}$  of plutonium are relatively large at low neutron energies but none of these is present in nature. Fissionable nuclides (i.e nuclei that can induced fission but only with incident neutron of energy higher than a certain threshold) also exist ( ${}^{238}\text{U}$  and  ${}^{240}\text{Pu}$ ).

## 1.3 Neutron detection

### 1.3.1 Slow neutron detectors

Because of the small kinetic energy of slow neutrons, very little energy can be transferred to the nucleus via elastic scattering. However, these interactions bring the slow neutrons into thermal equilibrium with the medium. Once thermalized they can undergo an absorption process and be indirectly detected through the energy deposited by the reaction product. One important factor to consider for neutron detection is the cross section of the reaction that should be as large as possible so that efficient detectors can be built with small dimensions. Secondly, intense fields of gamma rays are also produced along with neutrons and the detector should be able to discriminate these particles in the detection process. The higher the Q-value, the greater the energy given to the reaction products, and the easier the task of discriminating against gamma ray events using sample amplitude discrimination. All the slow conversion reactions are exothermic so that the kinetic energy of the reaction products is determined only by the Q-value of the reaction. Common reactions for slow neutrons are listed in Table 1.2.

**Table 1.2 Absorption reaction of nuclear reaction of interest for slow neutron detection [3].**

Absorption reaction	$\sigma_n$ (barn)
${}^3_2\text{He} + {}^1_0\text{n} \rightarrow {}^3_1\text{H} (0.191 \text{ MeV}) + {}^1_1\text{p} (0.574 \text{ MeV})$	5330
${}^{10}_5\text{B} + {}^1_0\text{n} \rightarrow {}^4_2\text{He} (1.47 \text{ MeV}) + {}^7_3\text{Li} (0.84 \text{ MeV}) + \gamma (0.48 \text{ MeV})$	3840
${}^{10}_5\text{B} + {}^1_0\text{n} \rightarrow {}^4_2\text{He} (1.78 \text{ MeV}) + {}^7_3\text{Li} (1.01 \text{ MeV})$	
${}^6_3\text{Li} + {}^1_0\text{n} \rightarrow {}^3_1\text{H} (2.73 \text{ MeV}) + {}^4_2\text{He} (2.05 \text{ MeV})$	940
${}^{155}_{64}\text{Gd} + {}^1_0\text{n} \rightarrow {}^{156}_{64}\text{Gd} + \gamma (0.09, 0.20, 0.30 \text{ MeV}) + e^-$	60791
${}^{157}_{64}\text{Gd} + {}^1_0\text{n} \rightarrow {}^{158}_{64}\text{Gd} + \gamma (0.08, 0.18, 0.28 \text{ MeV}) + e^-$	255011

#### 1.3.1.1 Detector based on the ${}^3\text{He} (n, p){}^3\text{H}$ reaction

The proportional counters filled with  ${}^3\text{He}$  are the ‘gold standard’ thermal neutron detectors since  ${}^3\text{He}$  has a large capture cross section for thermal neutrons and a negligible sensitivity to  $\gamma$  rays. Because  ${}^3\text{He}$  is a noble gas, no solid compounds can be fabricated and it must be used in gaseous phase. The products of the reaction are emitted in opposite directions. If the detector size is sufficiently large, all the kinetic energy of the proton and recoil  ${}^3\text{H}$  nucleus is deposited in the detector gas. However, if the neutron interaction takes place in the gas close enough to one wall of the detector chamber, either the proton or  ${}^3\text{H}$  strikes the wall and leaves the detector volume. As a result, the spectrum shows two peaks at 191 keV and 574 keV corresponding to the loss of the  ${}^3\text{H}$  or proton energy respectively (Figure 1.3). In order to decrease this wall-effect, besides to increase the detector size, the range of the charge reaction products needs to be reduced. The first method is to increase the gas pressure inside the detector. The second is to add a small amount of a heavier gas (such as Krypton or Argon) to  ${}^3\text{He}$  to provide an enhanced stopping power.  ${}^3\text{He}$  detector usually operate at 700-1500 V and work in pulse-readout mode where neutron and gamma rays signal are distinguishable by their amplitude. Noise and  $\gamma$  ray events can be discriminated with an adequate electronic threshold.

One of the main issues with  $^3\text{He}$  filled gas detector is that within the last few years, the availability of  $^3\text{He}$  gas for use in neutron detector has decreased while the demand has significantly increased, especially for homeland security applications. Other alternative are actually used such as the boron trifluoride filled ( $\text{BF}_3$ ) detector.

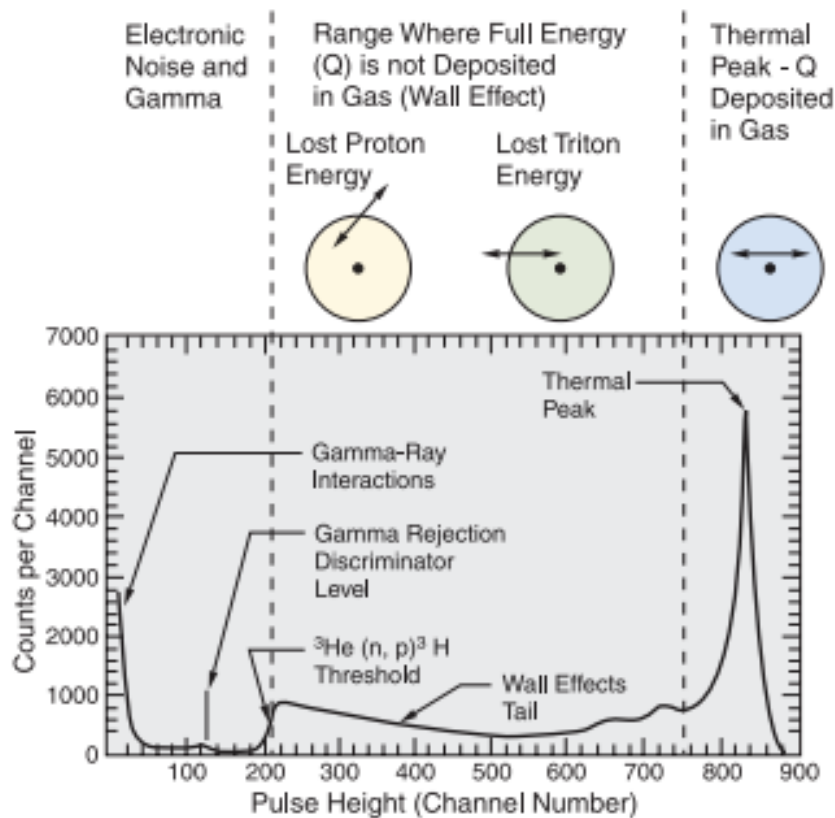


**Figure 1.3** Pulse height spectrum of  $^3\text{He}$  proportional counter [4].

### 1.3.1.2 Detector based on $^{10}\text{B}(n, \alpha)^7\text{Li}$ reaction

This is one of the most popular reactions for the conversion of slow neutrons.

The branching in the reaction indicates that the product  $^7\text{Li}$  either may be left in its ground state or in its first excited state. When thermal neutrons (0.025 eV) are used to induce the reaction, about 94% of all reactions lead to the excited state, emitting a photon with  $E = 478$  keV, and only 6% directly to the ground state. In both cases, the Q-value of the reaction is very large compared to the neutron incoming energy, so that the energy imparted to the reaction products is essentially the Q-value itself and thus it is impossible to extract any information on the original neutron energy. Boron can be used both in the form of a solid coating on the inner walls of a conventional proportional counter, and in the form of  $\text{BF}_3$  gas.

These detectors have some undesirable operation conditions such as a high operating voltage (1500-3000 V), which can cause electronic noise and gamma pulses that may exceed the threshold setting and generate false counts. The efficiency is lower compared to  $^3\text{He}$  (lower cross section) but the higher Q-value allows a better gamma/n discrimination.  $\text{BF}_3$  gas is less expensive than  $^3\text{He}$ , but in contrast it is toxic whereas  $^3\text{He}$  is an inert gas.

### 1.3.1.3 Detectors based on $^6\text{Li}(n, \alpha)^3\text{H}$ reaction

This reaction is widely used in neutron detection. The reaction only proceeds to the ground state. The products are emitted in opposite directions. It has a lower cross section than  $^{10}\text{B}$ , except at a salient resonance above 100

keV, in which the absorption cross section surpasses that of  $^{10}\text{B}$  (Figure 1.4). The lower cross section is generally a disadvantage but is partially offset by the higher Q-value resulting in greater energy given to the reaction products.

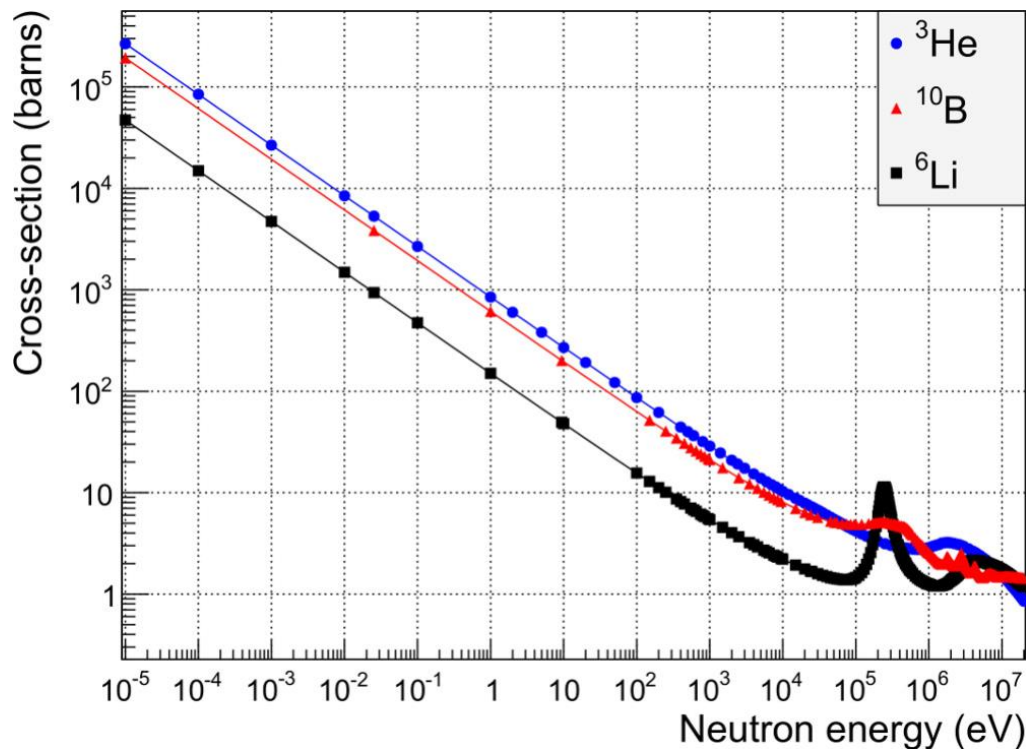


Figure 1.4 Cross section for  $^3\text{He}$ ,  $^{10}\text{B}$  and  $^6\text{Li}$  for increasing neutron energy. All cross sections show a  $1/v$  energy dependence [5].

Because a stable lithium-containing proportional gas does not exist, a lithium equivalent of the  $\text{BF}_3$  detector is not available. The more common application of this reaction employs the scintillation process. The pulse height response is free of wall effects because the distances the particles travel are very short in comparison with the size of the Li crystal. The gamma ray rejection is inferior to that of typical gas filled detectors, in which a gamma ray can deposit only a small fraction of its energy. Similar to NaI, the LiI crystal is sensitive to water vapour and it must be sealed in a canning material for its protection. Other recipes for Li containing scintillators have achieved some popularity such as a LiF dispersed in a matrix of  $\text{ZnS}(\text{Ag})$  with thickness of 0.6 mm. They are commercially available and offer a very effective gamma discrimination with an efficiency quoted as 25-30% (1 eV neutron).

#### 1.3.1.4 Detectors based on gadolinium neutron capture reaction

The cross section for thermal capture of these reactions are among the highest for any material. They result in reaction products that include low energy gamma rays and conversion electrons. Because they are directly ionizing, fast electrons are useful in the application of this reaction for neutron detection, the most significant one is the 72 keV electron, which is emitted in 39% of the capture reactions. Gadolinium can be employed as a converter of incident neutrons into fast electrons that can be recorded in an adjacent detector (like a semiconductor-based detector). However, there are two fundamental drawbacks of gadolinium. On one hand, the range of the conversion electron is limited to only a few microns, reducing the probability of the products to reach the sensitive volume of the detector. On the other hand, the low energy of the product (low Q-value) leads to difficulties to distinguish neutrons from the gamma background and electronic noise. Consequently, the gadolinium is not widely used.

### 1.3.1.5 Detectors based on neutron induced fission

A very important advantage of the fission-induced reactions is the very high Q-value (200 MeV) which mean that detectors based on the fission reaction can often give output pulses that are much larger than those induced from other reactions or incident gamma rays. These detectors show very low background and have excellent neutron- $\gamma$  discrimination capabilities. The most popular form of fission detector is an ionization chamber (with its inner surfaces coated with a fissile material) because the ionization caused by the fission fragments is sufficient to create signal and no further charge multiplication within the detector is necessary.

Almost all fissile nuclides are naturally alpha-emitters and thus detectors containing these isotopes also show an output signal due to alpha particles that represent an undesirable background. However, their energy is lower than the one released in a fission reaction. For this reason, it is sufficient to insert an appropriate threshold in the acquisition system to discard the alpha contribution. The size of the fission counter does not have to be very large because the fragments can travel only half the distances 5 MeV alpha particles can.

### 1.3.2 Fast neutron detectors

As we go higher in the neutron energy range, the probability that a neutron will be absorbed, becomes smaller. When the purpose of the measurement is simply to count fast neutrons without a measurement of their energy, a material that will slow down (or “moderate”) the fast neutrons is needed for detectors to be of useful efficiency. Hydrogen is often used for this purpose, and fast neutrons undergo elastic scattering while they are being slowed down. Such fast neutron detectors can employ moderator to convert neutrons to charged particles and then simply record all the pulses. Detectors of this type show a variation in efficiency with neutron energy.

However, an important distinction in the application of fast neutron detectors is the possibility to measure the energy of the incoming neutron. The energy of the reaction products varies significantly with incoming neutron energies and it is no longer negligible compared to the reaction Q-value. An accurate measurement of the reaction-product energies can then be used to deduce the incoming neutron energy simply by subtracting the reaction Q-value. These detectors do not required moderation and rely on neutron induced reaction, provided the incident neutron energy is high enough and the cross section of the reaction not negligible.

#### 1.3.2.1 Detector based on moderation

The inherently low detection efficiency for fast neutrons of any slow neutron detector can be improved by surrounding the detector with hydrogen-containing moderating material. The incident fast neutron can then lose a fraction of its initial kinetic energy in the moderator before reaching the detector as a low-energy neutron, for which the detector efficiency is much higher. By increasing the thickness of the moderator, the number of collisions will increase, leading to a lower value of the most probable energy when the neutron reaches the detector. One would therefore expect the detection efficiency to increase indefinitely with moderator thickness if this was the only factor under consideration. A second factor, however, tends to decrease the efficiency with increasing moderator thickness: the probability that an incident fast neutron ever reaches the detector will decrease, as the moderator is made thicker. The reason lies in the increased probability of a neutron to be thermalized and captured by the moderator, or escape from the surface of the moderator. Both probabilities, absorption and escaping, increase rapidly with increasing moderator thickness. To understand the effectiveness of a material as moderator, the moderating ratio  $MR$  was introduced in 1.4:

$$MR = \xi \Sigma_S / \Sigma_A \quad (1.4)$$

where  $\Sigma_S$  and  $\Sigma_A$  represent respectively the macroscopic scattering and absorption cross section, and  $\xi$  is the average logarithmic energy loss per collision [1]. Some example are given in Table 1.3:

**Table 1.3 Moderating powers and ratios of selected materials.**



Moderator	Moderating power $\xi \Sigma_S$ (1 eV - 100 keV)	Moderating ratio $\xi \Sigma_S / \Sigma_A$
Water	1.28	58
Heavy water	0.18	21000
Graphite	0.064	200
Polyethylene	3.26	122

Because of all these factors, the efficiency of a moderated slow neutron detector when used with a monoenergetic fast neutron source will show a maximum at a specific moderator thickness. By careful choice of the dimensions and composition of the moderator-detector system, its overall efficiency versus energy curve can often be shaped and tailored to suit a specific application.

- Bonner sphere spectrometer

One of the most famous detector based on neutron moderation is the Bonner spheres spectrometer (BSS). It consists of a thermal neutron detector located at the centre of a set of spherical polyethylene moderators of different diameter. The spherical geometry results in an isotropic response. To measure a neutron spectrum at a defined position, consecutive measurements should be made with each single sphere, which acts like an ‘integral’ device similar to a rem meter. Due to their different diameters, the spheres have different response functions and can thus provide different energy-integrated responses in the same neutron field. The incorporation of lead or other high Z element within the moderator increases the response to high-energy neutrons (up to GeV) through spallation reaction, where the response of conventional polyethylene sphere tends to fall off (the cross section of elastic scattering decreases significantly above 20 MeV). In addition, the insertion of a cadmium shell is used to reduce the sensitivity in the thermal energy range in order to have independent response functions.

There is no “best” BSS, it is always about a compromise. The choice of thermal detector and the number of sphere depends on the application. The CERN BSS [6] consists of seven spheres: five polyethylene spheres with outer diameter of 81, 108, 133, 178 and 233 mm, complemented by two other spheres, nicknamed Ollio and Stanlio, where cadmium and lead inserts were introduced. Their geometry is shown in Figure 1.5.

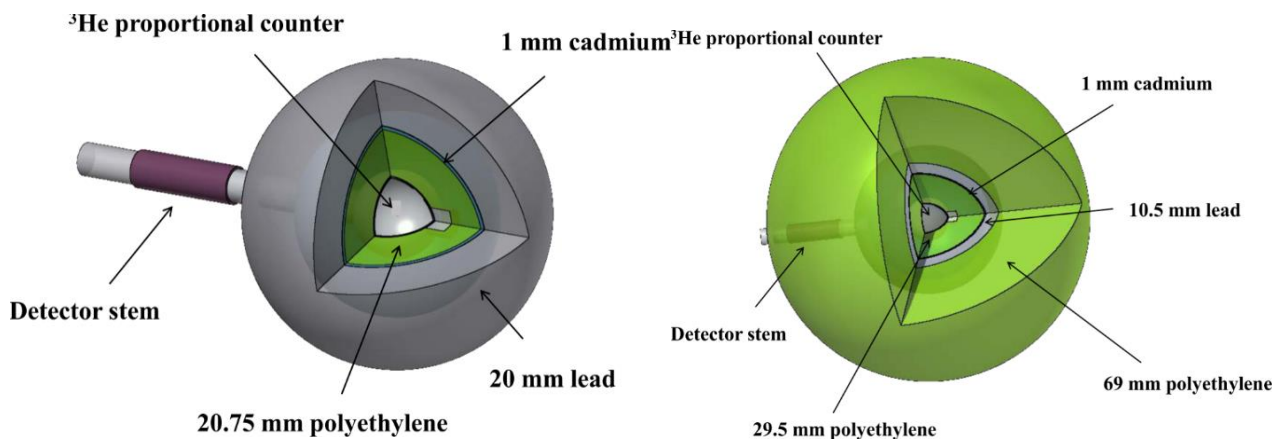


**Figure 1.5** Geometry of Stanlio (on the left) and Ollio (on the right).

The neutron fluence spectrum can then be determined from the set of readings via a mathematical procedure. The number of measured counts  $M_d$  by the detector  $d$  is related to the integral between the lower and upper energies of the detector response function  $R_d(E)$  and the neutron spectrum  $\phi_E(E)$  as written in the equation 1.5:

$$M_d = \int_{E_{min}}^{E_{max}} R_d(E) \phi_E(E) dE \quad (1.5)$$



The problem of deriving the neutron spectrum from a finite number of detectors ( $d$  is usually  $<10$ ) does not have a unique solution (i.e. a few points cannot determine a continuous function). The process of choosing a particular solution spectrum from the infinite number of spectra that fit the data is known as unfolding. To make this choice, additional criteria are needed to supplement the set of constraints imposed by the measurements. Generally, an ‘*a priori*’ information about the shape of the spectrum is supplied in the form of an initial guess spectrum, where the experimenter has some idea (may be only very approximate) about the shape of the spectrum to be determined. In order to unfold the spectrum, an initial trial spectrum is chosen, and modified using information from a set of measurements. Many deconvolution algorithms are used. In this work two unfolding codes were used: MAXimum Entropy Deconvolution (MAXED) [7] and GRAVEL [8].

The major advantage of the BSS is that it covers an energy range from thermal to GeV. No other spectrometer for use in radiation protection covers this entire energy range. Among its disadvantages are its inherently low energy resolution and its weight (up to 50 kg). In addition, the measurements are also time consuming and the spectral unfolding process is generally complex. BSS can be used, for example, in workplaces around nuclear reactors, high-energy accelerators, fabrication plants of radioactive sources, and at commercial flight altitude where the knowledge of neutron energy spectrum or dose is important.

### 1.3.2.2 Detector based on fast neutrons-induced reactions

These detectors have the advantage to have a fast response due to the fast reaction process (because the time taken by neutrons to undergo moderation is long) but they have cross sections orders of magnitude lower than the thermal reaction. Therefore, they inevitably show lower detection efficiency than their thermal neutron counterpart. This type of detector, which is probably the most common one in this field, directly detects the recoil nuclei produced in the elastic interactions. This technique has the advantage that the energy of the recoil nuclei is somehow dependent on the neutron energy, and thus it allows to perform neutron energy spectroscopy, not possible with other types of detector. One of the easiest way to detect neutron through neutron-induced reaction is based on scintillators. The popularity of scintillating materials is due to their versatility that allows them to be employed both for counting and for spectroscopy, to their fast response, especially in organic scintillators, to their relatively low cost (plastic and liquids) and, with the partial exception of plastic scintillators, to their capability to distinguish the type of radiation exploiting the Pulse Shape Discrimination (PSD) technique.

- Scintillators

Incident radiation interacts with a scintillator and produces detectable light (photons) proportional to the energy deposited in the scintillator. This light can then be detected by an optical readout unit such as a photomultiplier tube (PMT) or silicon photomultiplier (SiPM) and subsequently processed for analysis. All types of radiation produce light when interacting with a scintillator, but the process of how the light is created differs for each material.

When gamma rays interact with a scintillator either by the photoelectric effect, pair production or Compton scattering, electrons are produced that excite surrounding atoms. When these atoms de-excite, scintillation photons are emitted.

Fast neutrons interact with a scintillator by elastic scattering with hydrogen (protons) or carbon atoms. The imparted kinetic energy of the recoiling hydrogen or carbon atom is absorbed by the scintillator and scintillation photons are emitted.

For the case of thermal neutron interactions with a scintillator, the detectable light is created by yet another type of reaction. The  ${}^6\text{Li}$  embedded in some scintillators is commonly used for the detection of thermal neutrons. The  ${}^6\text{Li}(n, \alpha){}^3\text{H}$  reaction has an energy Q-value of 4.78 MeV; a 2.05-MeV alpha particle and a 2.73-MeV triton are emitted. The charged particles excite the atoms of the scintillator thus producing detectable light.

The working principle of scintillating materials is based on the emission of light pulses produced by the excitation and ionization of the material induced by ionizing radiations. These light pulses can be detected and used to achieve information about the particles originating them. At the basis of the scintillation process is the property called luminescence, which is the ability of a certain material to decay from an excited state through the emission of light. Depending on the type of material used for this application, scintillators are classified as inorganic scintillators or organic scintillators (organic scintillating crystals, liquid, plastic scintillators).

- Inorganic scintillators

Usually inorganic scintillators are inorganic crystals emitting light due to the presence of impurities or crystallographic defects. Their luminescence therefore is not an intrinsic property of the material itself, but comes from its crystallographic structure. For neutron detection, crystals based on Li compounds ( ${}^6\text{LiI:Eu}$ ,  $\text{LiBaF}_3$  and  $\text{Li}_6\text{Gd(BO}_3)_3\text{:Ce}$ ) have been developed.

A newly evolving group of cerium-activated fast inorganic materials known as elpasolites has shown encouraging scintillating performance capable of gamma ray and neutron detection simultaneously. The unique name elpasolite comes from a naturally occurring mineral originally found in El Paso County, Colorado. Elpasolites have the general formula  $\text{A}_2\text{B(RE)X}$  - where A and B are most often alkali metals, RE is a rare-earth metal, transition metal, or other trivalent ion, and X is a halogen ion [9]. Many elpasolites also contain cerium as an activator. Several elpasolite materials have been studied, investigating their gamma ray energy resolution, decay time, absolute light yield and pulse shape discrimination capabilities. These elpasolites include  $\text{Cs}_2\text{LiYCl}_6\text{:Ce}$  (CLYC),  $\text{Cs}_2\text{LiLaCl}_6\text{:Ce}$  (CLLC),  $\text{Cs}_2\text{LiLaBr}_6\text{:Ce}$  (CLLB), and  $\text{Cs}_2\text{LiYBr}_6\text{:Ce}$  (CLYB) among many others. A great amount of attention and effort has been invested in CLYC due to its excellent pulse shape discrimination capabilities. The CLYC can be enriched with either  ${}^6\text{Li}$  or  ${}^7\text{Li}$ . The presence of  ${}^6\text{Li}$  greatly increases the thermal neutron cross-section and thus leads to high thermal neutron detection efficiency. In contrast, in the CLYC with  ${}^7\text{Li}$ , the detection of thermal neutrons is suppressed, enhancing the detection of fast neutron through the following reactions 1.6 and 1.7 on chlorine (Fig. 1.6):

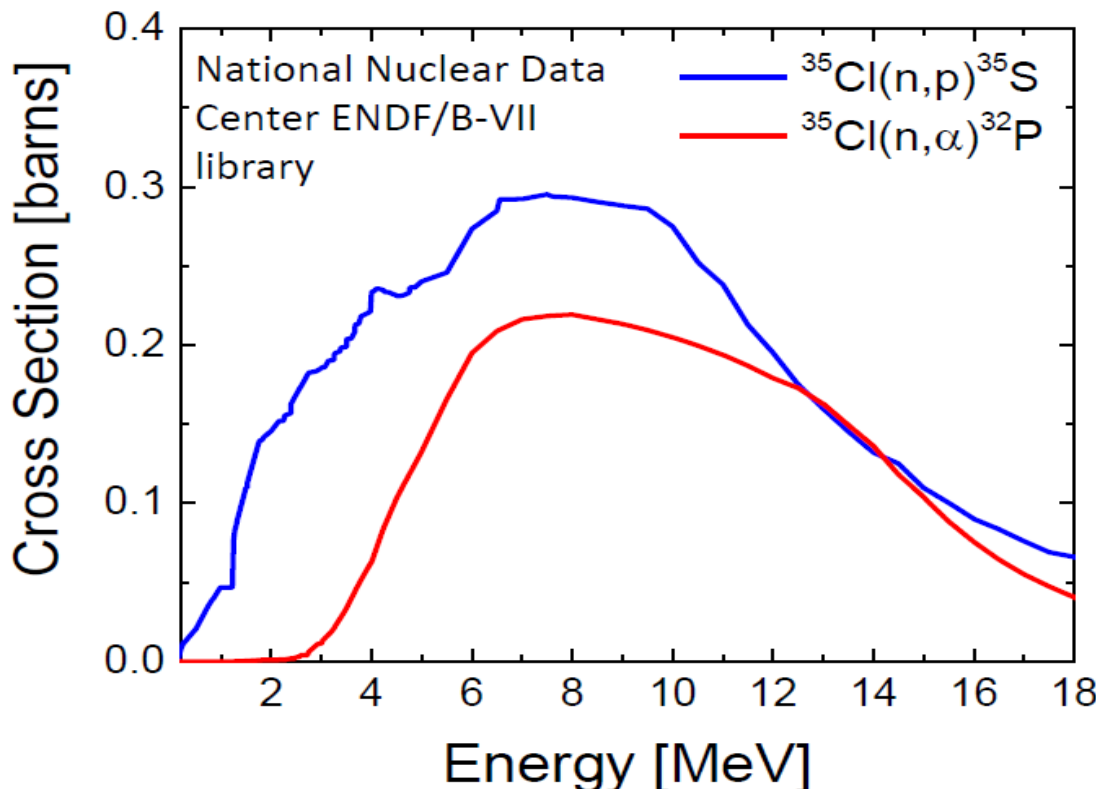
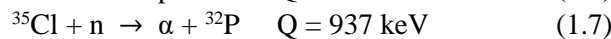
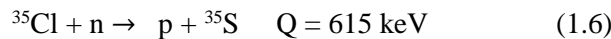


Figure 1.6 Cross section of neutron-capture reactions on  ${}^{35}\text{Cl}$  [10].

The energy deposition of the products linearly depends on the energy of the incident neutron. Thus, neutron spectroscopy without resorting to an unfolding code is possible up to 10 MeV. Above this energy, other channel reactions open and the fast neutron spectroscopy becomes more difficult.

The main advantages of inorganic scintillators are their high light output, good linearity, good energy resolution, high stopping power due to their high density, and radiation hardness. They have however in many cases the drawback of having a slow decay time and of being highly hygroscopic. Furthermore, the crystal growth technique used to produce them is not trivial and does not allow the fabrication of large size crystals. This makes these materials much more expensive than their plastic or liquid counterparts and more difficult to produce.

- Organic scintillators

Organic scintillators are generally made of hydrogen and carbon atoms. Due to its low density and low atomic number, organic scintillators have been predominantly used as fast neutron detectors. Low cost and ease of fabrication make organic scintillators, specifically plastic scintillators, highly desirable. Depending on their physical form, organic scintillators can be mainly divided into three classes: pure crystals, plastic and liquid scintillators. Liquid scintillators are out of the scope of this study.

The fluorescence mechanism in organic materials arises from transitions in the energy levels of a single molecule and therefore the fluorescence can be observed independently of their physical state (in contrast with inorganic scintillators, which require a regular crystalline lattice).

The  $\pi$ -electronic energy levels of molecule is illustrated in figure 1.7. Energy transitions made by these  $\pi$ -electrons provide the mechanism behind organic scintillation. Energy from a charged particle is absorbed and excites the electron into a variety of excited states. A series of singlet states (spin = 0) are labelled  $S_1, S_2, S_3$ , and correspond to paired electrons which remain paired also in case of excitation. A similar set of triplet (spin = 1) electronic levels are also shown as  $T_1, T_2, T_3$ . They correspond to unpaired electrons of parallel spin. For organic scintillators the spacing between  $S_0$  and  $S_1$  is 3 to 4 eV, the spacing between the upper states is much smaller. Each of the S levels is subdivided into a series of levels with much finer structure (corresponding to the vibrational states of the molecule). The typical spacing is 0.15 eV. A second subscript is often added to distinguish these vibrational states, and the symbol  $S_{00}$  represents the lowest vibrational state of the ground electronic state.

At room temperature, nearly all molecules are in  $S_{00}$  (the average thermal energy 0.025 eV is small compared with vibrational spacing states). When the charged particle passes through, kinetic energy is absorbed by the molecules and electrons are excited to the upper levels. The higher states  $S_2, S_3$ , de-excite quickly (picoseconds) to the  $S_1$  state through radiationless transitions (internal conversion). States such as  $S_{11}, S_{12}$  that have extra vibrational energy and are not in thermal equilibrium with neighboring molecules, quickly lose energy. After negligibly short time a population of excited molecules in the  $S_{10}$  state is produced as the net effect of the excitation process. Scintillation light, prompt fluorescence, is emitted in transitions between  $S_{10}$  and the ground state. The prompt fluorescence intensity at time  $t$  following excitation is described by 1.8:

$$I = I_0 e^{-t/\tau} \quad (1.8)$$

where  $\tau$  is the fluorescence decay time for the  $S_{10}$  level. In most organic scintillators,  $\tau$  is the order of a few nanoseconds (1-80 ns [11]) therefore organic scintillators are fast.

In addition, two other processes compete with the prompt fluorescence [1]:

- Phosphorescence: through a process called intersystem crossing, some excited singlet states may be converted into triplet states. The lifetime for the T1 state is much longer than the S1 state (ms). The de-excitation from T1  $\rightarrow$  S0 transitions gives rise to phosphorescence.

- Delayed fluorescence: two triplet states in close proximity may interact to produce an excited singlet in a process called triplet-triplet annihilation. The singlet state may then decay as normal to produce delayed fluorescence. In conditions where the triplet annihilation process is significant, the scintillation output exhibits an additional slow component with time constants greater than 100 ns, but with wavelengths similar to the prompt component. This process represents the origin of the delayed fluorescence observed for organics.

Figure 1.7 explains why organic scintillators can be transparent to their own fluorescence energy. All the fluorescence transitions have a lower energy than the minimum required for excitation, there is a very little overlap between the optical absorption and emission spectra (often called Stokes shift) and consequently little self-absorption of the material.

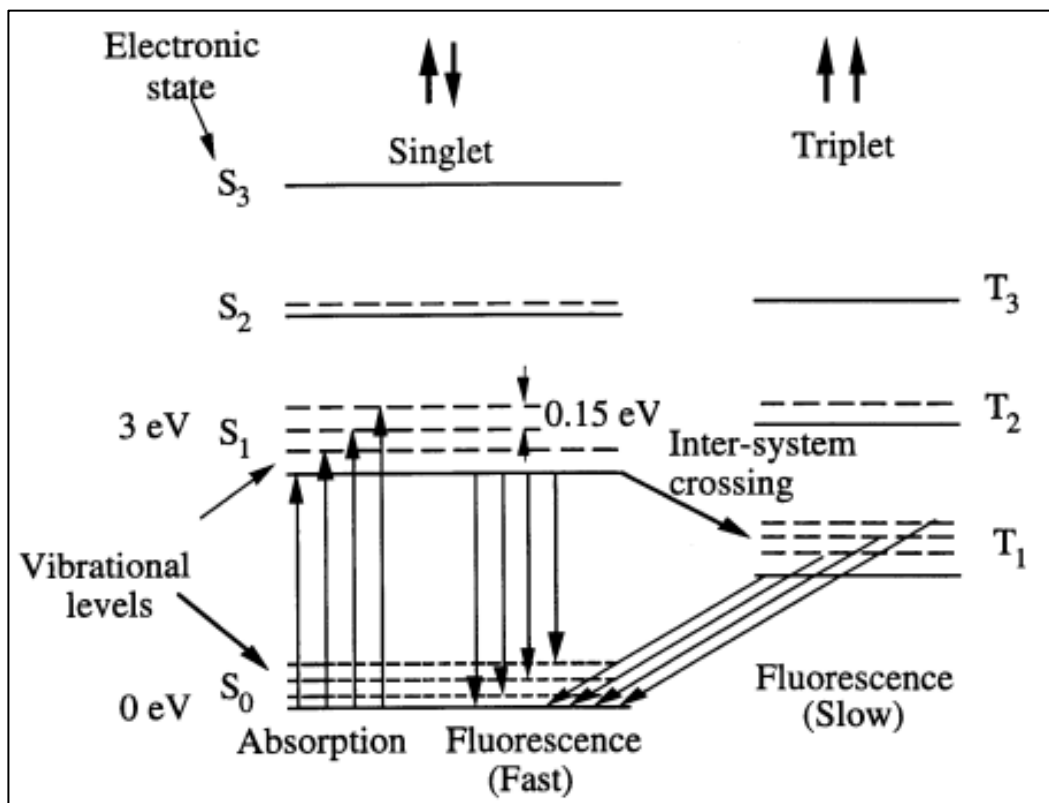


**Figure 1:7** Energy levels of an organic molecule with  $\pi$  structure [12].

We can classify different combinations of organic scintillators as unitary, binary, ternary or higher order, according to the number of compounds they contain. The ideal unitary system is a pure monocrystal scintillator such as anthracene or stilbene. Typical binary systems might be a liquid or a plastic scintillator consisting of a solute dissolved in a solvent. The solute is chosen such that its excited states have lower excitation energies than the corresponding solvent levels, playing a role similar to the activators in the inorganic scintillators. Once the solvent is excited by the ionising particle, the excitation energy of the solvent state is efficiently transferred to the corresponding solute state, i.e. the solvent  $S_1$  to the solute  $S_1$ .

Ideally, the characteristics that a scintillator should have are [1]:

- High scintillation efficiency
- Linearity between particle energy and light output
- High transparency, especially at the emission wavelength
- Emission wavelength matching the maximum sensitivity of the photodetector
- Fast decay time
- High manufacturability also in large volumes
- High refractive index (close to that of photodetector window)
- Low cost

- Pulse shape discrimination

At present, no material possesses these properties all together and for this reason, several scintillators exist, that are optimized for different specific applications and for the detection of different types of radiation.

In this work one pure organic and one plastic scintillator will be studied: the stilbene and the EJ-299.

## 1.4 Radiation protection quantities

Radiation protection is defined by the International Atomic Energy Agency (IAEA) as "the protection of people from harmful effects of exposure to ionizing radiation, and the means for achieving this". In a world where ionizing radiation is widely used in industry, medicine and research, and can present a significant health hazard by causing microscopic damage to living tissue, the determination of the dose (as more precisely defined below) is essential. In all fields where there is a need for quantitative measurements, it is necessary to have understandable and precise quantities and units.

In the field of radiation dosimetry and radiation protection, two international organisations are active in relation to quantities and units: The International Commission on Radiation Units and Measurements (ICRU), which is mainly working with the physical aspects of dosimetry, and the International Commission on Radiological Protection (ICRP), which mainly works with assessments and quantification of the biological effects of radiation and provides recommendations and guidance on all aspects of radiation protection against ionising radiation. The goal of the current system of quantities and units is to assess the biological effects resulting from external and internal exposures to ionising radiation in terms of stochastic (cancer induction, genetic effects) as well as deterministic effects (tissue effects) in order to control these effects.

As discussed by Stadtmann [13], various dose quantities have been designed by ICRP and ICRU to meet the need to protect human beings (protection quantities) and operational dose quantities which are designed for use in radiation measurements of external irradiation (operational quantities). All dose quantities are based on physical quantities.

### 1.4.1 Basic physical quantities

They are measurable and can be defined at any point of the radiation field. They allow field characterization: fluence, dose. The fluence  $\Phi$  is the number of incident particles  $dN$  traversing a sphere of cross-sectional area  $dS$  (see equation 1.9). The unit of the fluence is  $\text{cm}^{-2}$ .

$$\Phi = \frac{dN}{dS} \quad (1.9)$$

The absorbed dose  $D$  is the quotient of  $d\varepsilon$  over  $dm$ , where  $d\varepsilon$  is the mean energy imparted by ionising radiation to matter of mass  $dm$  (see equation 1.10). Its unit is Joule/kg and take the special name Gray:

$$D = \frac{d\varepsilon}{dm} \quad (1.10)$$

These quantities cannot be used for dose limitations because on the one hand, for a same dose the biological effects are different according to the radiation type (e.g., neutrons, photons, alpha particles, protons...); on the other hand, the tissues have different radio-sensitivity. To take into account this limitation, protection quantities were introduced.

### 1.4.2 Protection quantities

The protection quantities form the basis for dose limitation. These quantities are not directly measurable. The following two protection quantities are recommended by the ICRP: Equivalent dose  $H_T$  (for individual organs and tissues) and Effective dose  $E$  (for the whole body). The unit of the protection quantities is joule per kilogram ( $\text{J}\cdot\text{kg}^{-1}$ ) and its special name is Sievert (Sv). These quantities consider both the different biological effectiveness for different types of radiation by the introduction of a radiation weighting factor,  $W_R$ , and the different radiation

sensitivity of organs and tissues by the introduction of a tissue-weighting factor,  $W_T$ . The equivalent dose  $H_T$  is the absorbed dose in an organ or tissue T multiplied by the relevant radiation-weighting factor  $W_R$  due to radiation R (Table 1.4) as described by the equation 1.11:

$$H_T = \sum_R D_{T,R} \times W_R \quad (1.11)$$

As defined in equation 1.12, the effective dose, E, is a summation of the equivalent doses in tissue  $H_T$ , each multiplied by the appropriate tissue-weighting factor  $W_T$  (Table 1.5):

$$D = \sum_T H_T \times W_T \quad (1.12)$$

These human body-related protection quantities, equivalent dose in an organ/tissue and effective dose, are not measurable. To overcome these practical difficulties for external irradiation, ICRU has introduced and defined a set of operational quantities, which can be measured and which are intended to provide a reasonable estimate for the protection quantities avoiding both underestimation and too large overestimation.

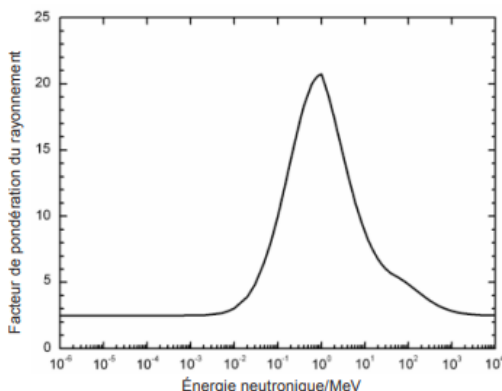
The operational quantities are based on point doses determined at locations in defined phantoms. One such phantom is the ICRU-sphere [14]. It is a sphere of 30 cm diameter with a density of 1 g/cm<sup>3</sup> and a mass composition of 76.2% oxygen, 11.1% carbon, 10.1% hydrogen and 2.6% nitrogen.

**Table 1.4 Recommended radiation weighting factors from ICRP 103 (2007) [15].**

Radiation type	Radiation weighting factor, $w_R$
Photons	1
Electrons and muons	1
Protons and charged pions	2
Alpha particles, fission fragments, heavy ions	20
Neutrons	A continuous function of neutron energy (Fig.1.8)

**Table 1.5 Tissue weighting factors (ICRP 2007) [11].**

Tissues	$W_T$	$\Sigma W_T$
Active bone marrow, colon, lungs, stomach, breasts and remainder tissues <sup>2</sup>	0.12	0.72
Gonads	0.08	0.08
Bladder, oesophagus, liver and thyroid	0.04	0.16
Bone surface, brain, salivary glands and skin	0.01	0.04
Total		1



$$w_R = \begin{cases} 2,5 + 18,2 e^{-[\ln(E_n)]^2/6}, & E_n < 1 \text{ MeV} \\ 5,0 + 17,0 e^{-[\ln(2E_n)]^2/6}, & 1 \text{ MeV} \leq E_n \leq 50 \text{ MeV} \\ 2,5 + 3,25 e^{-[\ln(0,04E_n)]^2/6}, & E_n > 50 \text{ MeV} \end{cases}$$

**Figure 1:8 Distribution and equation of radiation weighting factor for neutrons according to their energy [11].**

<sup>2</sup> Remainder tissues: Adrenals, extrathoracic region, gall bladder, heart, kidneys, lymphatic nodes, muscle, oral mucosa, pancreas, prostate, small intestine, spleen, thymus, uterus/cervix.

### 1.4.3 Operational quantities

The operational quantities are defined using the quantity dose equivalent,  $H$ .  $H$  is the product of  $D$ , the absorbed dose and  $Q$ , the quality factor at that point; thus,  $H = DQ$ .  $Q$  is defined as a function of unrestricted linear energy transfer,  $L$  (often denoted as LET), of charged particles in water. The recommended values of depth  $d$  are chosen for the assessment of various doses:

- 10 mm for the effective dose. This value is used for strongly penetrating radiation (neutrons, photons).
- 0.7 mm for the dose to the skin and to the hands and feet.
- 0.3 mm for the dose to the lens of the eye.

Due to the different tasks in radiation protection monitoring (area monitoring for controlling the radiation at work places and definition of controlled or forbidden areas, or individual monitoring for the control and limitation of individual exposures) several operational quantities were defined. For the area monitoring, two operational quantities are defined:

- The ambient dose equivalent,  $H^*(d)$ . It is the dose equivalent, which would be generated in the associated oriented and expanded radiation field at a depth of  $d$  mm on the radius of the ICRU sphere, which is oriented opposite to the direction of the incident radiation. An oriented and expanded radiation field is an idealised radiation field, which is expanded and in which the radiation is additionally oriented in one direction. For neutrons and photons,  $H^*(10)$  is a good estimator of the effective dose.
- The directional dose equivalent,  $H'(d, \Omega)$  at a point in a radiation field is the dose equivalent that would be produced by the corresponding expanded field in the ICRU sphere at a depth,  $d$  on a radius in a specific direction,  $\Omega$ .

For individual monitoring, the personal dose equivalent  $H_p(d)$  at a point in a radiation field is the dose equivalent in soft tissue at an appropriate depth,  $d$ , below a specified point in the body.

The unit of all three quantities is joule per kilogram ( $J \cdot kg^{-1}$ ), and its special name is also Sievert (Sv).

In practice, primary standards for ambient and directional dose equivalent,  $H^*(d)$  and  $H'(d)$ , do not exist. Instead, reference fields for calibration of instruments are usually realised in terms of radiation fluence rate,  $\Phi$  (for neutrons), air kerma rate (for photons), absorbed dose to tissue (electrons), and the application of fluence (or air kerma or tissue absorbed dose) to dose equivalent conversion coefficients. The monoenergetic values of conversion coefficients are fixed reference values recommended by ICRU and ICRP, defined to have no uncertainty and are used in all calibration procedures. In case of a continuous neutron spectrum, the following equation 1.13 is used with the ICRP 74 conversion coefficient  $h_{\Phi}^*(E)$  (Figure 1.9):

$$H^*(10) = \int_{E_{min}}^{E_{max}} dE \times \Phi(E) \times h_{\Phi}^*(E) \quad (1.13)$$

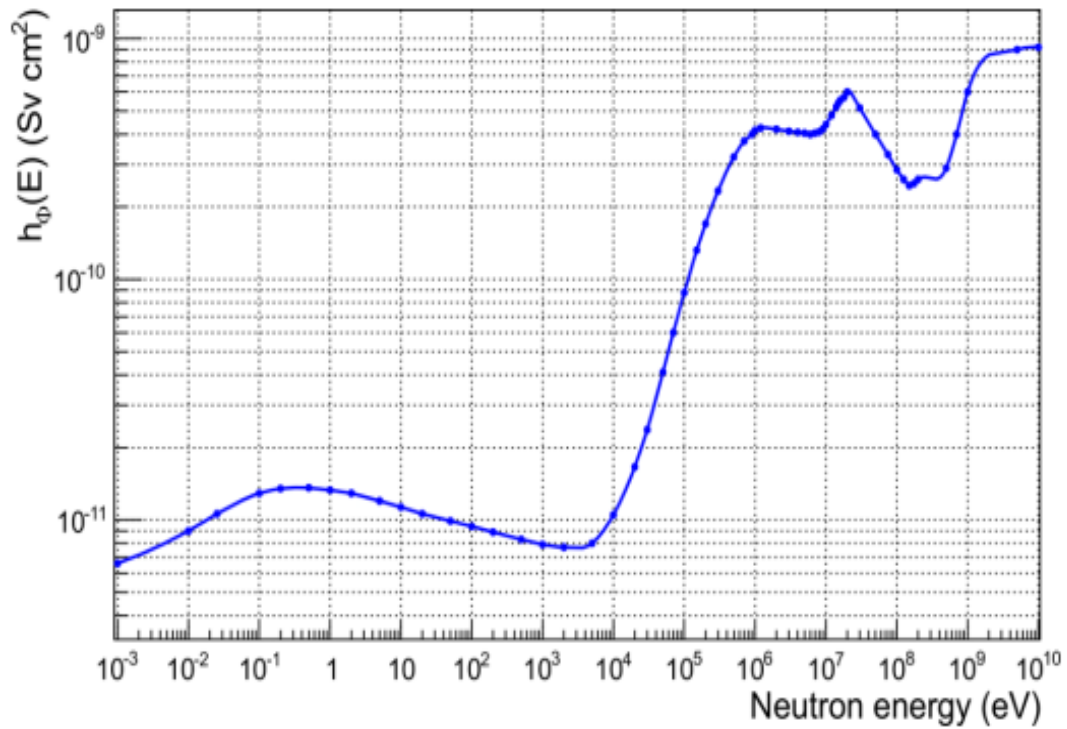


Figure 1.9. Fluence-to-dose equivalent conversion coefficient for neutron energies from 1 meV to 10 GeV, provided by ICRP 74 [16].

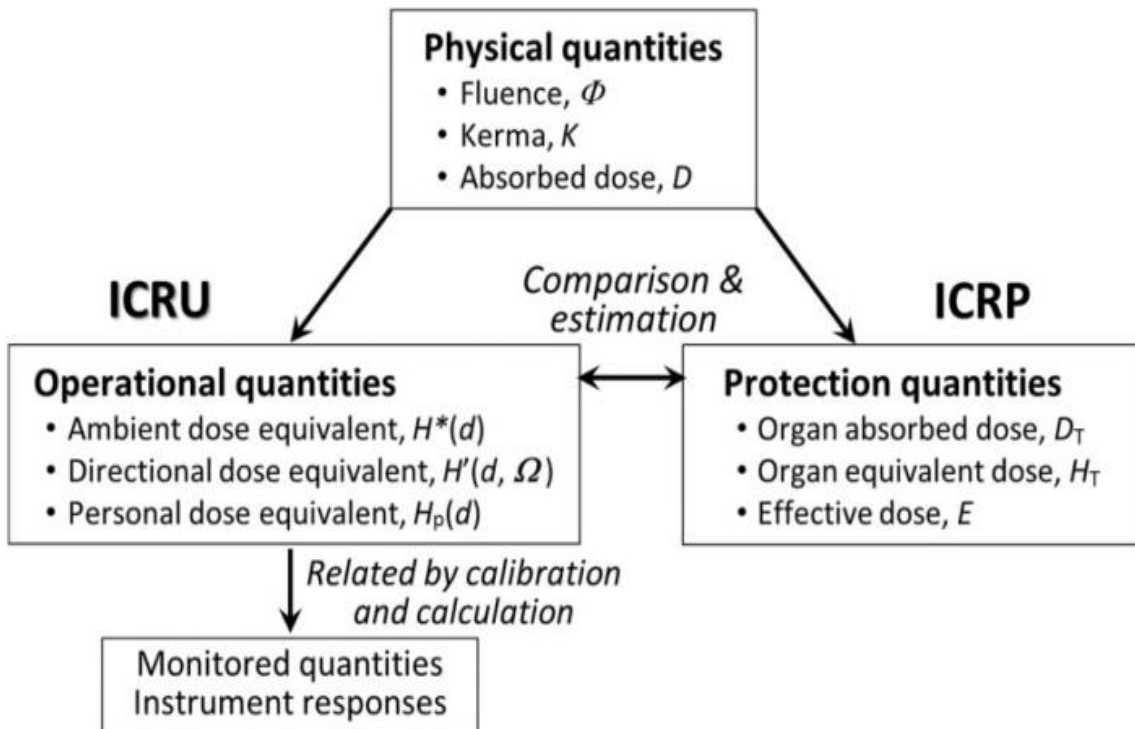


Figure 1:10. Summary of the radiation protection quantities and their relation.



## References

- [1] G. F. Knoll, *Radiation Detection and Measurement*, vol. 3. Wiley (2000).
- [2] P. Rinard, *Neutron Interactions with Matter*, Los Alamos Technical Report, U.S.A. (2009).
- [3] G. Salmeron, *Novel silicon sensor for neutron detection*, (2012).
- [4] *Mirion technologie, neutron detection and counting methods*, (2010).
- [5] *ENDF Evaluated Nuclear Data File* (2011).
- [6] C. Birattari, E. Dimovasili, A. Mitaroff and M. Silari, *A Bonner sphere spectrometer with extended response matrix*, *Nucl. Instrum. Meth. A* 620, 260-269 (2010).
- [7] M. Reginatto, P. Goldhagen, *MAXED a computer code for maximum entropy deconvolution of multisphere neutron spectrometer data*, *Health Physics* 77(5), 579-583 (1999).
- [8] E. Garcia-Dominguez, H. R. Vega-Carrillo, G. Miramontes de Leon, L. E. McBride, *Noniterative Unfolding Algorithm for Neutron Spectrum Measurements with Bonner Spheres*, *IEEE Transac. Nucl. Sci.* 46(1), 28-35 (1999).
- [9] F. Patrick Doty, Xiaowang Zhou, Pin Yang, and Mark A. Rodriguez, *Epasolite scintillators*, Sandia National Laboratories Report, (2012).
- [10] *ENDF-VII library at 300K*, (<http://atom.kaeri.re.kr>)
- [11] F. D. Brooks, "Development of organic scintillators," *Nucl. Instruments Methods*, vol. 162, no. 1-3, pp. 477-505 (1979).
- [12] J.B Birks, *The theory and practice of scintillation counting*, Pergamon Press, (1964).
- [13] H. Stadtmann, *Dose quantities in radiation protection and dosimeter calibration* *Radiat. Prot. Do sim.* 96 21-26 (2001).
- [14] *ICRU Rapport 39 Détermination des équivalents de dose dus uux sources externes de ruyonnement*, Pergamon press, Oxford (1985).
- [15] *The 2007 recommendations of the International Commission on Radiological Protection (ICRP Publication 103)* (2007).
- [16] *ICRP, Conversion coefficients for use in radiological protection against external radiation*, *Annals of the ICRP* 26 (3/4) (ICRP Publication 74) (1996).

# Chapter 2 Neutron instrumentation and CERN irradiation facilities

This chapter is divided into 2 parts. The first section presents the range of instruments usually employed at high-energy particle accelerators used in this study. The second part presents the irradiation facilities where the tests were performed: the CERN calibration laboratory (CALLAB) and the CERN-EU high-energy Reference Field facility (CERF).

## 2.1 Neutron Instrumentation

The instruments employed were the following: four extended-range rem counters (LINUS, WENDI, LUPIN, PRESCILA), a conventional rem counter (LB6411), an extended-range Bonner Sphere Spectrometer (BSS). A brief description of the detectors used as well as their response functions are given in the following subsections.

### 2.1.1 BSS

The extended-range BSS [1] consists of 7 spheres with a thermal neutron counter ( $^3\text{He}$  proportional counter Centronics SP9) at its centre (Figure 2.1): 5 polyethylene spheres with outer diameter of 81, 108, 133, 178 and 233 mm, complemented by two additional spheres, called “Ollio” and “Stanlio”, where cadmium and lead inserts are introduced in order to reduce the sensitivity to thermal neutrons and increase it for high-energies, up to the GeV range. Each detector has its response function (Figure 2.2) with a peak at a given energy range.

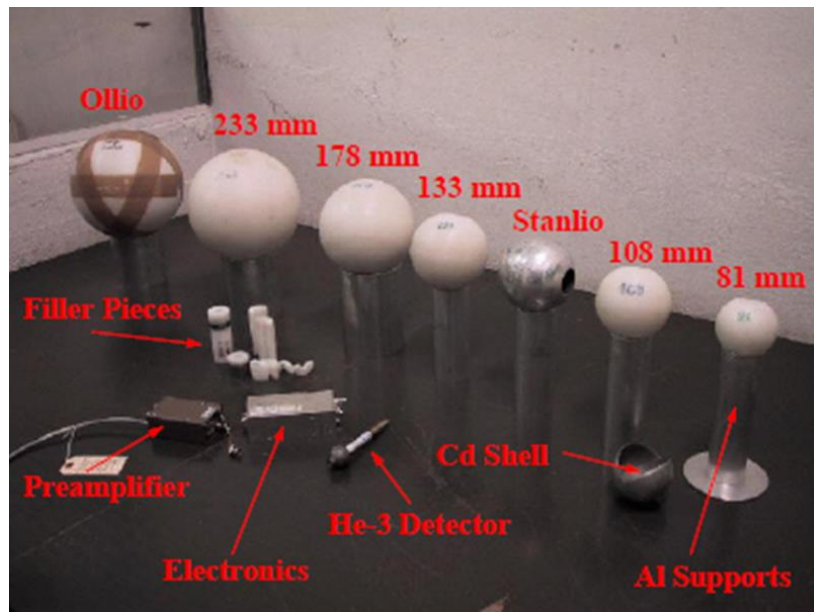
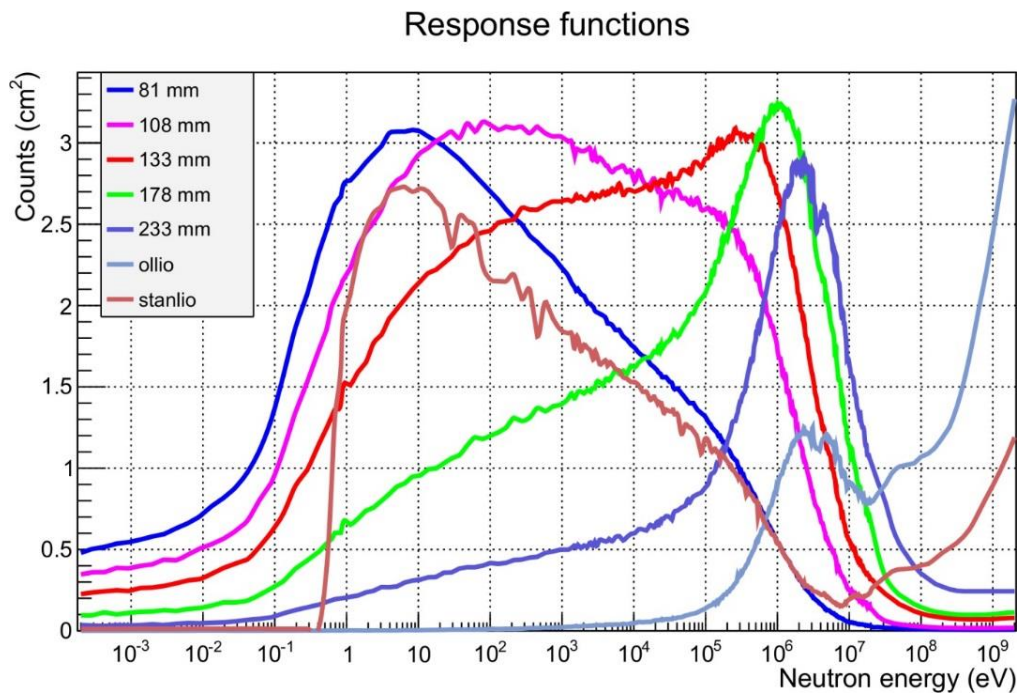


Figure 2.1 The BSS consisting of five polyethylene spheres and two polyethylene/lead spheres (*Stanlio* and *Ollio*). The filler pieces fitting around the proportional counter and the aluminium supports are also shown.



**Figure 2.2** BSS fluence responses as a function of the impinging neutron energy, as calculated via FLUKA simulations [2].

### 2.1.2 LINUS

The LINUS [3][4][5][6] is the original extended-range rem counter, developed in the early 1990s' by the University of Milan and the National Institute of Nuclear Physics (INFN) in Italy. It consists of a  $^3\text{He}$  proportional counter embedded in a spherical polyethylene moderator (Figure 2.3), which incorporates a boron-doped rubber absorber and a 1 cm thick lead shell so that its response function extends up to several hundred MeV. The signal is treated with a standard counting chain (pre-amplifier, amplifier, single channel analyser and counter) and the TTL output can either be read locally in the NIM crate with a counter or acquired by a National Instruments DAQ and analysed on a laptop. For the measurement at CERF the 2<sup>nd</sup> option was chosen. The response function of the detector is shown in Figure 2.4 together with those of the WENDI-II, LB6411 and LUPIN, and the ICRP74 fluence-to-ambient equivalent conversion coefficients; the graph is divided in 4 parts (black vertical lines) according to the neutron energy range. The response function of PRESCILA is missing because no raw data were found in the literature.



**Figure 2.3** The extended-range rem counter LINUS.

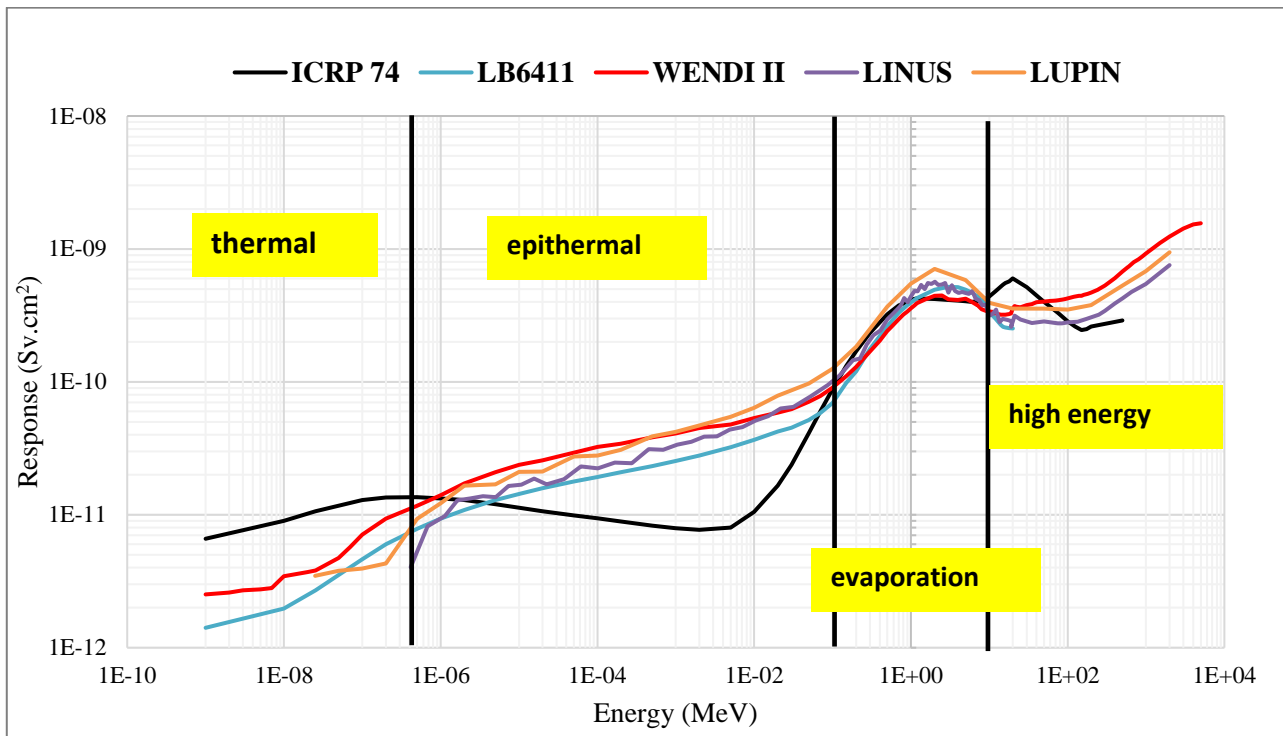


Figure 2.4 Energy response function of the LINUS, WENDI, LUPIN and LB6411 together with the ICRP 74 fluence-to-ambient dose equivalent conversion coefficients.

### 2.1.3 LB6411

The neutron probe Berthold LB6411[7] (Figure 2.5) is a commercial rem counter designed to measure  $H^*(10)$  in neutron radiation fields up to 20 MeV. It consists of a  $^3\text{He}$ /methane proportional counter surrounded by a spherical moderator of polyethylene with density of  $0.95 \text{ g/cm}^3$ .

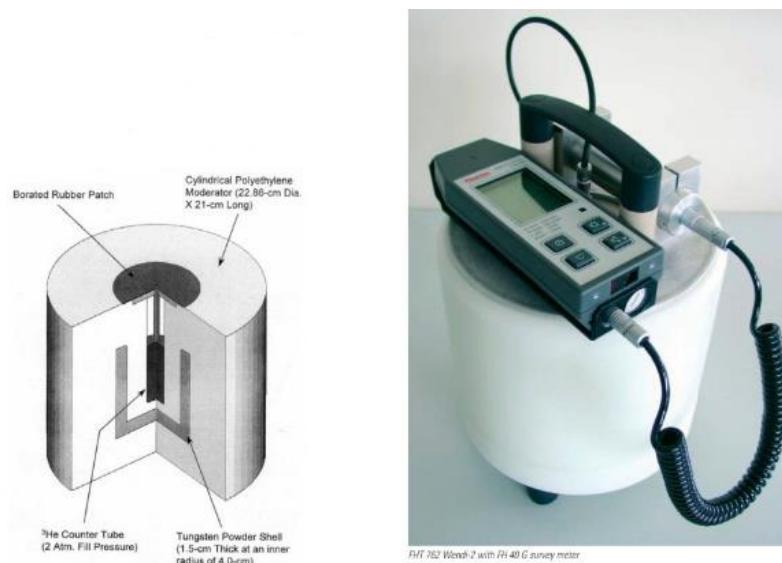


Figure 2.5 Berthold LB6411

### 2.1.4 WENDI

The Thermo Scientific WENDI is a commercial extended-range rem counter, based on the LINUS concept, designed to measure the  $H^*(10)$  rate within an energy range from thermal up to 5 GeV [8]. It consists of a  $^3\text{He}$  proportional counter surrounded by a cylindrical polyethylene moderator assembly and a layer of tungsten powder. As in the LINUS, this additional layer of high-Z material enhances the detector response to high-

energy neutrons via inelastic scattering interactions. The geometry and a photograph of the detector are shown in Figure 2.6.



**Figure 2.6 Scheme and photograph of the Thermo Scientific WENDI.**

### 2.1.5 LUPIN

The LUPIN-BF is a rem counter commercialised by ELSE Nuclear, designed to work in pulsed neutron fields [9]. The moderator consists of a polyethylene cylinder of 25 cm diameter with lead and cadmium inserts, hosting at its centre a BF<sub>3</sub> counter. A scheme and a photograph of the LUPIN-BF are shown in Figure 2.7.

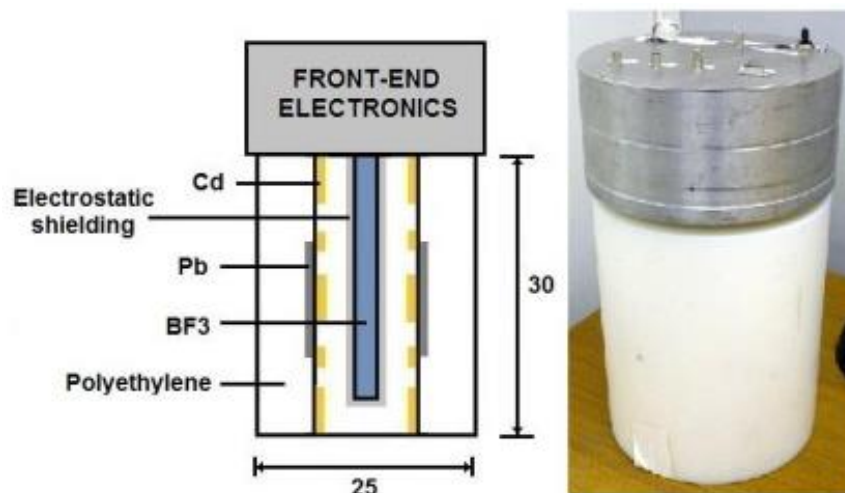


**Figure 2.7 Scheme and photograph of the ELSE Nuclear LUPIN-BF, dimensions in centimetres.**

### 2.1.6 PRESCILA

PRESCILA (Figure 2.8) was developed as a low-weight (2 kg) neutron detector with extended energy response, high sensitivity and moderate gamma rejection [10]. An array of ZnS(Ag) scintillators is located inside and around a Lucite light guide, which couples the scintillation light to a sideview bialkali photomultiplier tube. The use of both fast and thermal scintillators allows the energy response function to be optimized for a wide range of operational spectra. The light guide and the borated polyethylene frame provide moderation for the thermal scintillator element.

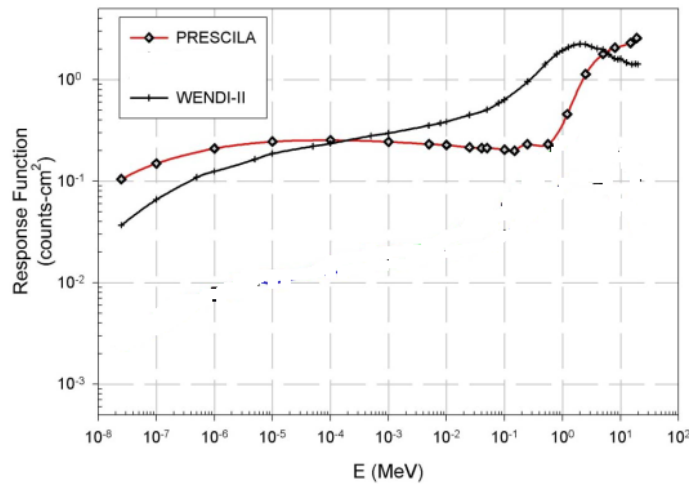
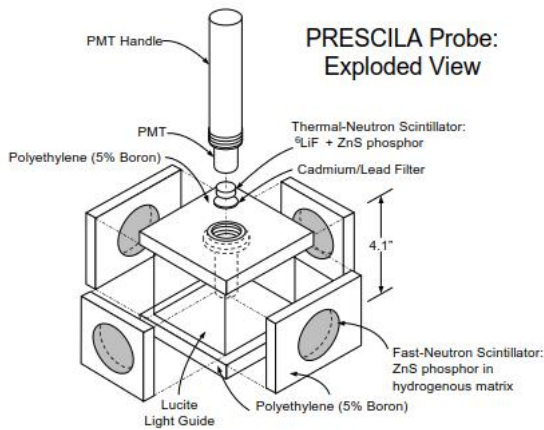


**Figure 2.8** An exploded view of the PRESCILA neutron rem counter (left) and its response function compared to the response of WENDI (right).

## 2.2 CERN irradiation facilities

### 2.2.1 The CERN calibration laboratory (CALLAB)

The CERN Radiation Protection (RP) group is in charge of the RP calibration laboratory that has been built over the last 5 years to replace the previous old facility (20 years) [11]. The new facility consists of three irradiation rooms, storage and control rooms, offices and two technical rooms (Figure 2.9):

- Irradiation room 1 houses a 10 TBq  $^{60}\text{Co}$  source to perform radiation damage studies on electronic components and to allow for limited material studies if samples are placed close to the source location.
- Irradiation room 2 is dedicated to the dosimeter calibration with a dedicated self-shielded irradiator.
- The calibration hall is the main part of the facility and is used for the calibration of RP survey meters, fixed monitors and dosimeters but also for testing prototype detectors. Three irradiation fields are available: neutrons, photons, X-rays; in the future a beta radiation field will be also available.

The calibration hall is a  $13 \times 13 \times 13 \text{ m}^3$  concrete vault, half of which is underground to take advantage of the natural shielding provided by the earth. It is fitted with a neutron panoramic irradiator placed in the geometrical centre of the room at the ground level. From their garage position on the bottom of the vault, the neutron sources are raised to the irradiation position at the floor level via an air-compressed system along a pipe of 7 m long. The floor is made of a metallic grid to minimise neutron scattering. Four Am-Be sources were installed in the calibration hall having the following activities: 888 GBq, 100 GBq, 10 GBq and 100 MBq. To provide gamma dose equivalent rates from  $\mu\text{Sv/h}$  to hundreds of  $\text{mSv/h}$ , five Cs-137 sources with the following activities are installed: 3 TBq, 300 GBq, 30 GBq, 3 GBq and 300 MBq. In addition, a 5 GBq  $^{60}\text{Co}$  source is available to provide higher photon energies.

The main advantage of this neutron and photon irradiator configuration is that it will allow performing simultaneous gamma/neutron measurements to test, e.g. the sensitivity of neutron survey meters to gamma radiation, as mixed fields are very common at CERN. The calibration hall will also house an X-ray generator with a 4 m long bench for X-ray calibrations. The X-ray tube will operate at 320 kV with a tungsten anode. The facility will also be equipped with a beta irradiator. All irradiators and the alignment system will be remotely controlled from the control room.



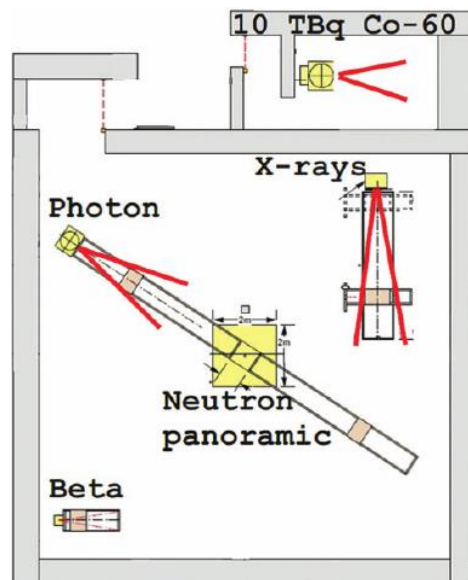


**Figure 2.9** Top view of the calibration hall with the four irradiators and of irradiation room 1 with the photon irradiator [12].

### 2.2.2 The CERN-EU high-energy Reference Field facility (CERF)

CERF is installed in one of the secondary beam lines (H6) from the Super Proton Synchrotron (SPS), in the North Experimental Area on the Preveessin (France) site of CERN. A 450 GeV/c primary proton beam is extracted from the SPS and directed on the T4 primary target. Typical intensities of this primary beam are several  $10^{12}$  protons per burst. From the T4 target, H6 and two secondary beams are derived. The CERF facility is situated about 410 m downstream of the T4 target [13].

A positive hadron beam (a mixture of 61% pions, 35% protons and 4% kaons, as determined experimentally) with a momentum of usually 120 GeV/c is stopped in a copper target, 7 cm in diameter and 50 cm in length, which can be installed either under 80-cm concrete shield or under a 40-cm iron shield (Figure 2.10). The interaction of the beam with the target produces secondary particles (mainly neutrons, but also photons, electrons, muons, pions and protons) which traverse a shielding, on top of these two positions and at 90° with respect to the incoming beam direction. The beam monitoring is provided by an air-filled ionisation chamber (IC) (formerly called PIC, precision ionisation chamber) placed in the beam a few meters upstream of the target. One IC-count corresponds to  $22000 \pm 2200$  beam particles. This calibration factor was determined through different technique: FLUKA simulation and activation experiments performed with hyperpure aluminum and copper foils [monitor]. More details of the beam set up can be found in ref [14].

The roof-shields produce almost uniform radiation fields over two areas of  $2 \times 2 \text{ m}^2$ , each of them divided into 16 squares of  $50 \times 50 \text{ cm}^2$ , as shown in Figure 2.11. Each element of these grids represents a reference exposure location. Moreover, 8 additional exposure locations are present on the concrete side. The neutron spectra differ on the concrete side (CS), concrete top (CT) and iron top (IT) reference locations. Between the concrete side (CS) and the concrete top (CT), only the amplitudes of the thermal, evaporation and high-energy peaks are different while their position is identical (Figure 2.12). The CS spectrum is more intense than the CT spectrum since the CS reference positions are slightly closer to the target and a backscatter neutron contribution is present, resulting in a higher thermal peak. The spectrum outside the IT is dominated by neutrons in the 0.1–1 MeV range. The energy distribution outside the concrete shield shows an additional large relative contribution of 10–100 MeV neutrons. Therefore, these exposure locations provide wide spectrum radiation fields well suited to test dosimetric instrumentation under different conditions. The fluence rate of other hadrons is much lower than that of neutrons. The photon fluence is almost one order of magnitude less than that of neutrons on the iron roof-shield, but almost a factor of two higher than the neutron fluence on the concrete roof-shield. The electron fluence is about one order of magnitude less than that of neutrons and the muon fluence almost three orders of magnitude less. However, an additional muon component is also present which directly comes from the upstream H6 beam line and adjacent lines, as well from pion decay in the beam line. Their

intensity depends on various factors, which are not under direct control, such as the intensity of secondary beams in neighbouring beam lines.

In addition to the interest for testing active and passive detectors used around high-energy particle accelerators CERF field shows another advantage. Since the CERF neutron field reproduces approximately the field at flight level, and because the shape of the neutron energy distribution in the atmosphere does not change much with altitude and latitude, the CERF spectrum is considered sufficiently similar to the cosmic ray field encountered at 10–20 km altitude. Thus, CERF is a “field calibration” facility for radiation protection instrumentation that simulates the workplace field that can be encountered in the proximity of high-energy accelerators and at flight altitudes, such that instrumentation can be tested, inter-compared and calibrated at CERN and subsequently used for in-flight measurements on aircraft. Such a facility is unique in providing a wide energy spectrum and is usually operated for one week twice per year. Many users from all over the world come to CERF to test and calibrate active and passive dosimeters, rem-counters, spectrometers and prototype detectors.

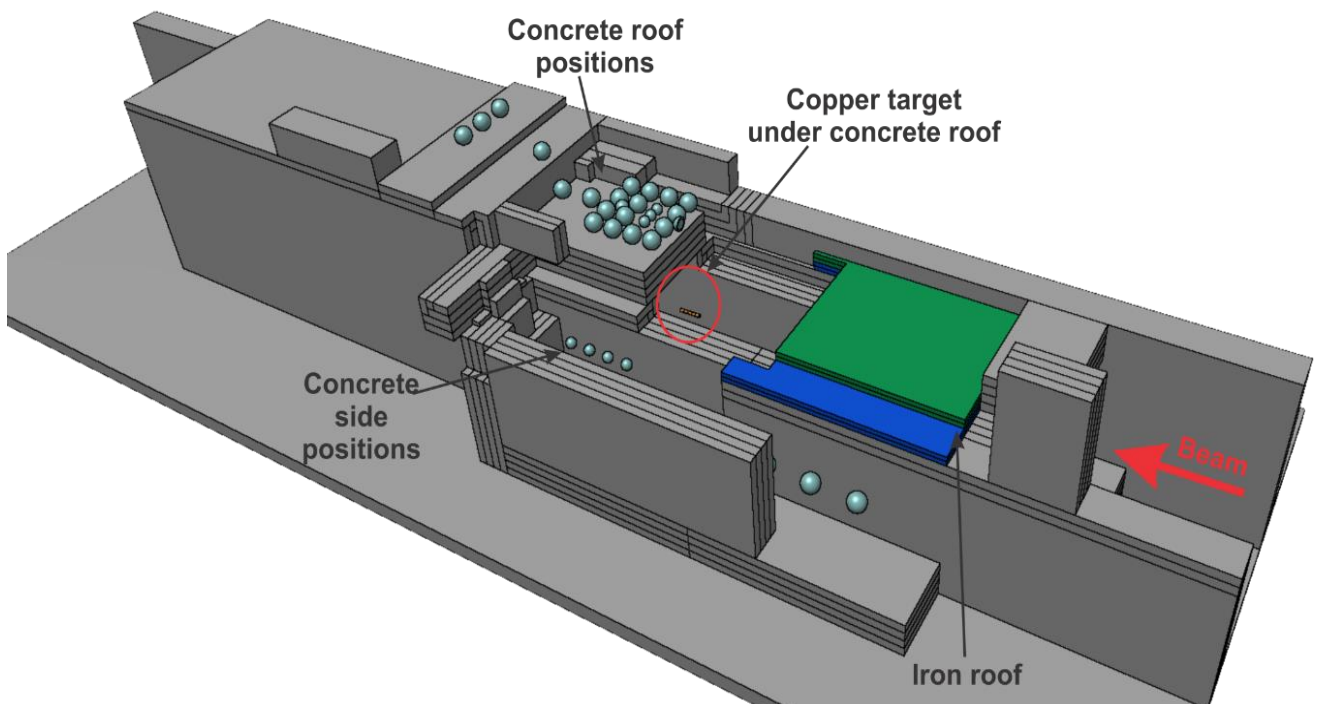


Figure 2.10 Cross sectional view of the CERF facility



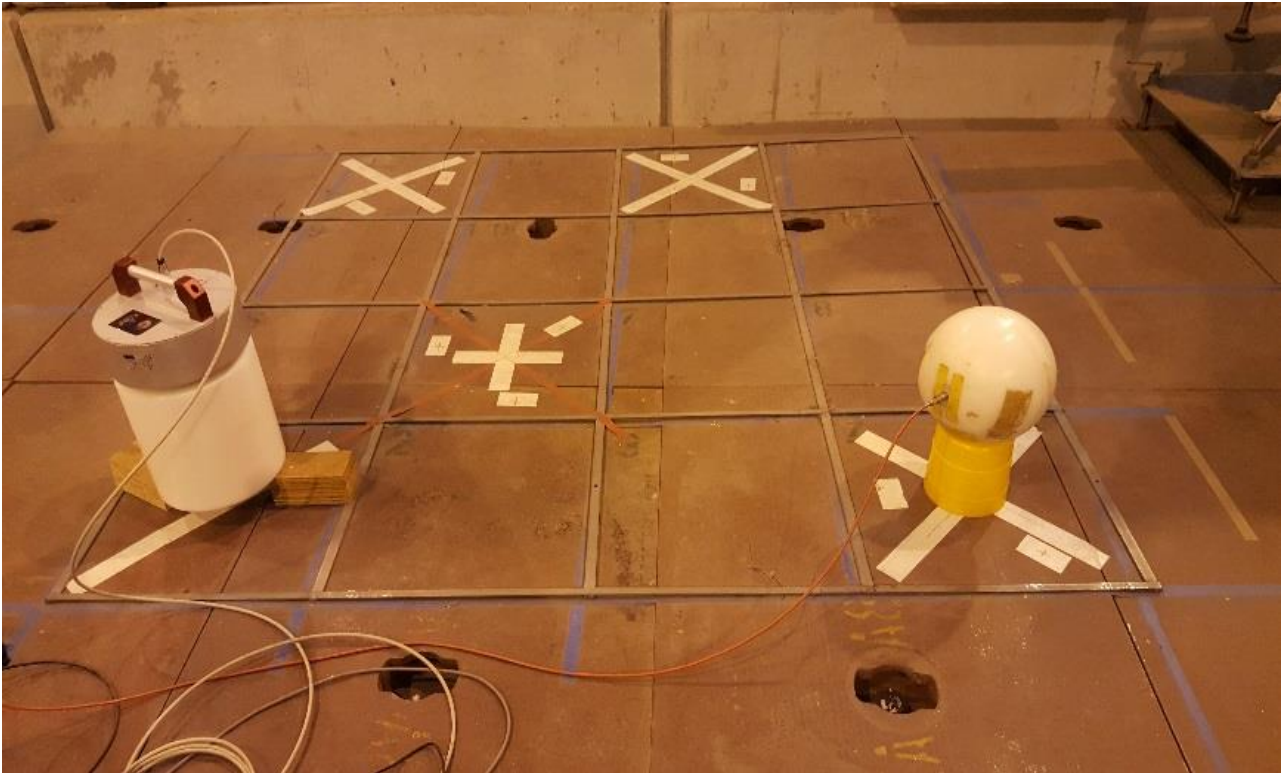


Figure 2.11 The reference grid with the 16 exposure locations used on the concrete roof shield.

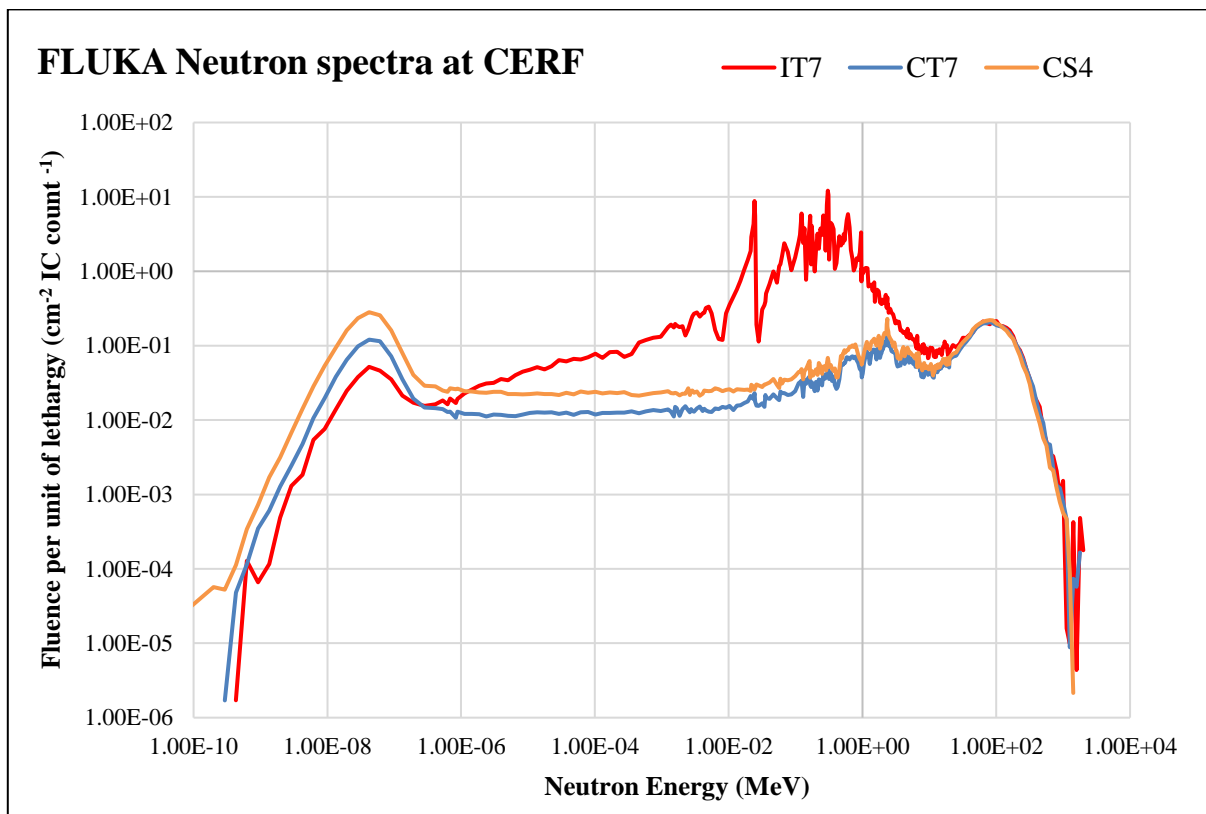


Figure 2.12 Neutron spectral fluence obtained with FLUKA for position IT7 (red), CT7 (blue) and CS4 (green). The statistical uncertainty on the fluence values is generally below 1%.

## References

- [1] C. Birattari, E. Dimovasili, A. Mitaroff and M. Silari, A Bonner sphere spectrometer with extended response matrix, *Nucl. Instrum. Meth. A* 620 260-269 (2010).
- [2] E. Aza, N. Dinar, G.P. Manessi, M. Silari, A Bonner sphere spectrometer for pulsed fields, *Radiat. Prot. Dosim.* 168, 149-153 (2016).
- [3] E. Aza, N. Dinar, G.P. Manessi, M. Silari, A Bonner sphere spectrometer for pulsed fields, *Radiat. Prot. Dosim.* 168, 149-153 (2016).
- [4] C. Birattari, A. Esposito, A. Ferrari, M. Pelliccioni and M. Silari. A neutron survey-meter with sensitivity extended up to 400 MeV, *Radiat. Prot. Dosim.* 44, 193-197 (1992).
- [5] C. Birattari, A. Esposito, A. Ferrari, M. Pelliccioni and M. Silari. Calibration of the neutron rem counter LINUS in the energy range from thermal to 19 MeV, *Nucl. Instrum. Meth.* A324, 232-238 (1993).
- [6] C. Birattari, A. Esposito, A. Ferrari, M. Pelliccioni, T. Rancati, M. Silari, The extended range Neutron rem counter 'LINUS': overview and latest developments, *Rad. Prot. Dosim.* 76, 135-148 (1998).
- [7] B. Burgkhardt, G. Fieg, A. Klett, A. Plewnia, B.R.L. Siebert, The neutron fluence and  $H^*(10)$  response of the new LB 6411 Rem counter, *Radiat. Prot. Dosim.* 70(1-4), 361-364 (1997).
- [8] R.H. Olsher, H.H. Hsu, A. Beverding, J.H. Kleck, W.H. Casson, D.G. Vasilik, R.T. Devine, Wendi: an improved neutron rem meter, *Health Phys.* 79, 170-181 (2000).
- [9] M. Caresana, M. Ferrarini, G. Manessi, M. Silari, and V. Varoli, LUPIN: A new instrument for pulsed fields, *Nucl. Instrum. Meth. A* 712, 15-26 (2013).
- [10] R.H. Olsher, T.D. McLean, High-energy response of the PRESCILA and WENDI neutron rem meters *Radiation Protection Dosimetry* 130, 510-513 (2008).
- [11] F. Pozzi et al., CERN irradiation facilities, *Proceedings of NEUDOS-13, Radiation Protection Dosimetry*, doi: 10.1093/rpd/ncx187 (2017)
- [12] M. Brugger, P. Carbonez, F. Pozzi, M. Silari and H. Vincke, New radiation protection calibration facility at CERN, *Radiation Protection Dosimetry*, Vol. 161, No. 1-4, pp. 181-184 (2014).
- [13] A. Mitaroff, M. Silari, The CERN-EU high-Energy Reference Field (CERF) Facility For Dosimetry at commercial flight altitudes and in space, *Radiat. Prot. Dosim.* 102 7-22 (2002)
- [14] N. Dinar, F.P. La Torre, G.P. Manessi, F. Pozzi, C.T. Severino, M. Silari, A new verification of the calibration factor of the CERF beam monitor, *CERN-RP-2013-083-REPORTS-TN*, (2013).

# Chapter 3 Performance intercomparison of conventional neutron detectors

At high-energy particle accelerators, stray radiation fields are comprised of neutrons, photons and charged particles. Behind thick shielding, the neutron component is the top contributor to the ambient dose equivalent ( $H^*(10)$ ) and its energy can range from thermal energy up to several GeV. A correct monitoring of the  $H^*(10)$  is essential to ensure the compliance with the radiological area classification. Radiation protection instrumentation usually employed to monitor the neutron  $H^*(10)$  have response functions attempting to reproduce the ICRP74 fluence-to-ambient dose equivalent conversion coefficients. Unfortunately, an exact replication is not fully possible and therefore these instruments can underestimate or overestimate some components of the neutron energy spectrum, resulting in a wrong estimation of the  $H^*(10)$ . The behaviour of each instrument can be assessed in simulated workplace reference fields and intercomparison with similar instruments can help the choice of the proper instrument according to the radiation fields to be measured. To evaluate the performance of the conventional detector used in radiation protection purpose, several detectors were selected.

The responses of detectors are first evaluated through different measurements. Particularly the LINUS, the reference detector at CERF was tested both in our laboratory and also during an aircraft campaign. Results of an intercomparison at CERF, a workplace reference field is then discussed in section 3.2. The results were compared with the latest reference values calculated in 2017 with the FLUKA Monte Carlo code (development version 2017 [1-2]). Finally, future extensions are suggested in section 3.3 to improve the response functions of the Bonner spheres spectrometer.

## 3.1 Characterization of detectors

### 3.1.1 Detector calibration

To check the response of the detectors used in this study, determination test of the calibration factor was performed at the CALLAB. Calibration means the determination of the instrument response in a specified radiation field delivering a known dose (or other magnitude) at the point reference of the instrument. The response or calibration factor of a device is a unique characteristic of the type of device, and may depend on the dose equivalent rate, the spectrum of the neutron source or the angle of incidence of the neutrons, but should not be a function of the characteristics of the calibration facility or experimental techniques employed [3]. The procedure used to calibrate radiation protection instruments in a radiation field is by substitution. This method consists in two steps; in the first the reference detector is placed at the calibration point to determine the reference radiation field. In the second step, it is replaced by the detector to be calibrated, and reading are taken. For the radiation field characterization of the neutron sources at CALLAB, the SmartREM rem-counter was employed [4]. The detector was calibrated at Physikalisch-Technische Bundesanstalt (PTB) primary standard laboratory [5].

In order to find the calibration factor of the LINUS, WENDI, LUPIN and PRESCILA, measurements with AmBe sources were performed. The minimum irradiation time corresponds to a statistical uncertainty of about 1% on the total acquired counts. The minimum distance between the detector and the source was fixed at 3 times the sum of the detector diameter and the height of the source [6]. Table 3.1-3.4 show the parameters used for the determination of the calibration factor. The calibration factor in nSv/count is calculated by dividing the integrated dose given by the reference detector (SmartREM) with the total count of each detector. The relative

uncertainty on the calibration factor is 4%, which takes into account the uncertainty on the radiation field characterization (4%) and the statistical uncertainty on the counts (generally less than 1%). Calibration factors determined at CALLAB are compared to the value given by the company except for the LINUS, which is not a commercial device. For all detectors, the calibration factors measured at CALLAB are within the uncertainty (1 sigma) of the calibration factors given by the manufacturer (Figure 3.1).

**Table 3.1 Parameters used to determine the calibration factor of the LINUS in nSv/ct.**

Source	Distance	H*(10) rate	Integration time	Integrated H*(10)	LINUS counts	Calibration factor	Calibration factor
GBq	cm	μSv/h	s	nSv	cts	nSv/ct	nSv/ct
888	80	1026.354	150	42765	48095	0.89	0.89
888	116.5	500.083	150	20837	23703	0.88	
888	169.5	250.66	150	10444	11876	0.88	
888	225	153.132	250	10634	11906	0.89	
100	80	133.904	300	11159	12539	0.89	
100	116.5	65.804	700	12795	14155	0.90	

**Table 3.2 Parameters used to determine the calibration factor of the WENDI in nSv/ct.**

Source	Distance	H*(10) rate	Integration time	Integrated H*(10)	WENDI counts	Calibration factor	Calibration factor
GBq	cm	μSv/h	s	nSv	cts	nSv/ct	nSv/ct
100	160	36.7	245	2498	7148	0.35	0.35
100	190	27	310	2325	6649	0.35	
100	210	22.6	450	2825	8091	0.34	
100	300	12.4	890	3066	8816	0.35	

**Table 3.3 Parameters used to determine the calibration factor of the LUPIN in nSv/ct.**

Source	Distance	H*(10) rate	Integration time	Integrated H*(10)	LUPIN counts	Calibration factor	Calibration factor
GBq	cm	μSv/h	s	nSv	cts	nSv/ct	nSv/ct
888	91.1	800	120	26667	50525	0.53	0.53
888	116.6	500	120	16667	31440	0.53	
888	192.7	200	180	10000	18558	0.54	
100	93.3	100	300	8333	15720	0.53	

**Table 3.4 Parameters used to determine the calibration factor of the PRESCILA in nSv/ct.**

Source	Distance	H*(10) rate	Integration time	Integrated H*(10)	PRES. counts	Calibration factor	Calibration factor
GBq	cm	μSv/h	s	nSv	cts	nSv/ct	nSv/ct
888	72	1257.9	298	1041	226667	0.47	0.46
888	250.8	127.5	110	390	8810	0.44	
888	250.8	127.5	300	106	22619	0.46	

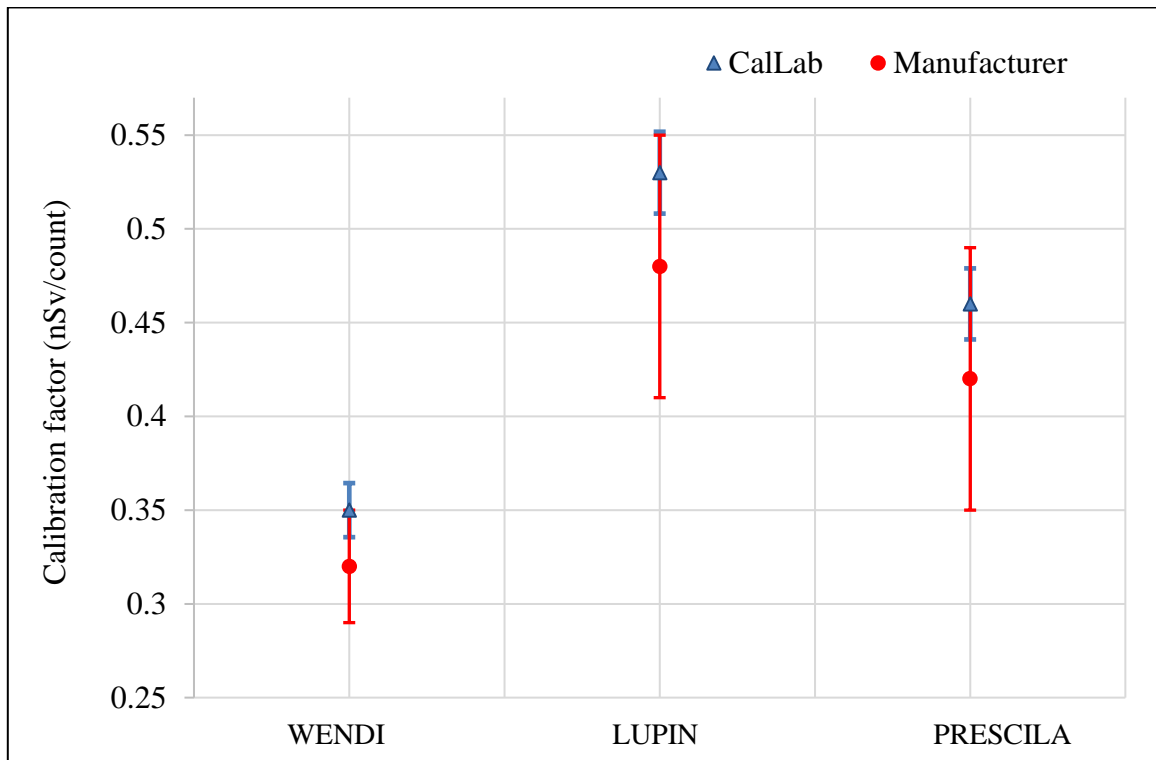


**Figure 3.1** Detector calibration factor in nSv/count measured at the CALLAB (blue) and given by the manufacturer (red).

### 3.1.2 Measurement with AmBe neutron source

In order to check their responses, measurements with WENDI, LINUS and the BSS were performed in the RP calibration laboratory with an 888 GBq AmBe source. Each detector was placed at 2.50 m from the source and irradiated for 5 minutes. At the time of the measurements, the LUPIN was not available. The BSS integrated counts were corrected for the dead time. Figure 3.2 shows the unfolded spectra as well as the FLUKA guess spectrum. The results were compared with the reference value measured by a secondary standard spherical Leake rem-counter, called SmartREM calibrated at the Physikalisch-Technische Bundesanstalt.

The spectra are in good agreement both in shape and absolute value of the neutron fluence (FLUKA= 2.45E- 6 cm<sup>-2</sup> per primary, BSS = 2.28E-6 cm<sup>-2</sup> per primary). In the evaporation part the MAXED and GRAVEL spectra overlap and are slightly lower than the FLUKA guess. This slight difference can be seen in the final H\*(10) calculation (see Table 3.5).

**Table 3.5** Measured and expected H\*(10) in the AmBe source neutrons of the RP calibration laboratory. The expected value is obtained from the simulation spectrum (FLUKA).

H*(10) [uSv/h]	REFERENCE	FLUKA	LINUS	WENDI	BSS	PRESCILA
Measured	129 ± 6	-	128 ± 11	118 ± 11	122 ± 9	114 ± 13
Expected [FLUKA]	-	131 ± 7	149 ± 13	127 ± 9	-	-

For the rem counters, the expected H\*(10) was calculated by folding their response function with the AmBe spectrum obtained with FLUKA simulations. The BSS H\*(10) was obtained by folding the unfolded spectrum with the ICRP 74 fluence to dose equivalent conversion coefficients. The expected FLUKA H\*(10) was obtained by folding the AmBe FLUKA spectrum with the ICRP 74 conversion coefficients. The total uncertainty

takes into account the statistical uncertainty of the measurement ( $< 1\%$ ), the uncertainty on the calibration factor given by the manufacturer (4% for the reference detector, 5% for the LINUS and 7% for the WENDI, 12% for the PRESCILA) and variations in the positioning of the instrument (3%). The total experimental uncertainties on the BSS  $H^*(10)$  were estimated at 7.7%, which include the statistical uncertainty on the counts, the uncertainty on the neutron flux (5%), the uncertainty on the response matrix (3%) and variation in positioning (5%). The total uncertainties on the expected  $H^*(10)$  takes into account the uncertainties related to the FLUKA spectrum as well as the response function of the detectors.

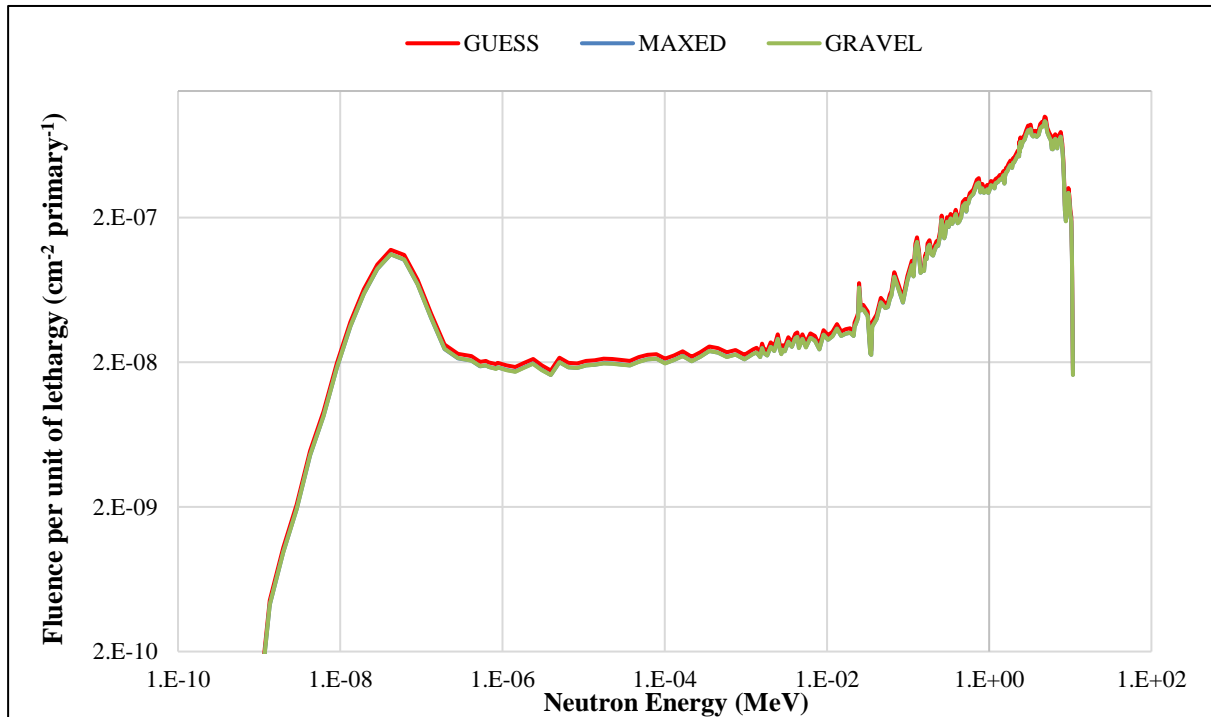


**Figure 3.2 Neutron spectral fluence obtained with the AmBe source in the RP calibration laboratory, measured with the BSS and compared with the guess spectrum. The uncertainties are not shown for clarity.**

All the measured  $H^*(10)$  values agree within one sigma (Figure 3.3). The LINUS  $H^*(10)$  agrees very well with the reference value (within 1%) while WENDI, PRESCILA and the BSS underestimate by 10%, 13% and 5%, respectively. All expected  $H^*(10)$  agree well with the measured  $H^*(10)$ . The expected LINUS and WENDI  $H^*(10)$  overestimate the measured  $H^*(10)$ . This could be due to discrepancies between the calculated and the experimental response function of the detector. The calculated response function overestimates the evaporation part.

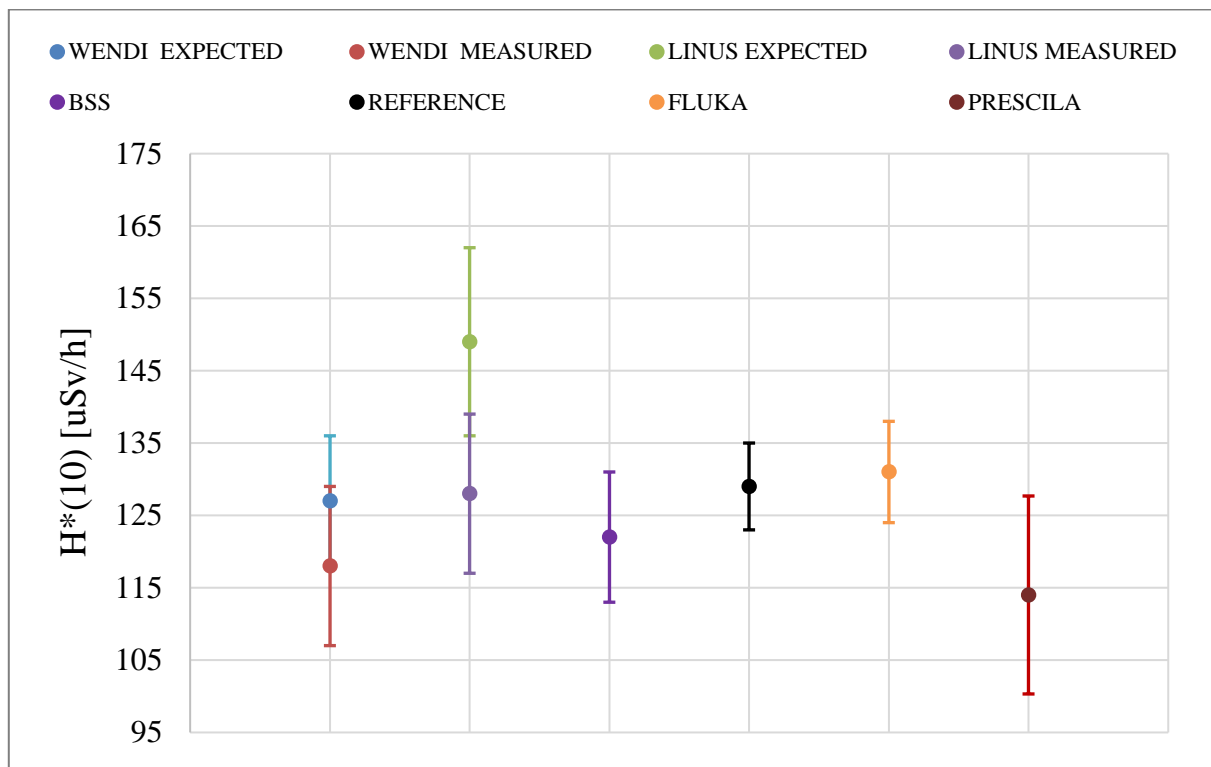


**Figure 3.3**  $H^*(10)$  in  $\mu\text{Sv/h}$  from AmBe source measured with BSS, WENDI, LINUS, PRESCILA and the reference detector SmartREM at the CALLAB. The expected value from the folding between the response function and the FLUKA spectrum are also given for the WENDI and LINUS.

### 3.1.3 LINUS reference detector at CERF

The section discusses laboratory testing and a new calibration of the LINUS, the reference rem counter used at CERF. Recently, the SP9 proportional counter had to be replaced after the connector of the original one was damaged last year. Measurements in the radiation protection laboratory (CALLAB) were performed to find the threshold to reject low energy noise and gamma rays events in order to count neutron only events. The plateau curve measurement allows defining the operating voltage range. Finally the calibration factor in nSv/count was determined.

The LINUS was placed in the track 2 and aligned with the laser system. An Amptek MCA 8000 D was connected (in parallel to the chain described in 2.1.2) to the output of the amplifier in order to acquire simultaneously the pulse height spectra and the total counts from the SCA NIM counter. The voltage was set at 816 V as recommended by the detector data sheet. Figure 3.4 shows a picture of the set up. Two AmBe sources were used with activities of 888 GBq and 100 GBq.



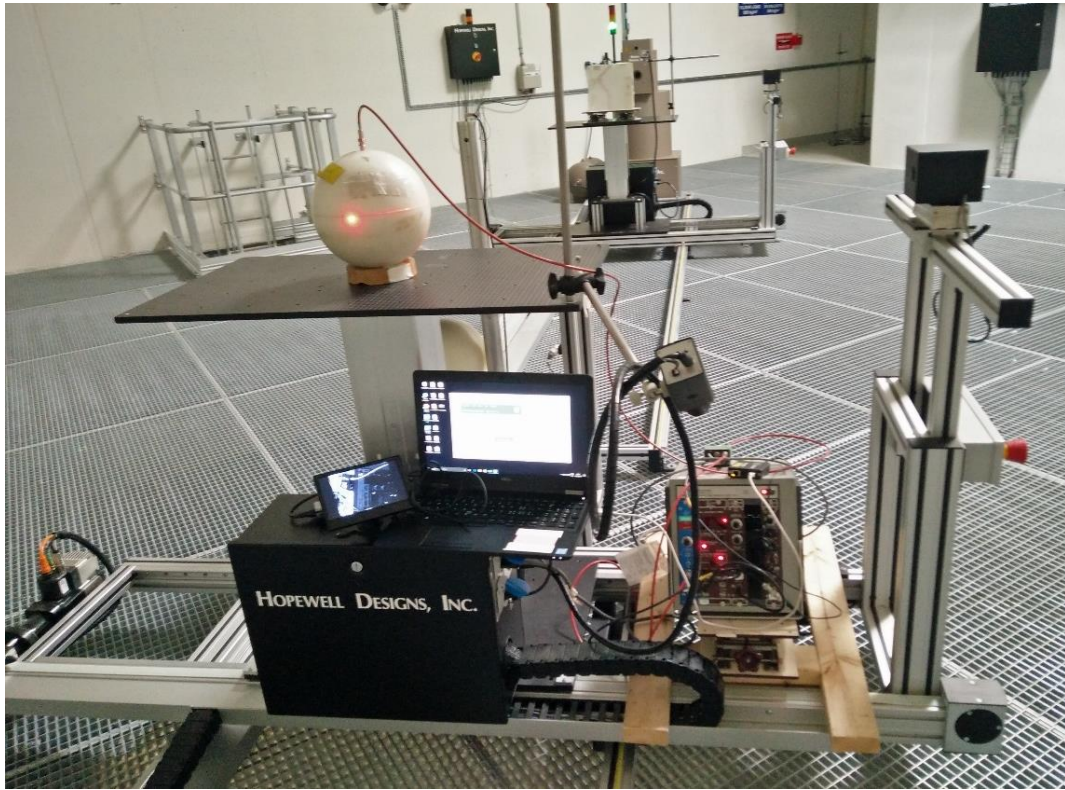
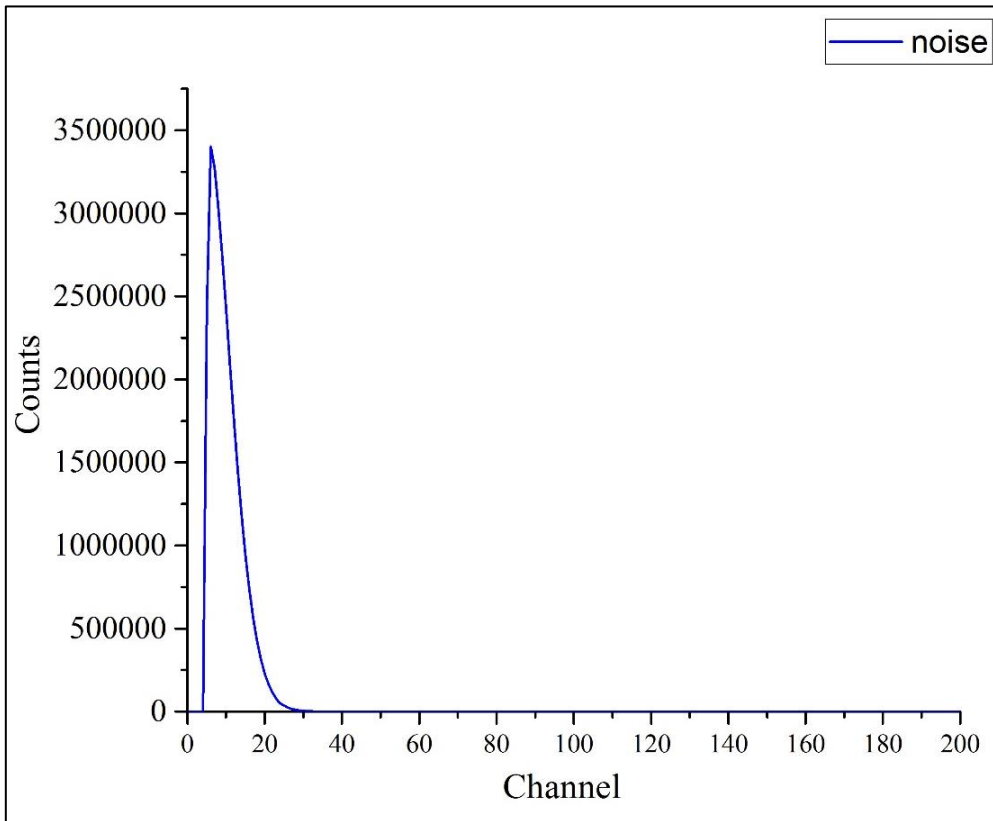


Figure 3.4 Experimental set up of the LINUS in the CALLAB (CERN).

### 3.1.3.1 Determination of the discriminator threshold

Neutron detectors are sensitive to some degree to gamma rays. Gamma rays can transfer energy to the system through Compton scattering in the walls or fill gas. Because gamma rays are normally present in neutron fields, the gamma sensitivity is an important criterion when working with neutron detectors (see, for example, ref. [7]). The gamma rejection is usually made by the electronics system. This is obtained by setting a discriminator below the low energy neutron signal to reject counts due to gamma rays and electronic noise. To determine this threshold, the pulse height spectrum of the  $^3\text{He}$  counter was acquired. Figure 3.5 is the pulse height spectrum from noise (electronics and gamma) obtained without setting any cut on the MCA channel. The MCA input range is 10 V divided in 1024 channels. The higher channel due to noise is located around 30 (293 mV). The information obtained with the MCA allowed us to fix the lower level threshold on the SCA. The SCA front-panel, 10-turn, locking dial determines the threshold setting (+20 mV to +10 V) for the lower-level discriminator. Therefore a linear function was applied to find the threshold on the SCA (knob) according to the MCA channel. Figure 3.6 shows the pulse height spectra obtained when irradiating the LINUS with the 888 GBq AmBe source for 150 s. Two thresholds were applied according to the noise spectrum: one at the channel 25 (244 mV) and another one at the channel 49 (478 mV).





**Figure 3.5** Pulse height spectrum from noise (electronic and gamma) data.

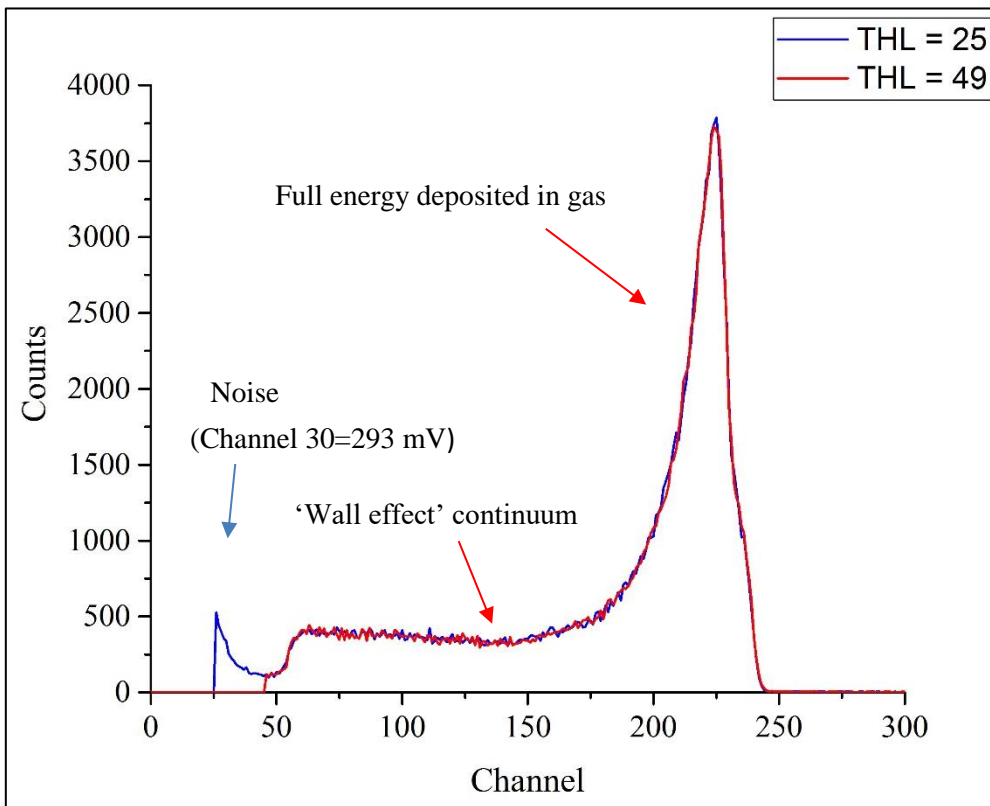


**Figure 3.6** Pulse-height spectra at two different MCA thresholds.

The pulse height spectrum from the  $^3\text{He}$  proportional counter obtained with the discriminator threshold of 49 looks reasonable. The channel 49 on the MCA corresponds to 0.46 on the knob of the SCA. The shape of the spectrum is due to the reaction kinematics. The full energy peak in the spectrum represents the collection of

the energy of both the proton and the tritium (765 keV released by the reaction). If one of the two particles enters the counter wall (wall effect), less energy is collected in the gas, which results in a low energy tail. Since the two charged particles are emitted back-to-back, one or the other is almost certainly detected. Thus there is a minimum in the collected energy, with a wide valley below, and then a low-energy increase resulting from noise and gamma events. The discriminator is set in the valley, such as small changes in the voltage will not affect the count rate. To understand if the threshold applied on the SCA according to the MCA channel was properly set, the total count given by the SCA and the count integrated from the pulse height spectrum of the MCA are compared in Table 3.6. The results agree within less than 1%.

**Table 3.6 – Counts integrated by the SCA (LINUS SCA) and the MCA (LINUS MCA).**

<b>Integration time</b>	<b>Distance</b>	<b>H*(10) rate</b>	<b>Integrated H*(10)</b>	<b>LINUS SCA</b>	<b>LINUS MCA</b>
s	cm	μSv/h	μSv	counts	counts
300	80	1026.354	85.5295	97064	96358

### 3.1.3.2 Operational voltage range

The SP9 detector is a “proportional” counter because the total amount of charge created remains proportional to the amount of charge liberated in the original neutron detection event. The neutron detector counting behaviour is mapped out by monitoring increases in detector count rate for increasing high voltage. The amplification parameters and the discriminator threshold (0.46) were held fixed. A convenient operating high voltage was chosen in the “plateau” region as shown in Figure 3.7. The plateau starts at around 810 V and ends at around 900 V. Over this range the increase in counting efficiency with voltage caused by improved charge collection is very slight, about 1%.

The new SP9 <sup>3</sup>He proportional counter was characterized:

- 1) the pulse height spectrum from the MCA allowed to set a reasonable discriminator threshold that removes the electronic noise and gamma events from the counting system. The lower lever was set at 0.46 on the SCA knob, i.e. 478 mV. The upper level was kept at 9.8 V.
- 2) the operating voltage ranges from 810 V to 900 V. Therefore, for commodity (difficulty to adjust the knob at exactly 816 V) a voltage of 820 V can be applied instead of 816 V without perturbing the counting efficiency.

Under these conditions, the LINUS works properly.

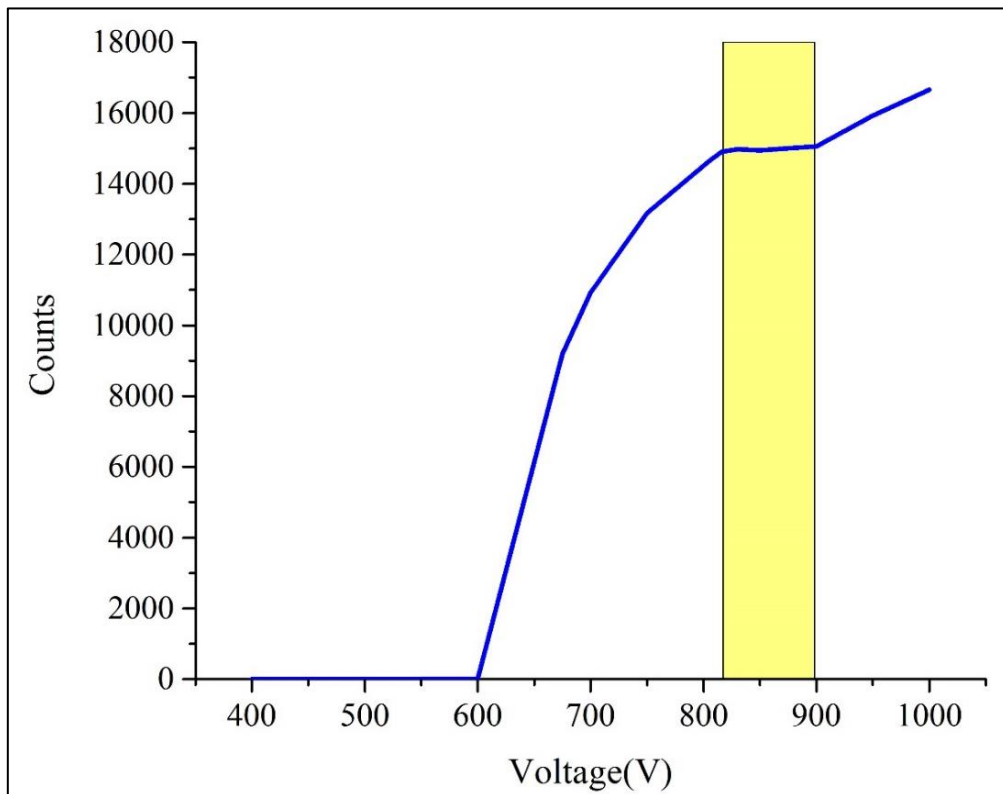


**Figure 3.7** Counts variation as function of voltage applied. The yellow square located between 810 V and 900 V corresponds to the plateau region of the LINUS.

### 3.1.3.3 Test measurement in aircraft campaign

LINUS is the reference detector at CERF, a field reproducing the neutron spectra at flight altitudes. To test its response under real conditions, it has been decided to include the LINUS in an aircraft intercomparison campaign organized by the Nuclear Physics institute of the Czech Republic. The flight used for the intercomparison was a private Embraer ERJ-135BJ where about 13 places were available. We took off and landed in Prague airport. We flew around Liberec and Pardubice (Figure 3.8). Various passive and active detectors were tested (TEPCs, rem counters, scintillators...).

LINUS was placed on the seat 13 and safely attached with a belt (Figure 3.9). The dose rate was registered each second. The flight started at 13:06 and flight level (about 12000 m) was reached at 13:38. Figure 3.10 shows the evolution of dose rate together with time and flight altitude. For clarity, the data were averaged over each minute. Because of safety reasons, we could not run the LINUS acquisition during take off. Therefore, a few points are missing at the beginning of the flight. The LINUS  $H^*(10)$  follows quite well the flight profile, increasing with the climb portion of the flight, stabilizing during the flight level and decreasing with the descent phase. Table 3.7 summarizes the results. The dose rate and the integral dose were averaged for both the flight level and the whole flight. The dose rate was  $3.94 \mu\text{Sv/h}$  at flight level and  $3.64 \mu\text{Sv/h}$  for the entire flight. As expected, this underlines that the majority (92%) of the integrated dose comes from the flight level (flight level:  $6.07 \mu\text{Sv}$  and whole flight:  $7.09 \mu\text{Sv}$ ).

The results of the others detector present on board are still under analysis by the different research teams involved. However comparing with literature data (see for example [8][9]), the dose rate at similar altitude was about  $4 \mu\text{Sv/h}$ . Even if it was measured with other kinds of detectors and not the same route, this value indicates that the LINUS result is correct.

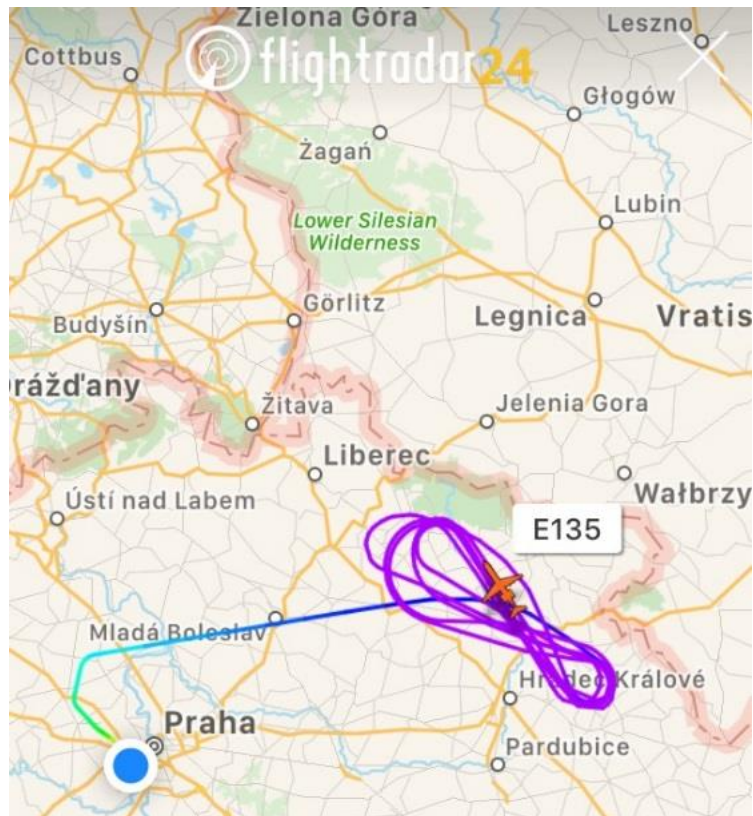


**Figure 3.8** Flight position according to the GPS.

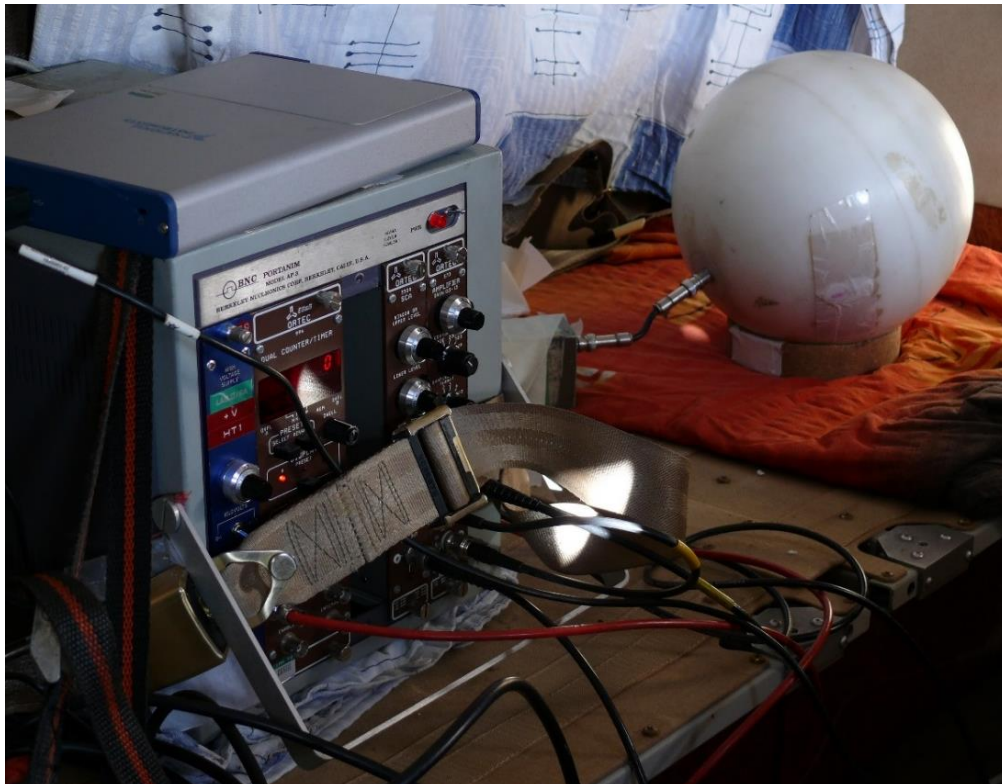


**Figure 3.9** Photo of LINUS during the aircraft campaign.

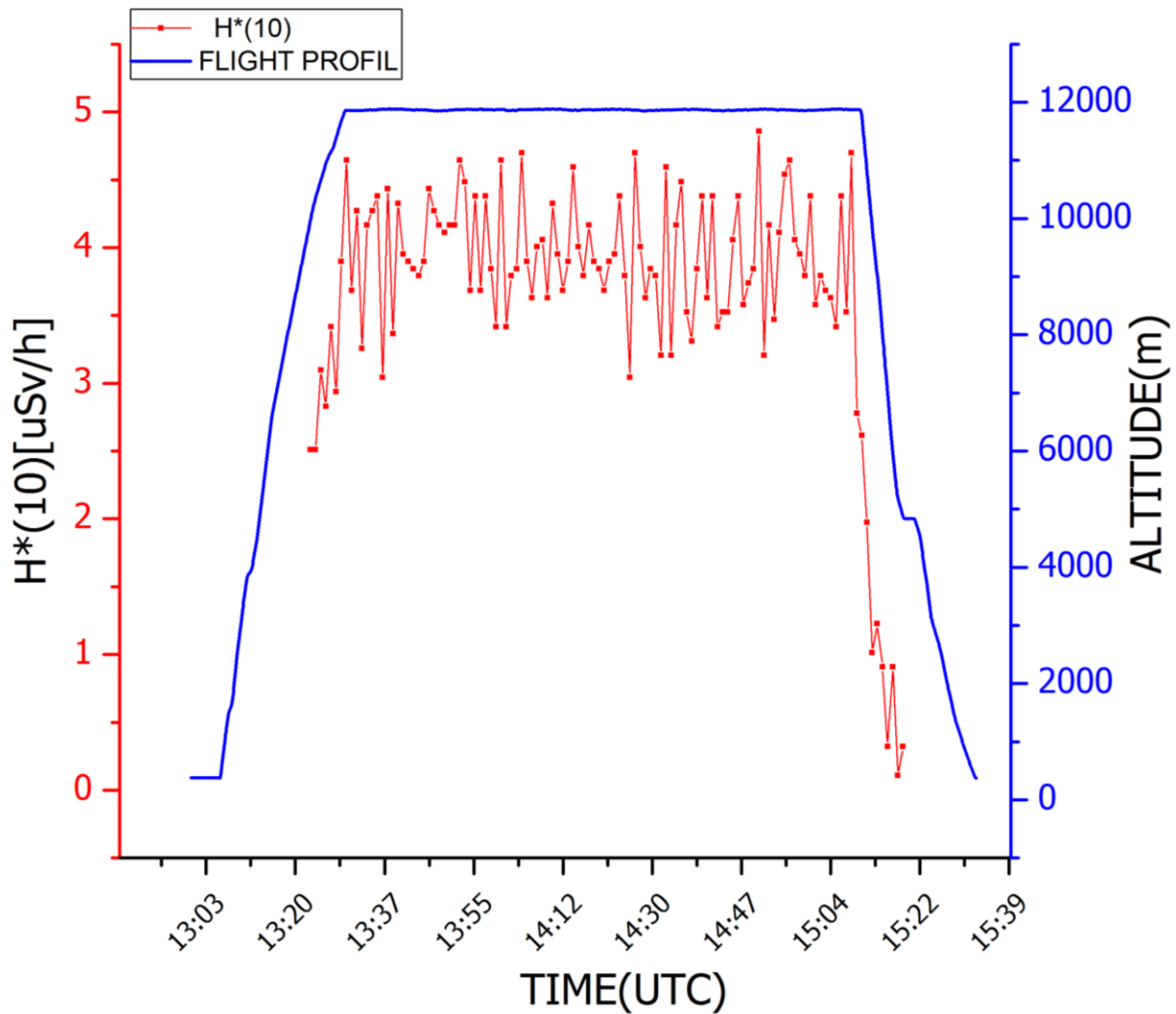


Figure 3.10 LINUS  $H^*(10)$  as function of time and flight level.

Table 3.7 LINUS results at flight level and for the entire flight.

	Start-End Time	Dose Rate (uSv/h)	Integrated Dose (uSv)
Fight altitude	13:38/15:08	3.94	6.07
Whole flight	13:06/15:34	3.64	7.09

## 3.2 Measurement at CERF

### 3.2.1 Neutron spectral fluence and $H^*(10)$ measurements

Measurements of the neutron spectral fluence were performed with the BSS in positions CS4, CT7 and IT7. The spectra were obtained by unfolding the experimental counts with the MAXED [10] and GRAVEL [11] codes. The so-called “guess spectrum”, required by the codes in order to start the unfolding procedure, was obtained by FLUKA [24] [25] Monte Carlo simulations. These FLUKA spectra are the results of new simulations and are not the spectra on which the reference values given in ref. [15] are based. The calculated spectra were folded with the ICRP 74 [12] fluence-to- $H^*(10)$  conversion coefficients in order to obtain the  $H^*(10)$  value, normalised to IC-counts. In addition,  $H^*(10)$  measurements were performed with the detectors listed in Section 2.1 on the CS, CT and IT (Table 3.8). The following section describes the experimental results as well as the FLUKA values updated recently.

**Table 3.8 Measurement positions in the CERF runs 2015, 2016 and 2017.**

	Detector name	Detector type	Institute	CT	CS	IT
2015	WENDI	Extended range rem counter	CERN	1, 2, 4, 10, 13, 14, 15	3, 4	1,13
	LB6411	Conventional rem counter	SCK•CEN, Belgium	1, 2, 4, 10, 13, 14, 15	3	2, 4
	BSS	Extended-range BSS	CERN	7	4	7
2016	LUPIN	Extended range rem counter	CERN	1, 2, 4, 10, 13, 14, 15	1, 2, 3, 4, 6, 8	1, 2, 4, 7, 13
2017	PRESCILA	Extended range rem counter	STFC-Rutherford Appleton Laboratory UK	1, 2, 4		1, 2, 4, 7, 13
	LINUS	Extended range rem counter	CERN	<i>All positions</i>	<i>All positions</i>	<i>All positions</i>
2017 FLUKA reference		Simulation	CERN	<i>All positions</i>	<i>All positions</i>	<i>All positions</i>

### 3.2.1.1 Measurement on Concrete Top (CT)

Each detector was placed on a support so that its centre was at 25 cm above the concrete top. For the BSS, the number of integrated counts was corrected for dead time losses and normalised to the number of particles impinging on the target (Table 3.9). The neutron spectrum was measured only in position CT7 (Figure 3.11), whereas the H\*(10) was measured in almost all positions by the other detectors (Table 3.8). The spectra calculated with the two codes are in good agreement with each other both in shape and absolute value of the neutron fluence (MAXED= 5.97E- 5 cm<sup>-2</sup> per primary, GRAVEL= 6.00E-5 cm<sup>-2</sup> per primary). The unfolded spectra show larger absolute values for all components (thermal, epithermal, evaporation and high energy) if compared with FLUKA (4.95E-5 cm<sup>-2</sup> per primary). As expected the thermal, evaporation and high energy peaks are well visible, with several resonances present in the MeV region. The BSS H\*(10), normalised to the IC counts, was obtained by folding the measured neutron spectra with the ICRP 74 fluence-to-H\*(10) conversion coefficients. The BSS measurement uncertainty is estimated at 12%. The sensitivity analysis and uncertainty propagation calculation were based on the statistical counting uncertainties (1%), the uncertainty on the number of delivered particles (10%), the uncertainty on the response matrix (3%) and the positioning uncertainty (3%). The rem counters data were recorded each second and analysed with a Python script which averages the H\*(10) for all spills. The total uncertainty includes the uncertainty on the number of delivered particles (10%), on the calibration factor (5% LINUS 7% WENDI, 7% LB6411 and 12% PRESCILA) and on the positioning of the detector (3%), whereas the statistical uncertainty on the number of counts was negligible (<1%).

**Table 3.9** Data obtained with the BSS in position CS4, CT7 and IT7 normalised to the number of particles impinging on the target.

Sphere	Counts per beam particle		
	CS4	CT7	IT7
81 mm	$6.98 \pm 0.78 \cdot 10^{-5}$	$5.21 \pm 0.58 \cdot 10^{-5}$	$6.36 \pm 0.71 \cdot 10^{-4}$
108 mm	$8.59 \pm 0.96 \cdot 10^{-5}$	$5.51 \pm 0.62 \cdot 10^{-5}$	$1.15 \pm 0.13 \cdot 10^{-3}$
133 mm	$9.26 \pm 1.04 \cdot 10^{-5}$	$6.59 \pm 0.74 \cdot 10^{-5}$	$1.34 \pm 0.15 \cdot 10^{-3}$
178 mm	$8.52 \pm 0.95 \cdot 10^{-5}$	$6.07 \pm 0.68 \cdot 10^{-5}$	$1.16 \pm 0.13 \cdot 10^{-3}$
233 mm	$8.08 \pm 0.90 \cdot 10^{-5}$	$5.12 \pm 0.57 \cdot 10^{-5}$	$6.75 \pm 0.76 \cdot 10^{-4}$
Ollio	$4.42 \pm 0.48 \cdot 10^{-5}$	$2.99 \pm 0.34 \cdot 10^{-5}$	$4.61 \pm 0.52 \cdot 10^{-4}$
Stanlio	$3.87 \pm 0.43 \cdot 10^{-5}$	$3.39 \pm 0.38 \cdot 10^{-5}$	$2.00 \pm 0.22 \cdot 10^{-4}$

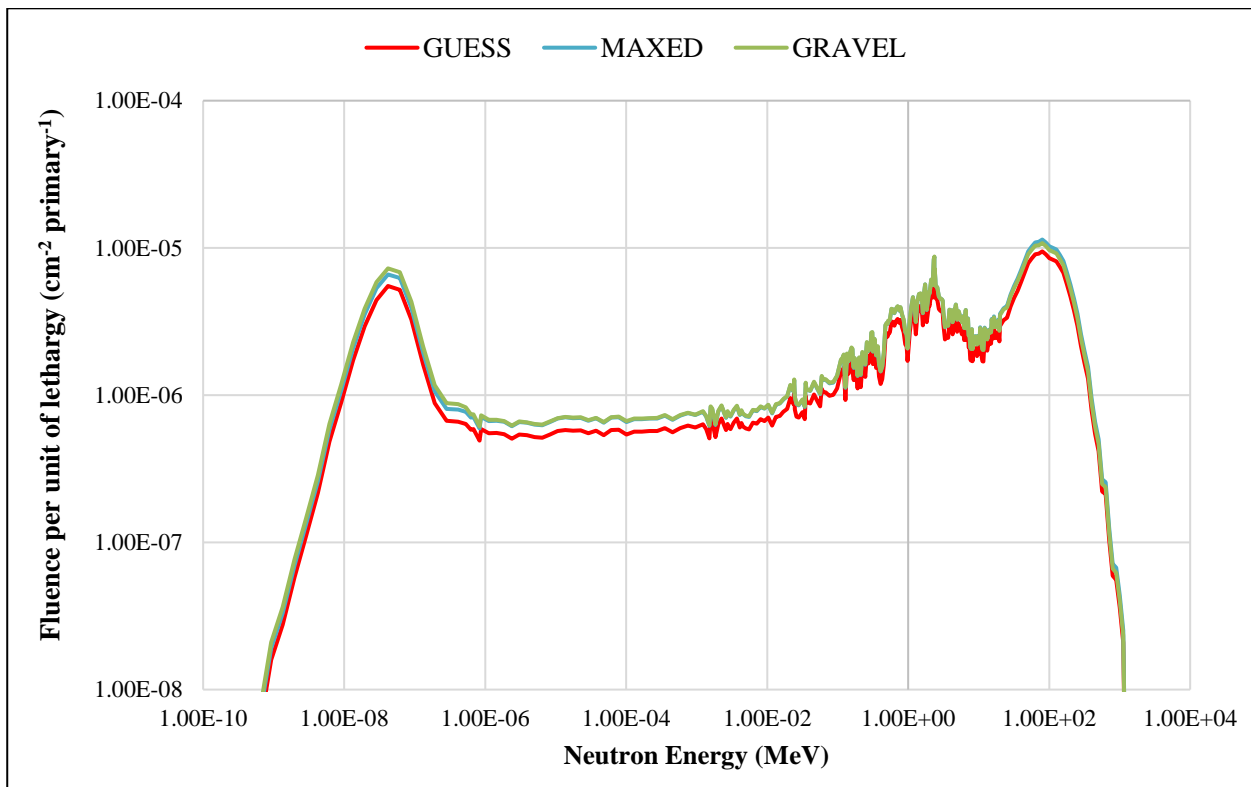


**Figure 3.11** Neutron spectral fluences obtained for position CT7, compared with the guess spectrum. The two unfolded spectra are nearly undistinguishable. The uncertainties are not shown for clarity.

All  $H^*(10)$  results are presented in Table 3.10 and Figure 3.12. All detectors show results in good agreement with the FLUKA simulations. To better visualize the agreement of the experimental results with the FLUKA values, the ratios between detector response and FLUKA predictions are plotted in Figure 3.13. For all positions if compared with FLUKA, the WENDI overestimates from 5% to 21%, while the LB6411 underestimates from 22% to 38%; the latter is explained by the fact that the LB6411 is a conventional rem counter with low response to high-energy neutrons. The agreement between LINUS and LUPIN with FLUKA  $H^*(10)$  is much better, with slight over or underestimations depending on the position (- 6% to +13% for LINUS, -12% to +5% for LUPIN). Concerning the BSS, the  $H^*(10)$  is about 20% higher than the FLUKA value. The PRESCILA/FLUKA  $H^*(10)$  ratios are presented in Figure 3.14, where an overestimation of PRESCILA by a



factor of 3.3-3.5 can be seen. This large overestimation is due to the strong dependence on the calibration spectrum and to the response function of the detector. The PRESCILA used at CERF was calibrated with a  $^{252}\text{Cf}$  source, as shown in Table 3.11; an overestimation of 2 to 5.6 is seen for the different neutron energies.

**Table 3.10 Neutron  $H^*(10)$  in nSv per IC count measured by the different detectors and simulated by FLUKA in the CT positions. The  $H^*(10)$  obtained from the unfolded BSS spectrum in CT7 is also shown. The BSS value is the average of the MAXED and GRAVEL values.**

Position	WENDI-II	LINUS	BSS	LUPIN	LB6411	PRESCILA	FLUKA
CT1	0.224±0.027	0.206±0.024	–	0.191±0.017	0.139±0.017	0.679±0.098	0.198±0.020
CT2	0.238±0.022	0.216±0.025	–	0.212±0.020	0.150±0.014	0.703±0.102	0.208±0.021
CT3	0.225±0.028	0.204±0.023	–	–	–	–	0.207±0.021
CT4	0.193±0.024	0.174±0.020	–	0.162±0.015	0.115±0.014	0.649±0.094	0.185±0.019
CT5	0.288±0.035	0.254±0.029	–	–	–	–	0.236±0.024
CT6	0.289±0.035	0.270±0.031	–	–	–	–	0.253±0.025
CT7	0.272±0.033	0.255±0.029	0.299±0.036	0.242±0.021	–	–	0.250±0.025
CT8	0.240±0.029	0.217±0.025	–	–	–	–	0.226±0.023
CT9	0.290±0.036	0.256±0.029	–	–	–	–	0.240±0.024
CT10	0.309±0.038	0.271±0.031	–	0.261±0.024	0.198±0.024	–	0.255±0.026
CT11	0.296±0.036	0.272±0.031	–	–	–	–	0.255±0.026
CT12	0.244±0.030	0.225±0.026	–	–	–	–	0.229±0.023
CT13	0.229±0.028	0.221±0.025	–	0.210±0.020	0.155±0.019	–	0.203±0.020
CT14	0.260±0.032	0.244±0.028	–	0.227±0.023	0.167±0.020	–	0.216±0.022
CT15	0.249±0.030	0.231±0.027	–	0.224±0.021	0.168±0.020	–	0.217±0.022
CT16	0.208±0.025	0.207±0.024	–	–	–	–	0.199±0.020



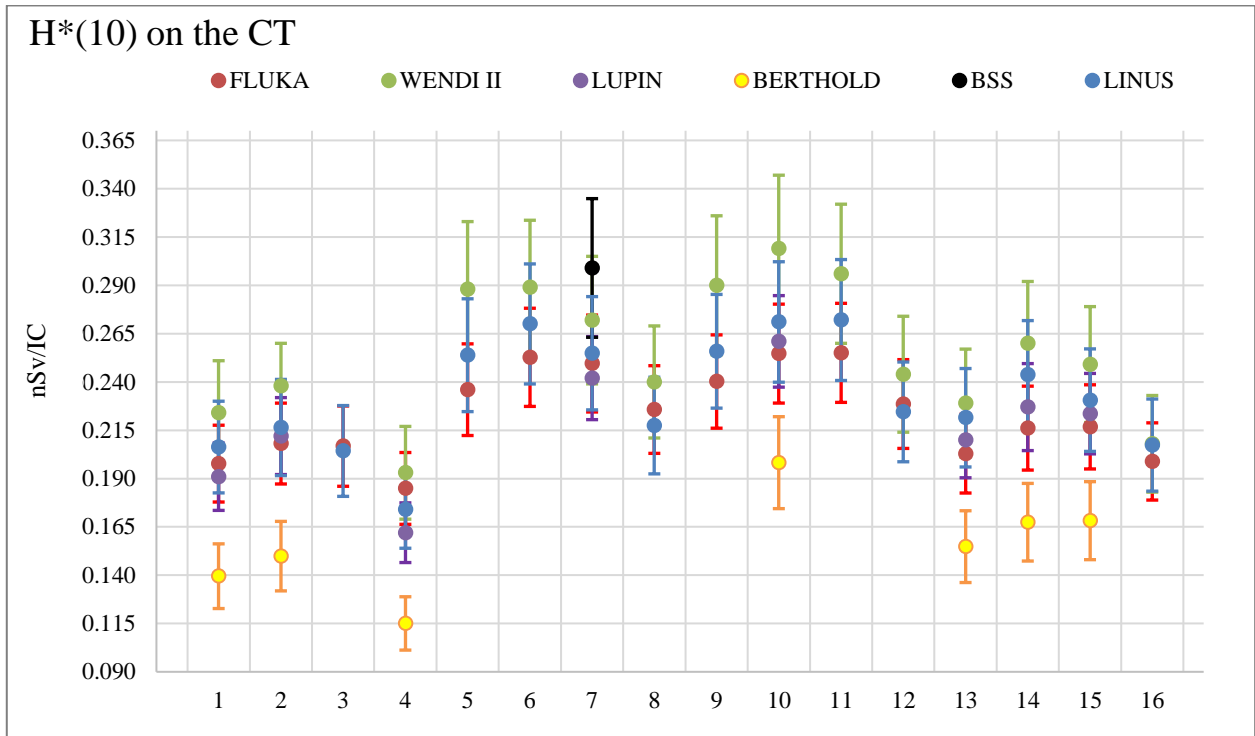


Figure 3.12 H\*(10) in nSv per IC count of WENDI, LUPIN, LB6411, LINUS and FLUKA on the CT positions.

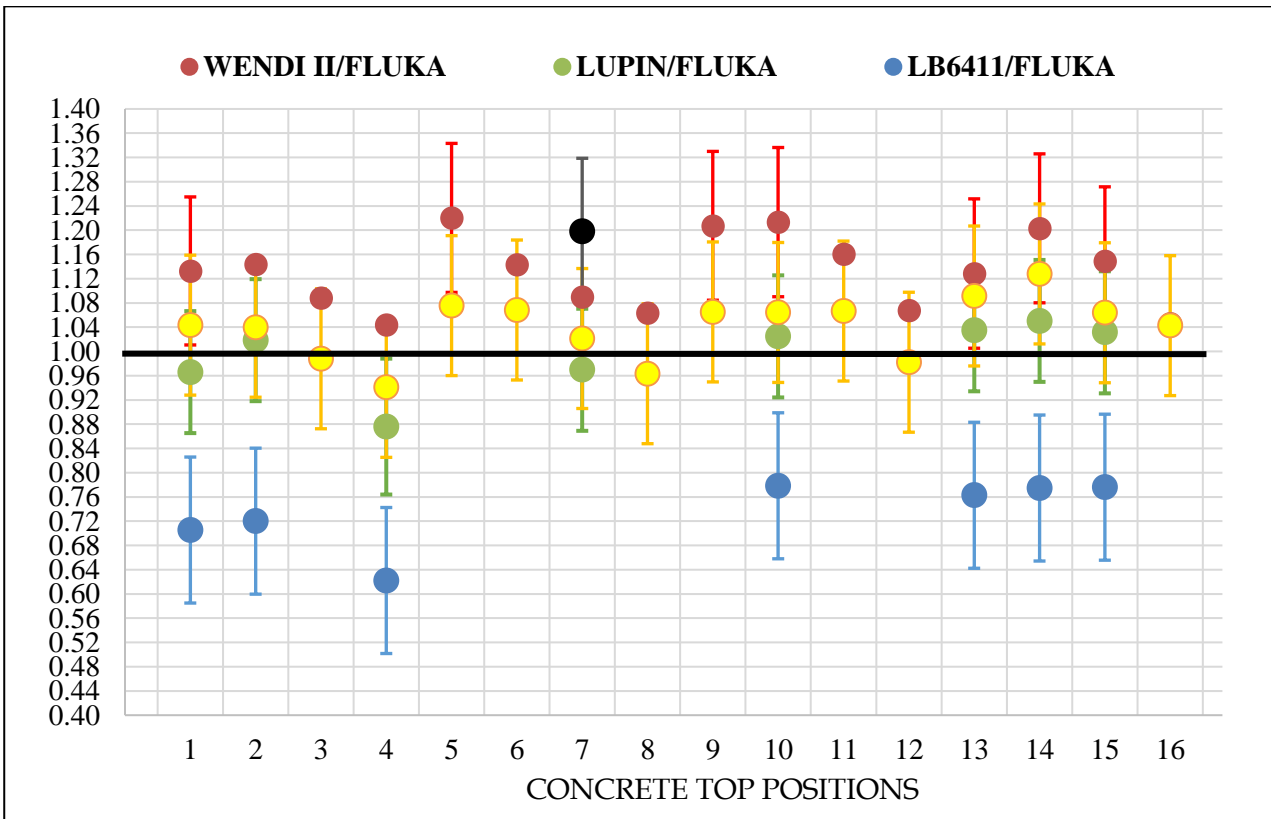


Figure 3.13 H\*(10) ratios between WENDI, LUPIN, LB6411, LINUS and FLUKA on the CT positions.

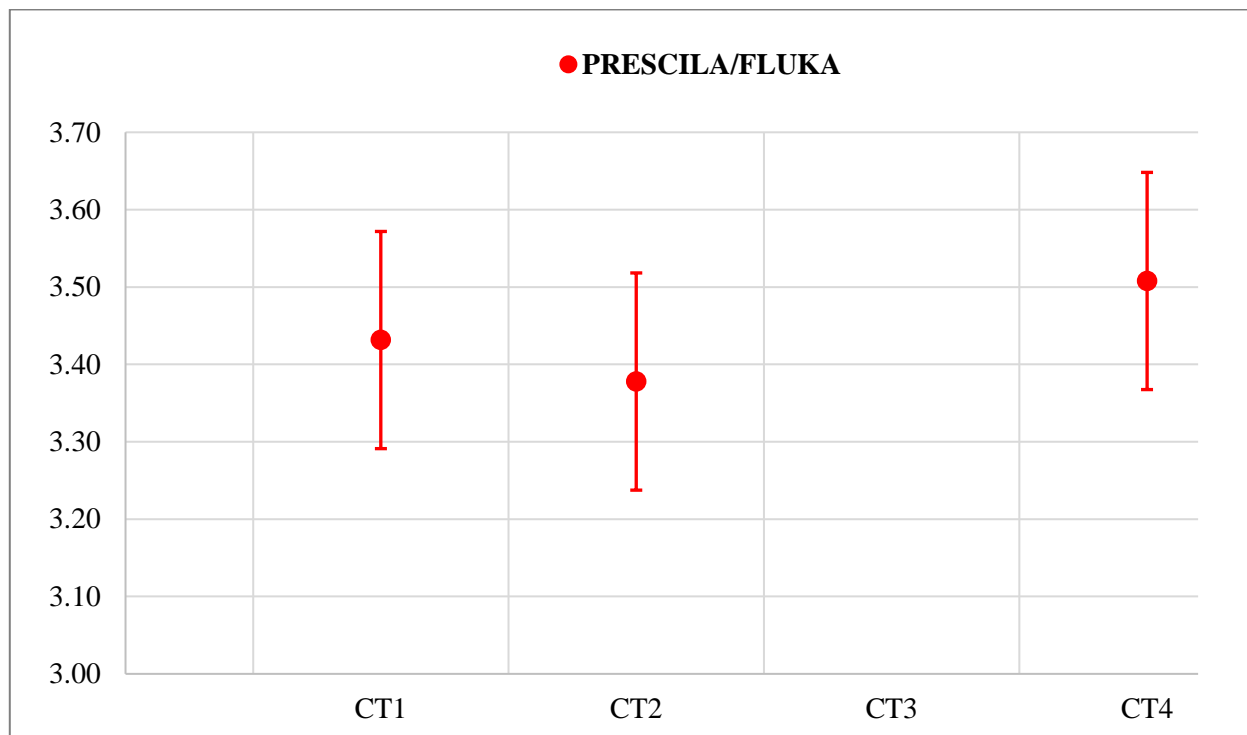


Figure 3.14.  $H^*(10)$  ratios between PRESCILA and FLUKA on the CT.

Table 3.11 PRESCILA Neutron Rem Meter energy response: response per unit ambient dose equivalent [ $H^*(10)$ ] relative to both bare  $^{252}\text{Cf}$  and  $^{241}\text{AmBe}$  Calibrations.

Neutron Energy	Irradiation Geometry	Normalized Response: bare $^{252}\text{Cf}$ calibration	Normalized Response: $^{241}\text{AmBe}$ calibration
Thermal (GKSS <sup>3</sup> )	Side 1	1.89	1.03
Thermal (GKSS)	Side 2	1.91	1.04
Thermal (GKSS)	Handle	2.82	1.54
Thermal (GKSS)	End Face	0.095	0.052
24 keV (PTB <sup>4</sup> )	Side	4.22	2.31
146 keV (PTB)	Side	0.59	0.32
250 keV (PTB)	Side	0.38	0.21
565 keV (PTB)	Side	0.24	0.13
1.2 MeV (PTB)	Side	0.47	0.26
2.5 MeV (PTB)	Side	1.31	0.72
4.849 MeV (PTB)	Side	2.59	1.42
8.079 MeV (PTB)	Side	3.17	1.73
14.8 MeV (PTB)	Side	2.85	1.56
19.0 MeV (PTB)	Side	2.59	1.42
46.5 MeV (TSL <sup>5</sup> )	End Face	3.00	1.53
94.5 MeV (TSL)	End Face	5.45	2.85
142.7 MeV (TSL)	End Face	5.25	2.69
172.8 MeV (TSL)	End Face	5.57	2.84
345 MeV (LANSCE <sup>6</sup> )	End Face	2.38	1.28

<sup>3</sup> Gesellschaft für Kernenergieverwertung in Schiffbau und Schifffahrt (GKSS) in Germany,

<sup>4</sup> Physikalisch-Technische Bundesanstalt (PTB) in German

<sup>5</sup> The Svedberg Laboratory (TSL) in Sweden

<sup>6</sup> Los Alamos Neutron Science Center (LANSCE) in USA.

### 3.2.1.2 Measurement on Concrete Side (CS)

Each detector was placed on an aluminium support at the target height with its centre at 25 cm from the side wall, and exposed for about 10 minutes to decrease the statistical uncertainty on the counts below 1% (Figure 3.15). The neutron spectrum was measured in position CS4 (Figure 3.16). The spectra calculated with the two unfolding codes are in good agreement both in shape and absolute value of the neutron fluence (MAXED=  $8.40\text{E-}5 \text{ cm}^{-2}$  per primary, GRAVEL=  $8.42\text{E-}5 \text{ cm}^{-2}$  per primary). As on the CT, the unfolded spectra show larger absolute values for all components (thermal, epithermal, evaporation and high energy) if compared with FLUKA ( $7.46\text{E-}5 \text{ cm}^{-2}$  per primary). Table 3.12 and Figure 3.17 present all the  $H^*(10)$  results at the different measurement positions. Figure 3.18 presents the ratio between the experimental results and the FLUKA  $H^*(10)$  values. Compared to FLUKA, the WENDI overestimates the  $H^*(10)$  from 1% to 22% while the LB6411 still underestimates (23%). The LINUS and LUPIN show a good agreement with FLUKA (within 12% for the LINUS and 17% for the LUPIN). For the LUPIN and the WENDI, the agreement with FLUKA  $H^*(10)$  are slightly better on the CT, for the BSS is better on the CS, whereas LINUS is about the same.

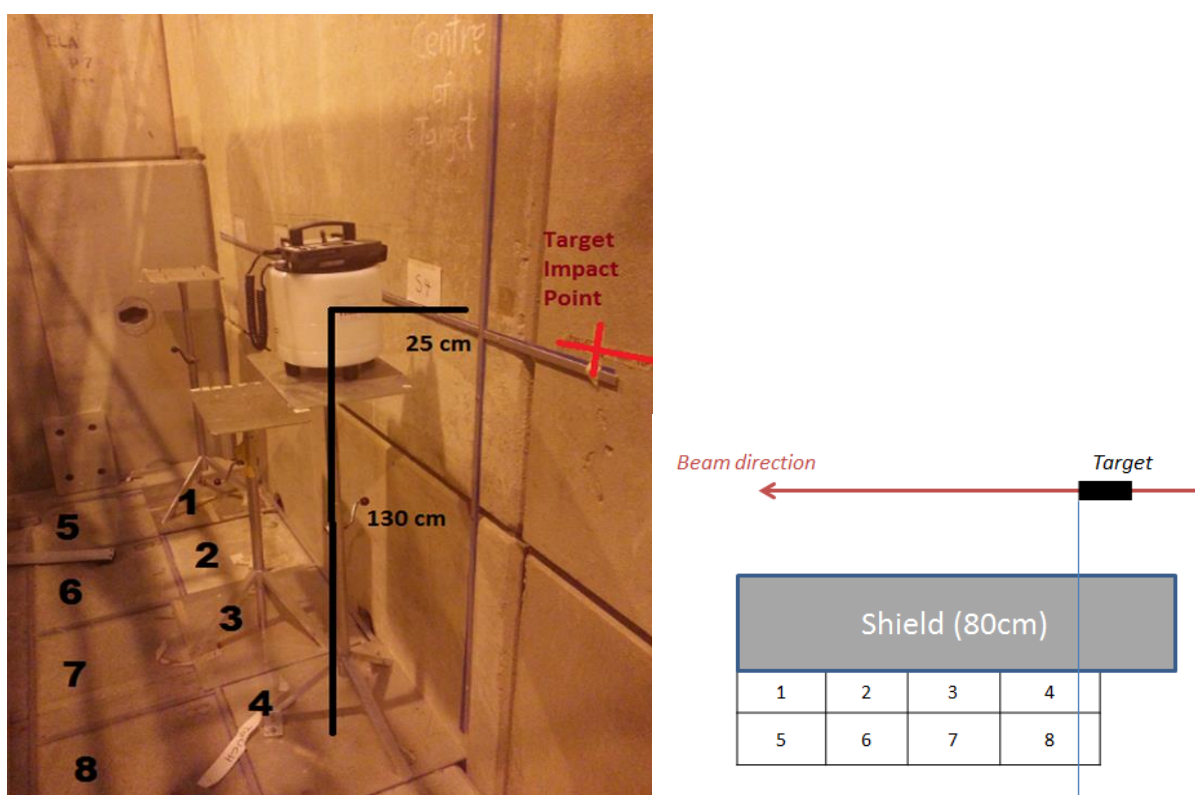


Figure 3.15 Experimental set-up of the measurements performed with the WENDI rem counter in the CS positions.

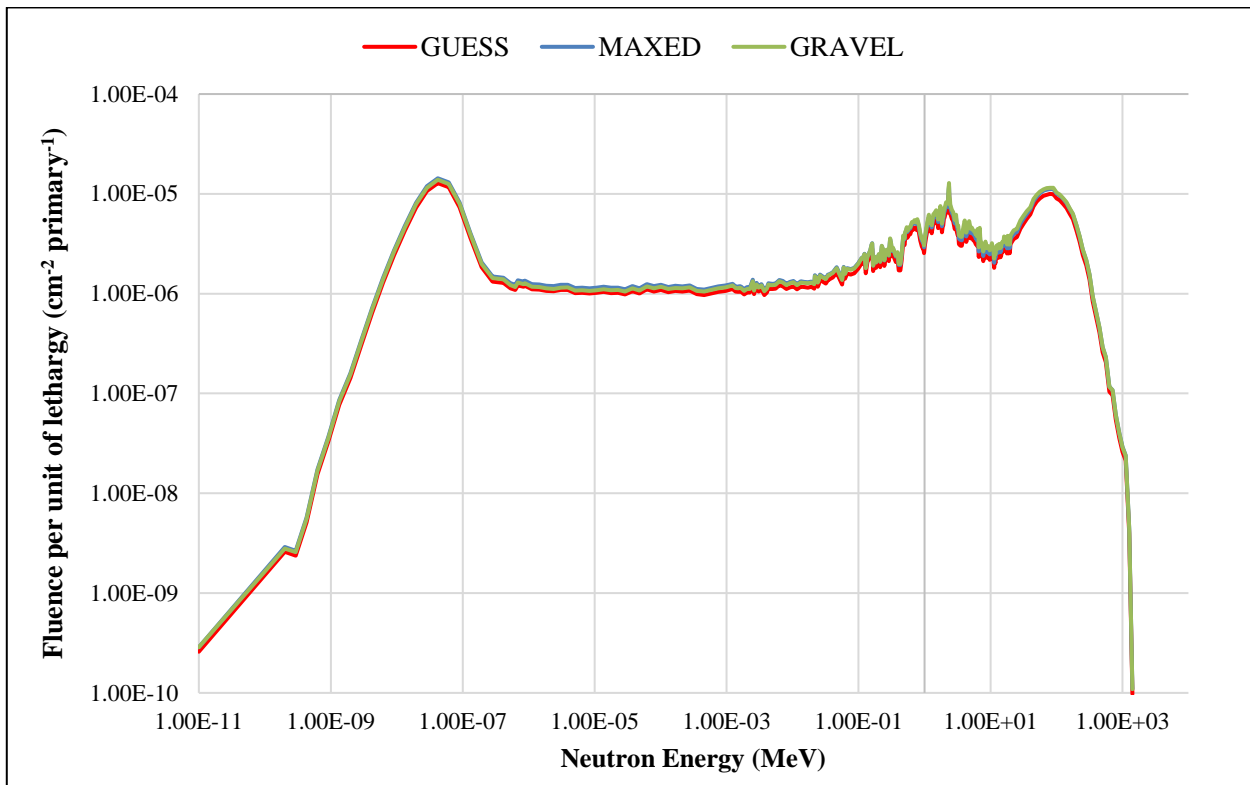


Figure 3.16 Neutron spectral fluences obtained for position CS4, compared with the guess spectrum. The two unfolded spectra are nearly undistinguishable. The uncertainties are not shown for clarity.

Table 3.12 Neutron  $H^*(10)$  in nSv per IC count measured with the different detectors and simulated by FLUKA in the CS positions. The  $H^*(10)$  obtained from the unfolded BSS spectrum in CS4 is also shown. The BSS value is the average of the MAXED and GRAVEL values.

Position	WENDI-II	LINUS	BSS	LUPIN	LB6411	FLUKA
CS1	0.395±0.048	0.354±0.043	–	0.371±0.037	–	0.335±0.034
CS2	0.417±0.051	0.369±0.044	–	0.404±0.040	–	0.346±0.035
CS3	0.392±0.048	0.358±0.043	–	0.377±0.038	0.258±0.031	0.336±0.034
CS4	0.358±0.044	0.304±0.037	0.343±0.041	0.327±0.033	–	0.296±0.025
CS5	0.284±0.035	0.271±0.032	–		–	0.249±0.025
CS6	0.310±0.038	0.274±0.033	–	0.276±0.028	–	0.254±0.026
CS7	0.297±0.036	0.260±0.031	–		–	0.243±0.024
CS8	0.217±0.027	0.225±0.027	–	0.244±0.024	–	0.216±0.022

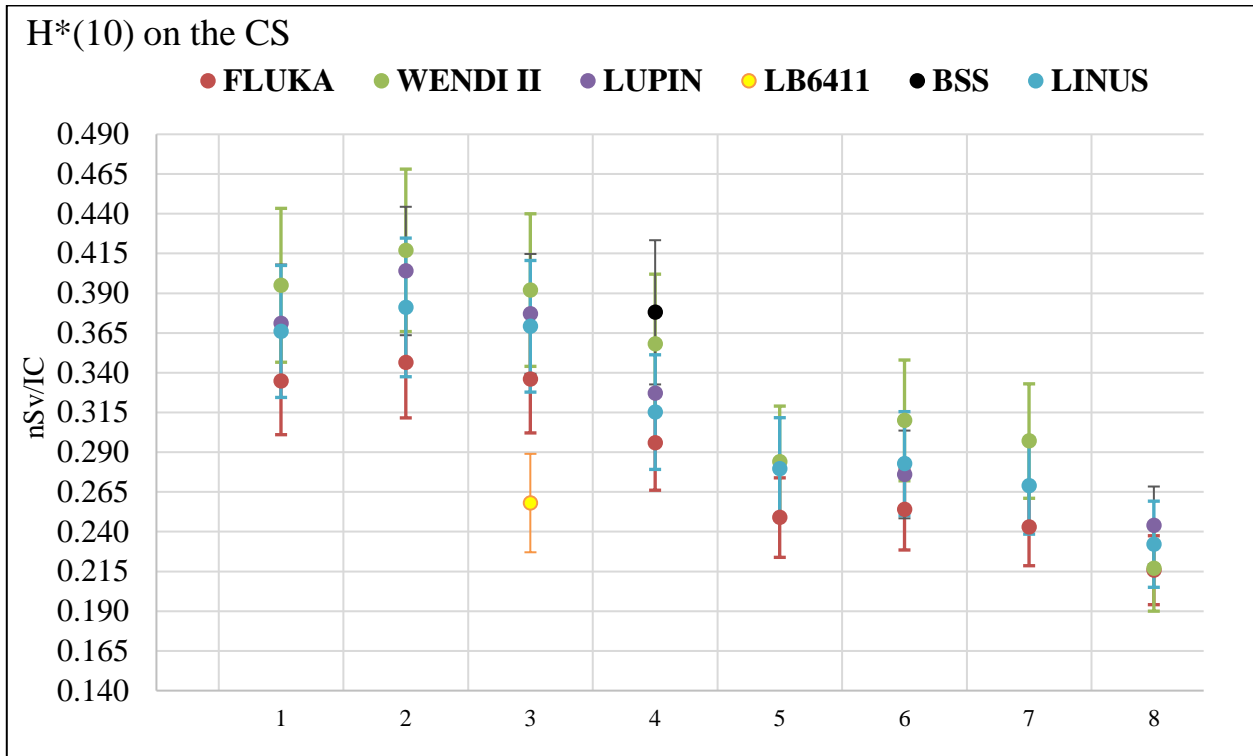


Figure 3.17  $H^*(10)$  in nSv per IC count measured with LINUS, WENDI, BSS, LB6411, LUPIN and calculated with FLUKA on the CS positions.

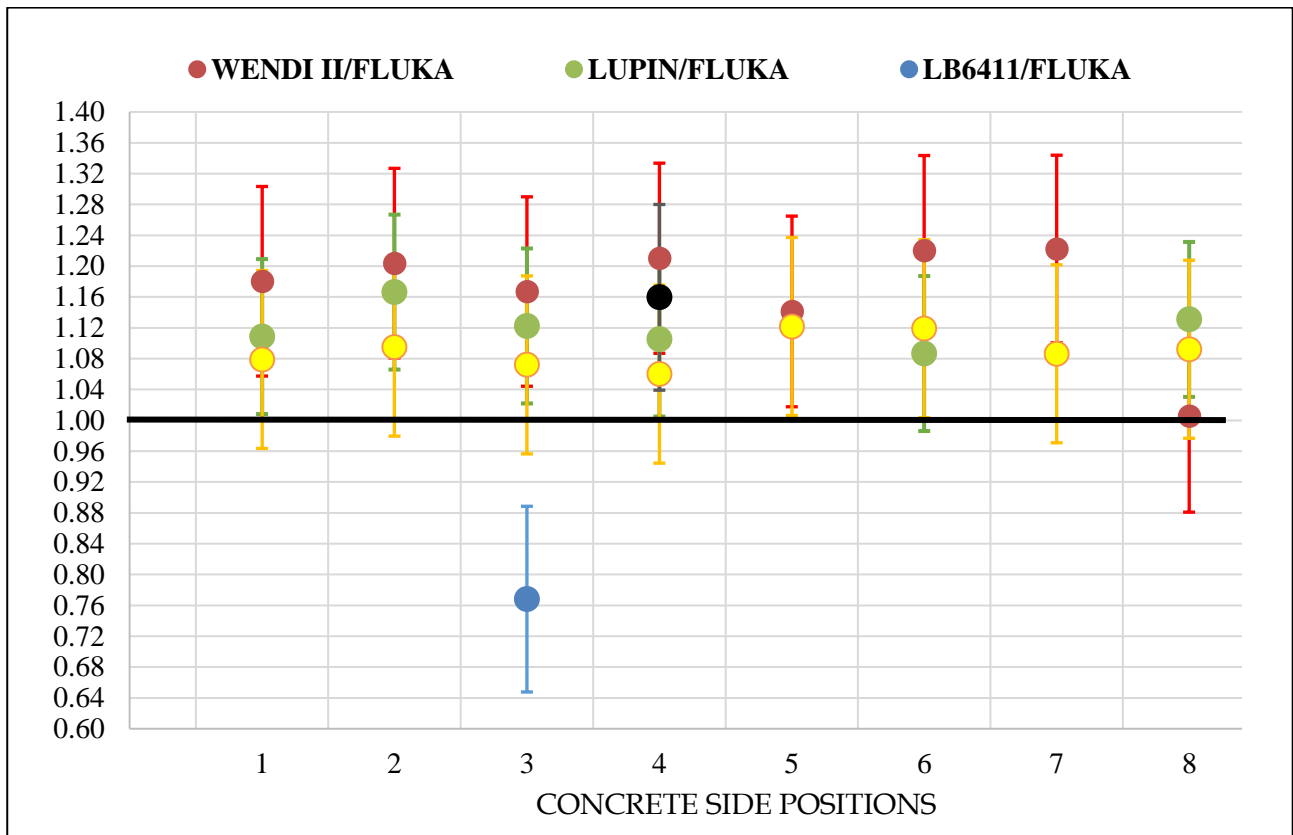


Figure 3.18  $H^*(10)$  ratios between WENDI, LUPIN, LB6411, LINUS and FLUKA on the CS positions.

### 3.2.1.3 Measurement on Iron Top (IT)

The IT neutron spectrum differs substantially from the CT one (see Figure 2.12). The IT spectrum presents an overwhelming evaporation part as compared to the spectrum from the concrete shields. On the IT, 93% of the  $H^*(10)$  is due to the evaporation part and 6.5% to the high energy part (Table 3.13). On the CT 46.1% and 52.5% of the  $H^*(10)$  are due to the evaporation and the high energy components, respectively. On the CS these fractions are inverted: 50.9% for the evaporation component and 46.5% for the high energy part. Except this inversion and the presence of a slightly higher thermal and epithermal part on the CS spectrum (due to the 80 cm back concrete shield), the CT and CS spectra are very similar.

**Table 3.13** Repartition of  $H^*(10)$  in nSv per IC count on IT7, CT7 and CS4.

	Spectral component				
	Thermal	Intermediate	Evaporation	High energy	Total
<b>IT7</b>					
$H^*(10)$ [nSv/IC]	0.001	0.003	1.982	0.138	2.124
Relative contribution (%)	0.1	0.1	93.3	6.5	100
<b>CT7</b>					
$H^*(10)$ [nSv/IC]	0.003	0.001	0.116	0.132	0.252
Relative contribution (%)	1.0	0.3	46.1	52.5	100
<b>CS4</b>					
$H^*(10)$ [nSv/IC]	0.006	0.002	0.150	0.137	0.295
Relative contribution (%)	2.1	0.6	50.9	46.5	100

The neutron spectrum was measured in position IT7. The spectra calculated with the two codes are in good agreement both in shape and absolute value of the neutron fluence ( $MAXED = 5.20E-6 \text{ cm}^{-2}$  per primary,  $GRAVEL = 5.17E-6 \text{ cm}^{-2}$  per primary and  $FLUKA = 5.34E-6 \text{ cm}^{-2}$  per primary). Contrary to the unfolded neutron spectra on the CT/CS, the measured spectra are in very good agreement with the FLUKA spectrum for all components (thermal, epithermal, evaporation and high energy) (Figure 3.19). Table 3.14 and Figure 3.20 present all  $H^*(10)$  results at the different measurement positions. Figure 3.21 presents the ratio between the detector and FLUKA  $H^*(10)$ . All detectors underestimate with respect to FLUKA in most positions. WENDI underestimates the  $H^*(10)$  up to 10%, LUPIN up to 16% and the LB6411 still underestimates considerably (-14% to -27%). The LINUS shows a better agreement with FLUKA (-9% to +10%). WENDI shows a better agreement with both FLUKA and LINUS if compared to the CT. This is due to the substantially different neutron energy distributions on the CT and IT and to the detector response functions. WENDI and LINUS have similar response functions at low and intermediate energies, whereas WENDI overestimates above 20 MeV (Figure 2.4): on the IT the high-energy component is much less relevant.

Figure 3.22 presents the  $H^*(10)$  ratio between PRESCILA and FLUKA. PRESCILA underestimates FLUKA from -25% to -38%. It has been shown above that PRESCILA overestimates the high energy component (see Figure 2.8 and Table 2.11). Thus on the CT, where the high energy part dominates, PRESCILA overestimates the  $H^*(10)$  by a factor of 3.4. On the IT, the more important region is the evaporation one. In this energy range PRESCILA strongly underestimates the  $H^*(10)$ . Therefore, PRESCILA overestimates the  $H^*(10)$  on the CT and underestimates it on the IT.

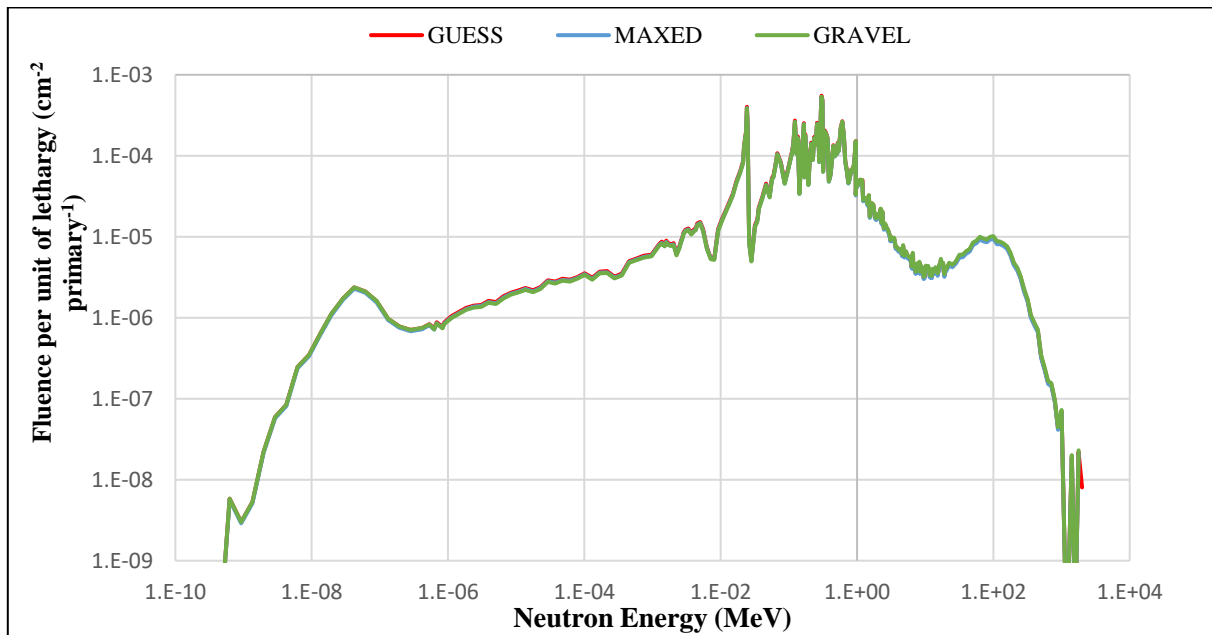


Figure 3.19 Neutron spectral fluence obtained for position IT7, compared with the guess spectrum. The three spectra are nearly undistinguishable. The uncertainties are not shown for clarity.

Table 3.14 Neutron  $H^*(10)$  in nSv per IC count measured with the different detectors and simulated by FLUKA in the IT positions. The  $H^*(10)$  obtained from the unfolded BSS spectrum in IT7 is also shown. The BSS value is the average of the MAXED and GRAVEL values.

Position	WENDI-II	LINUS	BSS	LUPIN	LB6411	PRESCILA	TEPCs	FLUKA
IT1	1.208±0.147	1.290±0.148	–	1.247±0.125	–	0.922±0.133	–	1.355±0.136
IT2		1.530±0.176	–	1.317±0.132	–	1.053±0.152	–	1.559±0.156
IT3		1.653±0.190	–	1.642±0.164	1.226±0.147	–	–	1.680±0.168
IT4		1.666±0.192	–	1.473±0.148	1.382±0.166	1.017±0.147	–	1.604±0.161
IT5	1.576±0.193	1.552±0.178	–	1.450±0.145	1.289±0.155	–	–	1.714±0.172
IT6		1.988±0.229	–	1.873±0.188	–	–	–	2.016±0.202
IT7		2.236±0.257	2.144±0.257	2.003±0.201	–	1.378±0.199	1.697±0.247 1.484±0.216	2.218±0.222
IT8		2.116±0.243	–	2.027±0.203	–	–	–	2.139±0.214
IT9	1.529±0.187	1.618±0.186	–	1.584±0.159	–	–	–	1.696±0.170
IT10	1.932±0.237	1.970±0.227	–	1.958±0.196	–	–	–	2.028±0.203
IT11		2.237±0.257	–	2.235±0.224	–	–	–	2.244±0.225
IT12		2.166±0.249	–	2.209±0.249	–	–	–	2.186±0.219
IT13	1.018±0.125	1.065±0.122	–	1.016±0.102	–	0.844±0.122	–	1.132±0.113
IT14	1.417±0.174	1.540±0.177	–	1.442±0.144	–	–	–	1.501±0.150
IT15	1.569±0.192	1.628±0.187	–	1.623±0.163	–	–	0.791±0.115 0.670±0.098	1.660±0.166
IT16		1.730±0.199	–	1.570±0.157	–	–	–	1.572±0.157

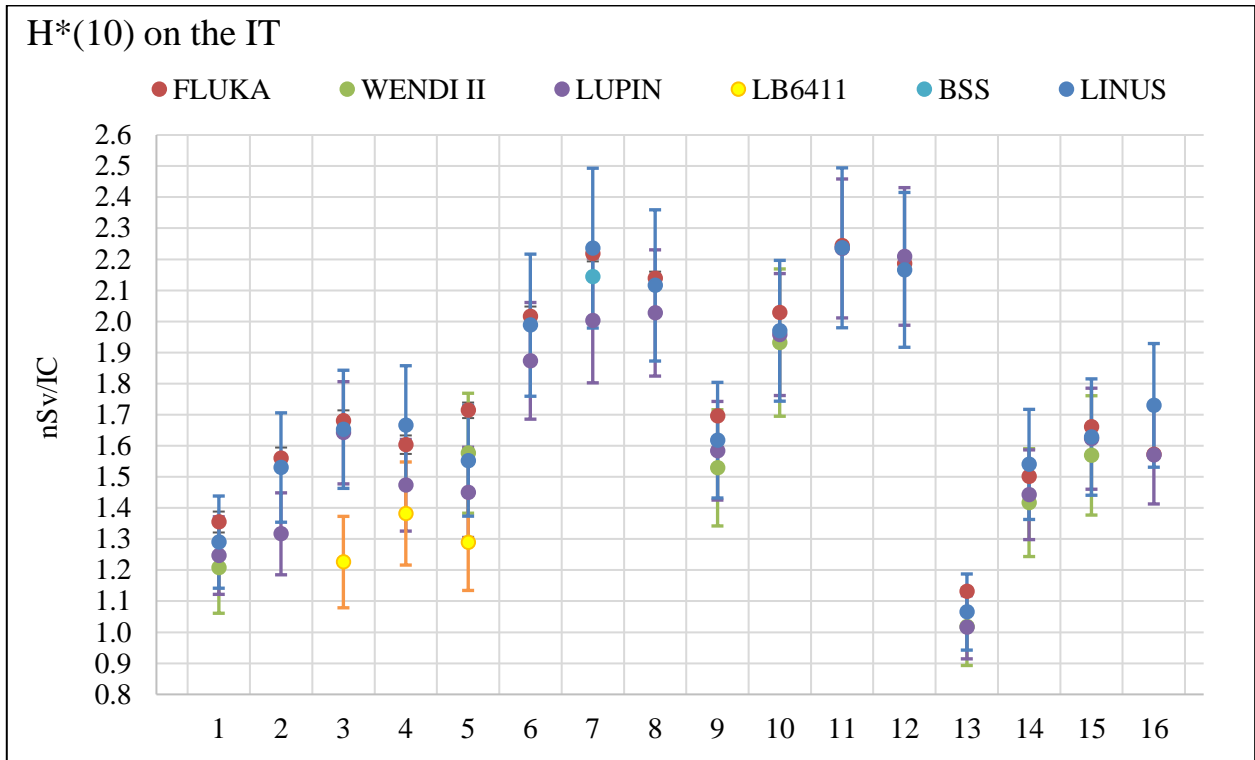


Figure 3.20  $H^*(10)$  in nSv per IC count measured by LINUS, WENDI, LUPIN, LB6411, BSS and calculated with FLUKA on IT.

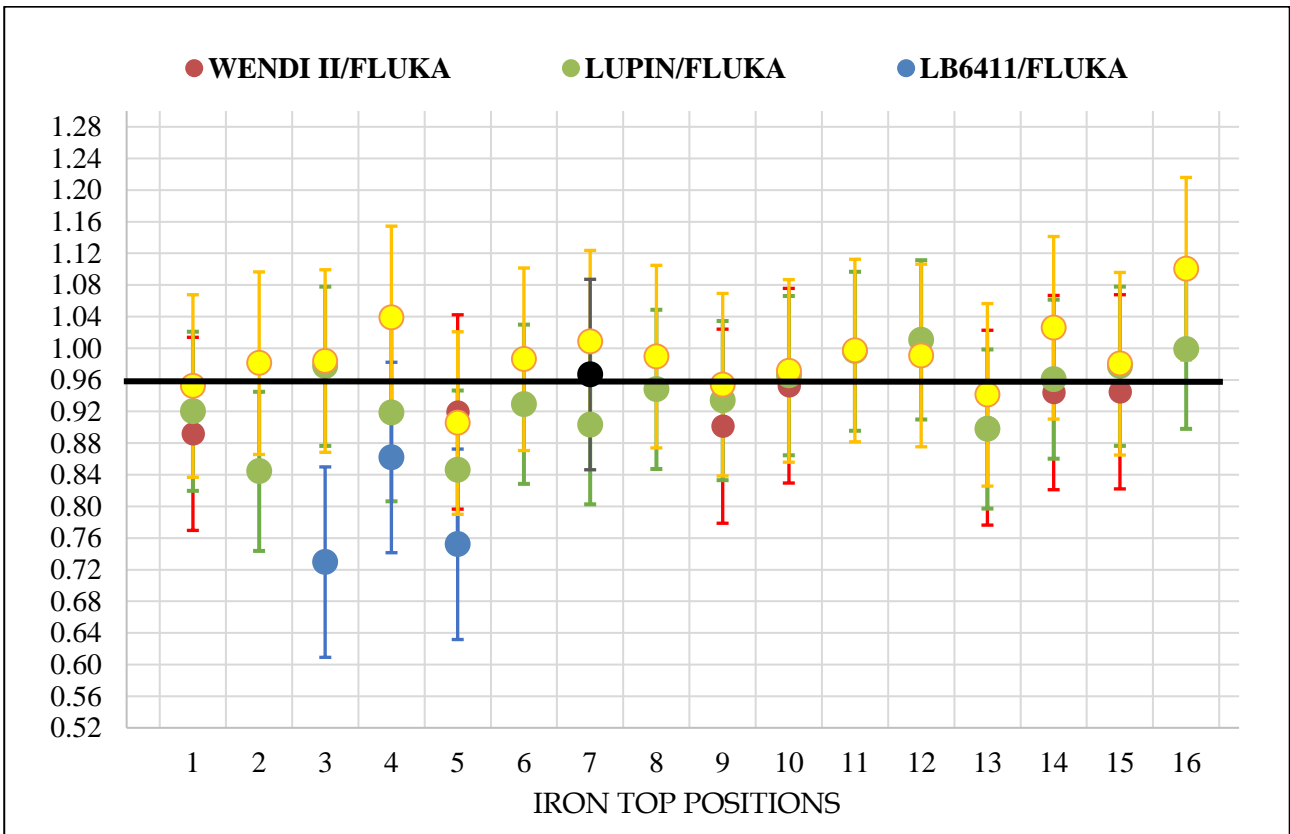
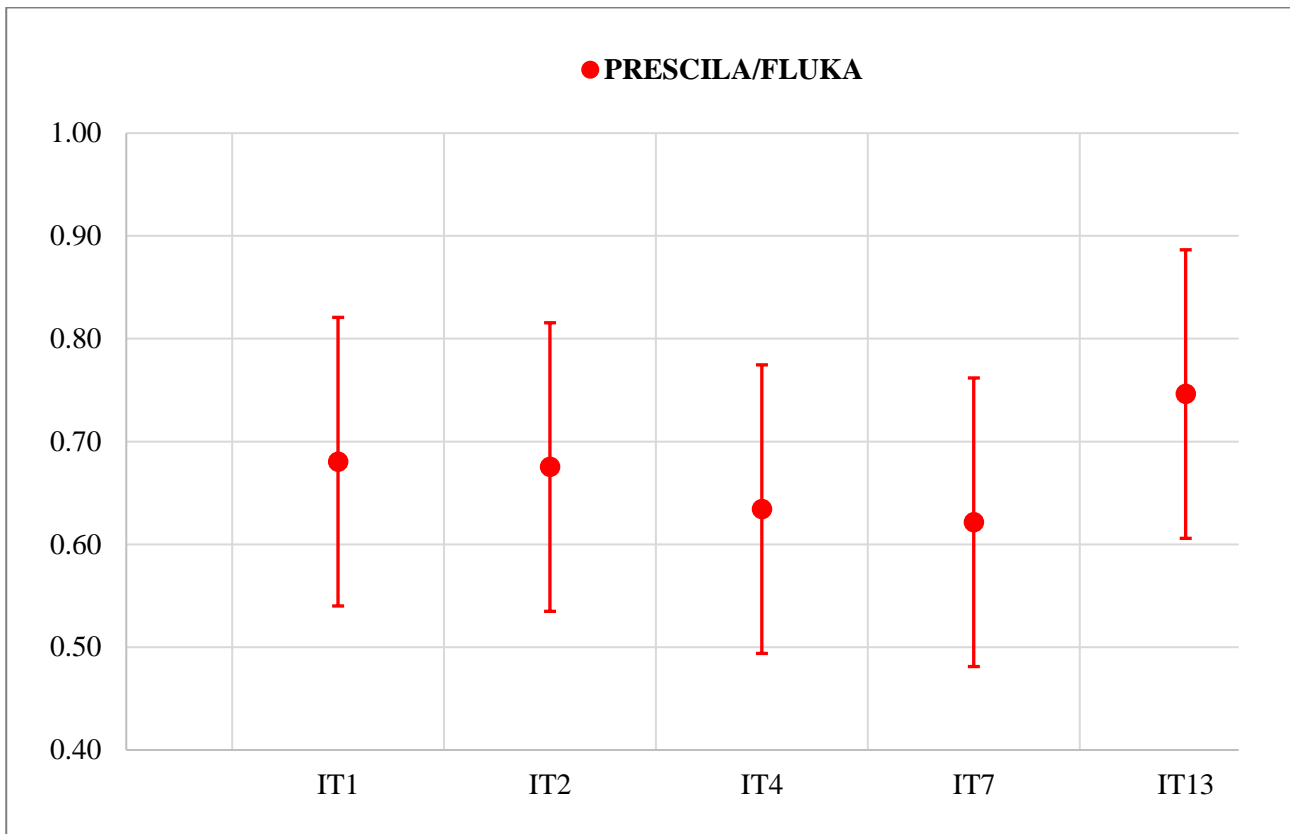


Figure 3.21  $H^*(10)$  ratios between WENDI, LUPIN, LB6411, LINUS and FLUKA on the IT.





**Figure 3.22 H\*(10) ratios between PRESCILA and FLUKA on the IT.**

### 3.2.2 Comparison of the expected and measured H\*(10)

This section focuses on the comparison between the expected and the measured H\*(10) at CERF with the LINUS and WENDI. The repartition of the H\*(10) according to the spectral component is also studied to understand the behaviour of rem counters in different energy ranges. The expected H\*(10) was calculated by folding the FLUKA spectrum with the response functions of the two rem counters with a linear interpolation. All H\*(10) are normalised per IC count. The uncertainties on the H\*(10) (about 5%) were obtained by folding the upper and the lower values of the energy bins of the FLUKA spectrum with the corresponding response function, using the uncertainties obtained for the two set of data. The uncertainties of the IC was then included leading to a final uncertainty of expected H\*(10) of 11%.

Figures 3.23 and 3.24 show the H\*(10) measured and expected with LINUS and WENDI on the CT positions. Table A.1 in appendix A presents the expected and measured H\*(10) values as well as their ratio. The deviation with WENDI varies from -3% and +10% and from +1% to +18% with LINUS (on CT4 and CT14 positions respectively). The average ratio is 1.03 for WENDI and 1.10 for LINUS. Figures 3.25 and 3.26 show the data obtained on the CS. H\*(10) measured with LINUS overestimates the expected H\*(10) from 11% (CS1) to 16% (CS6). WENDI overestimate up to +15% (CS7) except on CS8 where it underestimates by -4%. The average ratio is 1.09 for WENDI and 1.14 for LINUS. Figures 3.27 and 3.28 show the H\*(10) on the IT. The deviation goes from -10% to +9% for LINUS and from -1% to +7% with WENDI. The average ratio is 1.03 for WENDI and 0.98 for LINUS.

For both detectors and all positions (CT, CS and IT), the expected and the measured H\*(10) agree within 1 sigma of uncertainty. For WENDI the agreement between the expected H\*(10) and the measured H\*(10) is similar on the CT and IT but slightly worse on the CS. For LINUS the agreement between the two H\*(10) is better on the IT than on the CS.

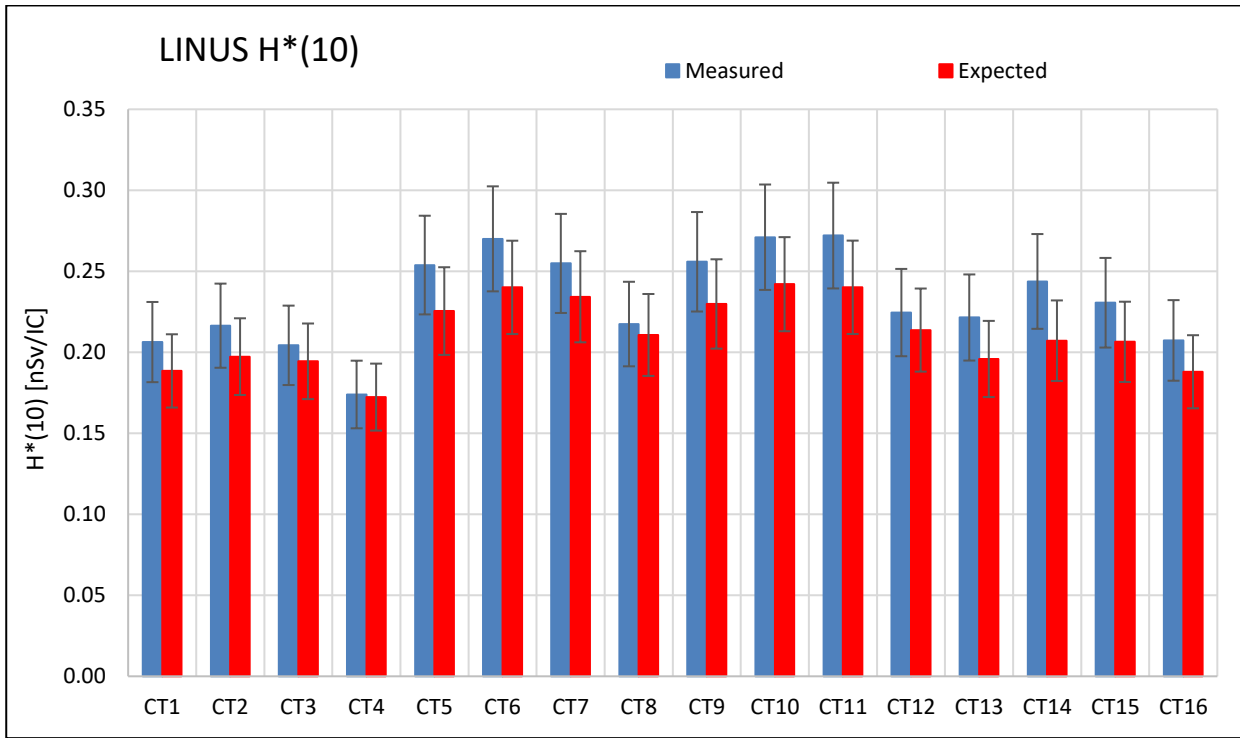


**Figure 3.23** H\*(10) in nSv per IC count measured and expected with LINUS on CT positions.

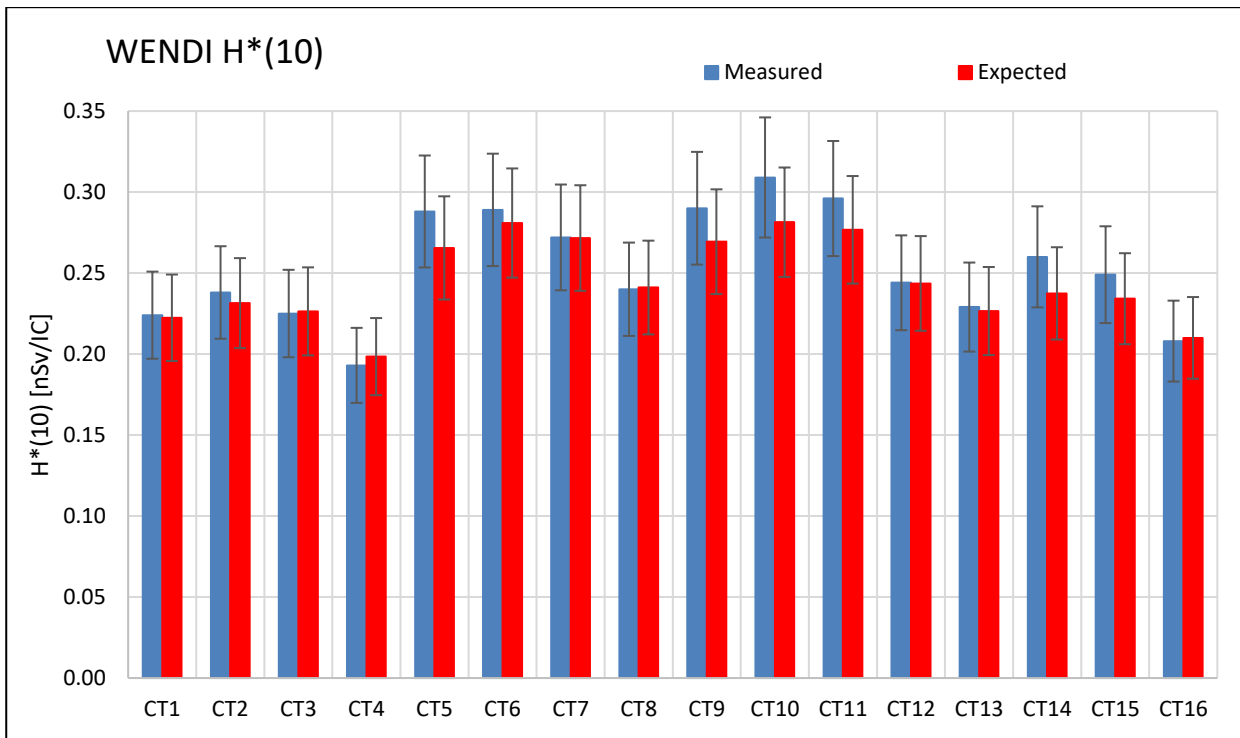


**Figure 3.24** H\*(10) in nSv per IC count measured and expected with WENDI on CT positions.

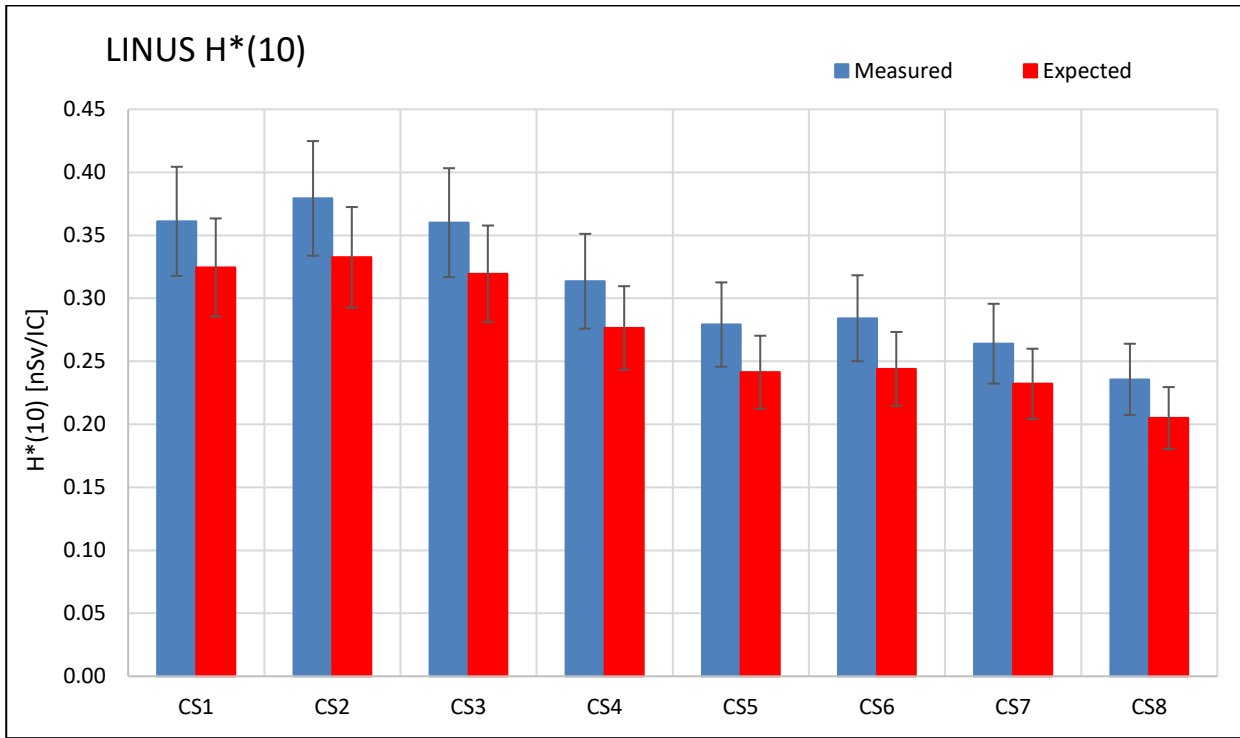


**Figure 3.25** H\*(10) in nSv per IC count measured and expected with LINUS on CS positions.

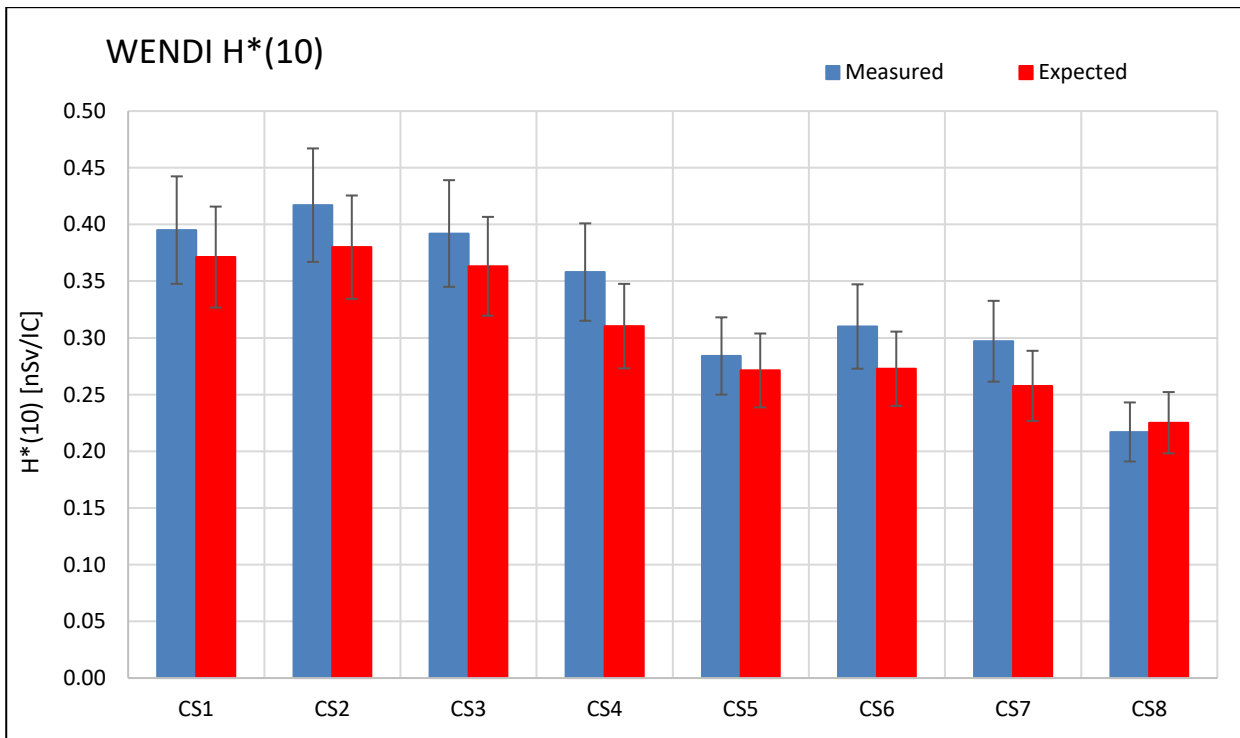


**Figure 3.26** H\*(10) in nSv per IC count measured and expected with WENDI on CS positions.

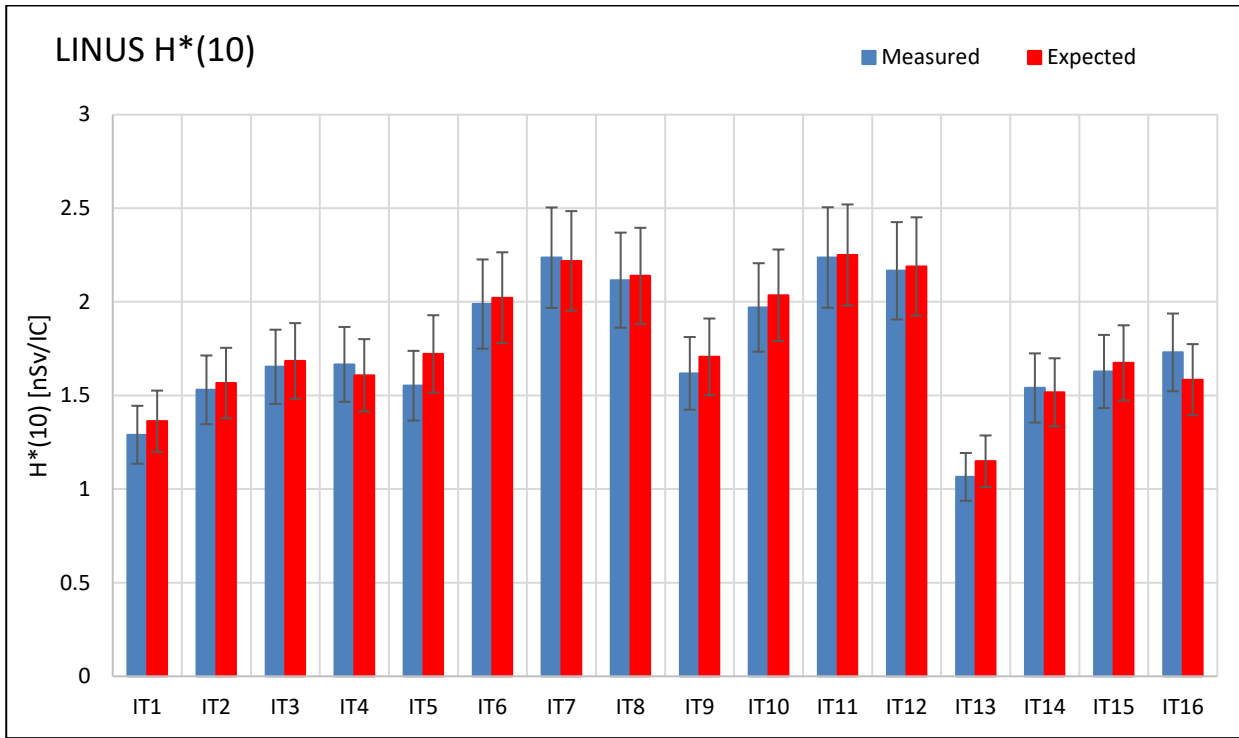


Figure 3.27 H\*(10) in nSv per IC count measured and expected with LINUS on IT positions.

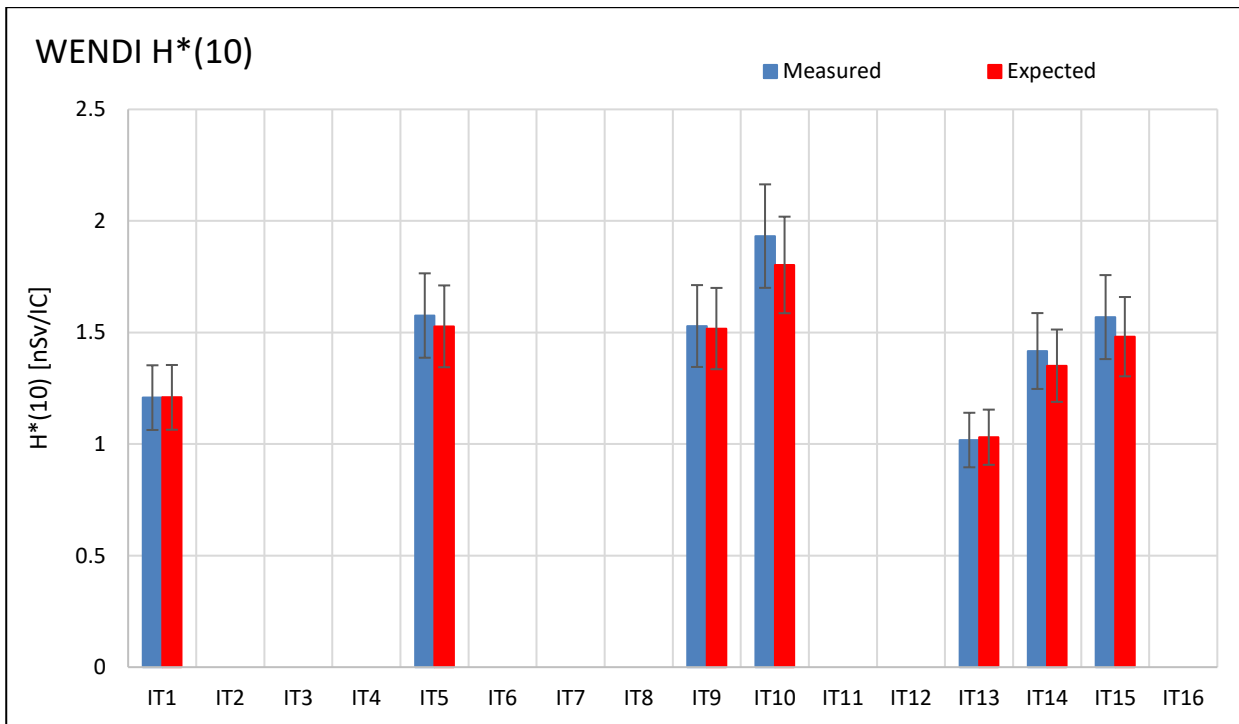


Figure 3.28 H\*(10) in nSv per IC count measured and expected with WENDI on IT.

The discrepancies between the two rem counters and FLUKA, and also between positions, can come from the response functions of the two rem counters used (measured and calculated) as well as to the neutron spectrum to which they are exposed. To understand how the H\*(10) is distributed among the different neutron components, Table 3.15 shows the fraction of expected H\*(10) in percentage due to the thermal, the epithermal, the evaporation and the high-energy components on CT (CT4 and CT7) CS (CS1 and CS8) and IT (IT1 and IT9). On CT, the main contribution to H\*(10) comes from the high energy and the evaporation component (about 53% and 44%). However on the IT, the evaporation dominates the contribution on H\*(10) with approximately 88%, whereas the high energy constitute only 7% of the total H\*(10). On the CS, the contribution on the

H\*(10) is equal between the evaporation and the high energy component from CS1 to CS4 (48% for each part) while between CS5 and CS8 the evaporation slightly dominates (52% due to the evaporation and 42% to the high energy range).

**Table 3.15 Relative contribution of H\*(10) in percentage according to the spectral component.**

Position	Relative contribution to the total H*(10) [%]			
	thermal	epithermal	evaporation	high energy
CT4	1.11	1.15	44.90	52.84
CT7	1.01	1.12	44.45	53.42
CS1	1.83	1.62	48.54	48.01
CS8	2.36	1.89	52.43	43.33
IT1	0.07	4.58	87.98	7.38
IT9	0.09	4.44	87.68	7.79

After understanding how the H\*(10) is distributed according to the neutron spectrum at CERF, the 2<sup>nd</sup> step was to fold the response functions of the two rem counters with the FLUKA spectra, obtain the H\*(10), and split it according to the same energy bounds used in Table 3.15. Table 3.16 shows the H\*(10) repartition in nSv per IC count with WENDI, LINUS and FLUKA and Table 3.17, the ratio between detectors and FLUKA H\*(10) according to the spectral component.

WENDI: Concerning the CT and neglecting the thermal and epithermal H\*(10) due to their little importance on the total H\*(10), one can see that WENDI clearly overestimates the high energy part by approximately 20% (20% on CT4 and 22% on the CT7) and underestimates the evaporation part by 11-12% %. Considering that the high energy dominates on the CT the final effect expecting is a slight overestimation of the total H\*(10). Indeed, WENDI overestimates the FLUKA H\*(10) by 4% on the CT4 and 9% on the CT7.

On CS1, WENDI shows the same trend as on CT: underestimation of the evaporation H\*(10) by 10% and overestimation of the high energy H\*(10) by 18%. On CS8, the evaporation H\*(10) is also overestimated by 1% but the high energy H\*(10) is overestimated by 31%. The contribution on the total H\*(10) on CS1 is equally distributed between evaporation and high energy component while the evaporation part dominates the final H\*(10) on CS8 (Table 3.15). This explain the larger overestimation on the total CS1 H\*(10) compared to CS8 (18% against 4%).

On the IT, the final H\*(10) are underestimated by 11%. This is due by the domination of the evaporation H\*(10) on the final H\*(10) (88%) and by the fact that on this region the WENDI underestimates the H\*(10) by 19% while it overestimates the high energy H\*(10) by 27%.

LINUS: On CT and CS, LINUS shows an underestimation of the high energy component of -11% (CS1) to -19% (CS8) and a slight overestimation of the evaporation part (about 5%). Therefore the final H\*(10) on the CT/CS should be an underestimated of few percent. However a slight overestimation on the final H\*(10) is seen. This difference confirms that there are discrepancies between the calculated and measured response functions. On the IT, the high energy and the evaporation components are underestimated by 14% and 3% respectively. On the IT, where the agreement between expected and measured H\*(10) is better (within 5%) a slight underestimation on the final H\*(10) is seen on the IT1 and IT9 positions.

**Table 3.16 Repartition of H\*(10) in nSv per IC count according to the spectral component.**

Position		H*(10) distribution in nSv per IC				
		Total	thermal	epithermal	evaporation	high
CT4	WENDI	0.198	0.001	0.005	0.074	0.118
	LINUS	0.172	5.34E-12	0.005	0.087	0.081
	FLUKA	0.185	0.002	0.002	0.084	0.099
CT7	WENDI	0.272	0.001	0.007	0.099	0.165
	LINUS	0.234	6.62E-12	0.006	0.116	0.112
	FLUKA	0.250	0.003	0.003	0.112	0.134
CS1	WENDI	0.371	0.003	0.013	0.145	0.210
	LINUS	0.324	1.54E-11	0.011	0.171	0.142
	FLUKA	0.335	0.006	0.005	0.162	0.160
CS8	WENDI	0.225	0.002	0.010	0.101	0.112
	LINUS	0.205	1.29E-11	0.009	0.120	0.076
	FLUKA	0.216	0.005	0.004	0.114	0.094
IT1	WENDI	1.209	4.23E04	0.133	0.950	0.125
	LINUS	1.363	2.70E-12	0.136	1.142	0.085
	FLUKA	1.355	9.27E-04	0.061	1.176	0.099
IT9	WENDI	1.518	6.71E-04	0.162	1.190	0.165
	LINUS	1.706	4.29E-12	0.164	1.430	0.112
	FLUKA	1.696	0.001	0.074	1.468	0.130

**Table 3.17 Ratio measured H\*(10) /FLUKA H\*(10) according to the spectral component.**

Position	Detector	Ratio H*(10) (measured/FLUKA)				
		Total	thermal	epithermal	evaporation	high energy
CT4	WENDI	1.04	0.44	2.43	0.89	1.20
	LINUS	0.94	-	2.13	1.04	0.82
CT7	WENDI	1.09	0.44	2.41	0.88	1.22
	LINUS	1.02	-	2.12	1.04	0.83
CS1	WENDI	1.18	0.44	2.43	0.89	1.31
	LINUS	1.08	-	2.11	1.05	0.89
CS8	WENDI	1.01	0.44	2.42	0.89	1.19
	LINUS	1.09	-	2.10	1.05	0.81
IT1	WENDI	0.89	0.46	2.18	0.81	1.27
	LINUS	0.95	-	2.22	0.97	0.86
IT9	WENDI	0.90	0.46	2.18	0.81	1.27
	LINUS	0.95	-	2.21	0.97	0.86

Calculating the expected H\*(10) by folding the response functions of the LINUS and the WENDI with the FLUKA spectra and comparing it with the measured H\*(10) gives an indirect comparison of the simulated and measured response functions of these detectors as well as an indication of the reliability of the FLUKA code to predict the neutron spectrum. For WENDI the agreement between the expected and the measured H\*(10) is

excellent (average ratio of 1.03 on CT and IT and 1.09 on CS). LINUS shows an agreement of 1.10, 1.14 and 0.98 on CT, CS and IT respectively.

Each instrument is mainly sensitive to different neutron energies. To understand the final discrepancies between the two rem counters and FLUKA, the relative importance on the total  $H^*(10)$  depending on the spectral component was studied. It was showed that WENDI overestimated the high energy part up to 22% and underestimate the evaporation part by approximately 11%. LINUS presents an underestimation of the high energy part (from 11% to 19%) and reproduce quite well the evaporation component. For both detectors, the epithermal component is overestimated by a factor 2.

Finally the agreement between experimental data and FLUKA results shows that not only the total  $H^*(10)$  but also the relative importance of the different spectral components are well predicted by the FLUKA code.

### 3.3 Modified BSS

The extended CERN BSS consists of 7 spheres. To understand some of the difficulties presented by the analysis of BSS data, it is useful to examine a plot of the response functions of a typical BSS. Figure 3.29 shows such a plot, together with a typical spectrum of a high-energy stray neutron field to give an idea of the neutron energy regions that are of relevance (in arbitrary units). Only a limited amount of information about the spectrum can be extracted by the BSS from measurements made in a high neutron energy field.

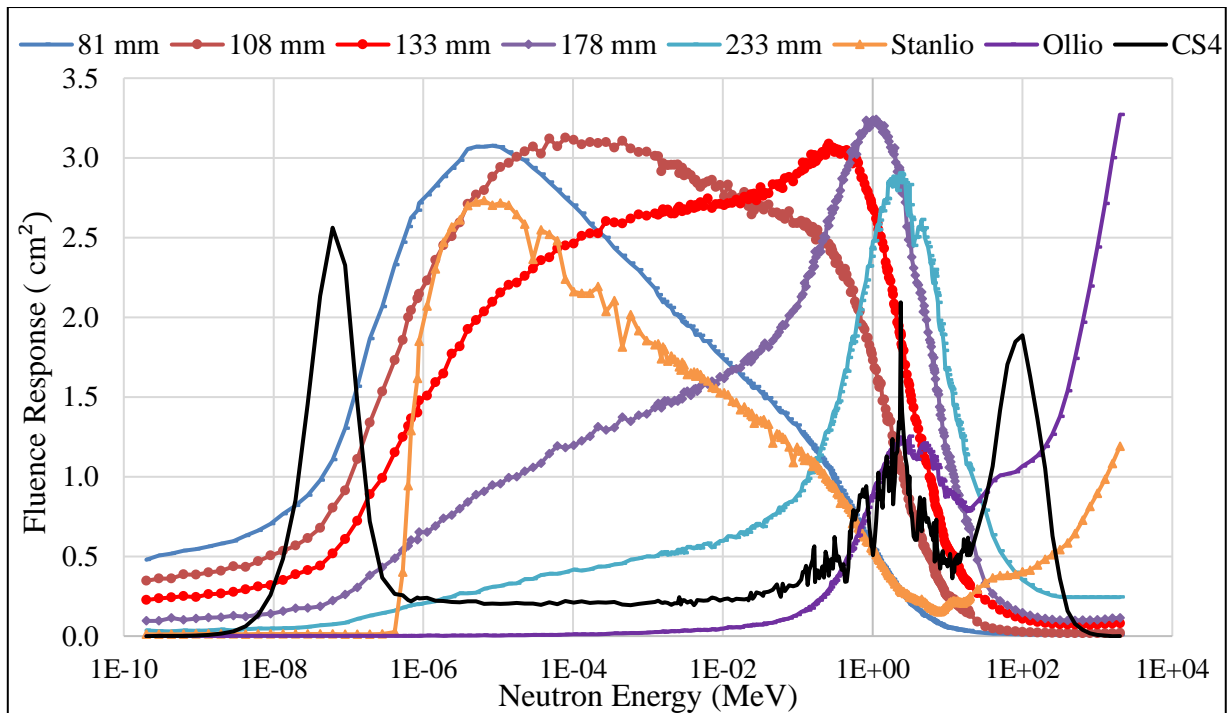


**Figure 3.29** CERN BSS response functions, together with an example spectrum of a high-energy stray neutron field (CS4, CERF).

The response function are not sharply peaked and overlap over many orders of magnitude. This explain the poor energy resolution of the system. The resolution is best at around 0.1-20 MeV, where the response functions of many of the spheres peak at different energies. The resolution is poorer at lower energies, where the response functions are all rather flat. The CERN BSS is lacking a sphere with a sensitivity peak in the thermal region. In fact, only two spheres have a non-negligible response to thermal neutrons, i.e. the 81 mm and 108 mm spheres. The situation is even worse in the high-energy domain since the responses of the two lead-modified spheres at high energies ( $E > 50$  MeV) grow very rapidly and have similar shape, which makes it very difficult to determine details of the spectrum at such high energies. In addition, the responses of all polyethylene spheres have a minimum at neutron energies of about a few hundred MeV, which correspond to the mean energy of the high-energy peak of the model spectrum shown in Figure 3.29. These observations suggest

that we cannot expect to determine the magnitude, mean energy and shape of the high-energy peak without a fair amount of uncertainty [13].

The observation above leads to an important question when making BSS measurements: how many spheres, and of which diameter, should be used for optimal performance? In principle, the answer is: as many spheres as possible (*provided* the shapes of their response functions differ sufficiently). Indeed, the unfolding problem in BSS spectrometry is under-determined, because the number of mathematical functions that could reproduce a given set of measured counts is theoretically infinite. In principle, the spectrometric information increases as the number of spheres increases, but the amount of added information decreases for each added sphere, because the response functions are not completely independent[14]. The information contained in a set of BSS measurements can be condensed in a curve representing the sphere reading (total counts) as a function of the sphere diameter. This plot serves to see by eyes if the number of spheres used is appropriate. For example if we remove the 133 from the IT the shape of the curve is not the same anymore, so the 133 is important. This plot serves also to see if the data are correct by the looking at the smooth shape of the distribution. Finally this plot also serves to intercompare the part of the spectrum: high energy part is more important in the cs4 than it7.

The BSS set used in any measurement should contain at least those spheres necessary to draw correctly the curve of reading against sphere diameter. An example of these plots is given in Figure 3.30 for the CS4 and IT7 exposure locations at CERF. All count were normalised to IC and to the higher sphere reading for convenience.

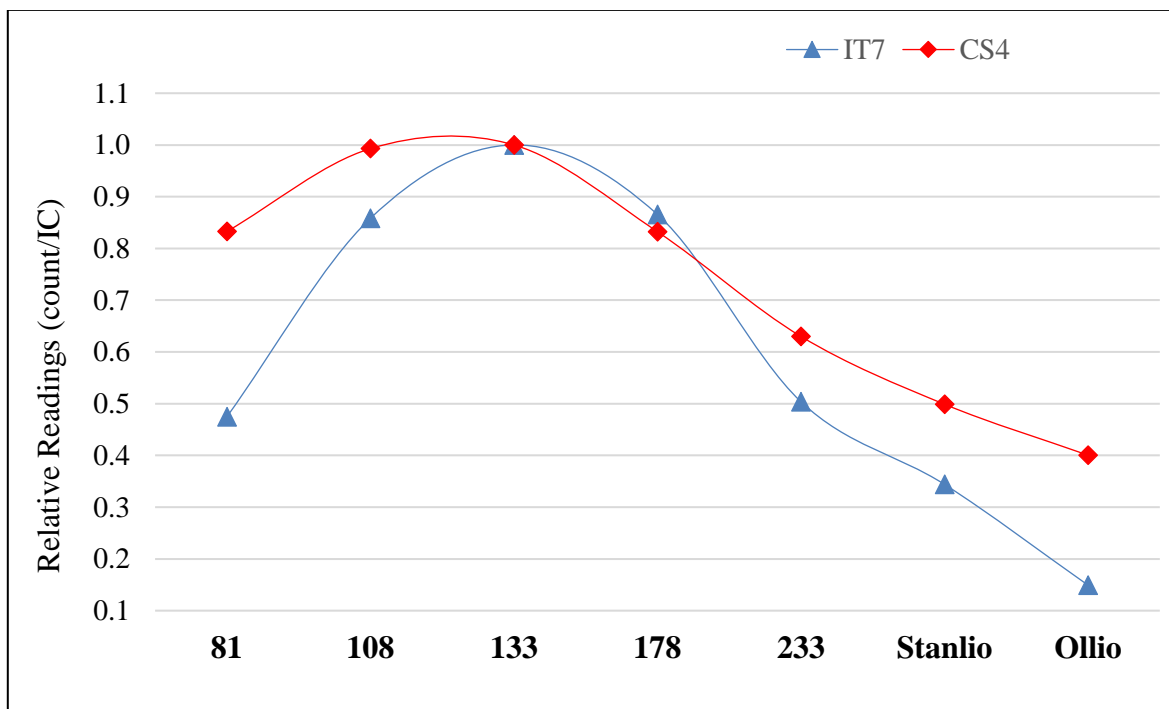


**Figure 3.30** The relative readings of the BSS as a function of sphere.

As small-diameter conventional spheres and Ollio show rather large readings, considerable contributions to the spectrum are expected in the thermal and high-energy regions. Above the iron shield this contribution appears to be lower, in agreement with the computed spectral shapes shown in Figure 2.12. This suggests that the use of additional detectors sensitive to high-energy and thermal neutrons, particularly if they had response functions with different shapes, would improve the spectrometric information. In order to increase the number of applications in which the BSS could efficiently be employed and to improve its sensitivity in specific energy ranges, some modifications to the existing BSS have been evaluated.



### 3.3.1 Response to thermal neutrons

The CERN BSS is lacking a sphere with a maximum of sensitivity in the thermal region. In the attempt to increase the response in this energy range, a design with FLUKA simulation of a new sphere called Calimero has been started in 2016 by E.Aza and finalised recently [15]. The sphere is constituted by graphite only and has a diameter of 130 mm. Graphite has been used instead of polyethylene due to its reduced moderation properties [16]. This limited moderation allows to closely reproduce the response function of a bare  $^3\text{He}$  counter, but without the issues usually related to its use, i.e. electrical noise, fragility, signal instability and high sensitivity to vibrations. Figure 3.31 show the response function calculated via FLUKA for Calimero and, for comparison, the response function of the bare counter. The sensitivity resembles the behaviour of the reaction cross section of the neutrons in the counter. The slight deviations are due to the neutron absorption cross section in graphite, which reduces the sensitivity below 0.1 eV, and to the slight moderation effects of graphite, which enhance the response above 0.1 eV. The response is essentially negligible above 100 eV.

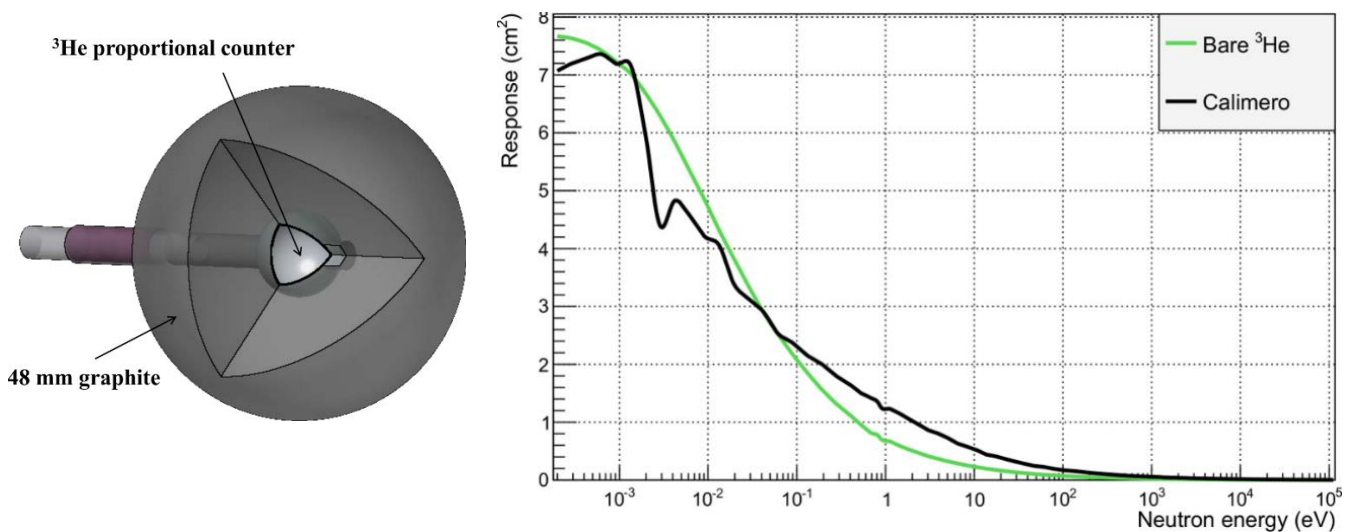


**Figure 3.31** Calimero and its response function as calculated with FLUKA. The response function of the bare detector is shown for comparison.

### 3.3.2 Response to high energy neutrons

In order to enhance the sensitivity of the BSS above 20 MeV, a modified configuration of Stanlio has been investigated. The idea, which originally brought to the development of Stanlio, was to build a sphere whose response function extended above 20 MeV but was suppressed as much as possible at a few MeV, i.e. where the 233 mm sphere and Ollio have their sensitivity peak [17], in order to keep the response functions of the three spheres as independent as possible. This requirement imposed to limit the polyethylene thickness to 20 mm; otherwise, a higher thickness would have increased the sensitivity at about few MeV. On the other hand, this forced the response function to be relatively low, if compared to Ollio, at high energies. In the view of better defining the details of the neutron spectrum in this region, it could be desirable to increase the high-energy part of the response function of Stanlio, even if this results in a slightly higher response at a few MeV. Stanlio is composed (from the  $^3\text{He}$  counter outwards) of 20.75 mm polyethylene, 1 mm cadmium and 20 mm lead. A modified configuration, nicknamed Stanlio-2, was investigated, having a polyethylene thickness of 30 mm. The corresponding response function obtained from FLUKA simulations is shown in Figure 3.32. The thicker layer of polyethylene in Stanlio-2 significantly increases the sensitivity for energies above 1 keV, and in particular above 20 MeV, where the sensitivity is three times higher than for Stanlio, whereas for lower energies the response function is substantially unchanged. The minimum at a few MeV is still present but the sensitivity in that region approximately doubled. Given that the main interest is to have response functions as independent as possible, having a second sphere with a good sensitivity at high energies, but with a depressed

response at a few MeV, the replacement of Stanlio with Stanlio-2 could be useful. The modified geometry would result in a reasonable additional weight of 3 kg: 9.5 kg for Stanlio-2 instead of the 6.5 kg for Stanlio.

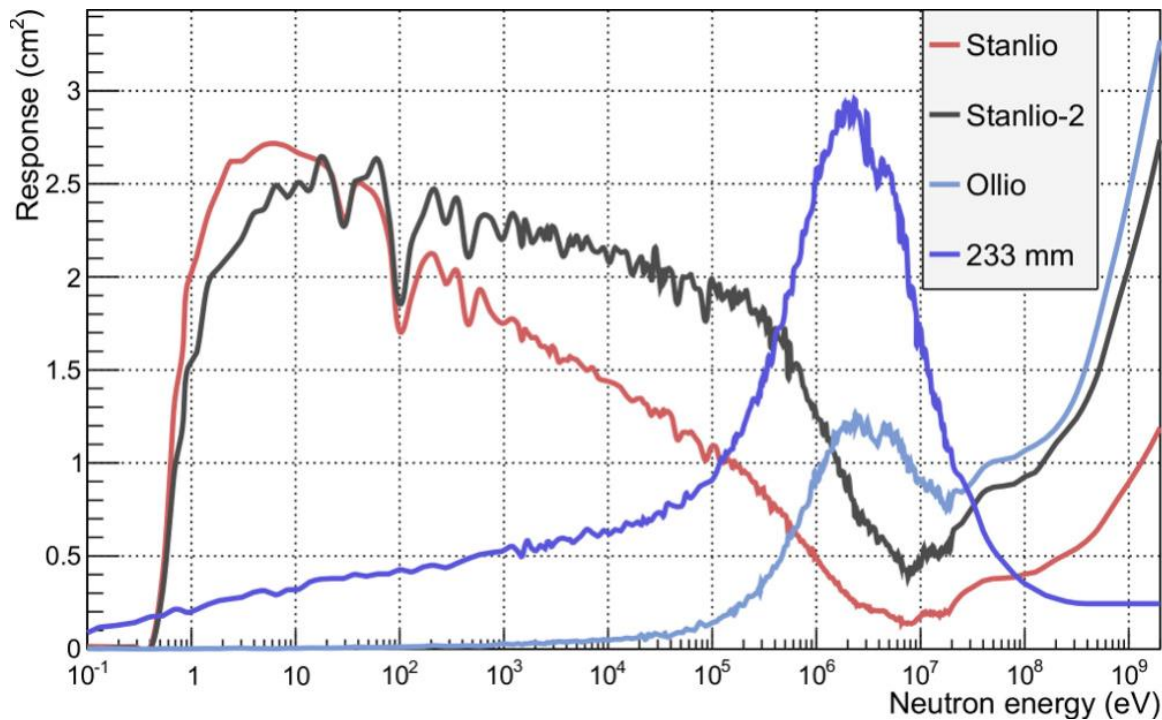


**Figure 3.32** Response functions of Stanlio and Stanlio-2, as calculated via FLUKA. The response functions of Ollio and the 233 mm sphere are also plotted for comparison.

In order to understand if these two new spheres can increase the spectrometric information and to avoid a pricey manufacturing of them, some numerical tests with the unfolding code were performed. First, the expected number of counts were calculated by folding the response function of the BSS with a FLUKA spectrum. To test Calimero, the Proton synchrotron spectrum was used because the thermal part dominates. The Proton synchrotron spectrum is the spectrum at the entrance of the access tunnel to the beam extraction area of the CERN Proton Synchrotron [18]. For Stanlio-2, the The CERF CS4 spectrum was used. Then a different guess spectrum was used as input in the unfolding process to see if the counts provided by the BSS were strong enough to modify in the right direction the ‘wrong’ guess spectrum. Different combination of spheres and spectra were used:

-in case of Calimero:

As input for the unfolding code (MAXED), the Proton synchrotron spectrum was divided by  $10^3$ . Two configurations were studied: one with the usual BSS, and one with the Calimero added.

Figure 3.33 shows the neutron spectra obtained with MAXED when using the conventional 7-sphere BSS (‘usual’) and with the additional Calimero (‘Calimero’). The thermal peak of the usual BSS spectrum is larger, higher and slightly shifted compared to the FLUKA spectrum. However, the Calimero spectrum is similar to the FLUKA spectrum in terms of peak position, amplitude and width. This improvement in the unfolding is due to the improvement of the resolution of BSS when adding a sphere with good response in the thermal region.

-in case of Stanlio-2:

As input for the MAXED unfolding code, position 1G in the Essen proton therapy centre was employed because it has the advantage to have similar shape of CERF CS4 spectrum but with a much lower amplitude of the evaporation/high energy parts. The position 1G is located at the end of the maze of the treatment room of the proton therapy center and the relative contribution from high-energy neutrons exceeds that of the evaporation neutrons [19].

Different sets of BSS were used: the “usual” combination is the set of seven spheres of the CERN BSS, a configuration with Stanlio-2 instead of Stanlio (‘STANLIO-2’), the 7 spheres plus the two Stanlio spheres (‘2 STANLIOS’), a configuration without Stanlio (‘NO STANLIO’) i.e. made of 6 spheres, and a final configuration without the two lead inserted spheres (‘NO HIGH’), that is only made of the five polyethylene spheres. Figure 3.34 shows the neutron spectra obtained for all configurations. The two FLUKA spectra are shown for comparison: CS4 (‘TRUE’) and 1G (‘FALSE’). All BSS configurations give similar result for the evaporation part. However, for the high-energy part, the results differ. First, it seems that replacing STANLIO with STANLIO-2 gives worse results. This is probably because the differentiation degree of the response function with OLLIO is higher for STANLIO than for STANLIO-2. Then, only the usual and the two STANLIO combinations are closer to the TRUE guess spectrum. These spectra are almost identical. Therefore, the actual STANLIO should not be replaced by STANLIO-2 but the latter can be added to the present BSS to decrease the uncertainty on the final spectrum. However, considering the time consumption of BSS measurements and the difficulty of transporting heavy spheres, we can consider that the present 7-sphere BSS is already optimized for high-energy spectra acquisition. The absence of both STANLIO spheres does not affect the neutron spectrum strongly. Indeed, the fact that the neutron spectrum given by the NO STANLIO configuration reproduces quite well the high energy peak suggests that the spectrometric information given by the Ollio sphere (in combination to the guess spectrum) is sufficient. This conclusion is confirmed by the NO HIGH spectrum that is not able to reproduce the high-energy peak of the TRUE spectrum.

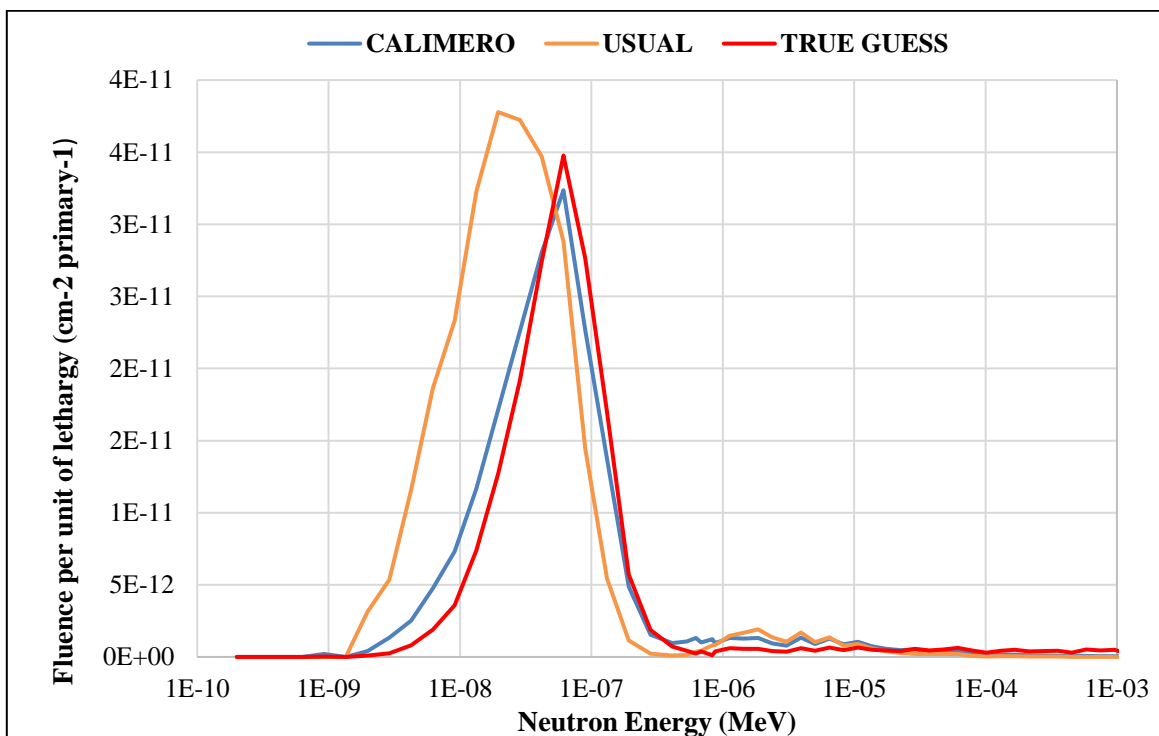


Figure 3.33 Proton synchrotron neutron spectra obtained with MAXED for the usual 7-sphere configuration of the BSS (in red) and with the additional Calimero (in blue). The FLUKA spectrum is given as comparison (in red)

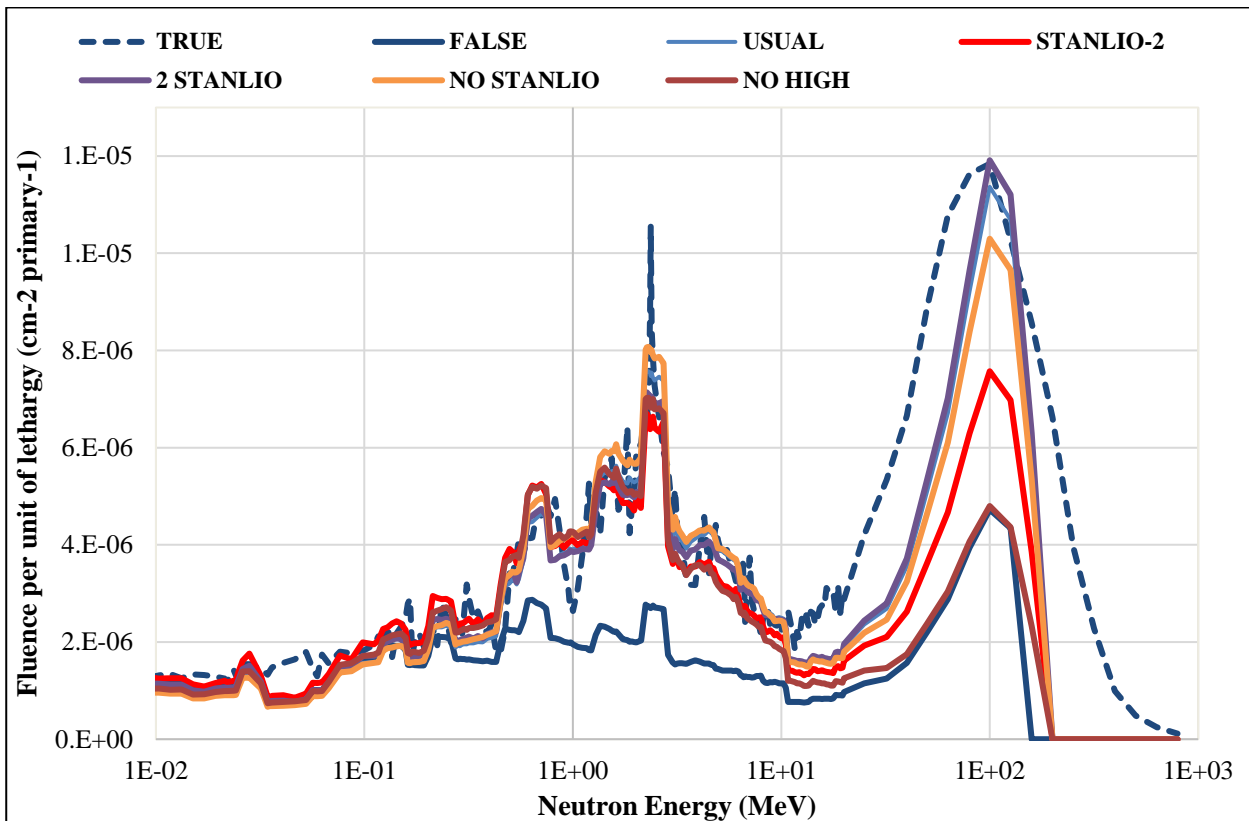


Figure 3.34 CERF CS4 neutron spectra obtained with MAXED for the different BSS configurations and the two FLUKA guess spectra for comparison. See text for details on the various BSS configurations.

### 3.4 Conclusion

The response of several detectors usually used in radiation protection were intercompared through measurements. First, all detectors were calibrated in the CERN calibration laboratory. All measured values agree with the manufacturer values within 1 sigma of uncertainty. The detector response were also compared with the simulated response obtained with FLUKA in terms of  $H^*(10)$ . All expected  $H^*(10)$  agree well with the measured  $H^*(10)$ . However some overestimation and/or underestimation were noticed for all detectors. These discrepancies were investigated quantitatively by comparing the expected and the measured  $H^*(10)$ . It was found there are due to the detector response in the different energy binning and the energy spectrum of the field. A particular attention was brought to the LINUS, after the replacement of the gas. The characterization of the detector was fully completed showing 5% of differences with the previous detector. The LINUS was tested for the first time during an aircraft campaign in Pragua, the results are under publication.

Finally, all detectors were used to characterize the CERF field and compared with FLUKA simulation. All values (except LB6411) are in good agreement within  $1 \sigma$  for all positions. The underestimation of LB6411 is due to its low response in the high energy range.

In addition 2 new Bonner spheres were investigated (CALIMERO, STANLIO-2) to investigate the possibility to increase the BSS response in the high energy range and the thermal region. Only CALIMERO could have an additional spectrometric information.

---

## References

- [1] T.T Böhlen and al., *The FLUKA code: developments and challenges for high-energy and medical applications*, *Nucl. Data Sheets* 120, 211-214 (2014).
- [2] A. Ferrari, P.R. Sala, A. Fasso, J. Ranft, *FLUKA: A multi-particle transport code*, CERN-2005-10, INFN/TC\_05/11, SLAC-R-773 (2005).
- [3] *Reference neutron radiations - Calibration fundamentals of radiation protection devices related to the basic quantities characterizing the radiation field*, 2000. ISO 8529-2.
- [4] [www.fst-sensortechnik.com](http://www.fst-sensortechnik.com),
- [5] F.Pozzi, *CERN radiation protection calibration facilities*, Ph.D. dissertation, University of Munich, (2016).
- [6] *International standard, Neutron ambient dose equivalent*, IEC 61005 (2014).
- [7] T. W Crane and M. Baker: *Neutron Detectors in Passive Non-destructive Assay of Nuclear Materials*, Los Alamos, ISBN 0-16-032724-5, (1991).
- [8] Vukovic et al, *Measurements of neutron radiation in aircraft*, *Applied Radiation Isotopes* 68 (2010).
- [9] Ian L. Getley and al, *Radiation dose along North American transcontinental flight paths during quiescent and disturbed geomagnetic conditions Space Weather Volume 3, Issue 1* (2015).
- [10] M. Reginatto and P. Goldhagen, *MAXED a computer code for maximum entropy deconvolution of multisphere neutron spectrometer data* (1999).
- [11] H.R.Vega-Carrillo, G. Miramontes de Leon and L.E. McBride, *Noniterative unfolding algorithm for neutron spectrum measurements with Bonner spheres*, *IEEE Trans. Nucl. Sci.* 46, 28-35. (1999).
- [12] ICRP, *Conversion coefficients for use in radiological protection against external radiation*, *Annals of the ICRP* 26 (3/4) (ICRP Publication 74) (1996).
- [13] M.Reginato, *What can we learn about the spectrum of high-energy stray neutron fields from Bonner sphere measurements?* *Radiation Measurements* 44 692–699 (2009).
- [14] D.J Thomas and A.V Alevra, *Bonner sphere spectrometers, a critical review*, *Nucl. Instrum. Meth.* A476, 12-20 (2002).
- [15] E.Aza, *SpectroGeM: a novel neutron spectrometer*, Ph.D. dissertation, University of Thessaloniki, (2016).
- [16] S. Glasstone, A. Sesonske, *Nuclear Reactor Engineering*, D. Van Nostrand Co.1967.
- [17] A. Mitaroff, *Design, calibration and tests of an extended-range Bonner sphere spectrometer*, Ph.D. dissertation,, CERN-THESIS-2002-029
- [18] E.Aza, N.Dinar, G.P Manessi, M.Silari, *A bonner sphere spectrometer for pulsed field*, *Radiat. Prot. Dosim.* 168 149-153 (2015)
- [19] V. Smet, M. Saint-Hubert, N.Dinar and al..*Secondary neutrons inside a proton therapy facility: MCNPX simulations compared to measurements performed with a Bonner Sphere Spectrometer and neutron H\*(10) monitors*, *Radiation.measurements* 99 25-40 (2017)

## Appendix A

**Table A.1 Measured and expected H\*(10) at CERF with the LINUS and WENDI. The ratios between measured and expected H\*(10) are also presented.**

Position	LINUS			WENDI		
	measured nSv/IC	expected nSv/IC	RATIO	measured nSv/IC	expected nSv/IC	RATIO
<b>CT1</b>	0.206	0.189	1.09	0.224	0.222	1.01
<b>CT2</b>	0.216	0.197	1.10	0.238	0.231	1.03
<b>CT3</b>	0.204	0.194	1.05	0.225	0.226	0.99
<b>CT4</b>	0.174	0.172	1.01	0.193	0.198	0.97
<b>CT5</b>	0.254	0.225	1.13	0.288	0.266	1.08
<b>CT6</b>	0.270	0.240	1.12	0.289	0.281	1.03
<b>CT7</b>	0.255	0.234	1.09	0.272	0.272	1.00
<b>CT8</b>	0.217	0.211	1.03	0.240	0.241	1.00
<b>CT9</b>	0.256	0.230	1.11	0.290	0.269	1.08
<b>CT10</b>	0.271	0.242	1.12	0.309	0.281	1.10
<b>CT11</b>	0.272	0.240	1.13	0.296	0.277	1.07
<b>CT12</b>	0.225	0.214	1.05	0.244	0.244	1.00
<b>CT13</b>	0.221	0.196	1.13	0.229	0.227	1.01
<b>CT14</b>	0.244	0.207	1.18	0.260	0.237	1.10
<b>CT15</b>	0.231	0.206	1.12	0.249	0.234	1.06
<b>CT16</b>	0.207	0.188	1.10	0.208	0.210	0.99
<b>CS1</b>	0.361	0.324	1.11	0.395	0.371	1.06
<b>CS2</b>	0.379	0.333	1.14	0.417	0.380	1.10
<b>CS3</b>	0.360	0.319	1.13	0.392	0.363	1.08
<b>CS4</b>	0.314	0.276	1.13	0.358	0.310	1.15
<b>CS5</b>	0.279	0.241	1.16	0.284	0.271	1.05
<b>CS6</b>	0.284	0.244	1.16	0.310	0.273	1.14
<b>CS7</b>	0.264	0.232	1.14	0.297	0.258	1.15
<b>CS8</b>	0.236	0.205	1.15	0.217	0.225	0.96
<b>IT1</b>	1.29	1.363	0.95	1.208	1.209	1.00
<b>IT2</b>	1.53	1.567	0.98	-	-	-
<b>IT3</b>	1.653	1.684	0.98	-	-	-
<b>IT4</b>	1.666	1.608	1.04	-	-	-
<b>IT5</b>	1.552	1.722	0.90	1.576	1.528	1.03
<b>IT6</b>	1.988	2.022	0.98	-	-	-
<b>IT7</b>	2.236	2.219	1.01	-	-	-
<b>IT8</b>	2.116	2.139	0.99	-	-	-
<b>IT9</b>	1.618	1.706	0.95	1.529	1.518	1.01
<b>IT10</b>	1.97	2.035	0.97	1.932	1.803	1.07
<b>IT11</b>	2.237	2.250	0.99	-	-	-
<b>IT12</b>	2.166	2.189	0.99	-	-	-
<b>IT13</b>	1.065	1.149	0.93	1.018	1.031	0.99
<b>IT14</b>	1.54	1.517	1.02	1.417	1.351	1.05
<b>IT15</b>	1.628	1.674	0.97	1.569	1.481	1.06
<b>IT16</b>	1.73	1.584	1.09	-	-	-

**Table A.2 Expected H\*(10) at CERF with FLUKA. The ratio between measured and FLUKA H\*(10) are also presented.**

Position	FLUKA	RATIO LINUS/FLUKA	RATIO WENDI/FLUKA
<b>CT1</b>	0.198±0.020	1.04	1.13
<b>CT2</b>	0.208±0.021	1.04	1.14
<b>CT3</b>	0.207±0.021	0.99	1.09
<b>CT4</b>	0.185±0.019	0.94	1.04
<b>CT5</b>	0.236±0.024	1.08	1.22
<b>CT6</b>	0.253±0.025	1.07	1.14
<b>CT7</b>	0.250±0.025	1.02	1.09
<b>CT8</b>	0.226±0.023	0.96	1.06
<b>CT9</b>	0.240±0.024	1.07	1.21
<b>CT10</b>	0.255±0.026	1.06	1.21
<b>CT11</b>	0.255±0.026	1.07	1.16
<b>CT12</b>	0.229±0.023	0.98	1.07
<b>CT13</b>	0.203±0.020	1.09	1.13
<b>CT14</b>	0.216±0.022	1.13	1.20
<b>CT15</b>	0.217±0.022	1.06	1.15
<b>CT16</b>	0.199±0.020	1.04	1.05
<b>CS1</b>	0.335±0.034	1.08	1.18
<b>CS2</b>	0.346±0.035	1.09	1.20
<b>CS3</b>	0.336±0.034	1.07	1.17
<b>CS4</b>	0.296±0.030	1.06	1.21
<b>CS5</b>	0.249±0.025	1.12	1.14
<b>CS6</b>	0.254±0.026	1.12	1.22
<b>CS7</b>	0.243±0.024	1.09	1.22
<b>CS8</b>	0.216±0.022	1.09	1.01
<b>IT1</b>	1.355±0.136	0.95	0.89
<b>IT2</b>	1.559±0.156	0.98	-
<b>IT3</b>	1.680±0.168	0.98	-
<b>IT4</b>	1.604±0.161	1.04	-
<b>IT5</b>	1.714±0.172	0.91	0.92
<b>IT6</b>	2.016±0.202	0.99	-
<b>IT7</b>	2.218±0.222	1.01	-
<b>IT8</b>	2.139±0.214	0.99	-
<b>IT9</b>	1.696±0.170	0.95	0.90
<b>IT10</b>	2.028±0.203	0.97	0.95
<b>IT11</b>	2.244±0.225	1.00	-
<b>IT12</b>	2.186±0.219	0.99	-
<b>IT13</b>	1.132±0.113	0.94	0.90
<b>IT14</b>	1.501±0.150	1.03	0.94
<b>IT15</b>	1.660±0.166	0.98	0.94
<b>IT16</b>	1.572±0.157	1.10	-

# Chapter 4 Investigation of the electronic readout for the CLYC scintillator

The CERN Radiation Protection (RP) group has recently developed a novel radiation survey meter called B-RAD [1][2] able to operate in the presence of a strong magnetic field, to be used for radiation surveys e.g. in the LHC experimental areas. The instrument will be provided with a number of probes for gamma dose rate, spectrometric and surface contamination measurements.

The feasibility of developing a neutron probe to be plugged into B-RAD is currently being investigated. The crystal  $\text{Cs}_2\text{LiYCl}_6\text{:Ce}$  (CLYC) was selected as potential candidate for neutron detection because of its promising properties, such as its capability to discriminate gamma rays from fast neutrons and its energy resolution. Scintillators are typically coupled to photomultiplier tubes (PMTs) as readout. However, the choice of solid state (silicon) photomultipliers (SiPMs) for the neutron probe is justified by crucial requirements: the insensitivity to external magnetic fields and the low operating voltage with respect to vacuum (around 30 V for a SiPM against 1000 V for a PMT). The gain (approximately  $10^6$ ) and the photo detection efficiency (PDE) (20-50% depending on device and wavelength) are similar to those of a PMT. The small size allows to build an extremely compact, light and robust mechanical device.

This chapter is divided in three main sections. The first presents the general characteristic of the CLYC scintillator.

The second section deals with the photodetector used to read the signal output from the scintillator: PMT and SiPM. PMT were characterized to find the optimal voltage to apply. For SiPM, the determination of the bias voltage ( $V_{\text{BIAS}}$ ) and its temperature dependence have a critical influence on the detector performances. Therefore, a current-voltage (I-V) characterization was performed in order to check the array uniformity. Moreover the uniformity of the gain and the PDE were also studied.

The third section describes an electronic board that was designed and tested to extract the pulse shape discrimination of the CLYC when coupled with the SiPM.

## 4.1 CLYC scintillator

CLYC is one of the more interesting of the new scintillators developed during the last fifteen years. It is the first generation of dual mode detection (gamma and neutron). CLYC was discovered at the Delft University of Technology in 1999. The crystals were grown at the University of Bern. At the time the material was proposed for thermal neutron detection based on the  ${}^6\text{Li}(n,\alpha)$  reaction. In the following years, the Delft group continued to study the scintillation properties of the material, and discovered that CLYC exhibits core-to-valence luminescence (CVL) between 225 nm and 300 nm. A characteristic feature of CVL is that it only appears under gamma ray excitation, therefore, it was suggested that it can be used to discriminate between gamma rays and neutron particles by means of pulse shape discrimination. Recently, Bubble Technology Industries of Canada discovered the possibility of fast neutron detection with CLYC, increasing its versatility even further.



A cylindrical CLYC ( $Cs_2LiYCl_6:Ce$ ) crystal 25 mm in diameter and 25 mm thick was purchased from Radiation Monitoring Devices [3]. The CLYC scintillator is characterized by a light yield of 20 photons/keV, a density of  $3.3\text{ g}\cdot\text{cm}^{-3}$  and peak scintillation wavelength at 370 nm. Contrary to the CLYC-6, a CLYC crystal with the lithium element enriched in  $^7\text{Li}$  at  $>99\%$  is used in this work. This enrichment suppresses the sensitivity to thermal neutrons allowing a better detection of fast neutrons through the  $^{35}\text{Cl}(n,p)^{35}\text{S}$  and  $^{35}\text{Cl}(n,\alpha)^{32}\text{P}$  reactions. The Q values of these reactions are 615 keV and 937 keV, respectively. The energy deposition of the products linearly depends on the energy of the incident neutron. Thus neutron spectroscopy without resorting to an unfolding code is possible up to 10 MeV. Since the CLYC is hygroscopic, a cylindrical housing protects it from moisture. Figure 4.1 shows a picture of the CLYC package.

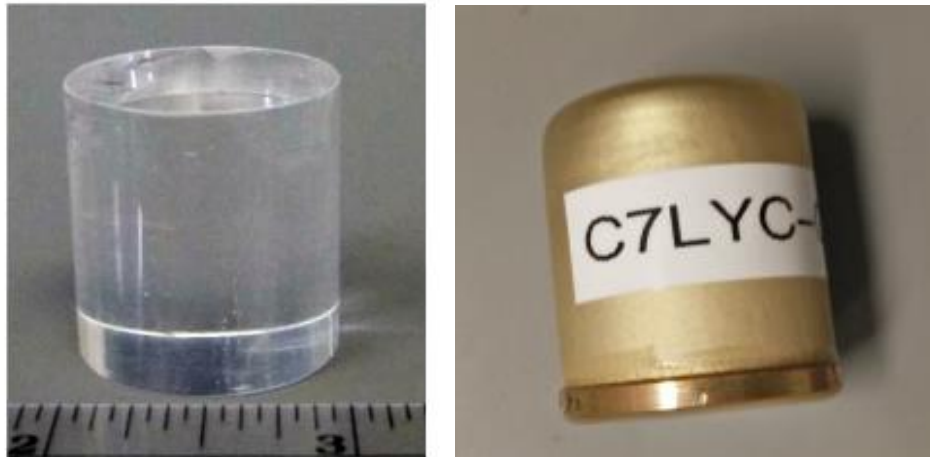


**Figure 4.1** The CLYC scintillator used for the measurements with (right) and without (left) package.

The characterization of the CLYC scintillator was performed first with a PMT and then with an array of SiPMs to understand and compare its performances with the two types of readout.

## 4.2 PMT characterization

### 4.2.1 Plateau characteristic

There are output pulses associated with a PMT even in the absence of light; these pulses are called dark current pulses or noise. The noise depends on the applied voltage and increases faster than the gain, which is one of the principal factors that sets a practical limit to gain. Moreover, its rate of increase is not constant. These undesirable pulses affect the performance of the system particularly for spectrometry applications, where optimum time or energy resolution is required [4]. A general method to minimize this effect is to find the optimal voltage to apply by plotting the count rate as a function of the supplied voltage at a fixed discrimination threshold. The high voltage to apply to the PMT needs to be set within a range where all the events are counted; this is the plateau part.

In this work, two PMT models from HAMAMATSU were employed: the bialkali R580 and the Superbialkali R6231-100, connected to two standard voltage dividers (E2183-500 and E1198-27, respectively). Because of the difference in the areas between the scintillator and the PMT, the area of the PMT exceeding the crystal surface was covered with a black and light-tight insulating tape. The CLYC was placed in a light-tight box together with the photodetector and the source. A Silena amplifier (7611/L) was used for both PMTs (gain  $50\times 0.9$ ; shaping time  $1\ \mu\text{s}$ ). An ortec SCA discriminator (ORTEC 550) working in integrated mode was used so no higher threshold was fixed. A lower level discriminator of 20 mV was fixed. For each step, an acquisition time of 60 s was fixed.

Figure 4.2 shows three curves obtained with the PMT R6231-100: the signal+noise (count rate with a  $^{137}\text{Cs}$  source) in blue, the noise (count rate without the  $^{137}\text{Cs}$  source) in orange and the signal to noise ratio in grey. The latter was calculated as the ratio of the mean value of the signal count rate to the fluctuation of the counted signal and noise pulses expressed in standard deviation. A counting plateau is found between 1050 V-1150 V, within which the count rate due to a constant radiation flux varies very little as a function of the high voltage applied to the tube. Placing the working point at 1100 V assures the stability and accuracy of the measurements. The same exercise was done for the PMT BA R580 leading to an optimal voltage of 1300 V. Along this work, these two optimum values were used.

#### 4.2.2 Energy resolution of CLYC coupled with PMTs

To compare the performance of the two PMTs, measurements of the gamma energy resolution when coupled with the CLYC were performed with  $^{241}\text{Am}$ ,  $^{137}\text{Cs}$  and  $^{60}\text{Co}$  sources. The crystal was calibrated with the gamma photopeaks according to the source employed, leading to 0.25 keV/channel for the PMT BA R580 and 0.23 keV/channel for the PMT SBA R6231-100. The energy spectra were acquired using a NIM amplifier (SILENA 7611). The amplifier output was connected to a multichannel analyser (Amptek pocket MCA 8000d). Data were analysed with the Amptek DppMCA Digital Acquisition software. The energy resolution is calculated as the ratio of the Full Width Half Maxima (FWHM) with the peak centroid. Figure 4.3 shows the energy spectrum of a  $^{137}\text{Cs}$  source obtained with the PMT BA R580. The 662 keV photopeak has a resolution of 6.3% FWHM, versus a resolution of 4.0% when measured with the PMT R6231-100 (Figure 4.4). This discrepancy is due to the PMT: a super bialkali PMT provides better energy resolution because of its higher quantum efficiency. Indeed, at the peak scintillation wavelength of the CLYC, a difference of 10% point on the quantum efficiency is seen between the BA PMT R580 and the SBA PMT R6231-100 (25% and 35% respectively) (figure 4.5).

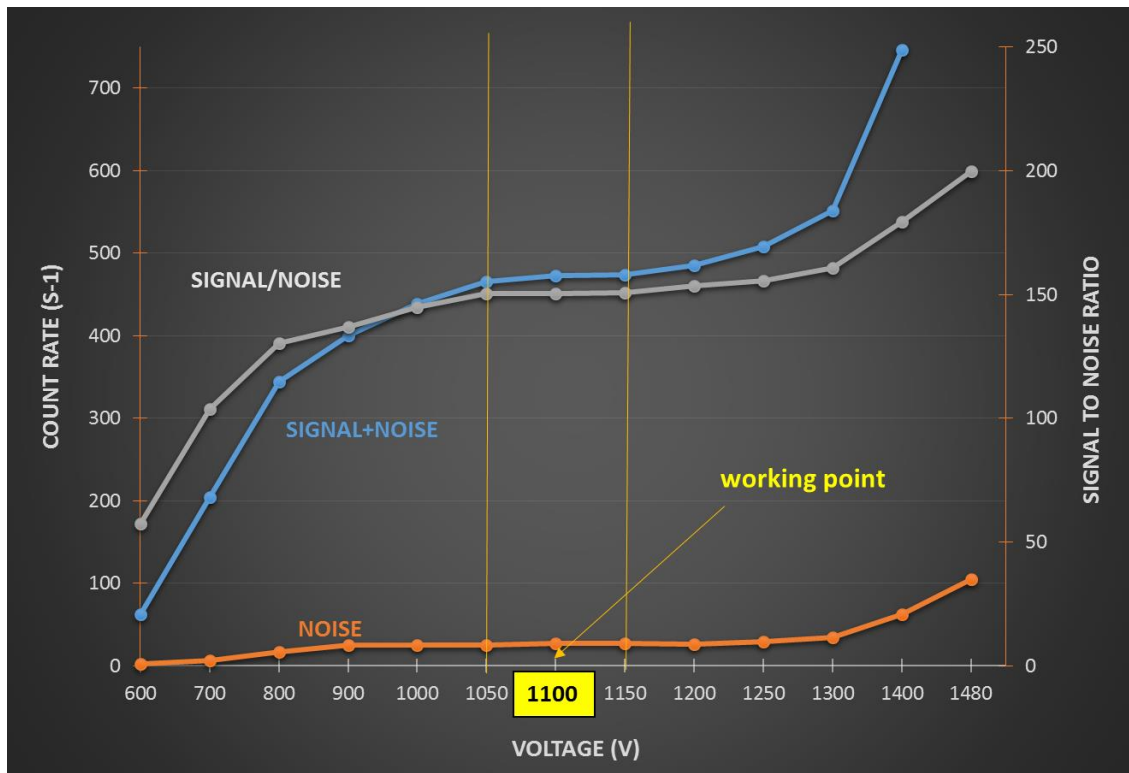


Figure 4.2 Plateau characteristic measurement for the SBA PMT R6231-100.

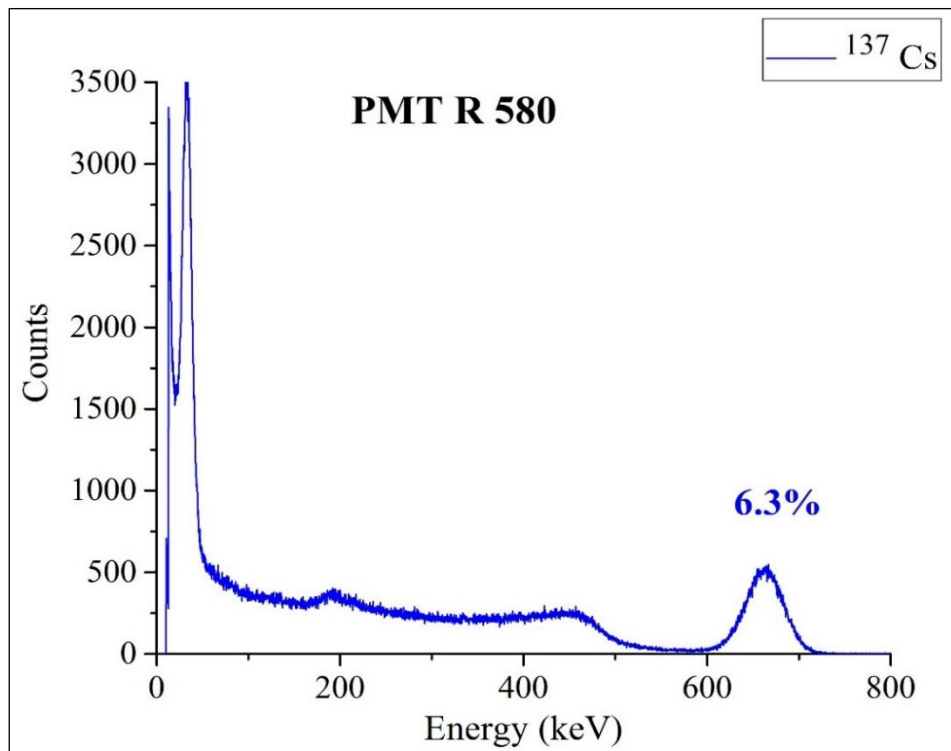


Figure 4.3  $^{137}\text{Cs}$  spectrum and energy resolution obtained with the CLYC and the PMT BA R580.

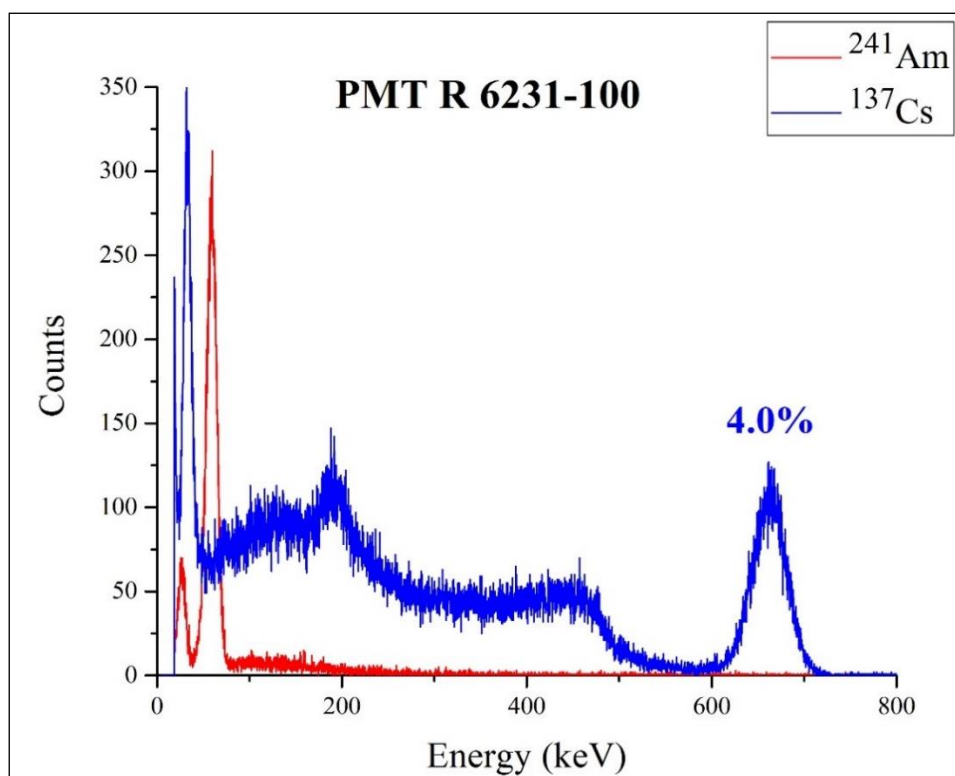


Figure 4.4  $^{241}\text{Am}$  and  $^{137}\text{Cs}$  spectra and energy resolution obtained with the CLYC and the PMT SBA R6231-100.

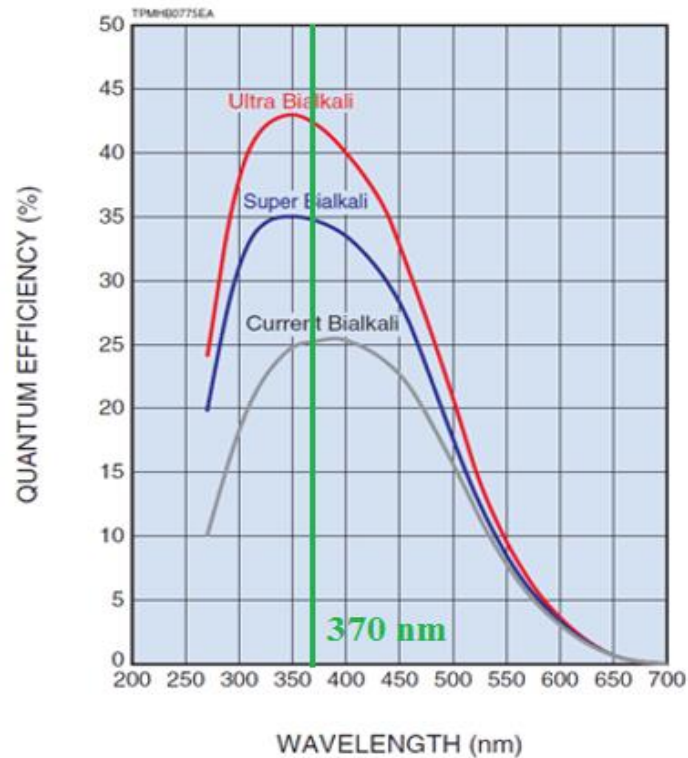


Figure 4.5 Quantum efficiency versus wavelength of the different technologies of PMT (Ultra Bialkali, Super Bialkali and Bialkali). In green the mean peak scintillation wavelength of CLYC [4].

### 4.3 SiPM characterization

One 8x8 SiPM array from SensL [5] was used. As shown in Figure 4.6, the array is made up of sixty-four 3x3 mm<sup>2</sup> silicon elements each consisting of 5676 APD-cells (Avalanche Photo Diodes of 35x35 μm<sup>2</sup> size). The whole size of the array well matches 1 inch (2.54 cm) cylindrical scintillators. A breakout evaluation board is provided by SensL to easily read out the signals from each sensor. A new board was designed to match the SensL board and to easily sum all the outputs, obtaining a single-channel output.

Each SiPM sensor consists of microcells<sup>(7)</sup> connected in parallel. Each microcell can be schematize with an avalanche photodiode (APD) and a quenching resistor in series. In normal operation, an external reverse voltage,  $V_{BIAS}$ , biases the SiPM over its breakdown voltage,  $V_{BD}$ . The difference  $V_{BIAS} - V_{BD}$  is known as **overvoltage  $\Delta V$** , which is one of the most important parameters affecting the operation of a SiPM.

A strong electric field is established in the sensitive volume of the Si microcell through the reverse bias, triggering an avalanche multiplication for each electron-hole pair generated in the sensor. The multiplication effect, whose intensity depends on the intensity of the electric field (so the  $\Delta V$ ), stops as soon as the local  $\Delta V$  crosses the zero and the signal passes through the quenching resistor. **This operation mode is also called Geiger mode operation of silicon devices.**

Thus, knowing the value of  $V_{BD}$  is crucial to determine the required value of  $V_{BIAS}$  for the desired  $\Delta V$  and gain.

<sup>(7)</sup> The single 3x3 mm<sup>2</sup> element is called either sensor or pixel, the individual microcells making up a sensor are also called APD



**Figure 4.6 SiPM array SensL J-30035-64P-PCB with its breakout board.**

#### 4.3.1 I-V characterization

In order to carry out the I-V characterization, the SiPM array was placed inside a light-tight box in order to shield it from ambient light completely. The SiPM array was connected to a power supply (Keithley 2450 source meter [6]), which is also a current meter, and all the data were collected by a computer for further analysis. The Keithley Kickstart software was used for the automatic acquisition of 51 measurement points. Varying the  $V_{BIAS}$  from 1 V to values above  $V_{BD}$  (28 V) the reverse current was measured for each step every 4 s, focusing with narrow steps (0.1 V) around the expected  $V_{BD}$  (24.5 V [7]). Each measurement was acquired for 4 s.

A power fit in the leakage current region was applied to find the voltage value where the deviation in the avalanche region starts. To determine the expected current for each pixel a power fit between 7 and 17 V was applied:  $\ln(I) = A \ln(V) + B$ .

The  $V_{BD}$  for each pixel was considered as the point where the measured current was 100 times higher than the current estimated by the power fit. Applying the same  $V_{BIAS}$  to all pixels, slight discrepancies in  $V_{BD}$  between the pixels imply different gain. The frequency histogram of the  $V_{BD}$  for the array was plotted.

All the 64 pixels have the same behaviour as shown in Figures.4.7-10. Below  $V_{BD}$ , the leakage current increases linearly with the voltage. Above  $V_{BD}$  the current increases dramatically with the voltage as the avalanche effect dominates. Figure 4.11 shows the good uniformity of the array since a proper Gaussian distribution of the  $V_{BD}$  of its elements has been measured. According to our parameters, the mean value of the  $V_{BD}$  was found to be 26 V and the  $V_{BIAS}$  was fixed at 28.5 V, which corresponds to a  $\Delta V$  of 2.5 V. This value was determined experimentally:  $^{137}\text{Cs}$  spectra were acquired with the CLYC scintillator applying different  $V_{BIAS}$  from 27 V to 30 V. The spectrum with the best energy resolution for both photo-electric peaks at 662 keV and 33 keV was chosen, corresponding to a  $V_{BIAS}$  of 28.5 V. Above 28.5 V the peak at 33 keV disappears, due to the increased noise from dark current. In principle, the higher the  $\Delta V$ , the higher are the SiPM performances in terms of resolution. In reality, since the

detection efficiency tends to saturate with increasing  $\Delta V$  while the noise keeps increasing (even more than linearly) with  $\Delta V$ , an upper limit exists to the optimum  $V_{BIAS}$ .

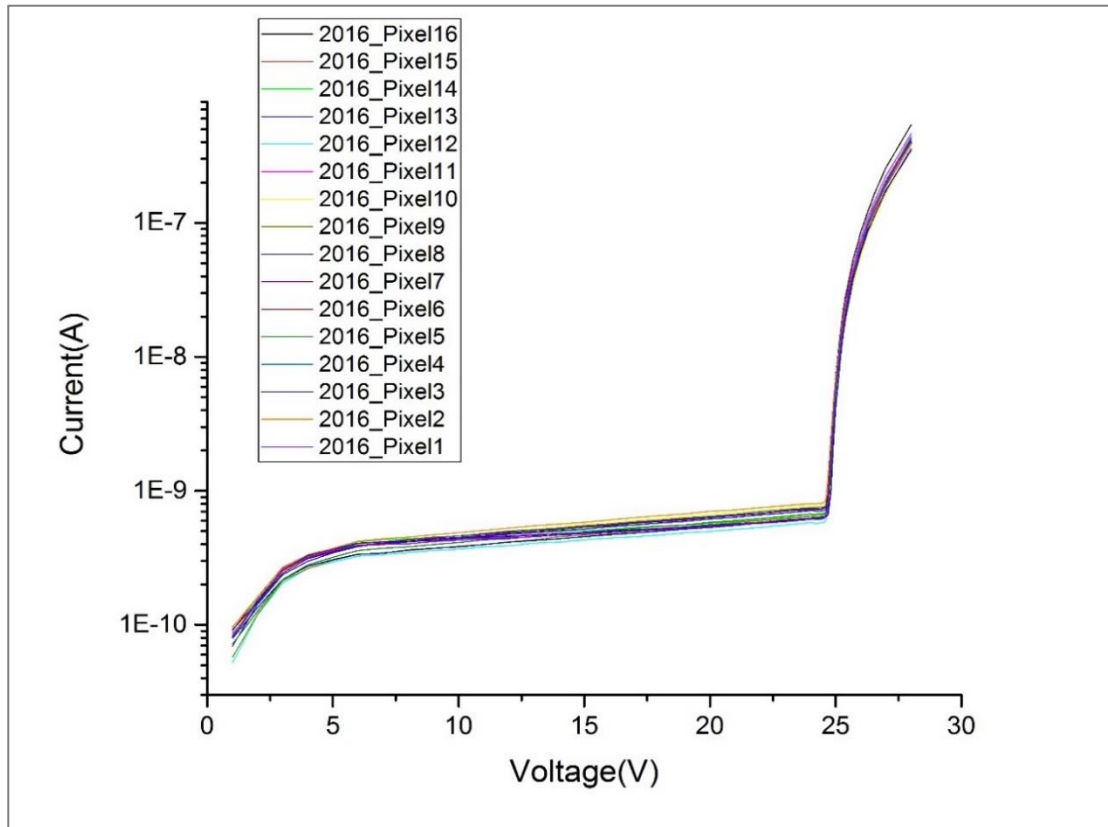


Figure 4.7 I-V curves for the 1<sup>st</sup> set of data (pixels 1 to 16).

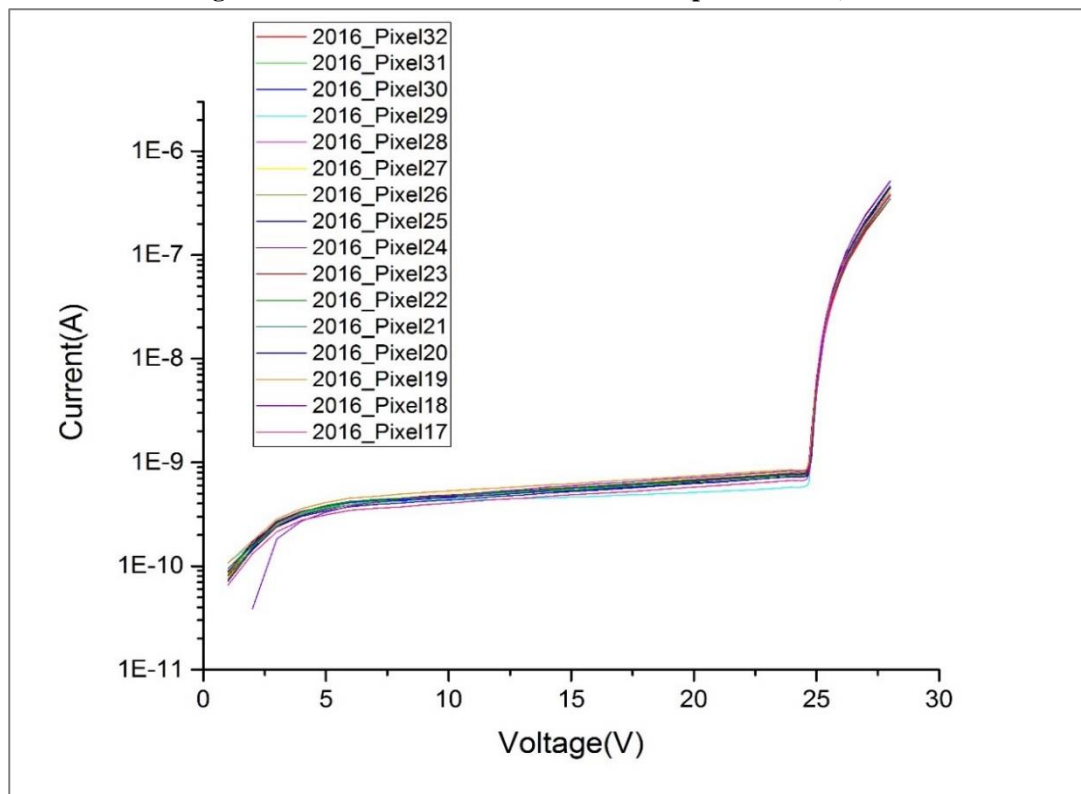


Figure 4.8 I-V curves for the 2<sup>nd</sup> set of data (pixels 17 to 32).



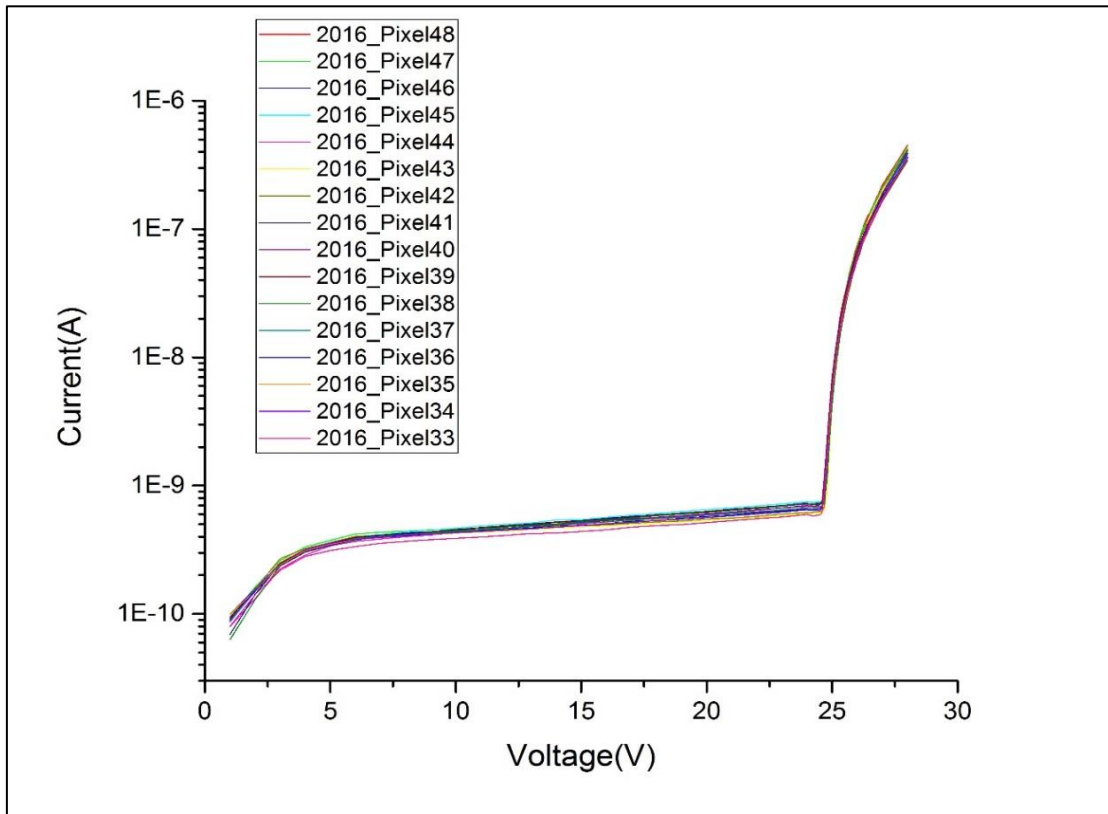


Figure 4.9 I-V curves for the 3<sup>rd</sup> set of data (pixels 33 to 48).

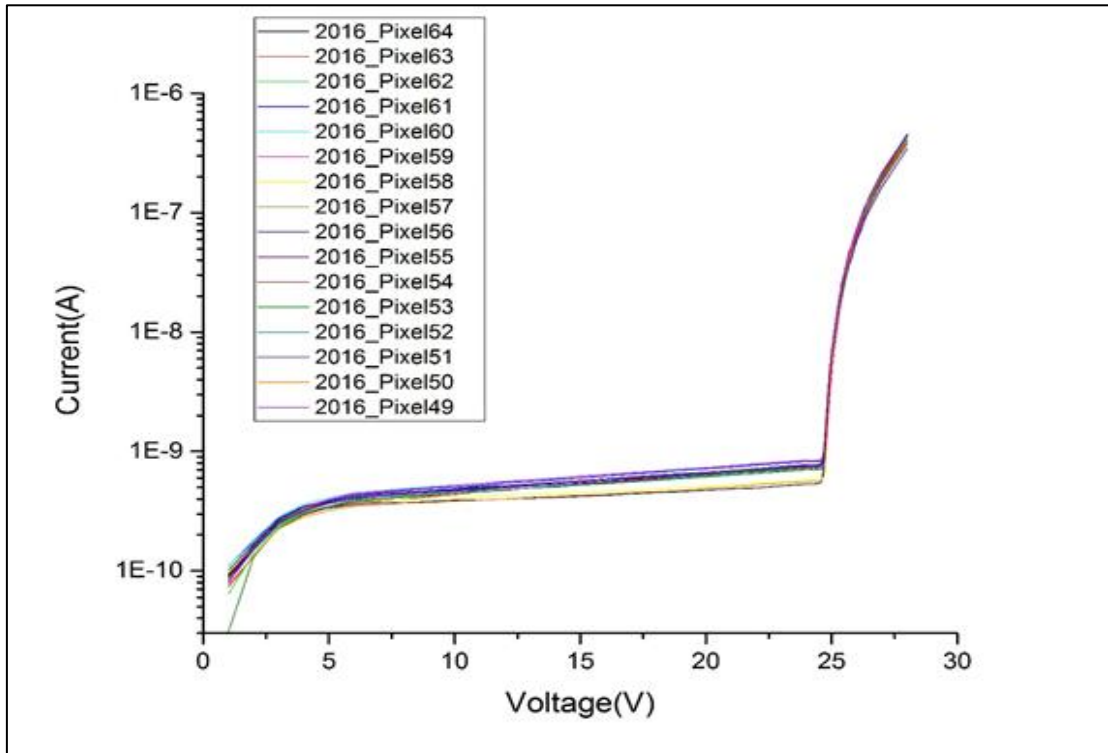
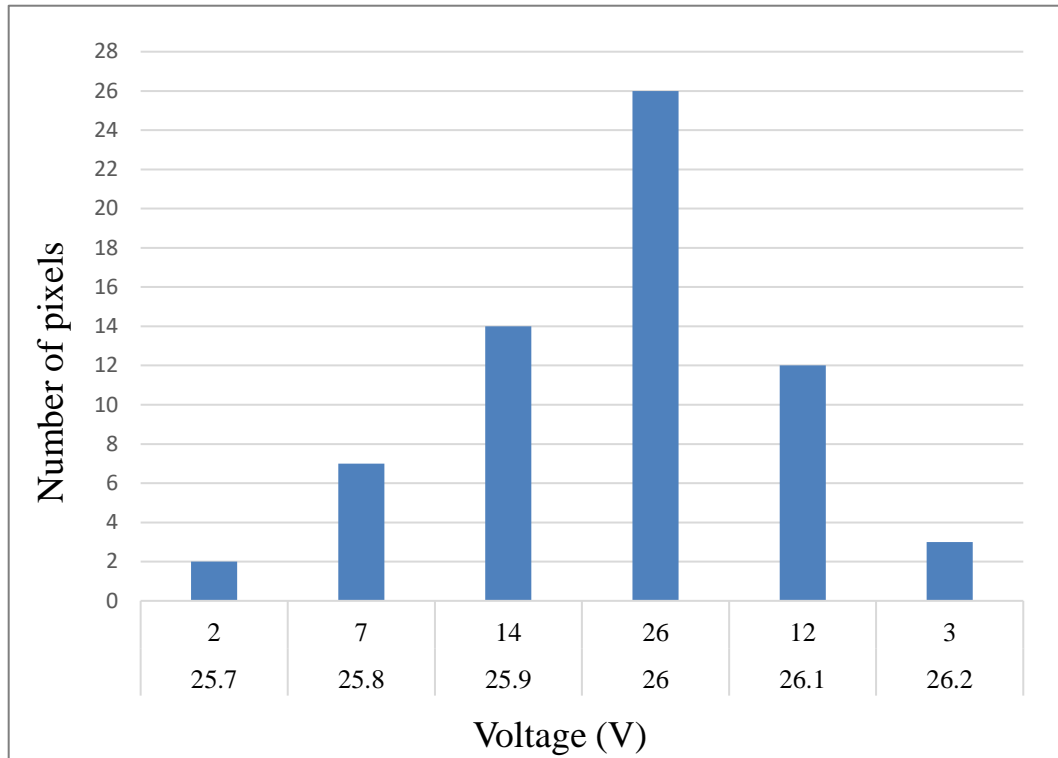


Figure 4.10 I-V curves for the 4<sup>th</sup> set of data (pixels 49 to 64).



**Figure 4.11** Frequency histogram of the  $V_{BD}$  distribution in the array.

#### 4.3.2 Comparison with ArrayC-30035-16P-PCB coupled with $\text{LaBr}_3$

To compare the gamma energy response of the actual system (8x8 SiPM array and 1 inch CLYC scintillator) measurements were performed with a  $\text{LaBr}_3$ . The set-up of comparison consisted in a smaller crystal and SiPM array : 15  $\text{\AA}$  x 15 mm  $\text{LaBr}_3$  and 4x4 SiPM array from SensL. This array was previously purchased in order to investigate it as alternative solution to the SiPMs by ST Microelectronics, which was used in the first prototype of B-RAD [8]. This array was coupled to a  $\text{LaBr}_3$  crystal from EPIC [9] to develop a gamma probe. As shown in Figure 4.12, the array is made up of sixteen 3x3 mm<sup>2</sup> silicon elements with 4774 cells each (35x35  $\mu\text{m}^2$ ). The whole size of the array considering the external edges of each pixel is 16.8x16.8 mm<sup>2</sup> so that it well matches 15  $\text{\AA}$  x 15 mm cylindrical scintillators.

A  $V_{BIAS}$  of 28 V, a shaping time of 1  $\mu\text{s}$  and a gain amplification of 19 were applied. A MCA Amptek 8000D was used to check the performance of the crystal-SiPM system.  $^{137}\text{Cs}$  and  $^{241}\text{Am}$  spectra were acquired, and the crystal was then calibrated exploiting the three peaks at 33 keV, 60 keV and 662 keV. The best results obtained in terms of energy resolution at 662 keV was 7.2% (Figure 4.13). The same measurements were performed to check the quality of the SiPM 8x8 ArrayJ-30035-64P-PCB. A 1 inch  $\text{LaBr}_3$  crystal (from the same company, EPIC) was chosen to match the size of the SensL SiPM array. Similar parameters were used with the system  $\text{LaBr}_3$  (1 inch) + 8x8 SiPM array.  $^{137}\text{Cs}$ ,  $^{241}\text{Am}$  and  $^{60}\text{Co}$  spectra were acquired (Figure 4.14), and the crystal was then calibrated exploiting the four peaks at 60 keV, 662 keV, 1173 keV and 1332 keV. In this case the energy resolution of the 662 keV photopeak is 4.6%. This improvement in the energy resolution is due to the ArrayJ-30035-64P-PCB. This recent version of SiPM has a highest PDE since the microcell fill factor <sup>(8)</sup> is 75% while the previous C array

<sup>(8)</sup> An increase in the fill factor implies an increase of the number of microcells per pixel. The J array shows more microcells per pixel as compared to the C array (about 1000 microcells per pixel).



has only 64% and, from a geometric point of view, the new through silicon via package strongly reduces the non-sensitive area between pixels with respect to the previous package.

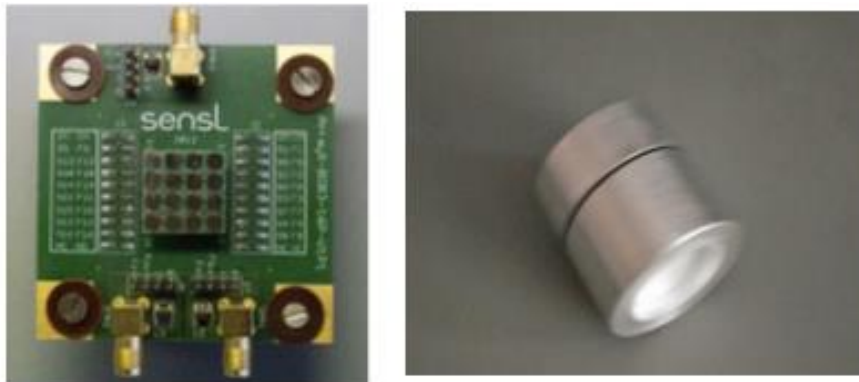


Figure 4.12 The ArrayC-30035-16P by SensL and the breakout board on the left and the 15 Ø x 15 mm LaBr<sub>3</sub> crystal on the right.

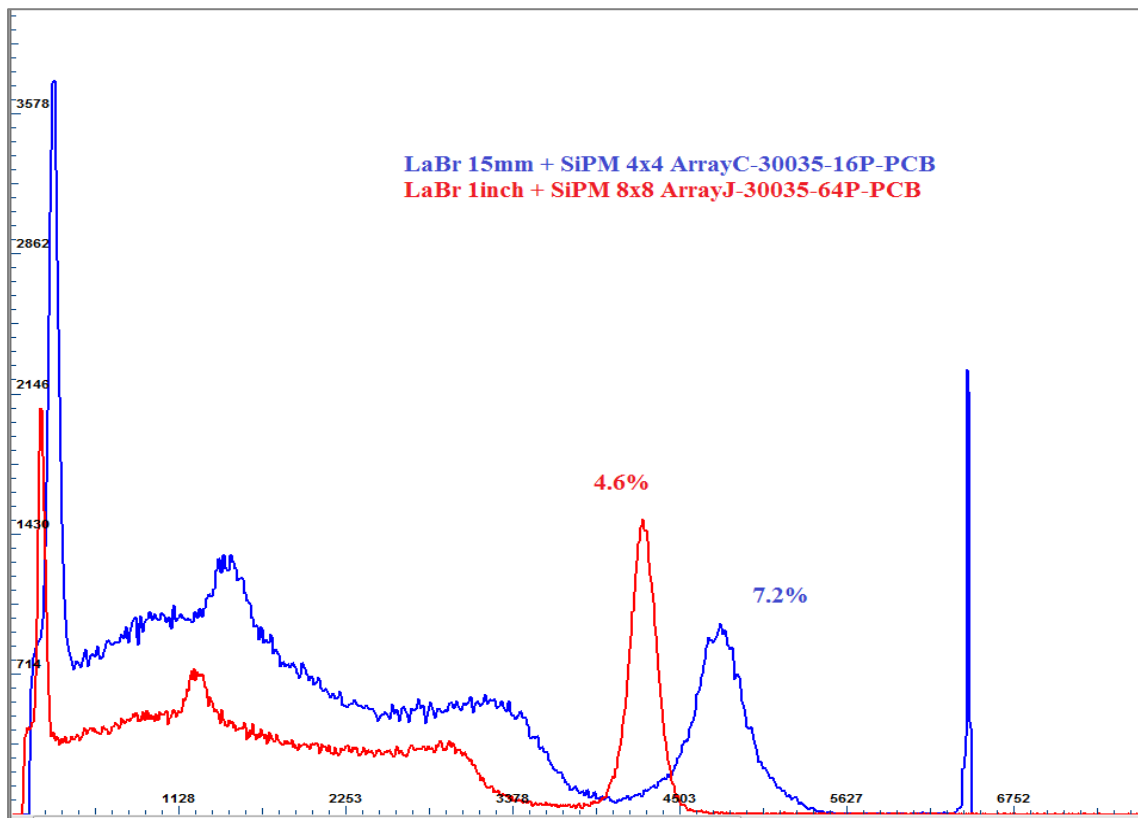


Figure 4.13 <sup>137</sup>Cs spectra and energy resolution at 662 keV. The blue spectrum represents the system LaBr<sub>3</sub> (15mm) + 4x4 ArrayC-30035-16P. The energy resolution of the 662 keV peak is 7.2%. The red curve represents the system LaBr<sub>3</sub> (1 inch) + 8x8 ArrayJ-30035-64P-PCB. An energy resolution of 4.6% was obtained for the 662 keV peak.

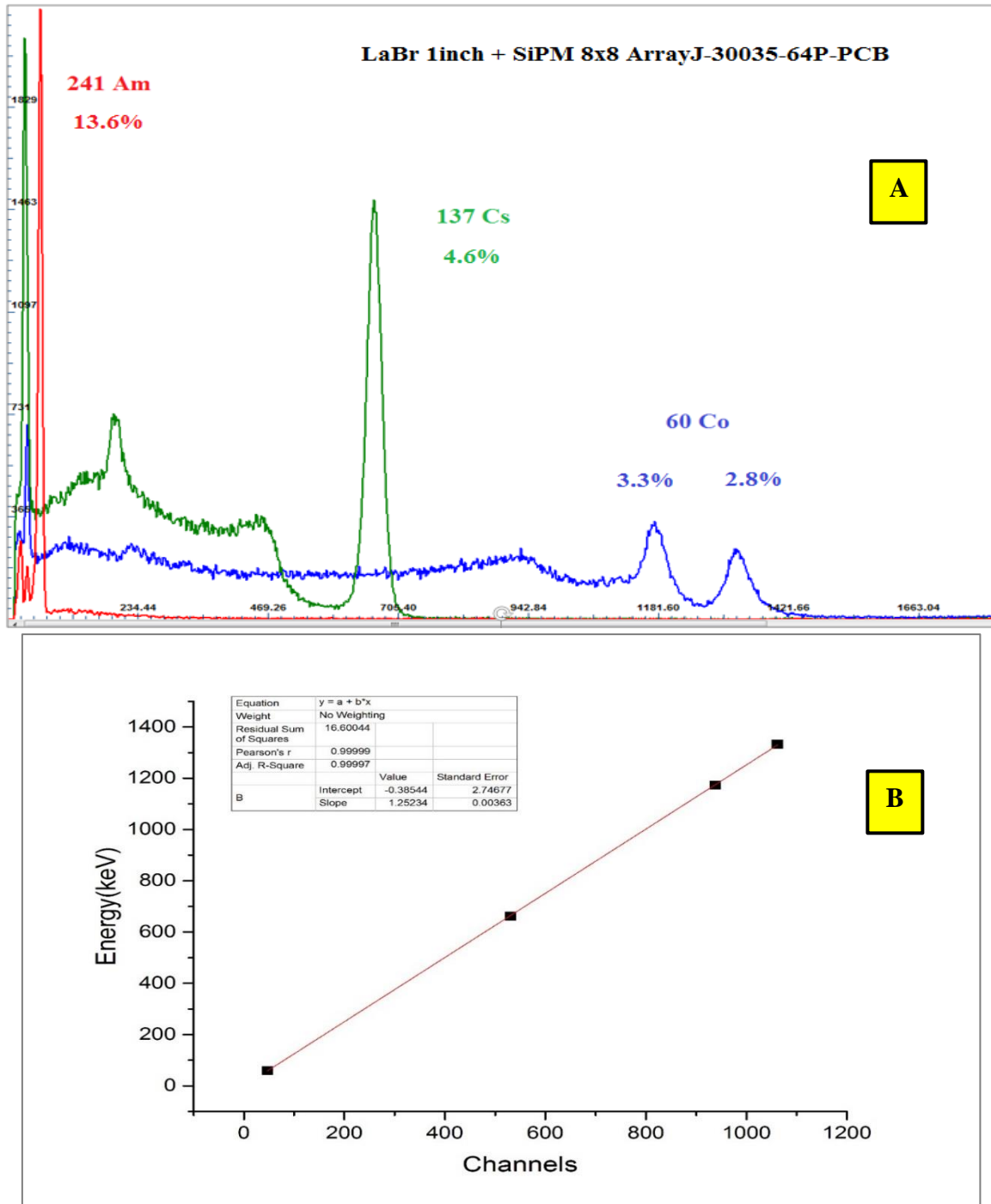


Figure 4.14  $^{241}\text{Am}$ ,  $^{137}\text{Cs}$  and  $^{60}\text{Co}$  spectra and energy resolutions obtained with the LaBr<sub>3</sub>, the 8x8 ArrayJ-30035-64P-PCB (A) and the energy-channel calibration (B).

#### 4.3.4 Energy resolution of CLYC coupled with ArrayJ-30035-64P-PCB

The 8x8 ArrayJ-30035-64P-PCB SiPM was coupled with the CLYC. After investigation of the best energy resolution of the  $^{137}\text{Cs}$  photopeak at 662 keV, the parameters were fixed as follow:

- $V_{\text{BIAS}} = 28.5 \text{ V}$
- Silena amplifier with a gain of 19.4 and a shaping time of 1  $\mu\text{s}$ .

---

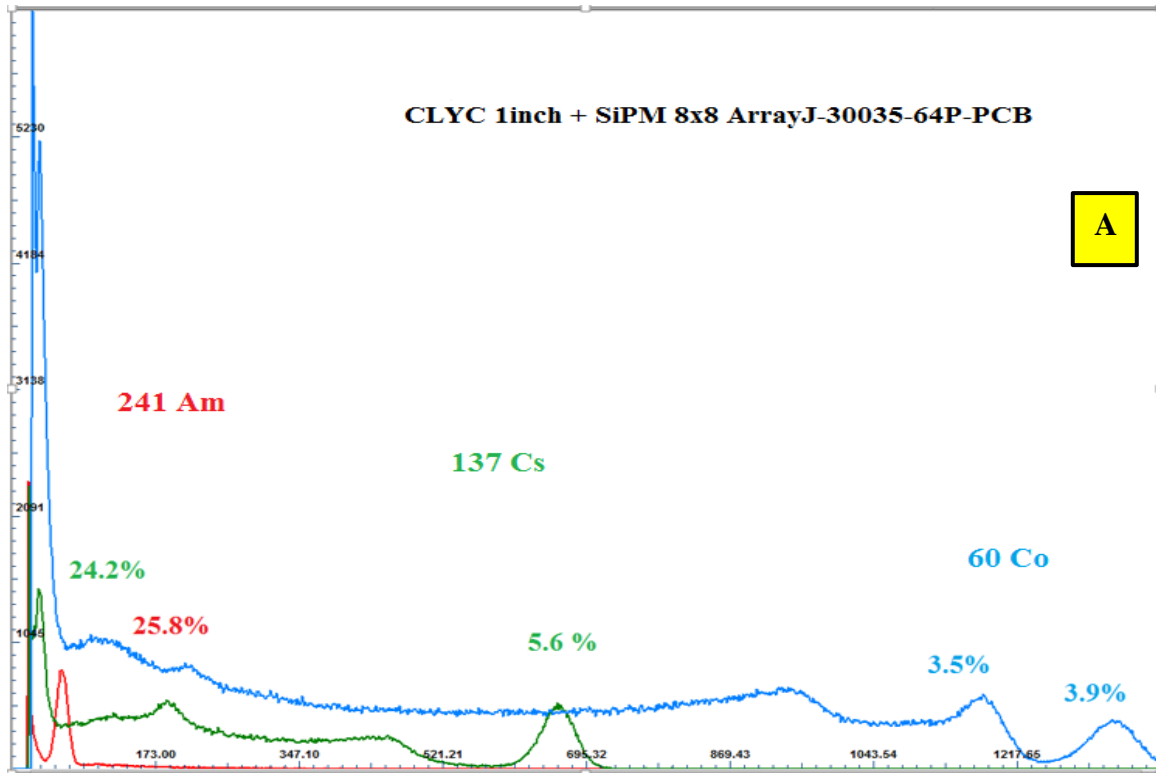
A MCA Amptek 8000D was used to acquire the spectra of  $^{241}\text{Am}$ ,  $^{137}\text{Cs}$  and  $^{60}\text{Co}$ . The crystal was calibrated exploiting the 33 keV, 60 keV, 662 keV, 1173 keV and 1332 keV lines (Figure 4.15). An energy resolution of 5.6% for the  $^{137}\text{Cs}$  peak at 662 keV was measured. This value is in good agreement with literature data [10] where a resolution of 6.6% was found for the CLYC coupled with a SensL SiPM array.

The light yield of CLYC is around 20,000 photons/MeV. It exhibits excellent proportionality between the deposited energy and the light output, which leads to good energy resolution. Indeed, the CLYC showed an excellent energy resolution of 4.0% (PMT R6231-100), which is better than those of commonly used scintillators for gamma detection such as NaI(Tl) and CsI(Tl), having 6.5% and 7-9% energy resolution at 662 keV, respectively. Compare to the  $\text{LaBr}_3$ , the CLYC exhibits a satisfactory energy resolution considering that the light yield of the  $\text{LaBr}_3$  is 3 times higher than the CLYC (60 000 ph/MeV).

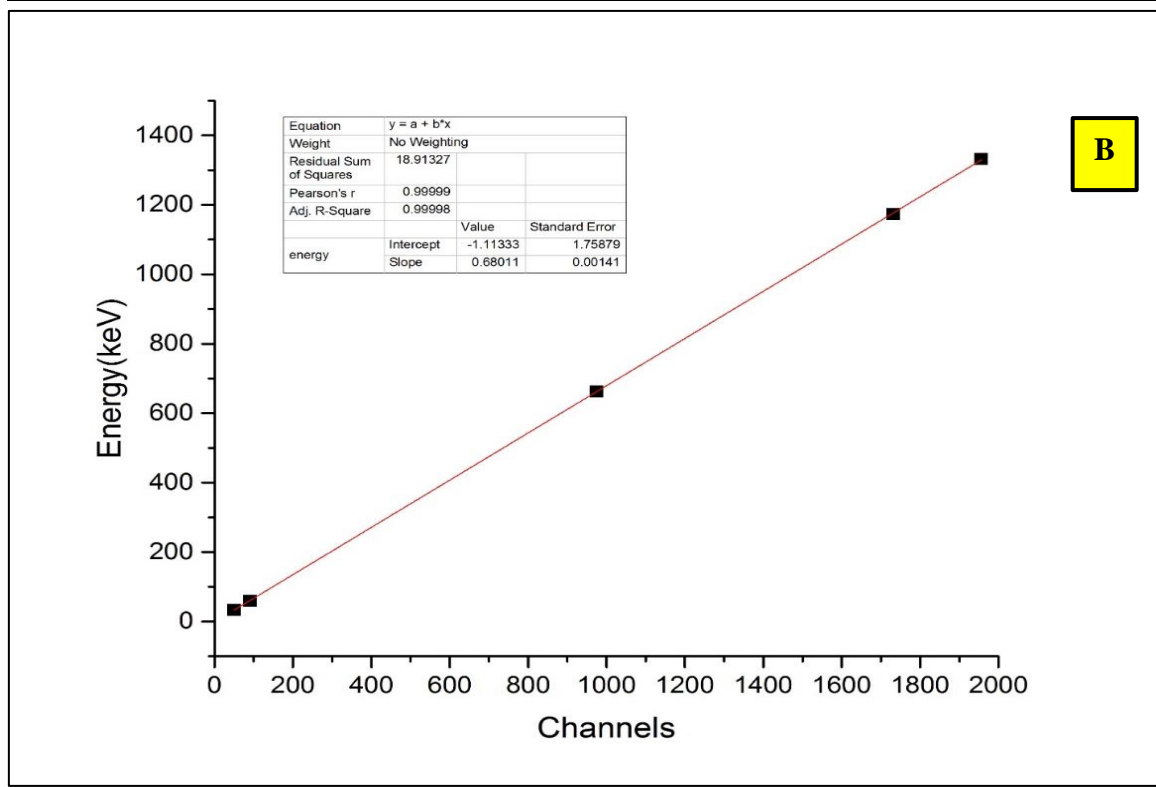
Moreover, when coupled with the SiPM, the CLYC gives a slightly better energy resolution than the Bialkali PMT but has a lower performance when compared to a super Bialkali PMT (6.3% and 4.0% respectively). This make the SiPM a promising competitor for the replacement of PMT.

#### 4.3.5 Temperature sensitivity of the system CLYC+ArrayJ-30035-64P-PCB

Measurements were performed in the climate chamber of the RP group. The light-tight box containing the CLYC, the SiPM array and the  $^{137}\text{Cs}$  source was placed inside the chamber, while the power supply and the readout electronics were located outside. The SiPM was connected to an MCA Amptek 8000D via a Silena NIM amplifier (gain: 25(50\*0 with 0=0.5 on the amplifier scale), shaping time (ST): 1  $\mu\text{s}$ ), applying a 28.5  $V_{\text{BIAS}}$ . During the measurement, the temperature was varied from -10 °C to +40 °C in steps of 10 °C. A thermocouple was placed inside the light-tight box to check the temperature close to the detection system. A 20 minutes acquisition was performed for each spectrum. The channel position of the 662 keV photopeak served as a relative measurement of the temperature sensitivity. As shown in Figure 4.16, the peak centroid varies by about 10% over the investigated temperature range with a maximum at 10 °C. The energy resolution of the 662 keV photopeak versus temperature was measured (Figure 4.17). The energy resolution improves as the temperature increases from -10 °C to +20 °C, where it reaches a minimum of 7.4%, and levels off thereafter.



**A**



**B**

Figure 4.15 <sup>241</sup>Am, <sup>137</sup>Cs and <sup>60</sup>Co spectra, and energy resolutions obtained with the CLYC coupled with the 8x8 ArrayJ-30035-64P-PCB (A) and the energy-channel calibration (B).

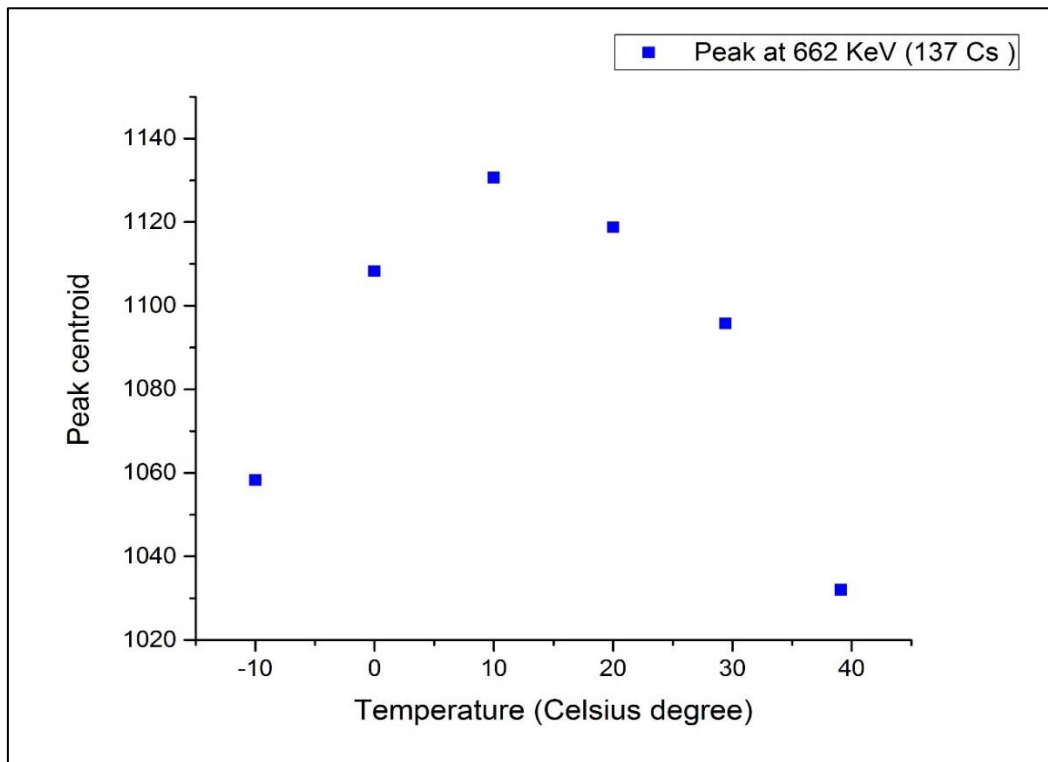


Figure 4.16 The 662 keV photopeak channel position of the system CLYC+ ArrayJ-30035-64P-PCB as a function of temperature from -10 °C to +40 °C.

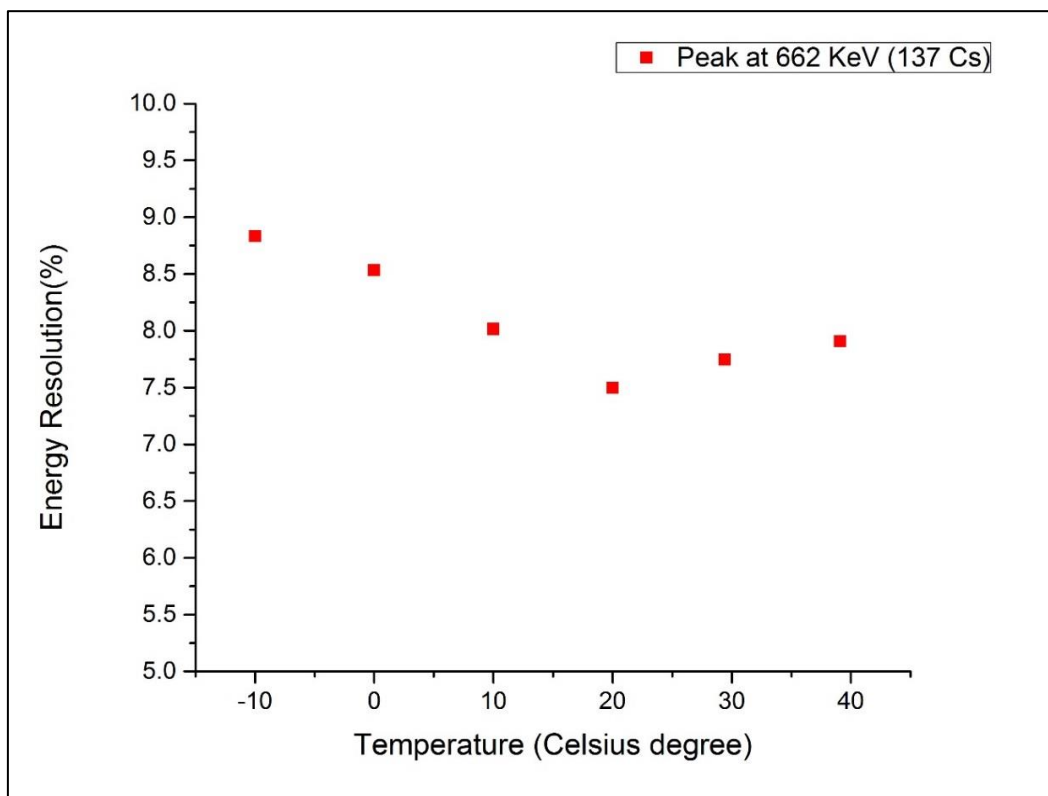
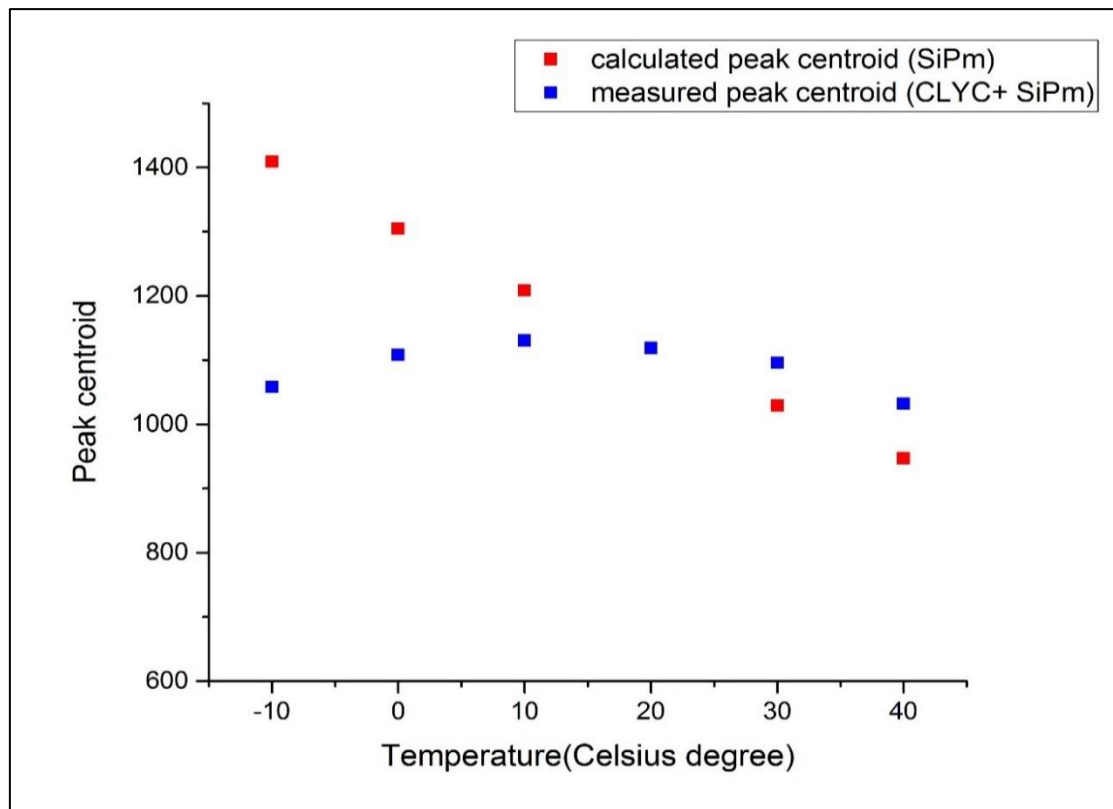


Figure 4.17 The energy resolution of the system CLYC+ArrayJ-30035-64P-PCB as a function of temperature from -10 °C to +40 °C. Data refer to the 662 keV photopeak.

The response of the system CLYC+ArrayJ-30035-64P-PCB as a function of temperature depends on two overlapping effects: the variation of the  $V_{BD}$  of the SiPM and the variation of the crystal light yield. The first effect can be understood from the SiPM physics. In a p-n junction a potential difference acts as a barrier forbidding the charges to cross the junction (electrons toward the p side, holes toward the n side). The potential barrier depends directly on the concentration of free charge carriers per  $\text{cm}^3$  ( $n_i$ ), which depends on the temperature ( $n_i^2 = BT^3 \exp(E_g/kT)$ )<sup>(9)</sup>. Therefore, when the temperature increases, the potential barrier of the p-n junction decreases. Working in reverse bias, this leads to an increase of the  $V_{BD}$  value [11]. Thus when the temperature increases,  $V_{BD}$  increases as well, leading to a decrease of the gain. The 662 keV photopeak centroid is therefore shifted to the left. This effect has been estimated taking into account the temperature dependence of  $V_{BD}$  and gain given by the datasheet (i.e. 21.5 mV/°C and -0.8%/°C). Figure 4.18 shows the linear trend of the theoretical peak centroid. This curve represents the effect of the SiPM on the 662 keV photopeak centroid if no effect of temperature on the crystal is considered. In blue, the measured peak centroid represents the response of the system CLYC+ SiPM, which is rather flat. From -10 °C to +40 °C it seems that the light output of CLYC increases compensating the effect of the SiPM on the peak centroid.



**Figure 4:18** Variation of peak centroid as a function of temperature from -10 °C to +40 °C. The blue points represent the measured peak centroids with the system CLYC+ArrayJ-30035-64P-PCB. The red points are the theoretical peak centroids calculated from the response of SiPM ArrayJ-30035-64P-PCB only.

#### 4.3.6 Uniformity

To achieve the best performance for a given application, SiPM physics parameters like gain, breakdown voltage, signal shape, dark count rate, photon detection efficiency and their impact on the measurement

<sup>(9)</sup> with B=parameter depending on the material, T=temperature in kelvin,  $E_g$ =energy of band gap and k= Boltzmann constant

quality should be understood. Moreover when working with a SiPM array, the uniformity of these parameters within a satisfactory uncertainty range is essential. In order to study the uniformity response of the ‘CLYC+SiPM’ prototype, the uniformity of the SiPM array was first studied. The parameters of importance were the breakdown voltage, the gain and the photon detection efficiency (PDE).

#### 4.3.6.1 Experimental set-up and test-bench calibration

Figure 4.19 shows the experimental set-up used for the characterisation of the ArrayJ-30035-64P SiPM array. It consists in a light source (LED), an integrating sphere, a QDC (charge to digital converter), a data acquisition system and two photodetectors: a reference photodiode and the SiPM array with the associated electronics. A LED placed in an external light tight box is powered with a LED driver to produce pulses. The light pulses propagate in the integrating sphere through an optical fibre.

The SiPM is biased with a constant voltage by a source-meter and the current from the reference photodiode is measured by a pico-amperometer. Both devices are controlled by a computer. Figure 4.20 shows the electrical devices and the light tight boxes. A DRS4 digitizer is used to acquire the signal from the SiPM detector. An acquisition is triggered when a light pulse from the LED occurs. Each event is sampled in 1024 channels and sent to the computer for further analysis.

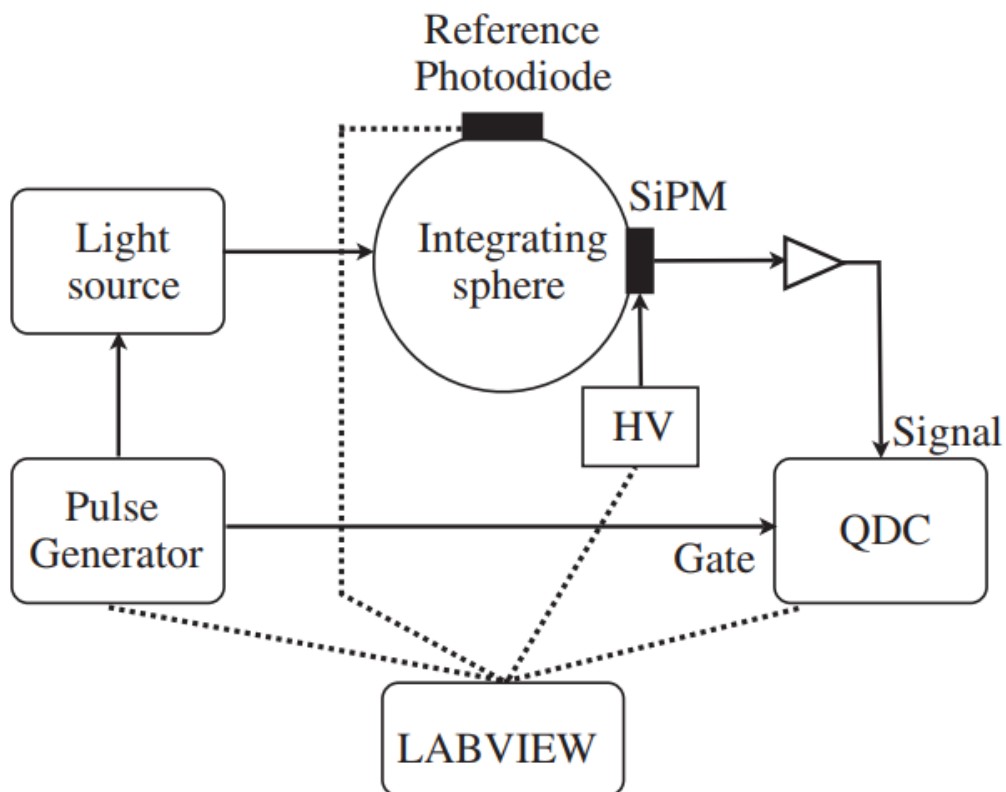
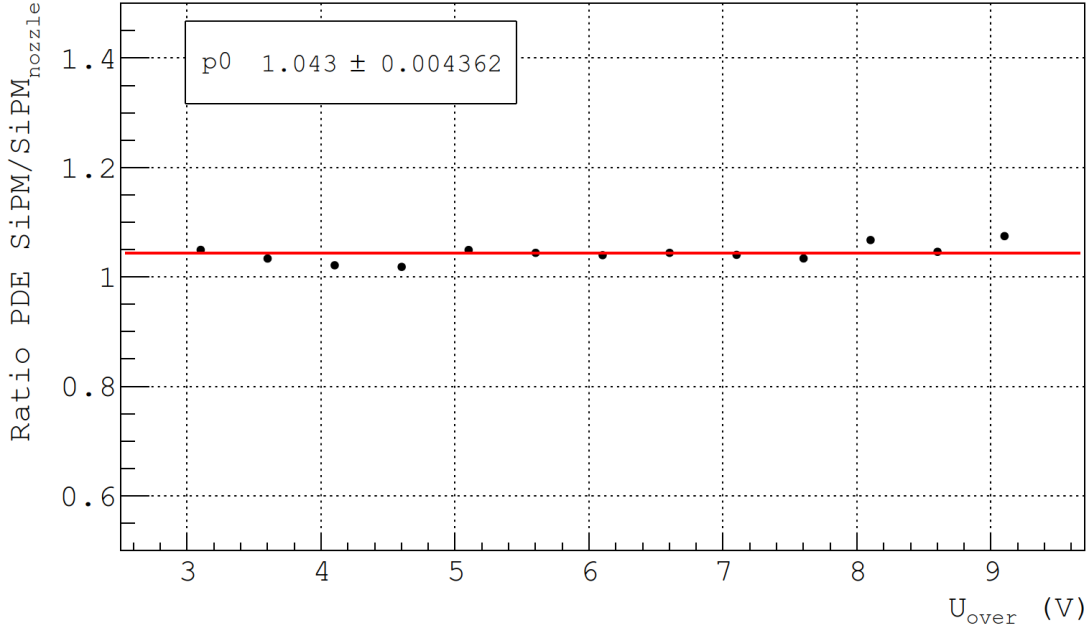


Figure 4.19 Layout of the experimental set-up [12].





PDE obtained for the different pixels of the array, we decided to multiply each PDE measurement by the average value of 1.043.



**Figure 4.21** PDE ratio of the HAMAMATSU (S13360-3050PE) used for the calibration with and without nozzle.

#### 4.3.6.2 Statistical analysis

- PDE

The PDE is defined as the probability that a SiPM detects an incoming photon. From a theoretical point of view, the PDE depends on the efficiency to absorb an impinging photon in the active part of a SiPM and to create an electron-hole pair, called quantum efficiency ( $QE$ ). In the following we will refer to each of the SiPMs that compose the array as *pixels*. Furthermore, the PDE includes the probability to subsequently trigger an avalanche, called trigger probability  $P_{trig}$ , and the fill factor  $FF$ , which is the ratio of photosensitive area to total area, as written in equation 4.1:

$$PDE(\lambda, \Delta V) = QE(\lambda) \times P_{trig}(\Delta V) \times FF \quad (4.1)$$

The PDE depends on the wavelength  $\lambda$  of the light emitted and the overvoltage  $\Delta V$  applied. The wavelength of 370 nm, corresponding to the mean wavelength of the CLYC was used. The measurement of the PDE was performed using the so-called “counting method” that uses the simultaneous measurement of the average number of photons detected after a light trigger ( $N_{light}$ ) and the average number of photons measured under dark conditions ( $N_{dark}$ ). The difference between these two values represents the number of detected photon  $N_{det}$  i.e. the number of primary fired cells triggered by incoming photons and can be calculated from the single photon electron spectrum (4.2):

$$N_{det} = N_{light} - N_{dark} \quad (4.2)$$

The PDE, introduced in expression (4.3), is therefore defined as the ratio between  $N_{det}$  and the total number of photon impinging the SiPM  $N_{tot}$ :

$$PDE(\%) = \frac{N_{det}}{N_{tot}} \times 100 \quad (4.3)$$

$N_{tot}$  is determined from the calibration of the light incident flux as described below.

The integrated charge values measured by the QDC are filled into a histogram as shown in Figures 4.22 and 4.23. Each peak corresponds to a certain number of fired pixels (photoelectrons). The first peak is called pedestal  $N_{ped}$  and corresponds to the number of events in which no photons have been measured. The photoelectron distribution is affected by the correlated noise (crosstalk and afterpulsing) so the charge spectrum has a quasi-Poisson statistics except for the pedestal peak. This first peak is based on the integration of the baseline, so no correlated noise affects the number of events in this peak. For this reason, the probability of no detection follows a Poisson statistics. Thus, it can be used to calculate the real detected-photon rates  $N_{light}$  and  $N_{dark}$  in light and in dark conditions, respectively. The Poisson probability to populate the pedestal peak in light and in the dark with the mean  $N_{det}$  is calculated following the equations 4.4-4.6 below:

$$P(0, N_{det}) = e^{-N_{det}} \times \frac{N_{det}^0}{0!} = e^{-N_{det}} \quad (4.4)$$

$$N_{det} = -\ln(P(0, N_{det})) \quad (4.5)$$

$$N_{det} = -\ln(N_{light}) + \ln(N_{dark}) \quad (4.6)$$

$N_{light}$  is detected by the SiPM with the LED on, and  $N_{dark}$  is the dark count rate which had been obtained in the same way, but with the LED turned off and the QDC triggered arbitrarily. The number of detected photons  $N_{light}$  and  $N_{dark}$  are determined thanks to the charge histogram. First, peaks are detected and a gaussian is fitted in a symmetric range centered on the position of the pedestal maximum. Once fitted,  $N_{light}$  and  $N_{dark}$  are calculated as the sum of the bins contents  $[-3\sigma; 3\sigma]$  where  $\sigma$  is the standard deviation of the Gaussian. The total number of events was set at 20000. Figure 4.24 shows the number of photons detected during the pulse. The dark noise leads to a higher number of photons. Figure 4.25 shows the PDE obtained for one pixel.

- Gain and breakdown voltage

Another important parameter to consider is the gain of the SiPM. The gain increases with the bias voltage. The gain is defined as the difference between the mean of the first two photopeaks and it was obtained from the histograms for each pixel. Theoretically, the gain should decrease linearly with the bias voltage and, as soon as the  $V_{bd}$  is reached, it goes to zero. Seen the fact that the relation is linear, we used the method of the intercept to find the voltage for which the gain is zero to extract the  $V_{bd}$ . The gain is given as a function of  $V_{bias}$  and in arbitrary units. An example of the gain for pixel X is shown in figure 4.26.

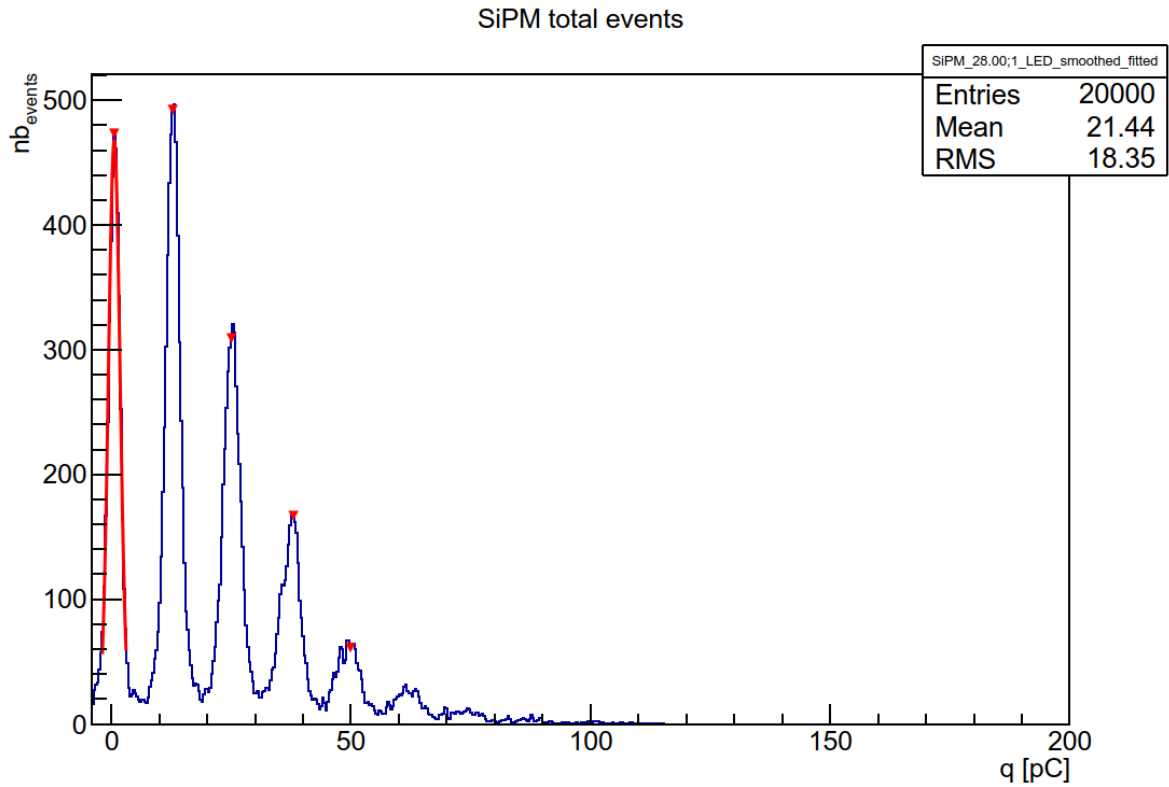


**Figure 4.22** Single photoelectron spectrum recorded for one pixel of the SiPM array J-30035-64P. Each peak corresponds to a certain number of photoelectrons (pe). The highlighted area corresponds to the number of pedestal events.

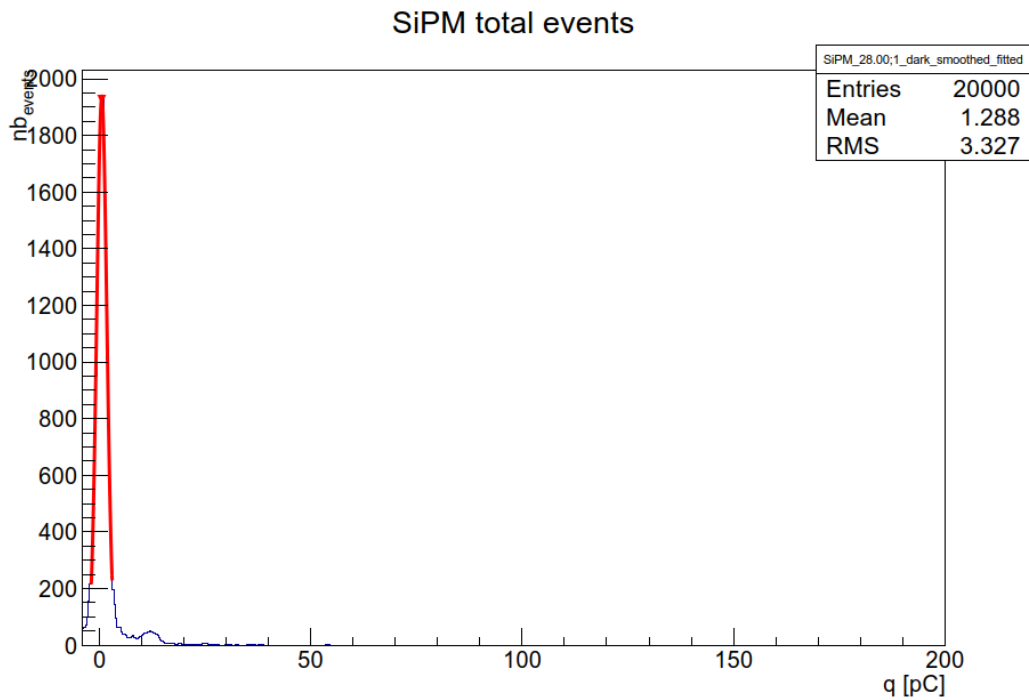


**Figure 4.23** Dark noise spectrum recorded for one pixel of the SiPM array J-30035-64P.

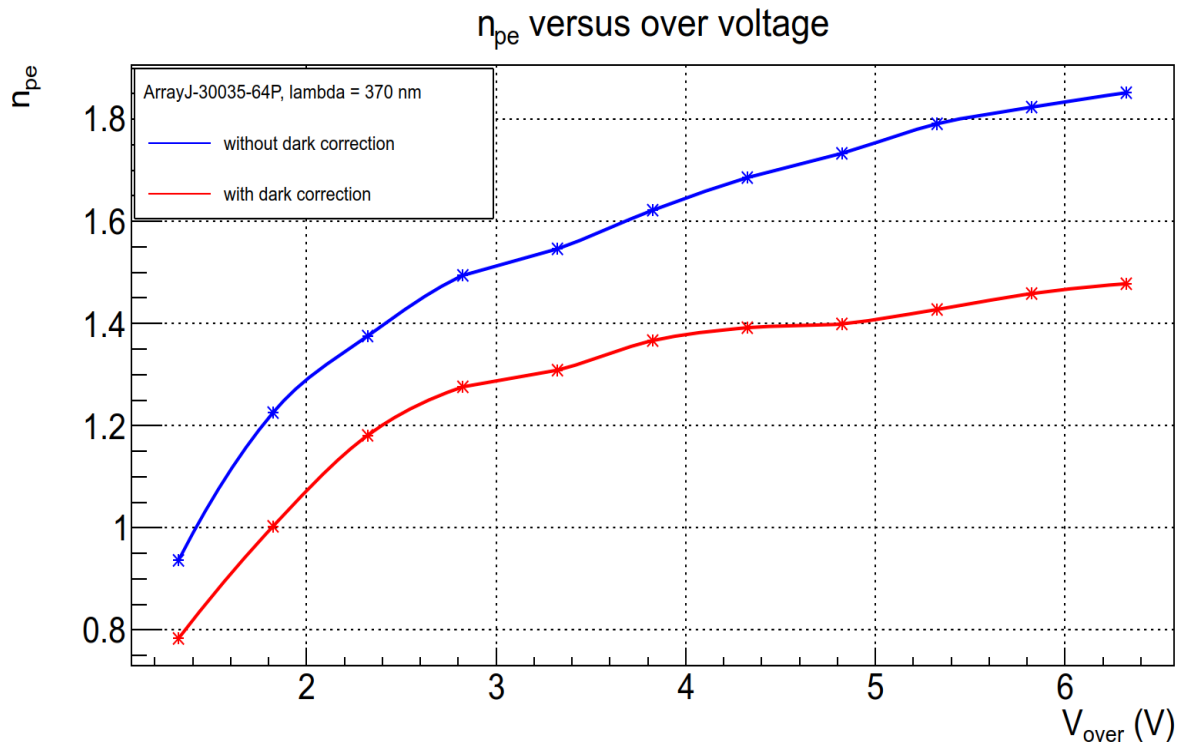


Figure 4.24 Number of photoelectrons before (blue curve) and after dark correction (red curve) for one pixel of the SiPM array J-30035-64P.

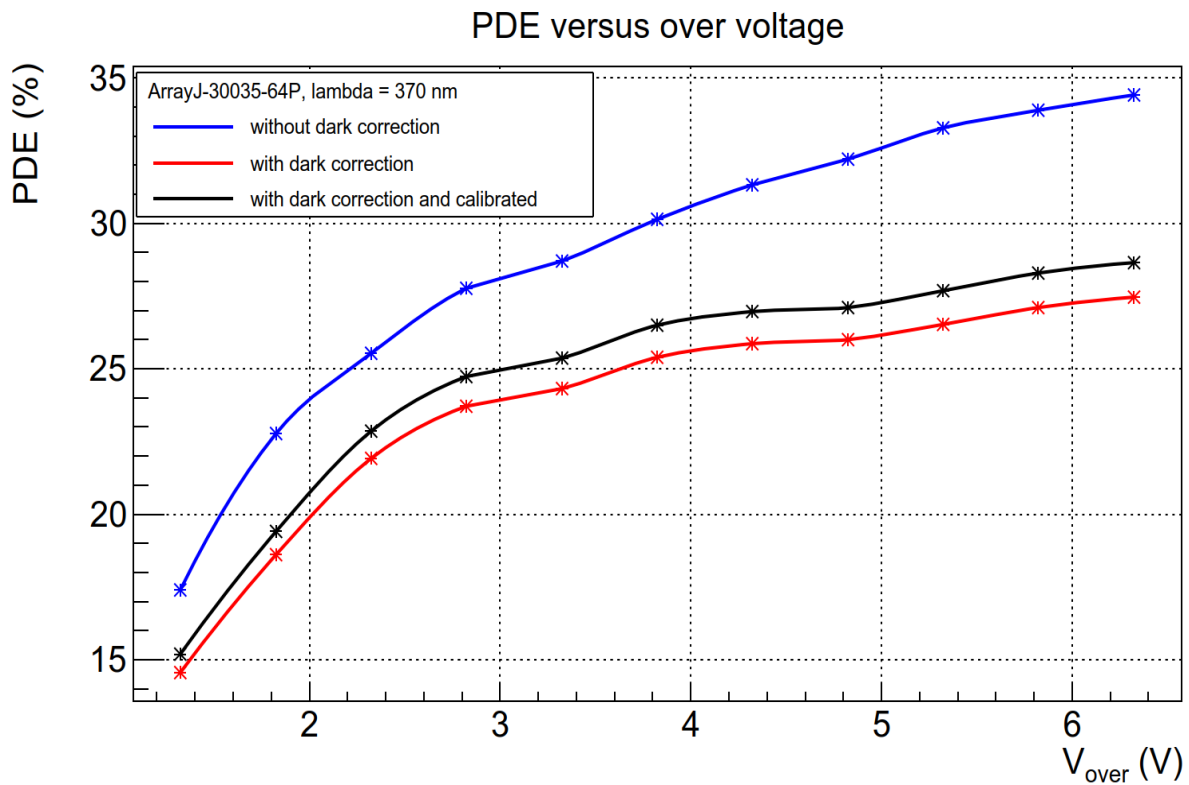
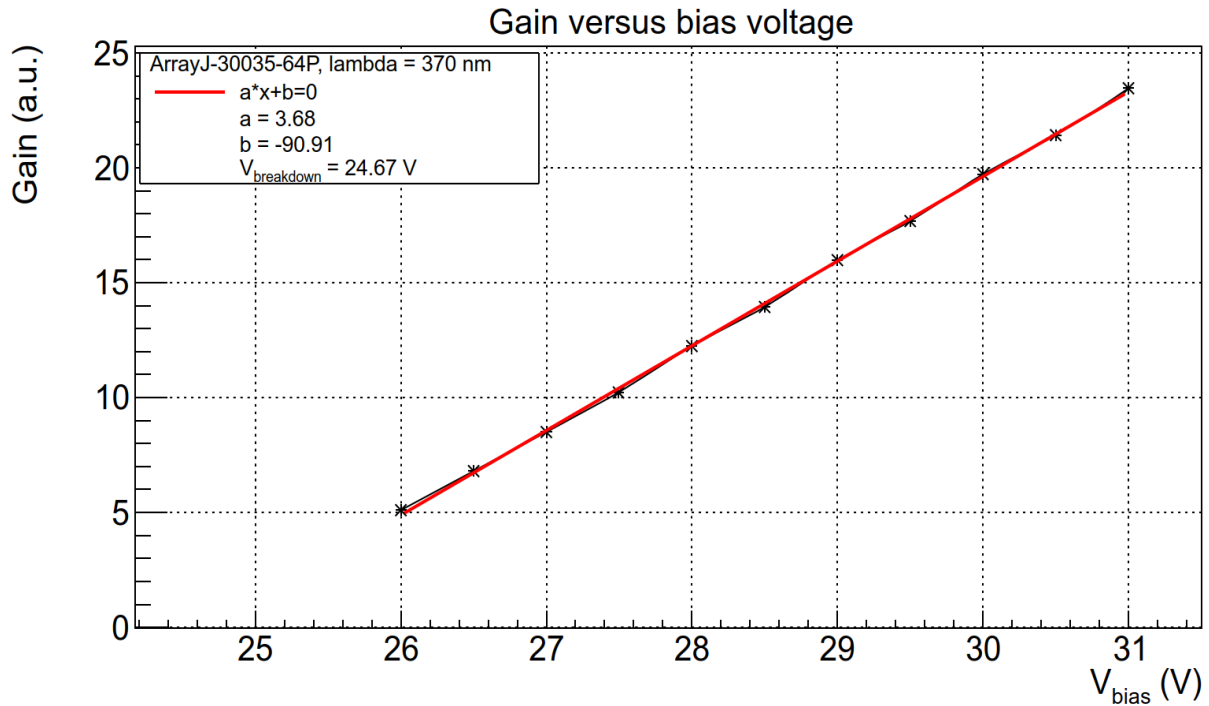


Figure 4.25 PDE before (blue curve) and after dark correction (red curve) for one pixel of the SiPM array J-30035-64P.



**Figure 4.26 Gain versus bias voltage for one pixel.**

#### 4.3.6.3 Results and discussion

The 3D mapping of the  $V_{BD}$ , the gain, the  $N_{pe}$  and the PDE are presented in figures 4.27-4.30. The relative difference between the highest and the lowest values of pixel for each parameter is calculated as shown in expression 4.7:

$$\frac{Max-Min}{Max} \times 100 \quad (4.7)$$

The pixel 1 (left upper corner on the map) was excluded from the measurement since it was found that it has been damaged. It should be noticed that there is no particular trend between the pixels in center and on the border. After analysis, the following values were found:

- Vbd difference : 0.7%
- Gain difference: 9.0 %
- $N_{pe}$  difference: 19.6 %
- PDE difference: 18.6 %

The pixel-to-pixel variation in the breakdown voltage is less than 1%. The gain distribution shows variations of less than 10%. These indicate that the SiPm Array J-30035-64P module has very good uniformity over its 64 pixels.

Concerning the  $N_{pe}$  and the PDE the fluctuations are larger. This values are acceptable taking into account that the majority of the difference comes from the important uncertainty in the positioning of the array when moving the nozzle in front of each pixel.

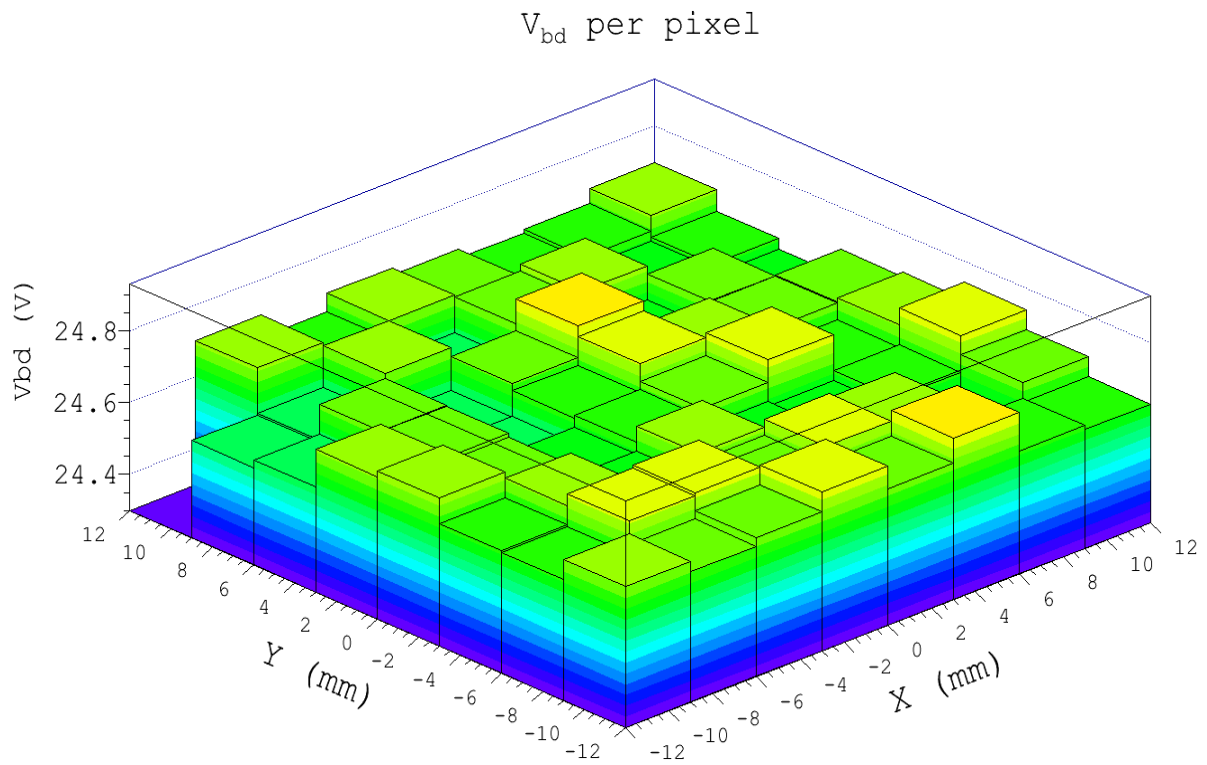


**Figure 4.27 Breakdown voltage distribution per pixel at 28.5 V.**

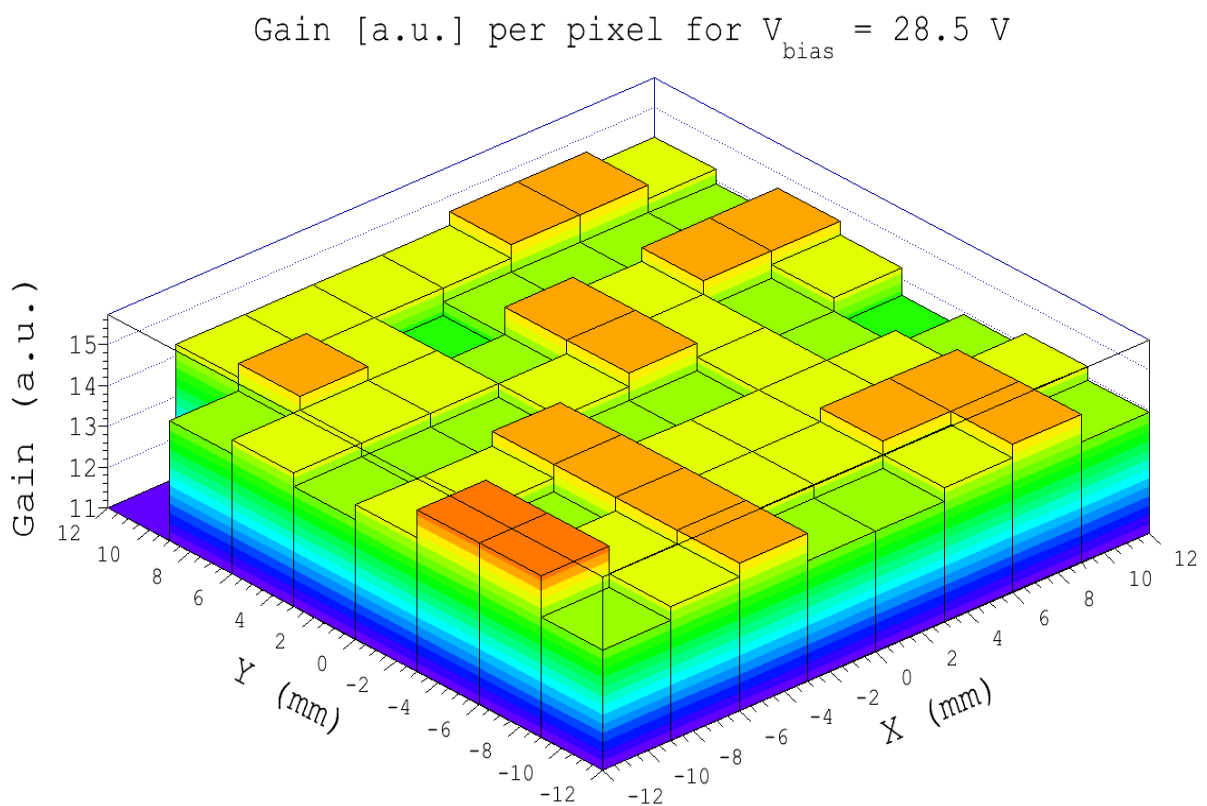


**Figure 4.28 Gain distribution per pixel at 28.5 V.**

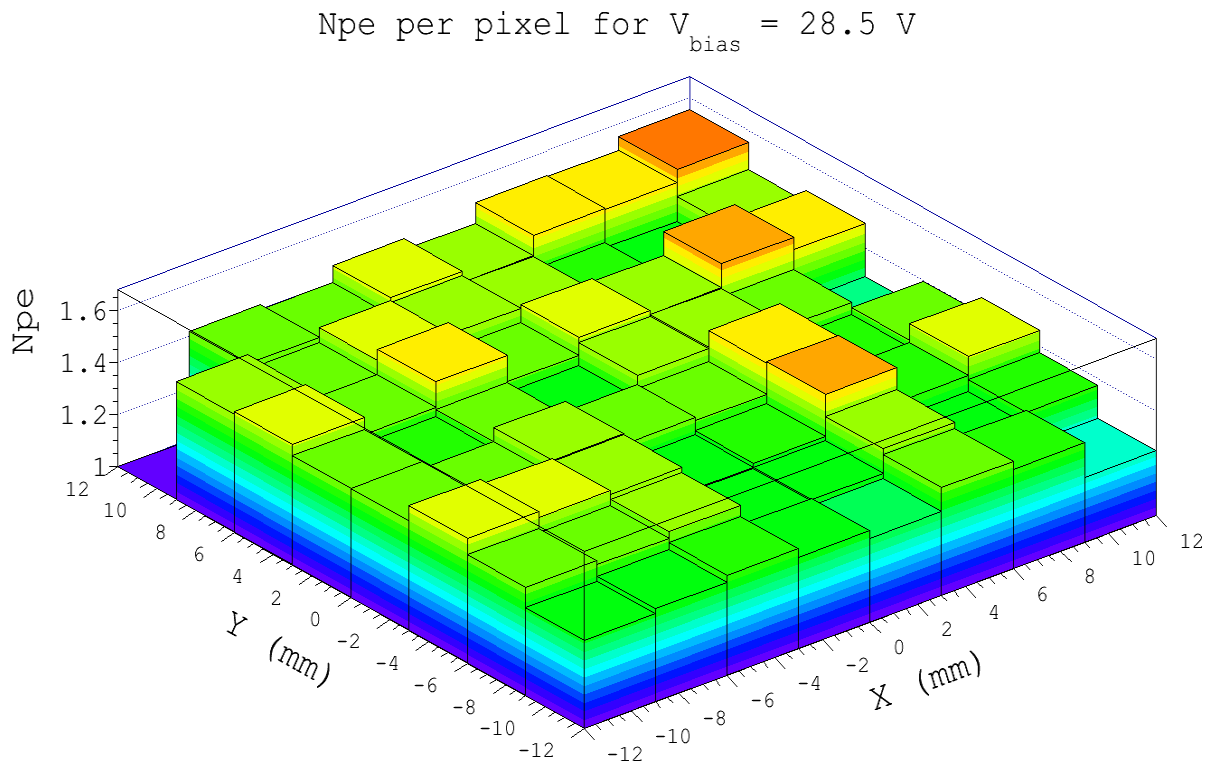


**Figure 4.29** Photoelectron number ( $N_{pe}$ ) distribution per pixel at 28.5 V.

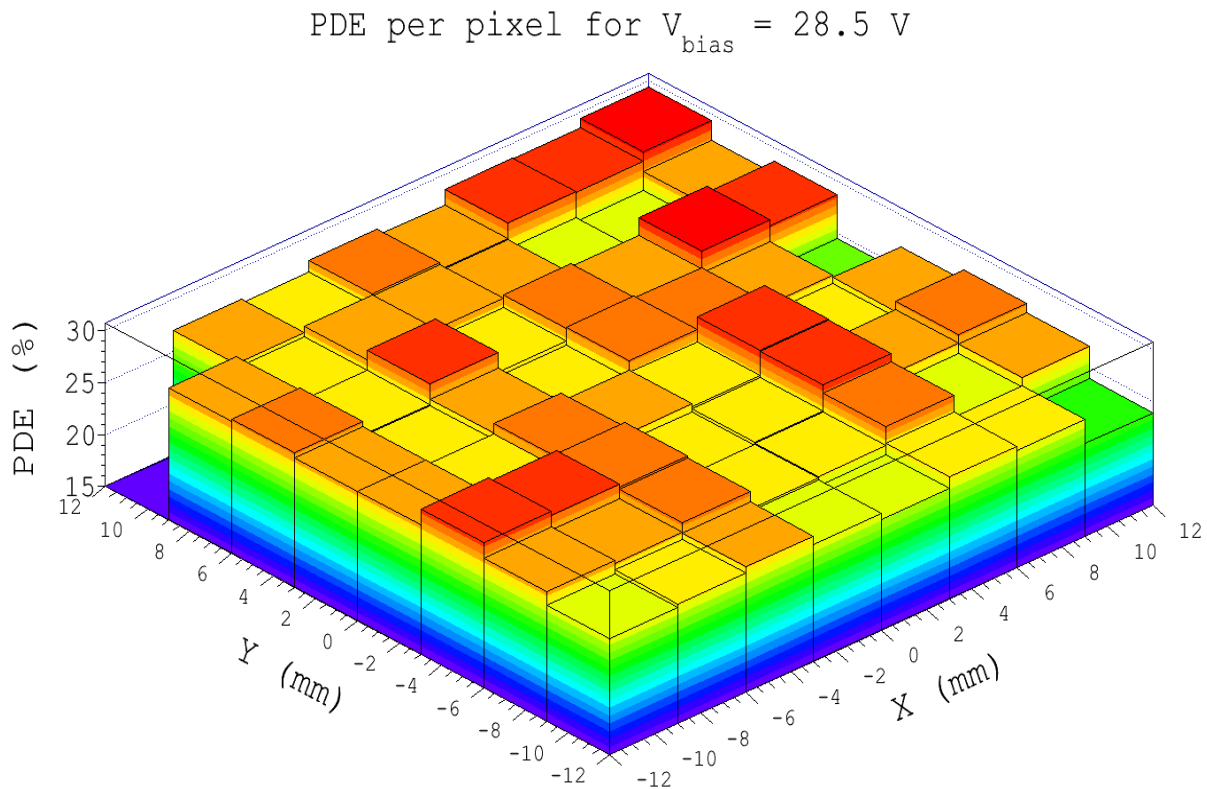


**Figure 4.30** Photodetection efficiency (PDE) distribution per pixel at 28.5 V.

---

## 4.4 Electronic probe prototype

This section discusses a set of measurements to evaluate the capability of a recent type of silicon photomultipliers, SiPM (ArrayJ-30035-64P-PCB from SensL) when coupled with a new scintillator, the CLYC to discriminate neutron signals from gamma events. The excellent performance of  $\gamma/n$  discrimination of the CLYC when coupled with the PMT has already been reported in the literature. Our goal was to reach similar performances with a large SiPM array. This point is challenging when dealing with a large SiPM array, since the total capacitance increases with the number of pixels. This effect leads to slow output signals where the gamma/neutron discrimination is not possible anymore. Therefore several tests were performed in collaboration with colleagues from the Department of Energy of the Polytechnic of Milan (POLIMI) to better understand the electronic parameters to apply to process properly the signal. Following the work started in Milan, a first electronic board was designed by Damiano Celeste and tested at CERN.

### 4.4.1 Characterization at PoliMI

Two outputs are available on SiPM: a standard and a fast output. The fast output is mainly characterized by a lower capacitance compared to the standard output. The first idea was to exploit the bipolar fast output of the SiPM array for PSD (integrating and extracting all information over the positive part) and the unipolar standard slow output for spectroscopy. However, the electronic will have been more difficult to design. A measurement campaign at POLIMI was organised from the 2nd to the 5th of May 2017, under the supervision of Prof. Alberto Fazzi and Prof. Vincenzo Varoli. During this week, we could deepen our knowledge of the electronic setup and understand the effects of all components in our electronic chain, in order to start finding a way to exploit the same output for both PSD and spectroscopy, by modifying the standard output via hardware. The following points were analysed:

- The influence of the load resistor on the standard output (STD output) on the fast output, and vice versa.
- The effect of the presence of the coil (balun transformer) in the fast output chain and the reason for the bipolarity of the fast output.
- The choice of the load resistor value on the STD output in order to have the best fast output shaping and timing.
- The attempt to make the STD output faster and make it follow the fast decay time component of the crystal.

The CLYC is coupled to the SensL ArrayJ-30035-64P-PCB through optical grease to match the refraction indexes and avoid total internal reflection. The SiPM array is connected to the breakout evaluation board ArraJ-BOB3-64P; a board was designed in order to sum up all contributions coming from each of the 64 elements of the SiPM into a single-channel output. The entire setup is enclosed inside a light-tight box with BNC panel connectors (Figure 4.31).

A positive reverse bias voltage of 28.5 V is applied to the *n-type* common cathode of the array, with an overvoltage of approximately 3.5 V (average breakdown voltage  $V_{BD} \approx 25$  V). The STD and fast output chains are extracted as shown in the schematic in Figure 4.32. The STD output is then read on a load resistor whose best value is fixed in the following measurements, while the fast output is obtained through an AC coupling (series capacitors) on the output and a balun transformer on the summed signal.



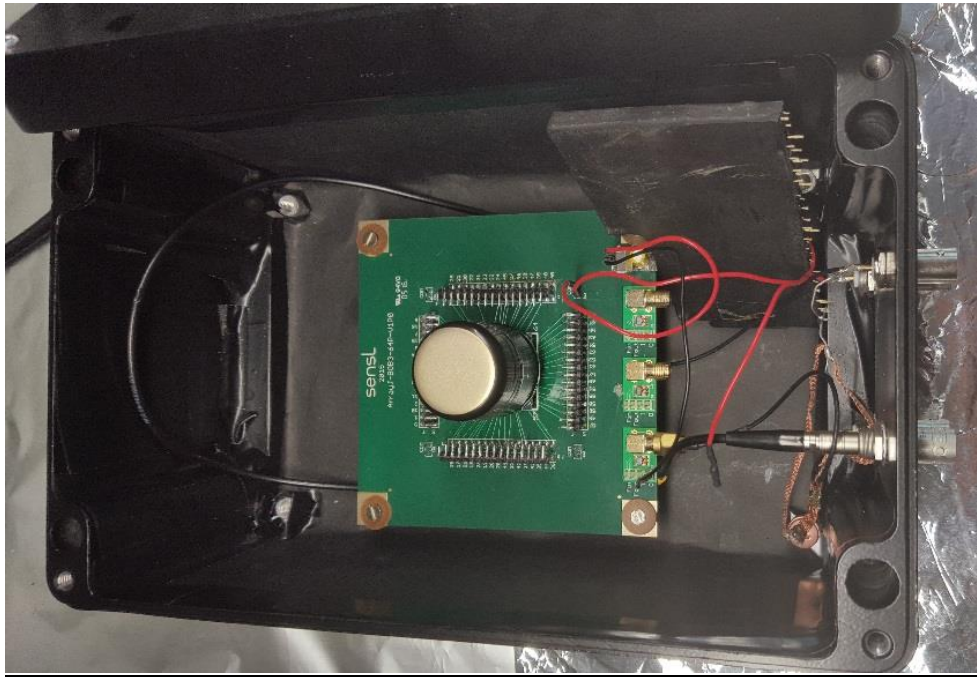


Figure 4.31 The measurement setup employed at POLIMI.

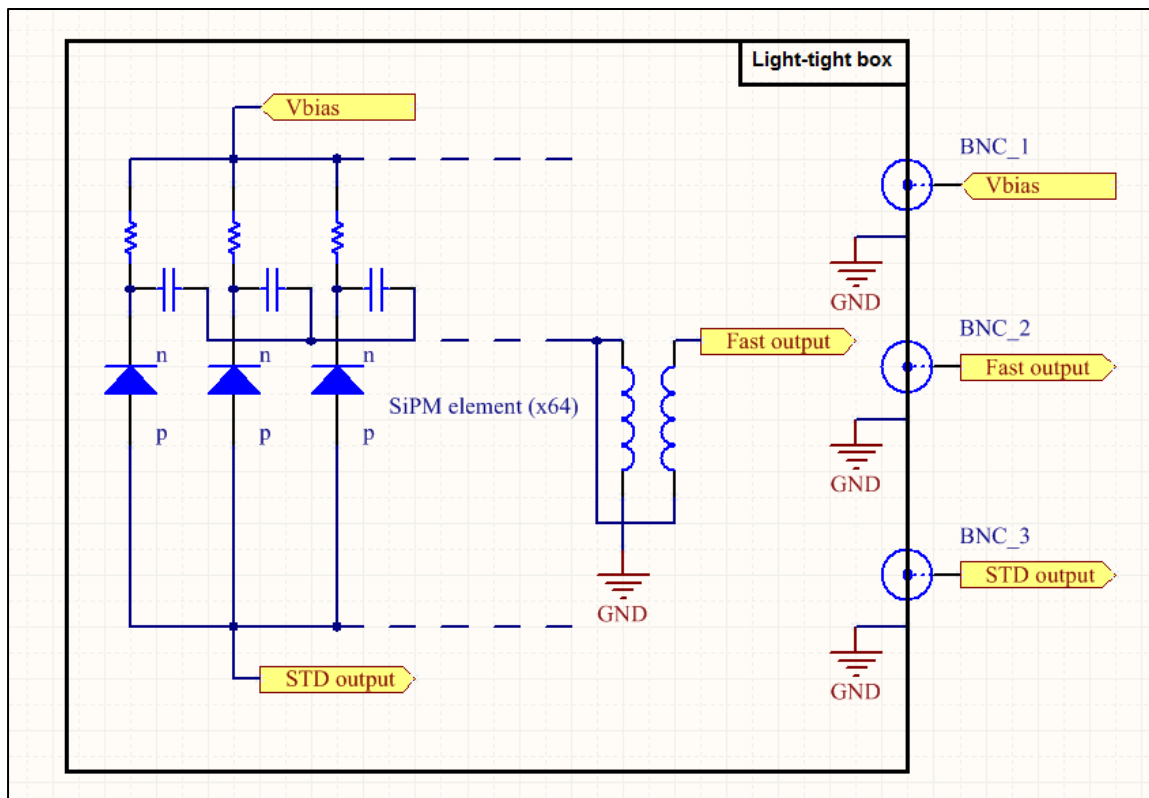


Figure 4.32 Schematic of the standard and fast outputs.

#### 4.4.1.1 Effects of load resistor on STD output

As a first test, the effect of the load resistor on the STD output was studied. A  $50\ \Omega$  load resistor (internal resistor of the oscilloscope) was fixed on the fast output and the signals were acquired with two different values of load resistors ( $R_{load}$ ) on the STD output,  $50\ \Omega$  and  $50/3\ \Omega$ .

Measurements were taken exploiting the 662 keV gamma from  $^{137}\text{Cs}$ . Figures 4.33 and 4.34 show both output signals in these two configurations (STD on Channel 1 and fast on Channel 2). As expected, when reducing the  $R_{\text{load}}$  value the STD output amplitude is reduced (from 230 mV to 180 mV) and the rising time is shortened (from  $\sim 2 \mu\text{s}$  to  $\sim 1 \mu\text{s}$ ). At the same time, the fast output features are modified as well, affected by the change of  $R_{\text{load}}$  on the STD output. Its amplitude increases from 24 mV to 31 mV while the rising time is reduced from  $\sim 500 \text{ ns}$  to  $\sim 200 \text{ ns}$ . It is clear from the signals shown in the pictures that the fast output is the result of a derivative operation on the STD output, due to the presence of the balun transformer.

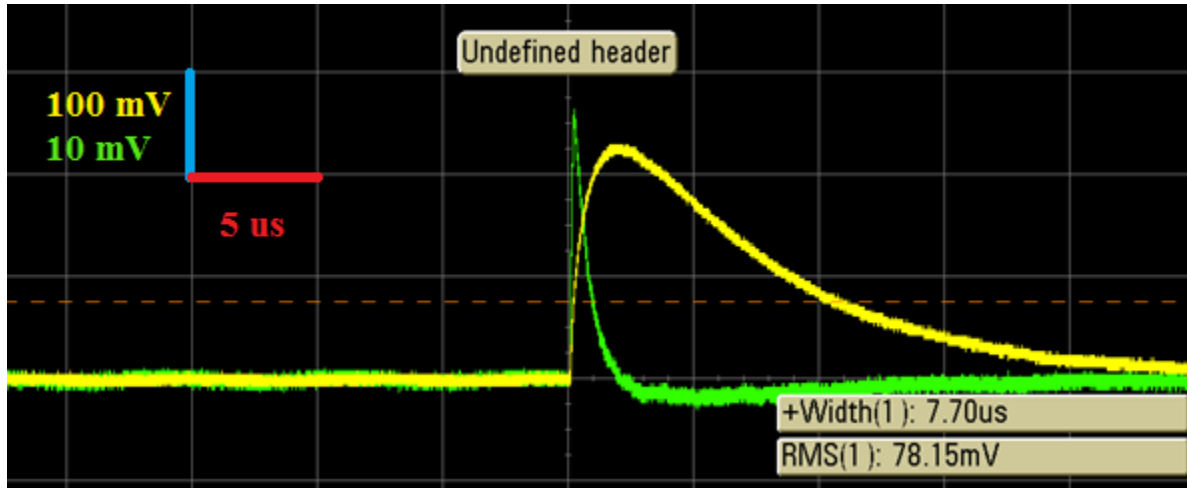


Figure 4.33 STD output (Ch. 1, yellow) with  $50 \Omega$  and fast output (Ch. 2, green) with  $50 \Omega$ .

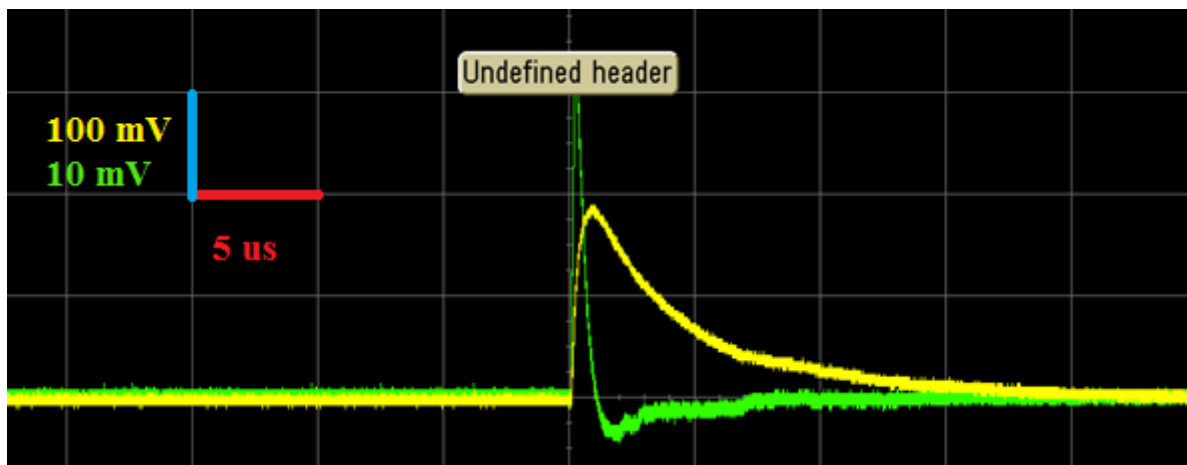


Figure 4.34 STD output (Ch. 1, yellow) with  $50/3 \Omega$  and fast output (Ch. 2, green) with  $50 \Omega$ .

The opposite test was performed, by changing the load resistor on the fast output and no effects were remarked on the STD one. We also checked if any differences were noticed on the STD output if the fast pins were connected or not and the results are shown in Figure 4.35. Except for a slight offset, no remarkable difference can be seen.

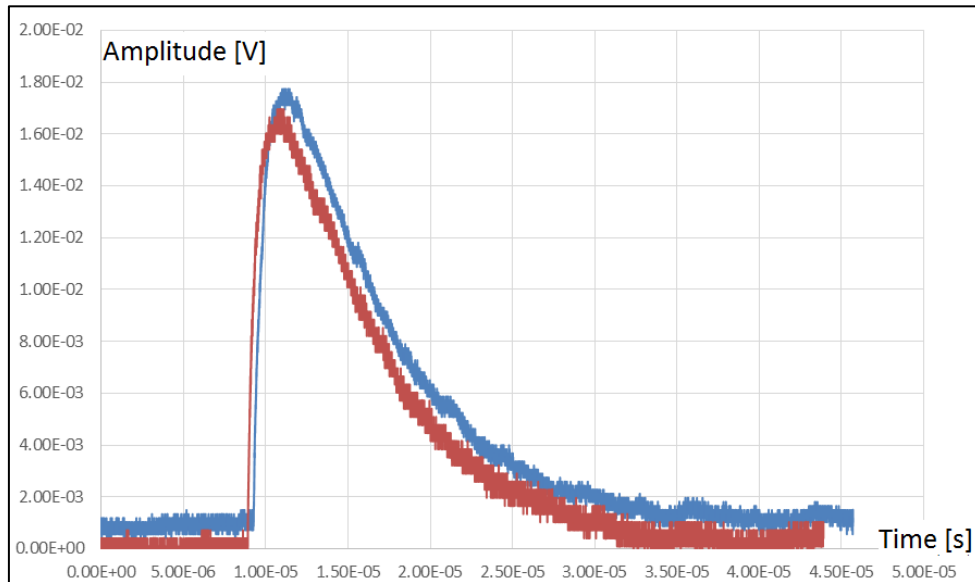


Figure 4.35 STD output with (blue) and without (red) connection of fast output.

#### 4.4.1.2 Effects of the balun transformer

To validate the previous conclusions concerning the effect of the balun transformer, the STD output was connected to the coil and the results are shown in Figure 4.36, for two different values of load resistor ( $50 \Omega$  and  $12.5 \Omega$ ). The presence of the coil makes the STD output bipolar and its rising time shorter. By reducing the load resistor the amplitude is reduced and the time needed to come back to the baseline is longer.

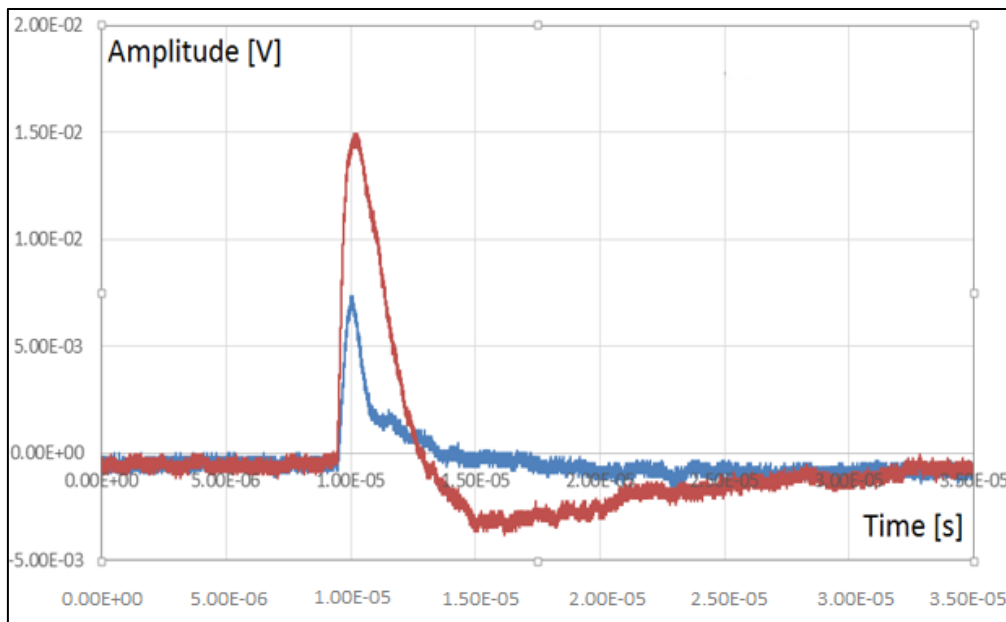


Figure 4.36 STD output connected to balun transformer with  $R_{load}=50 \Omega$  (red) and  $R_{load}=12.5 \Omega$ .

#### 4.3.1.3 Effects of the load resistor

To obtain the best STD output in terms of timing and shape, some tests were performed by changing the value of the load resistor. Three different values were tested,  $50 \Omega$ ,  $10 \Omega$  and  $3.6 \Omega$ . With the smallest value we were not able to see the  $^{137}\text{Cs}$  source peak and the s/n ratio significantly decreases so it was excluded from our analysis. With a  $50 \Omega$  resistor the STD output time-to-peak is  $2 \mu\text{s}$  and it comes back

to baseline in 30  $\mu\text{s}$ , while with a 10  $\Omega$  resistor the time-to-peak decreases to 700 ns and it comes back to baseline in less than 20  $\mu\text{s}$ . In this second case, the amplitude of the signal is lower ( $V_{\text{signal}}=R_{\text{load}}*I_{\text{SiPM}}$ ) but this does not prevent us from clearly distinguishing the  $^{137}\text{Cs}$  peak from the noise. The 10  $\Omega$  load resistor was chosen for future developments.

#### 4.4.1.4 Pole-zero cancellation

This study aimed to find a way to exploit the STD output for neutron/gamma PSD instead of the fast output. In this way all information (spectroscopy and  $\gamma/n$  discrimination) can be extracted from the same output, considerably simplifying the electronic design of the probe. To achieve this goal, we had to speed up the STD signal by trying to extract the fastest scintillation decay time constants from the crystal (tens of nanoseconds) and shorten the falling time of the signal without cutting the crystal response. The timing features of the STD signal result from folding the crystal response with the response of the electronics (SiPM and signal processing). First of all we studied the response of a single  $3\times 3\text{ mm}^2$  element of the array (Figure 4.37) on  $R_{\text{load}}=10\ \Omega$ , connected to a large bandwidth trans-impedance amplifier (calculated gain = 9.9). The rising time of a single APD avalanche is approximately 30 ns with an amplitude of 1 mV (two APDs were fired in the example) and a very particular after pulse effect can be noticed after 50 ns. From this test, we understood that the single SiPM element is not a limitation to achieve our goal and that the whole array with all 64 connected pixels is the cause of the slow signal timing, because of its total capacitance ( $C_{\text{tot}} \approx 64\ \text{nF}$ ).

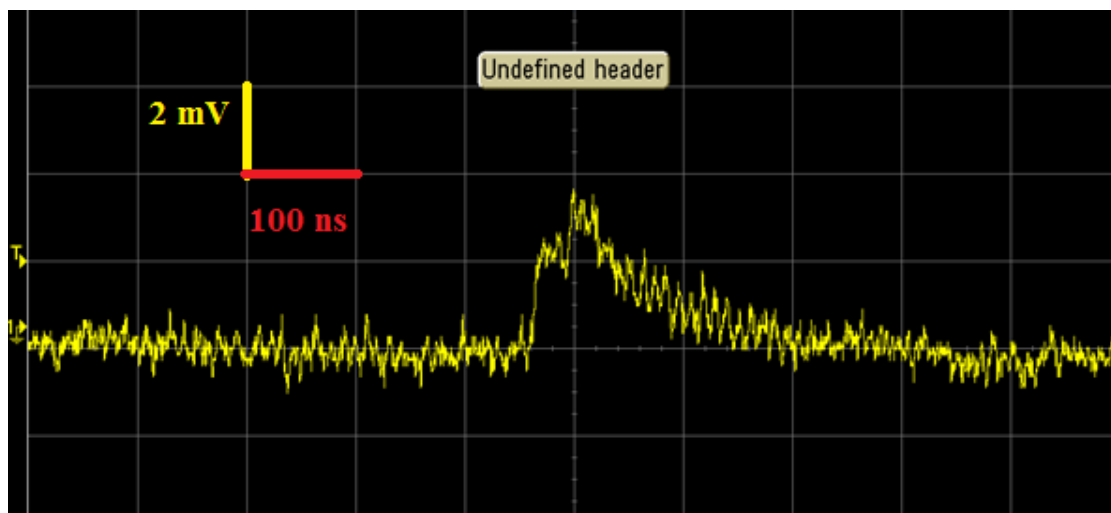


**Figure 4.37** Signal from single APD avalanche in the SiPM array.

To study the response of the whole electronic chain we decided to exploit a  $1''\times 1''$   $\text{LaBr}_3$  scintillating crystal (St. Gobain) and a plastic scintillator (EJ-404): these scintillators have one of the fastest possible decay times amongst inorganic and organic scintillators, respectively, so that they approximate well the theoretical  $\delta(t)$  pulse. In this case the folding between the two effects is dominated by the electronics. Thanks to these fast scintillators, the response of the electronics on the signal can be extracted and adjusted to obtain the final response of the CLYC coupled with the SiPM. Figure 4.38 shows the  $^{137}\text{Cs}$  signal obtained with the  $\text{LaBr}_3$  crystal ( $\tau_{\text{decay}}=16\ \text{ns}$ ) coupled to the SiPM array, with  $R_{\text{load}}=3.6\ \Omega$  and Gain=9.9. The rising time is around 100 ns and the falling time 500 ns.

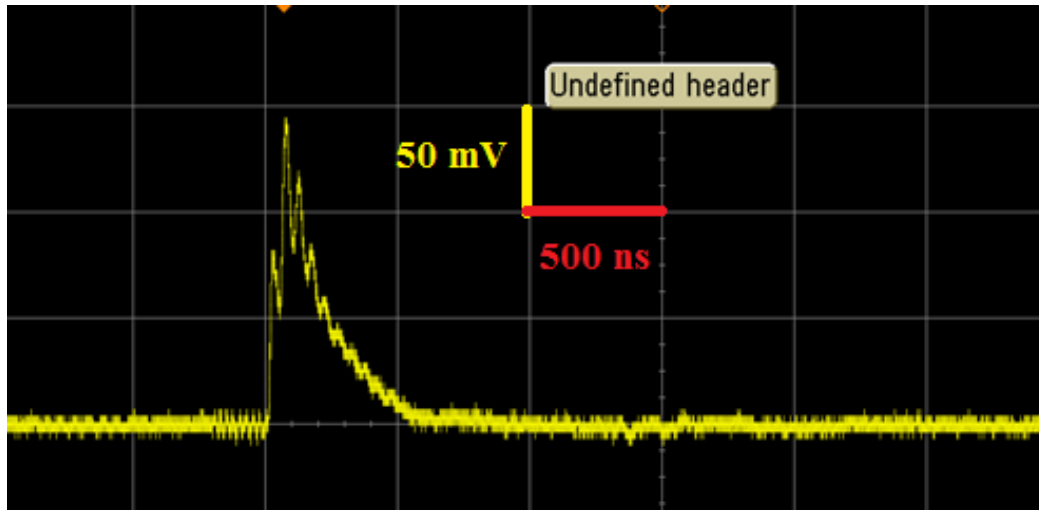


**Figure 4.38**  $^{137}\text{Cs}$  signal from  $\text{LaBr}_3$  coupled with the SiPM array with  $R_{\text{load}}=3.6 \Omega$  and Gain = 9.9.

It was decided to proceed implementing a pole-zero cancellation method (see schematic B.1 in Appendix B) to compensate for the pole introduced by the high capacitance of the detector, with a simple RC circuit in series after the amplification. In the following different tests are presented for three different time constants RC (1000 ns, 930 ns and 500 ns). The signal undershoots in the first two cases (Figures 4.39a and 4.39b) are due to an over compensation of the electronic response so that the component due to the light coming from the crystal gives a negative contribution. The optimum is found with  $R=3.3 \text{ k}\Omega$  and  $C=150 \text{ pF}$  as shown in Figure 4.39c, where the electronic response is correctly compensated with no influence on the polarity of the signal. With respect to the original signal, the rising time is reduced to  $\sim 50 \text{ ns}$  and the falling time to 400 ns. With this compensation it is possible to better approximate the decay time of the light coming from the crystal.

To validate the choice of the compensation, the same test was performed with the EJ-404 ( $\tau_{\text{decay}}=1.7 \text{ ns}$ ) and a  $^{241}\text{Am}$  source. The final response of the system ( $R_{\text{load}}=10 \Omega$ , Gain=9.9) is shown in Figure 4.40. The oscillation that can be seen after 400 ns is due to a signal reflection: the impedance matching of the electronic chain has not been optimized and it causes this kind of effect, which can be noticed in case of such short signals ( $<200 \text{ ns}$ ). With the EJ-404 plastic scintillator the resulting output after compensation has a rising time  $<50 \text{ ns}$  (which should correspond to the response of the SiPM APDs avalanches) and a falling time  $<100 \text{ ns}$ .

Following the previous tests, the pole-zero compensation network was dimensioned as explained above ( $R \cdot C = 3.3 \text{ k}\Omega \cdot 150 \text{ pF} \approx 500 \text{ ns}$ ), ensuring that only the electronic component is cancelled.

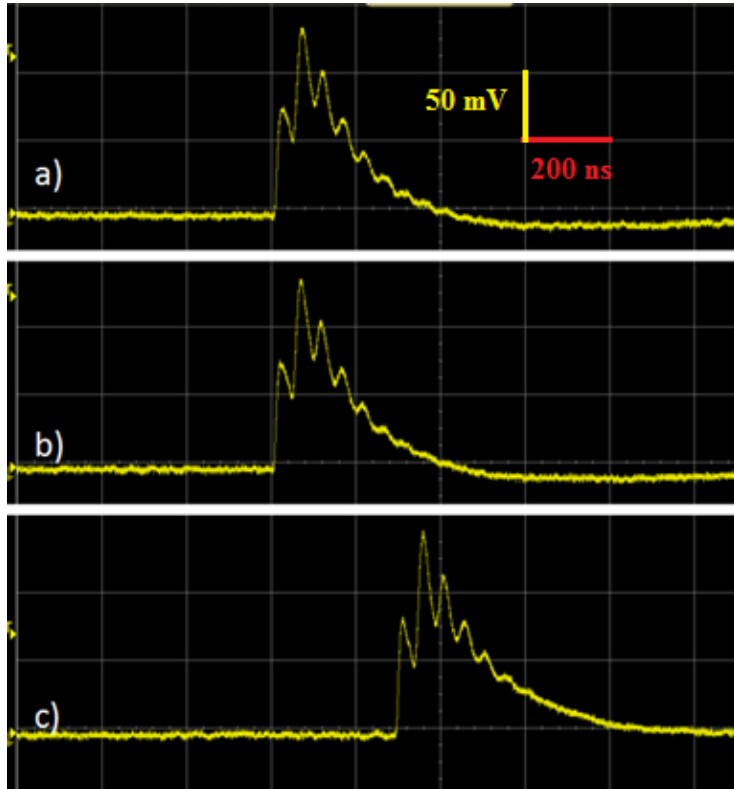


Figure 4.39  $^{137}\text{Cs}$  signal from  $\text{LaBr}_3$  coupled with the SiPM array with  $R_{\text{load}}=3.6 \Omega$  and Gain = 9.9, with pole-zero compensation with  $RC=1 \mu\text{s}$  (a), 930 ns (b) and 500 ns (c).

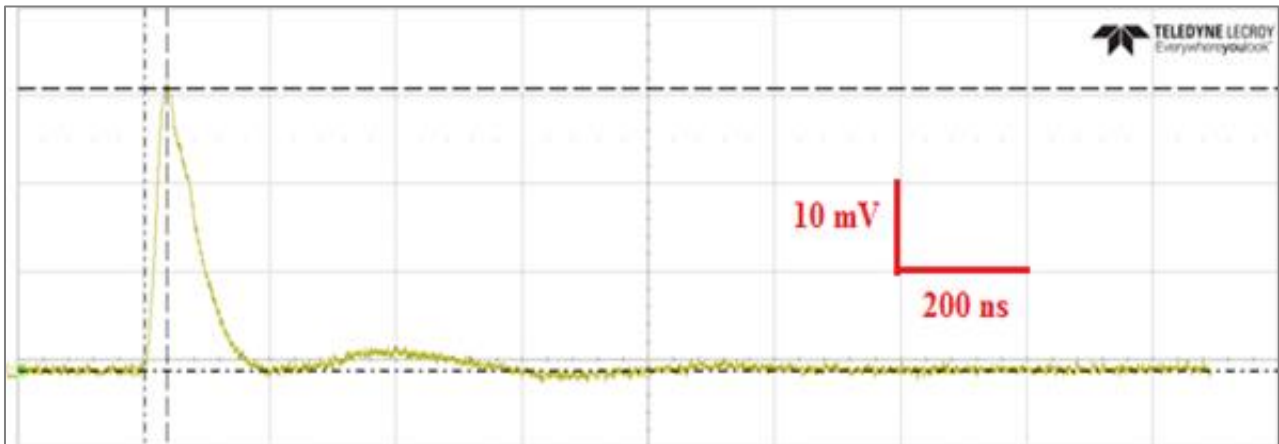
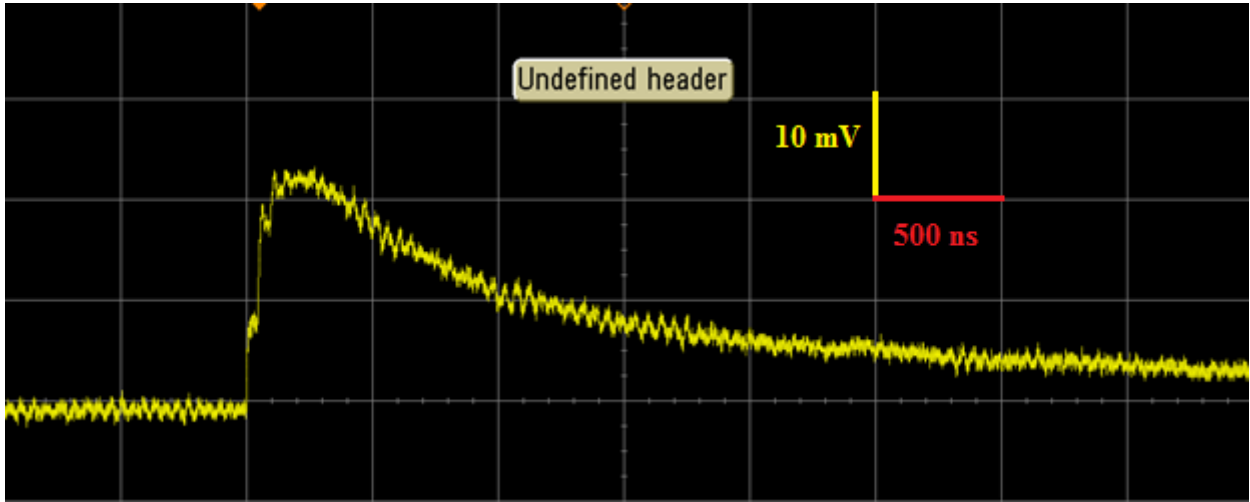


Figure 4.40  $^{241}\text{Am}$  signal from the EJ-404 coupled with the SiPM array with  $R_{\text{load}}=10 \Omega$ , Gain = 9.9 and pole zero compensation at 500 ns.

Concerning the CLYC scintillator, the STD output without any compensation is shown in Figure 4.34 and the resulting output after pole-zero compensation is shown in Figure 4.41. The time-to-peak is shortened from 700 ns to 100 ns and the signal length is now 6  $\mu\text{s}$  instead of 20  $\mu\text{s}$ . With these new timing features we are able to extract and highlight the different scintillation decay times for gammas and neutrons and perform the PSD exploiting the STD output.



**Figure 4.41**  $^{137}\text{Cs}$  signal from CLYC coupled with the SiPM array with  $R_{\text{load}}=10\ \Omega$ , Gain = 9.9 and p-z compensation at 500 ns.

The following conclusions can be drawn from the tests performed at POLIMI:

- The best value for  $R_{\text{load}} = 10\ \Omega$  was found taking into account the signal-to-noise ratio, the amplitude and the timing features of the signal, in order to obtain the fastest possible signal while keeping the energy threshold just above 600 keV.
- The role of the coil (balun transformer) present on the fast output was analysed, explaining the bipolar and faster shape of the signal. The fast output appears as a derivate of the STD output.
- It is now clear that the fast output does not influence the STD output, if it is connected or not and if it has different  $R_{\text{load}}$  values. On the contrary, the  $R_{\text{load}}$  on the STD output affects the shape of the fast output, so it is always recommended to use the two signals independently.
- The folding between the scintillation decay times and the slow electronics response due to the high capacitance of the SiPM array is the reason why the timing features of the STD output are not suitable for PSD. The pole-zero cancellation method was employed to compensate for the pole introduced by the electronics and speed up the signal. Through different tests with  $\text{LaBr}_3$ , EJ-404 and CLYC, an R parallel to C circuit was added in series and dimensioned with parameters  $R=3.3\ \text{k}\Omega$  and  $C=150\ \text{pF}$  ( $\sim 500\ \text{ns}$ ). This compensation let us employ the STD output for n/ $\gamma$  PSD.

#### 4.4.2 Electronic design

In the framework of the development of a portable neutron probe and following the work started at POLIMI, a first electronic board was designed and tested at CERN for n/ $\gamma$  discrimination based on pulse shape discrimination (PSD) for neutron counting and spectroscopy based on the standard output.

##### 4.3.2.1 Design of the PCB

For the sake of user-friendliness, we decided to design a compact PCB for laboratory tests. This idea came up to avoid using noisy power supplies for SiPM arrays and operational amplifiers (OpAmps) and



---

to allow the remote control of some crucial parameters such as bias voltage, output current and temperature. Last but not least, we could free the operator from using heavy NIM modules and crates for signal processing. We developed this board starting from a compact power supply module designed by Nuclear Instruments (NI) [14], able to supply a bias voltage in the range between 20 V and 85 V starting from the 5 V of the USB connector. This power module is provided with a control software, called Zeus, whose main features are described in section 3.2.3.2.2.

In order to have a multipurpose system, which can be used by different operators with different crystals and SiPMs, we designed a circuitry divided into two main boards. Figure B.2 and B.3 in appendix B show the schematics of the signal processing board and the SiPM array board, respectively, which are connected through a 10-pins header connector. This solution was studied to allow future operators to design new SiPM boards for different SiPM models, always keeping the same signal processing board. Moreover, the choice of large bandwidth and fast timing OpAmps such as the TI AD8000 [15] will also allow testing different scintillating crystals with much faster decay time constants with respect to CLYC. Concerning our case, the ArrayJ-30035-64P-PCB from SensL is connected through its pair of 80-way board-to-board connectors from Hirose (DF17(3.0)-20DS-0.5V(57)); the fast and STD outputs are connected in parallel to sum up the contributions from all of the 64 elements (anode, p-region). The fast output then passes through the balun transformer RFXF9503 [16]. We chose to adopt the same balun coupling as on the SensL evaluation board ArrayJ-BOB3-64P, in order to have, as much as possible, similar conditions to our first test board. Both signals are sent to the signal processing board through the header connector. At the same time, the positive reverse bias voltage generated by the power module is sent to the COM pins (cathode, n-substrate) of the SiPM through the header connector. Finally, the temperature sensor TI TMP37 [17], fed by 4.5 V coming from the signal processing board, is also located on this board, right close to the photodetector. The information is sent to the SiPM power module, able to adjust the bias voltage as a function of the temperature. This allows the operator to keep stable the gain of the photomultiplier through the software.

The signal processing board can be divided into two main sections: the power supply system and the signal processing system.

The first part consists of the SiPM power module by NI, the LTM8045 [18] power inverter and the LP5907 [19] and LT3090 [20] voltage regulators. The SiPM power module was specially modified to let the USB 5 V pass to our board as well and to exploit this power supply to feed our OpAmps. Given the usual noise on the USB 5 V, we needed to clean up, invert and regulate this power supply to a lower level ( $\pm 4.5$  V) which is still acceptable for the AD8000. To do that, we obtained +4.5 V thanks to a simple positive linear regulator LP5907(4.5) fed with 5 V and we obtained -4.5 V by inverting the voltage through the LTM8045 and regulating the voltage with a LT3090. This system gives us a stable and reliable  $\pm 4.5$  V power supply for the OpAmps.

The signal processing section receives the fast and the STD signals from the SiPM board. With the first jumper it is possible to select the signal we want to process, which passes through a 10  $\Omega$  load resistor, on the non-inverting input of the first AD8000. This first stage is a simple non-inverting amplification, with gain  $G=41$  (where  $G=1+R_g/R_{pot}$ ). The values of  $R_g$  and  $R_{pot}$  (gain resistors) were chosen taking into account the dynamic range of the AD8000 (approximately 0-3.5 V) and the energy range we are interested in (0.6-10 MeV). The amplifier output is then sent to a R/C ( $R=1.65$  k $\Omega$ ,  $C=580$  pF) network to actuate a pole-zero cancellation and make the signal faster by suppressing the slow electronic contribution due to the high capacitance of the photodetector. These values have been adjusted in order to avoid reducing considerably the signal amplitude (the lower the capacitance the lower the amplitude of the signal) and to avoid having a bipolar signal due to high compensation (the lower the resistor the higher the compensation). Then, for the same RC product, different combinations can be used and a compromise has to be found in order to maximise the signal-to-noise ratio. A 100  $\Omega$  resistor was added on the amplifier output in order to reduce the noise fluctuation. Given the fast timing features of this modified signal ( $\sim 10^2$  ns rising time), a shaping stage is needed to send the signal to the pocket MCA



---

Amptek 8000D, which accepts signals above 0.5-1  $\mu$ s as rising time. This shaping network is characterised by a complex-conjugate poles pair, whose shaping time is 1  $\mu$ s. For system stability, it is essential that the values of C1, C2 and C3 are the same.

Every stage of this circuit can be read out through a Lemo connector and the operator can decide to isolate each output from the section downstream thanks to the jumper network.

The current needed to supply all components on the boards (in particular SiPM array, 2xAD8000, SiPM power module) is around 200 mA, which does not exceed the power limit of USB ports and cables. In case of failure, the board is provided with an external power supply connector. In this case, the operator should be careful to disconnect the jumper J1, in order to avoid any shortcut between the USB power supply and the external generator.

The following section describes the set up and the different measurements performed to test each part of the PCB.

#### ***4.4.2.2 Description of the set up for PCB testing***

The CLYC crystal is coupled to the SensL ArrayJ-30035-64P-PCB through optical grease to match the refraction indexes and avoid internal reflections. The SiPM array is connected to a SiPM board that was designed in order to sum up all contributions coming from each of the 64 elements and to end on a single-channel output. The SiPM board is then connected to the signal processing board where the signal follows different steps:

- raw signal from the STD output read on 10  $\Omega$  load resistor.
- amplification with a gain of 41, ( $R_{pot} = 50 \Omega$  ;  $R_9 = 2 k\Omega$  )
- pole zero cancellation with RC of 957 ns ( $R_{23} = 1.65 k\Omega$  ;  $C_{25} = 580 pF$ )
- shaping time of 1  $\mu$ s ( $C_1 = C_2 = C_3 = 14.7 nF$ )

Each element of the chain can be connected through jumpers or read independently from the 4 outputs present in the board (Figure 4.42).

A positive reverse bias voltage of 28.5 V is applied to the *n-type* common cathode of the array, through the SiPM power module from NI fed by the 5 V of the USB cable. A software (Zeus), allows to set up the bias voltage and access different parameters such as the current. The correction of the bias voltage as a function of the temperature is also possible. A  $^{137}\text{Cs}$  source was used to test the performance of the board. All this setup is enclosed inside a light-tight box with BNC panel connectors (Figure 4.43). The signals from the CLYC coupled with the SiPM were sent to an oscilloscope (Tektronix TDS 2024C, 200 MHz, 2Gs/s) and the waveforms continuously saved.

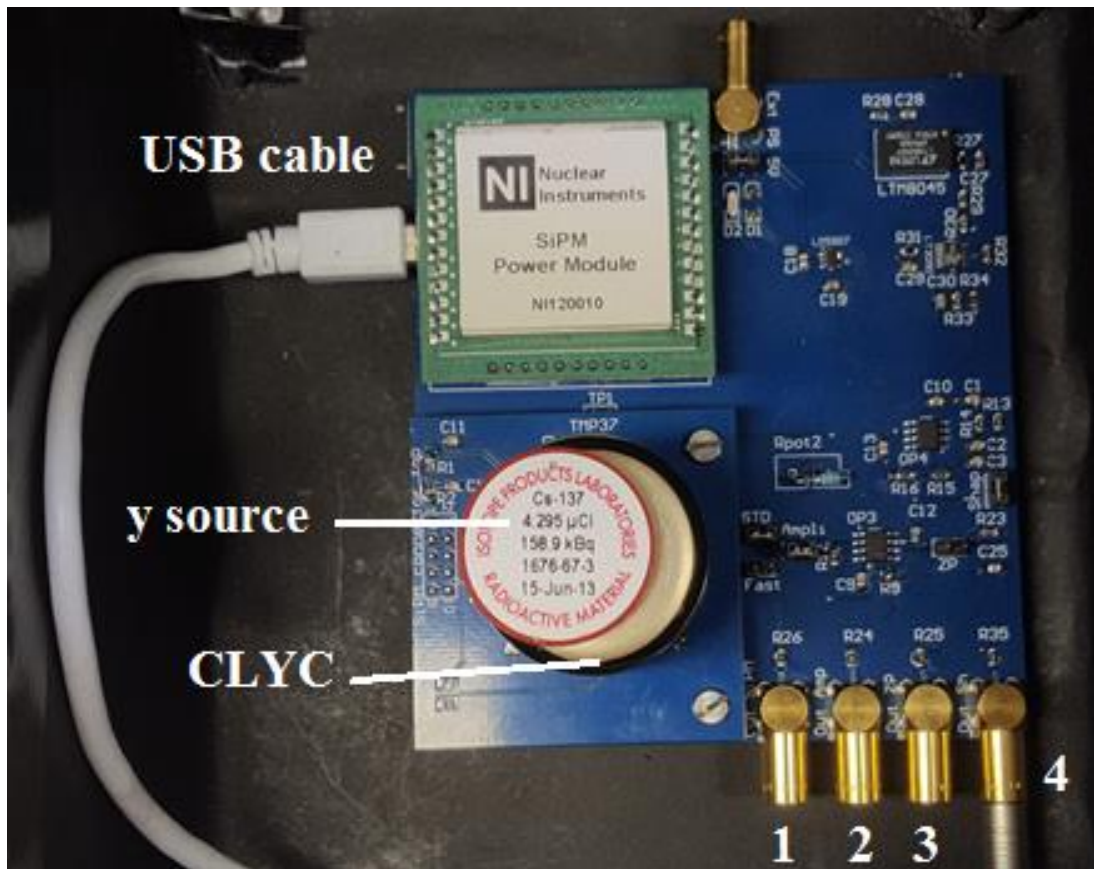


Figure 4.42 The CLYC coupled with the SiPM and the electronic board. 1, 2, 3 and 4 are the SiPM, the amplifier, the pole zero and the shaper outputs, respectively.

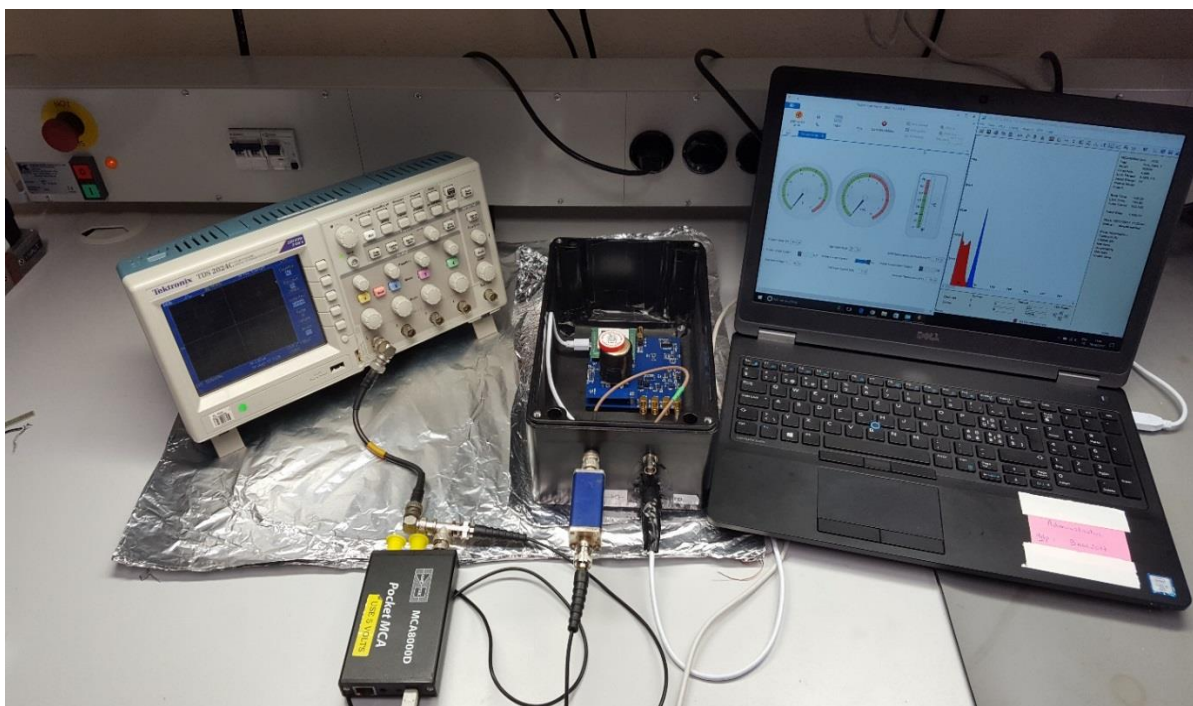


Figure 4.43 Measurement setup.

### 4.3.2.3 Test measurement of the PCB

- STD output

Three jumpers were connected: one to feed the signal processing board with the 5 V from the USB, one to select the STD output and the last one to connect the STD output to the amplifier. The signal was sent from the channel 1 (Figure 4.42) to the oscilloscope (1 M $\Omega$  resistor, AC coupling). The aim was to see the voltage drop on the 10  $\Omega$  load resistor (signal that enters the amplifier) so no additional resistors were placed.

Figure 4.44 shows the  $^{137}\text{Cs}$  662 keV signal from the STD output. The STD output amplitude is 8 mV and the rising time is around 700 ns. The signal length is approximately 12  $\mu\text{s}$ .

- Amplification output

The gain of the amplifier is given by the ratio between  $R_{pot}$  and  $R_9$ . A very noisy signal was collected when setting the potentiometer to a low value (around 20  $\Omega$ ). For the test it was decided to replace the potentiometer with a 50  $\Omega$  resistor. After testing different configurations, the value of  $R_9$  was increased to 2 k $\Omega$  in order to have a final gain of 41. This value allows a sufficient amplification without saturating the amplifier within the range (0.5 -10 MeV). The signal was then sent from channel 2 to the oscilloscope with a 50  $\Omega$  termination and a 50  $\Omega$  for impedance matching.

Figure 4.45 shows the signal from the amplifier output. As expected, the length and the rising time of the signal are similar to the STD output signal (12  $\mu\text{s}$  and 700 ns). The signal amplitude of 150 mV corresponds to the gain applied ( $41 * 8 \text{ mV} / 2$ ).

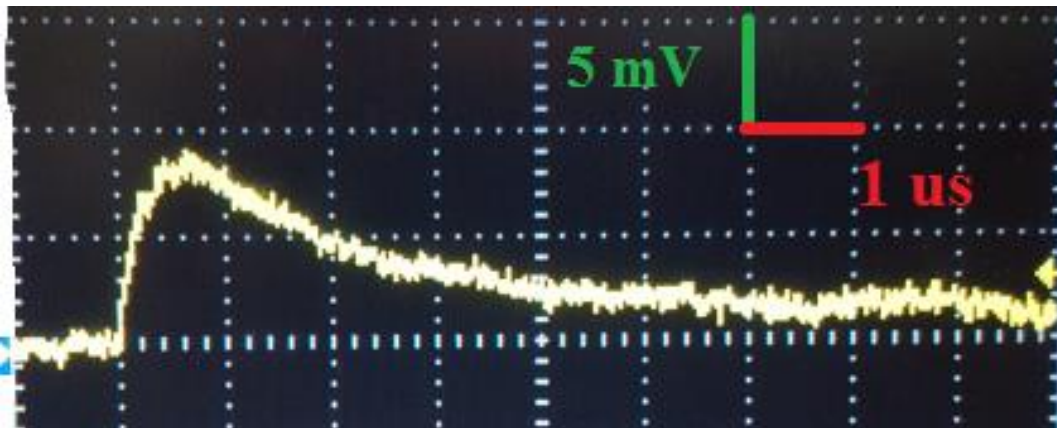


Figure 4.44 : Picture of the STD output with 10  $\Omega$ .

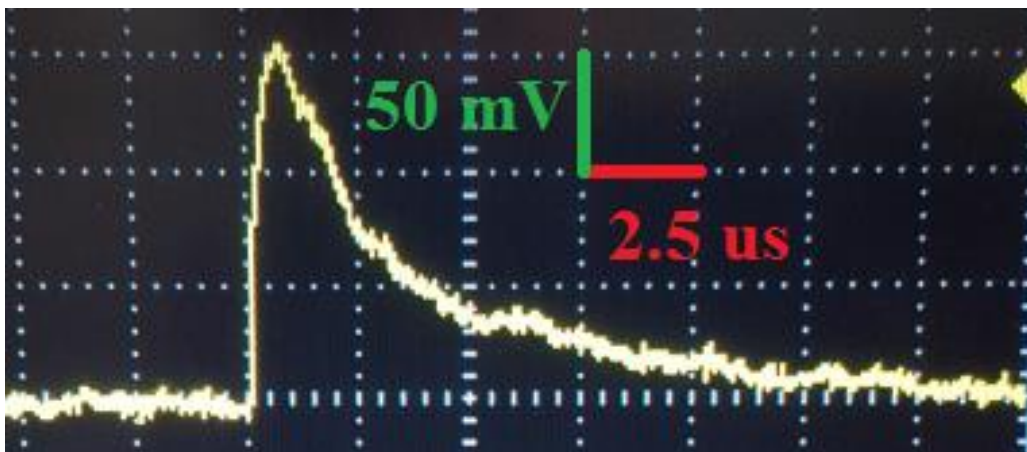


Figure 4.45 Amplifier output with 50  $\Omega$  termination.



- Zero-pole cancellation output

Several tests were conducted to find the proper RC circuit to be integrated on the board. A first value of 500 ns (similar to the RC found at Polimi) was tested but the signal presented too many oscillations. It was decided to increase the capacitance to reduce the sensitivity of the set-up to small charge variations. A final RC value of 957 ns ( $R_{23} = 1.65 \text{ k}\Omega$ ;  $C_{25} = 580 \text{ pF}$ ) was found to give a sufficient compensation without too large oscillations on the signal. The output resistor of the amplifier was fixed at  $100 \Omega$  to reduce noise fluctuation. The signal was then sent from channel 3 to the oscilloscope with a  $50 \Omega$  termination, without any impedance matching resistors.

Figures 4.46 and 4.47 show the output signal from the pole zero cancellation. As expected, the amplitude is lowered by the capacitance effect (15 mV). However the time-to-peak is shortened from 700 ns to 100 ns and the signal length is now  $7 \mu\text{s}$  instead of  $12 \mu\text{s}$ .

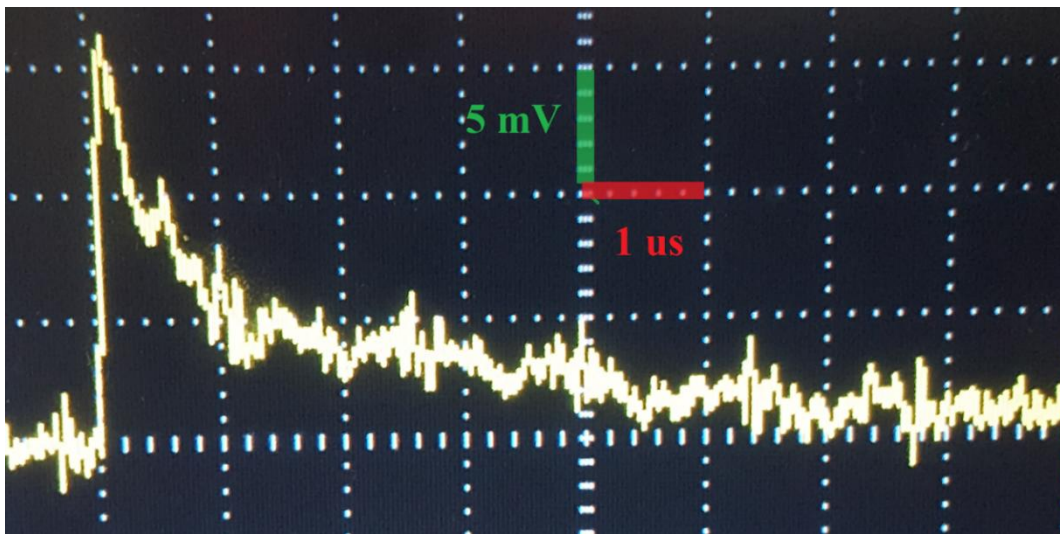


Figure 4.46 Pole zero output with  $50 \Omega$  termination.

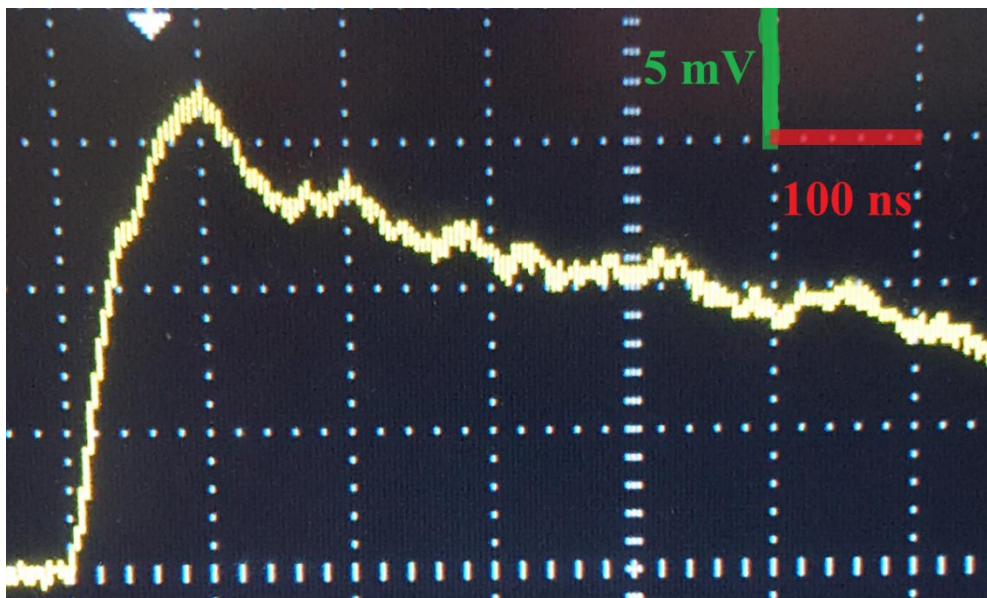


Figure 4.47 Zoom of pole zero output with  $50 \Omega$  termination.

The STD output without any compensation is shown in Figure 4.48 together with the resulting output after pole-zero compensation with  $R=3.67 \text{ k}\Omega$  (a potentiometer was used) and  $C=150 \text{ pF}$  ( $\sim 550 \text{ ns}$ ). The time-to-peak is shortened from 700 ns to 100 ns and the signal length is now  $6 \mu\text{s}$

instead of 20  $\mu\text{s}$ . Both signals were taken with the 10  $\Omega$  load resistance and under  $^{137}\text{Cs}$  irradiation source.

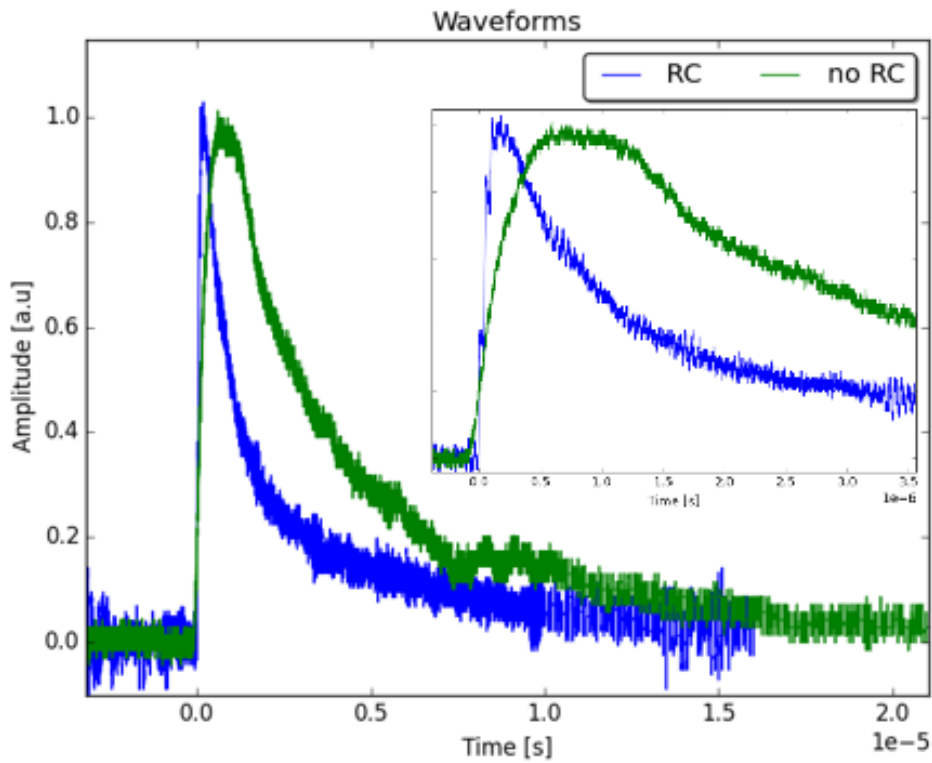


Figure 4.48 Waveform from CLYC coupled with SiPM before (green) and after (blue) pole zero cancellation.

- Shaper output

The last step of the electronic board consists of shaping the signal to feed the MCA. The output resistance ( $R_{35}$ ) was set to 100  $\Omega$  to reduce the noise on the signal. In addition a capacitance of 100  $\mu\text{F}$  was placed in series to remove the signal offset. The signal was then sent from channel 4 to the oscilloscope without a 50  $\Omega$  termination. Figure 4.49 shows the signal from the shaper output. The length of the signal is about 20  $\mu\text{s}$ . The time to peak is 2.5  $\mu\text{s}$  and its amplitude is 8 mV.

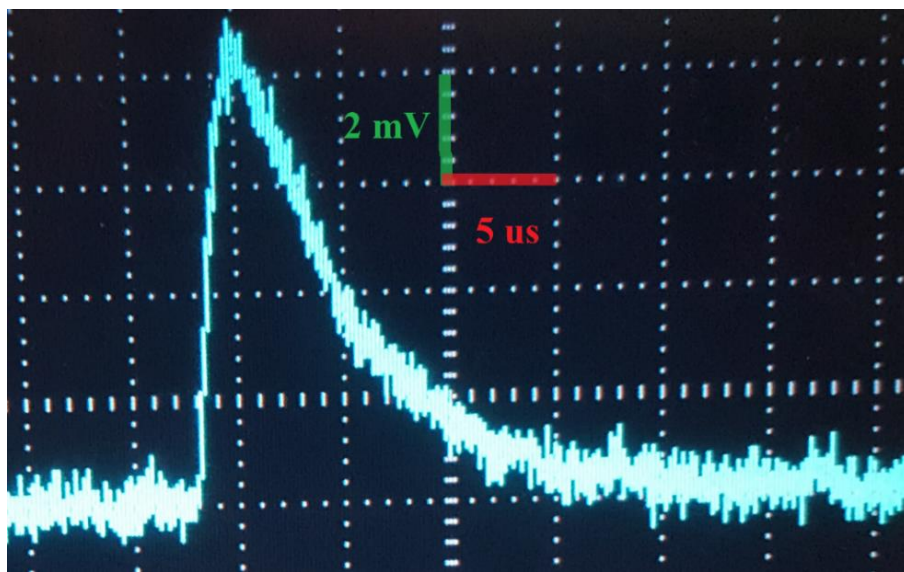


Figure 4.49 Shaper output.

The three capacitances values were first fixed to 4.7 nF and then to 14.7 nF. To evaluate the performance of the shaping time with these two different times, a  $^{137}\text{Cs}$  spectrum was acquired with the MCA 8000D and the energy resolutions of the 662 keV photopeak were compared (Figure 4.50). A slightly better energy resolution was found with the capacitance at 14.7 nF (7.3% instead of 8.4% obtained with 4.7 nF). Previous results showed that increasing the shaping time leads to a better energy resolution. Tests are planned to increase the shaping time up to an optimized value in a future version of the PCB.

The following conclusions can be drawn from this work:

The slow electronic component of the STD output signal was successfully suppressed allowing the different decay times ( $n$  and  $\gamma$ ) of the CLYC scintillator to be extracted.

A PCB was designed and tested. Concerning the zero pole cancellation, a RC circuit of 957 ns was applied. The new electronic board provides a more compact device that frees the operator from using heavy NIM modules, crate and external power supply for signal processing. The PCB is adjustable, so that different SiPMs and crystals can be used.

For the future version of the PCB, the shaping time needs to be determined and increased to obtain a better energy resolution.

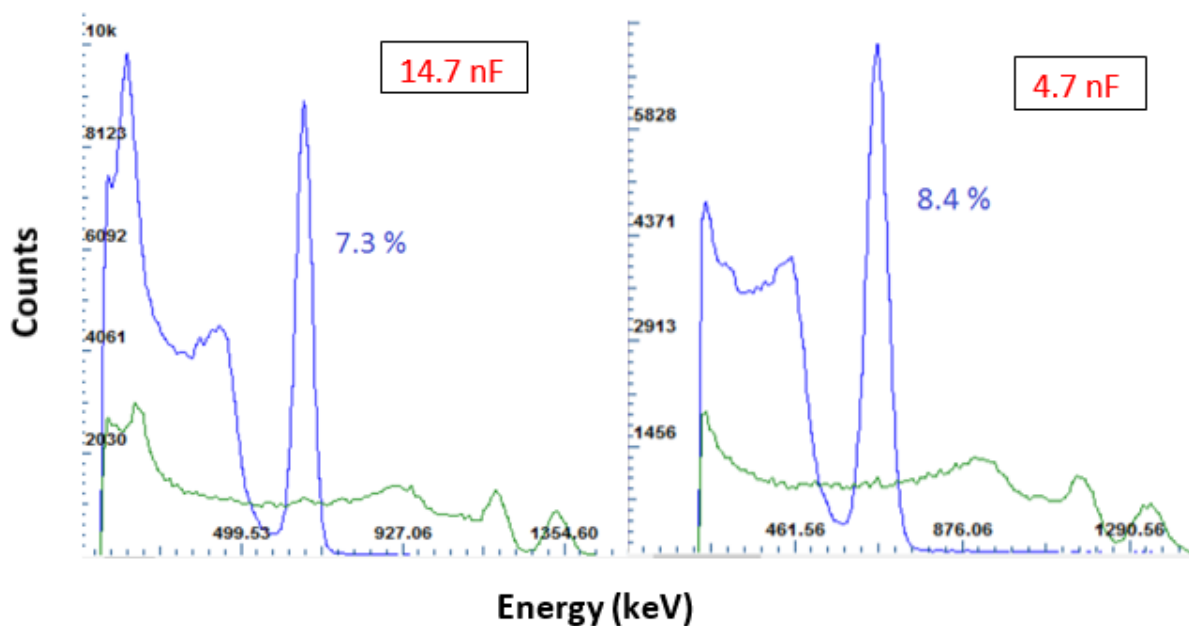


Figure 4.50  $^{137}\text{Cs}$  signal from CLYC coupled with the SiPM array with shaping time  $ST=330$  ns (on the left) and  $ST=1$   $\mu\text{s}$  (on the right).

## 4.5 Conclusions

The two potential read out, the PMT and the SiPM, to be used with the CLYC were compared. The optimal voltage to apply with the PMT was found at 1150 V, and 27.5 V for the SiPM. The temperature sensitivity of the system CLYC+SiPM was evaluated leading to the conclusion that no temperature compensation is needed since the light output of the CLYC increases with the temperature, thus compensating the effect of the gain reduction of the SiPM.

Thanks to the experience obtained with the electronic characterization and the collaboration with POLIMI, a compact electronic board, light and versatile (can be used with other SiPMs and crystal) was designed and tested.

---

## References

- [1] *D. Celeste, A. Curioni, A. Fazzi, D. Perrin and M. Silari, Status report on the radiation survey meter operating in strong magnetic field - KT funded project, Technical Note CERN-RP-2015-004-CONFIDENTIAL-TN, EDMS no. 1504386 (2015).*
- [2] *A. Fazzi and M. Silari, Portable radiation detection device for operation in intense magnetic fields, Patent Grant number 9977134 (13 July 2017).*
- [3] <http://rmdinc.com/clyc/>
- [4] *Hamamatsu Photonic, Photomultiplier tubes, basic and applications, third edition (2007).*
- [5] <http://SensL.com/downloads/ds/DS-MicroJseries.pdf>
- [6] [http://www.tek.com/sites/tek.com/files/medi/rsources/1KW609040\\_2450\\_DataSheet\\_0.pdf](http://www.tek.com/sites/tek.com/files/medi/rsources/1KW609040_2450_DataSheet_0.pdf)
- [7] *N. Dinar, D. Celeste, A. Curioni, M. Silari, The ArrayJ-30035-64P-PCB SiPM characterization for use in CLYC neutron probe, Technical Note CERN-RP-197-CONFIDENTIAL-TN(2016).*
- [8] <http://SensL.com/downloads/ds/DS-MicroCseries.pdf>
- [9] <http://www.epic-crystal.com/>
- [10] *K. E. Mesick, L. C. Stonehill, J. T. Morrell, D. D.S. Coupland, Performance of Several Solid State Photomultipliers with CLYC Scintillator Nucl. Instrum. and Methods in Phys. A841 139.(2015)*
- [11] *A. S. Sedra, K. C. Smith, Microelectronic circuits, 5th edition, Oxford University Press, (2004).*
- [12] *P.Eckert, H. Schultz-Coulon, W.Shen, R.Stamen, A.Tadday, Characterisation studies of silicon photomultipliers, Nucl. Instrum. Meth. A 620 217 (2010)*
- [13] *N.Dagoneau, master thesis, Development of a photon detection efficiency set up and characterization of silicon photomultipliers (2017)*
- [14] <http://www.nuclearinstruments.eu/nipm12-sipm-power-supply-module/>
- [15] <http://www.analog.com/media/en/technical-documentation/data-sheets/AD8000.pdf>
- [16] <http://www.minirf.com/pdf/transformers/RFXF9503DS.pdf>
- [17] [http://www.analog.com/media/en/technical-documentation/datasheets/TMP35\\_36\\_37.pdf](http://www.analog.com/media/en/technical-documentation/datasheets/TMP35_36_37.pdf)
- [18] <http://cds.linear.com/docs/en/datasheet/8045fc.pdf>
- [19] <http://www.ti.com/lit/ds/symlink/lp5907.pdf>
- [20] <http://cds.linear.com/docs/en/datasheet/3090fa.pdf>

## Appendix B

### Principle of pole zero cancellation

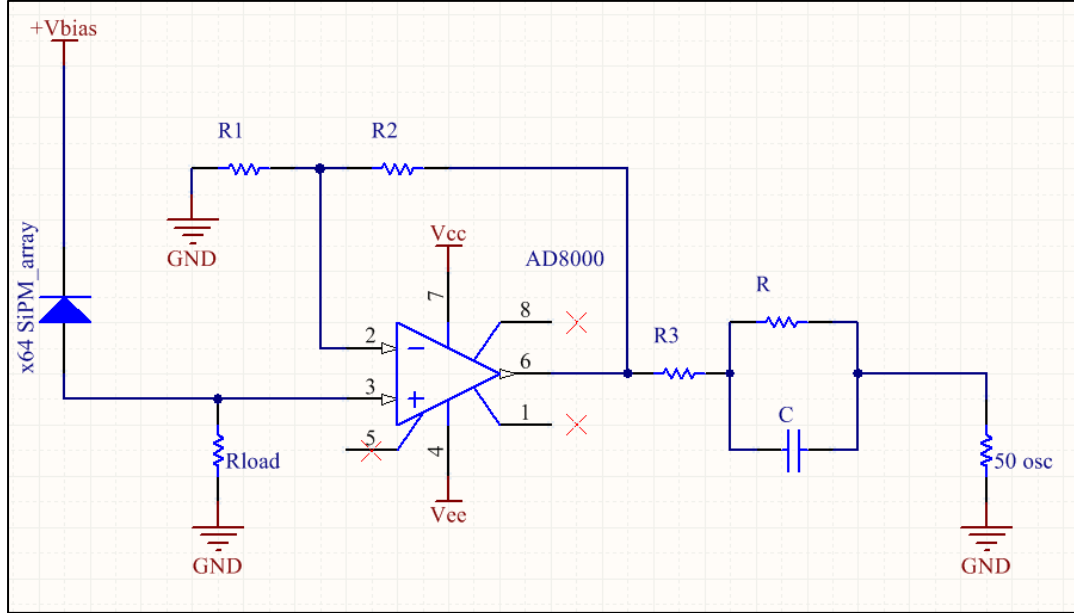
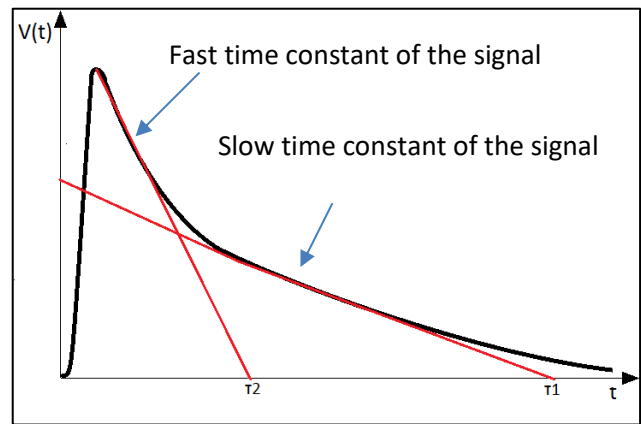


Figure B.1: Schematic of the electronic read-out with the amplification and the compensation circuit.

$$\text{Signal: } V^+(t) = \left( A1e^{-\frac{t}{\tau_1}} + A2e^{-\frac{t}{\tau_2}} \right)$$

Laplace transform:

$$\begin{aligned} V^+(s) &= \left( \frac{A1}{s + \frac{1}{\tau_1}} + \frac{A2}{s + \frac{1}{\tau_2}} \right) = \\ &= \frac{(A1 + A2)s + \frac{A1}{\tau_2} + \frac{A2}{\tau_1}}{\left( s + \frac{1}{\tau_1} \right) \left( s + \frac{1}{\tau_2} \right)} \end{aligned}$$



Where  $\tau_1$  is the slow time constant due to the pole introduced by the electronics.

$$\text{Transfer function of RC network: } H(s) = \frac{\left( s + \frac{1}{\tau_2} \right)}{\left( s + \frac{1}{\tau_1} \right)} \quad \lim_{s \rightarrow \infty} H(s) = 1, \quad H(s=0) = \frac{\tau_2}{\tau_1} < 0$$

Where  $\tau_z = \tau_1 = R * C$  and  $\tau_p = \tau_2 = C * (R // (R3 + 50 \text{ osc}))$ , so:

$$V(s) = V^+(s) * H(s) = \frac{(A1 + A2)s + \frac{A1}{\tau_2} + \frac{A2}{\tau_1}}{\left( s + \frac{1}{\tau_1} \right) \left( s + \frac{1}{\tau_2} \right)} * \frac{\left( s + \frac{1}{\tau_1} \right)}{\left( s + \frac{1}{\tau_2} \right)}$$

$$V(t) \approx \left( -\frac{A2}{\tau_2} t e^{-\frac{t}{\tau_2}} + (A1 + A2) e^{-\frac{t}{\tau_2}} \right) \text{ where } \tau_2 \text{ is the time constant of the output signal.}$$



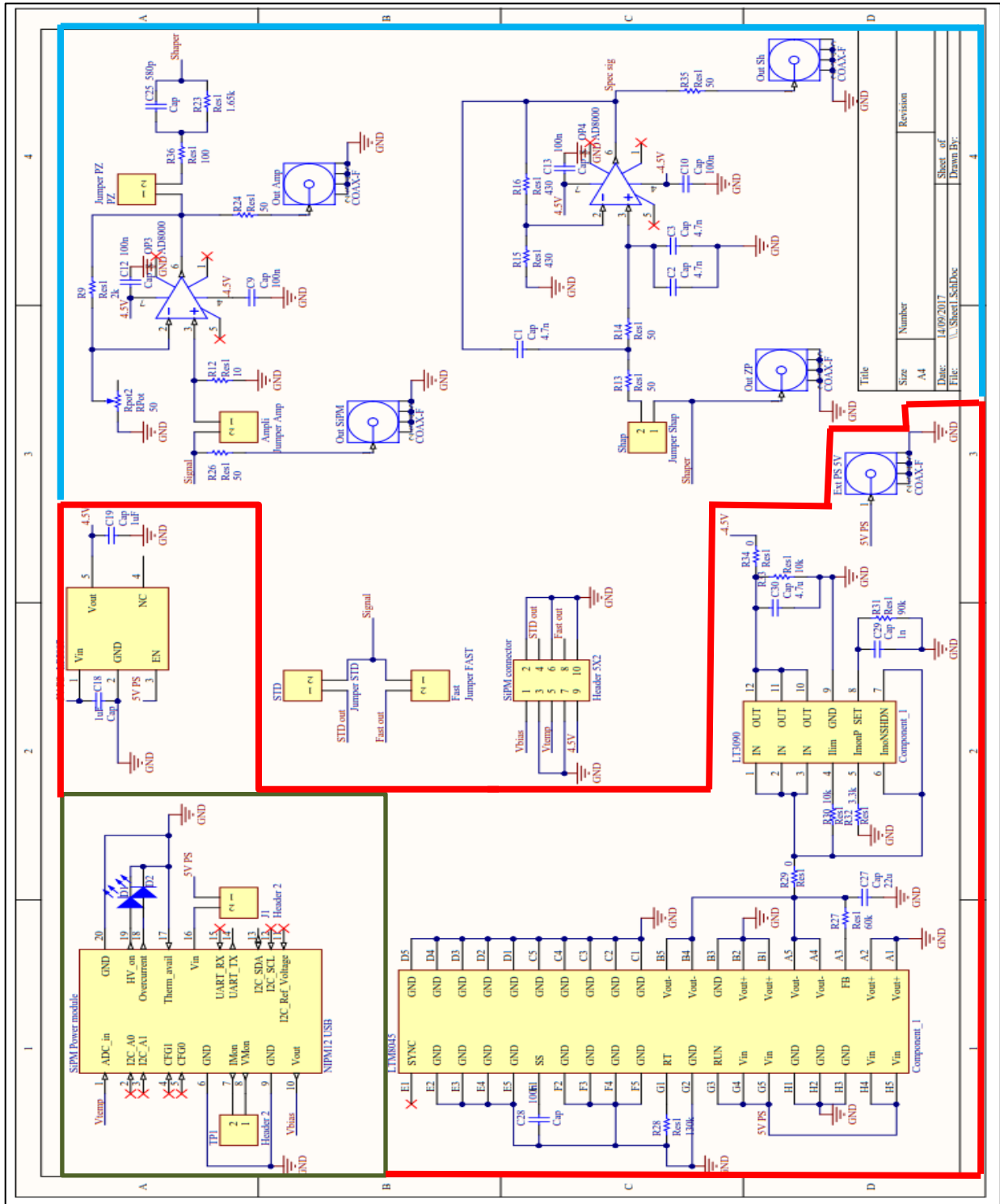


Figure B.2: Schematic of the signal processing board: the power module connector (green box), the power supply system (red box) and the signal processing with amplifier and shaper (blue box).

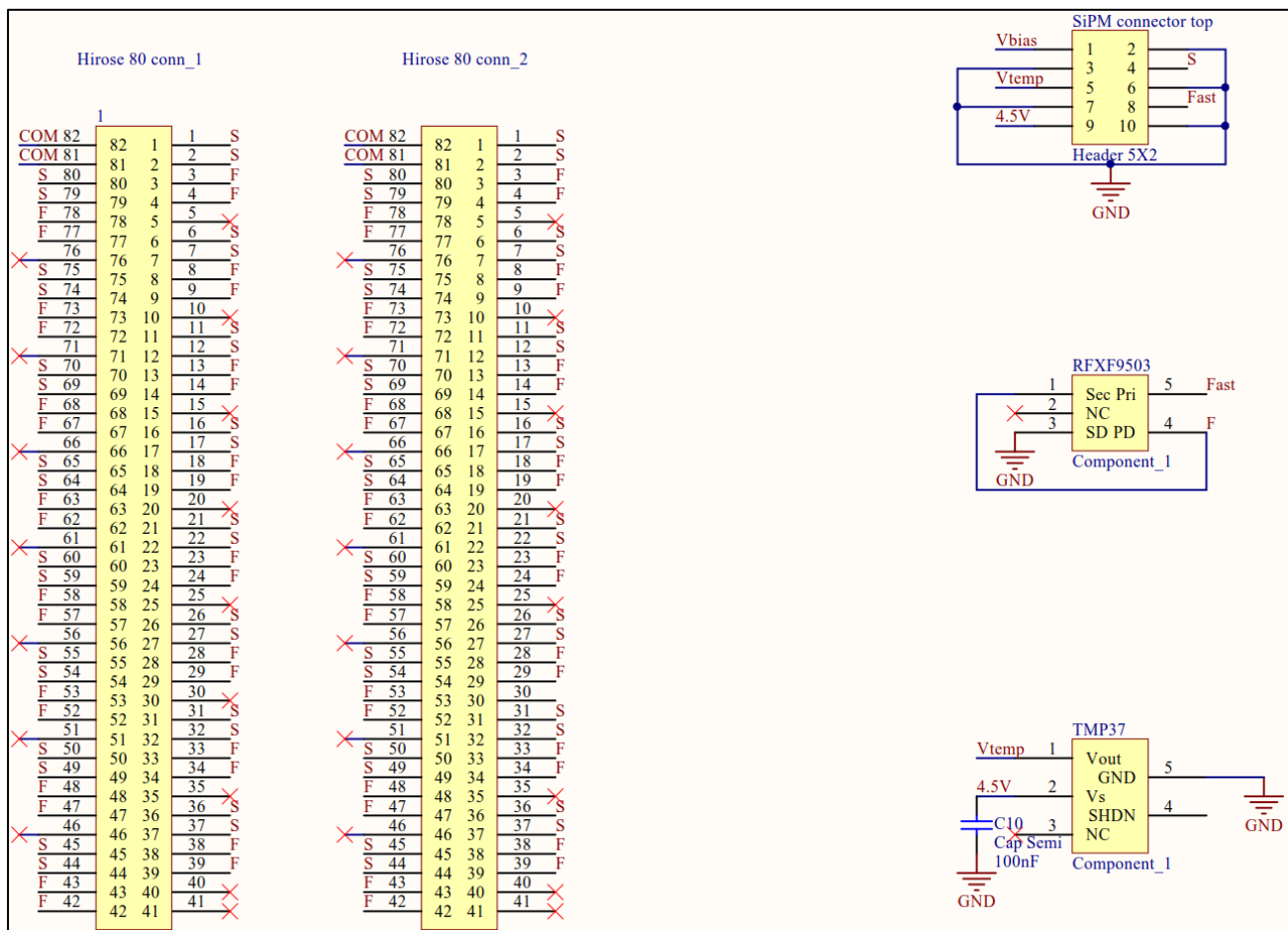


Figure B.3 SiPM array board: the Hirose connectors on the left, the temperature sensor (TMP37) and the balun transformer (RFX9503) on the right.

---

# Chapter 5 Evaluation of the performance of the CLYC scintillator

The chapter presents the measurements performed to characterize the CLYC. The uniformity, the neutron efficiency (measured and simulated with MCNP), the directional dependence of both neutrons and gamma photons were evaluated. Moreover, the pulse shape discrimination capability and the scintillation mechanisms with the PMT and SiPm were intercompared.

## 5.1 Pulse shape discrimination

Pulse shape discrimination (PSD) is basically used to discriminate between different type of radiations ( $\gamma$ \_rays,  $\alpha$ \_rays,  $\beta$  particles and neutrons). A difference in the shape of the pulse is due to the difference in the time profile of the current produced at the detector by radiation interaction. Different methods of extracting the difference in the shape of the pulses have been developed and employed over the years [1]. In this work, we use the more commonly used method: the charge integration technique.

### 5.1.1 Charge integration method

The discrimination is necessary to distinguish neutron radiation from  $\gamma$  signals. The pulse shape discrimination is based on the scintillation mechanisms triggered by different incident particles. Scintillators display significantly different pulse shapes produced by two groups of particles:

- heavy charge particles (p, d, t, alpha particles), which are products of neutron interactions with the scintillator (elastic scattering or capture).

- electrons, which are the products of gamma ray interaction with the scintillator (Compton electrons).

Heavy charge particles produced by neutrons drive greater specific ionization mechanisms, hence the scintillator reaches higher excited states that take longer to de-excite. On the other hand, lighter Compton electrons produced by  $\gamma$ -rays cause lower ionization, resulting in lower excitation states in the scintillator that take shorter to de-excite. The principle of the charge comparison method is to integrate two parts of each pulse: the entire charge of the pulse and the charge in the tail. The comparison of the two integrated charges will reveal which particle created the pulse: proton (neutron) or electron ( $\gamma$ -ray). This method takes advantage of the difference between the expected decay time distribution for a heavy ionizing particle featuring a remarkable tail and the one of an electron with a much shorter tail. Afterward, the separation between the neutron and  $\gamma$ -ray signals can be quantified and used to determine a metric performance. A figure of merit (FOM) has been identified for fast neutron detectors, which is used to establish their ability to discriminate between pulses generated by  $\gamma$ -rays and pulses generated by neutrons. The FOM is calculated after a PSD has been performed to identify the neutron and  $\gamma$ -ray pulses with the following formula:

$$FOM = \frac{S}{FWHM_n + FWHM_\gamma} \quad \text{with } S = (\text{centroid}_n - \text{centroid}_{\gamma\gamma}) \quad (5.1)$$

Where  $\text{centroid}_n$  and  $\text{centroid}_\gamma$  are the mean of the Gaussian for n and  $\gamma$  distribution,  $FWHM_n$  and  $FWHM_\gamma$  are the full width at half maximum of the peaks. The larger the FOM the better the performance of the detector for  $\gamma$ -n discrimination. A baseline performance requirement can be established by starting with the definition that for two peaks to be considered well separated it should be  $S > 3(\sigma_\gamma + \sigma_n)$ , where  $\sigma$  is the standard deviation. For a Gaussian distribution the  $FWHM = 2.36 \sigma$ . Thus substituting these definitions into equation 5.1 any detector with a FOM above 1.27 can be considered to have adequate PSD for fast neutron detection in the presence of  $\gamma$ -rays [2]. The choice of the two timing intervals, at which the integration of the pulse should be measured, is based upon a series of measurement that optimize the discrimination.

### 5.1.2 PSD with CLYC + PMT R6231-100

The CLYC and a Hamamatsu PMT R6231-100 were placed inside a light-tight box. The anode signals were directly sent to the 12 bit, 1 GHz Lecroy HDO6104 oscilloscope with a 50 Ohms termination. To calibrate the energy scale, the detector was irradiated with  $^{60}\text{Co}$  and  $^{137}\text{Cs}$  sources. About 20,000 pulses were recorded for each source. The waveforms were aligned (on time and amplitude) and integrated to yield a spectrum (Figure 5.1). From the spectra, the 662 keV (from  $^{137}\text{Cs}$ ), 1173 keV and 1332 keV peaks (from  $^{60}\text{Co}$ ) were fitted with a Gaussian curve. The plot of the mean charge value as a function of energy of these peaks shows a linear trend. In the following of this document the energy scale of all 2D PSD plots are given in terms of energy electron equivalent (keVee).

A  $^{252}\text{Cf}$  source was used to study the  $\gamma/n$  discrimination. About 100,000 signal traces were recorded and analyzed off-line. The first step for the PSD analysis was to align all the waveforms to a common zero, so the point where the amplitude was 20% of the maximum was chosen. Moreover, to remove the variable off-set on the y axis, the baseline mean value (estimated in the first 700 ns before the trigger) was determined and subtracted from the signal.

Figure 5.2 shows 100 signal outputs from the PMT: two pulses generated by neutrons can already be well identified. To better distinguish the pulse shape differences, the first 20 signals were normalized to their maximal amplitude (Figure 5.3). Significantly, intrinsic differences can be found between neutron pulses and  $\gamma$ -rays pulses due to different scintillation mechanisms. First of all the pulses generated by neutrons have a longer tail than the pulses generated by  $\gamma$ -rays. Moreover the time-to-peak is longer for neutrons ( $\approx 200$  ns) than  $\gamma$ -rays ( $\approx 30$  ns).

Thus, the difference in the ratios of the charge in the tail of the pulse to the total charge in the pulse (PSD ratio) can be calculated and used to discern which type of radiation generated the pulse. According to the previous conclusion, the PSD ratio for neutron pulses should be larger than the PSD ratio for gamma ray pulses for the same total charge deposited. The automated waveform analysis algorithm determines the optimal windows by the following process:

- (1) the width of the first integration window (prompt component) was varied from 20 ns to 400 ns starting from the positive part of the signal (Time > 0),
- (2) the second integration window (delayed component) started where the prompt window ended at 2  $\mu\text{s}$ , so that its width varied in correlation with the width of the prompt window,
- (3) for each combination of the prompt and the delayed integration windows, the charge integrals  $Q_{PROMPT}$  and  $Q_{DELAYED}$  as well as the PSD ratio were calculated for each waveform in the dataset :

$$PSD_{ratio} = Q_{TAIL} / (Q_{PROMPT} + Q_{TAIL}) \quad (5.2)$$

- (4) the PSD ratio was plotted in a histogram (projection of the PSD ratio axis), resulting into two peaks: neutrons and  $\gamma$ -rays.
- (5) Gaussian fits were performed to the neutron and  $\gamma$ -ray peaks in the histogram, yielding the centroid positions and FWHMs of the two peaks,
- (6) the FOM value was calculated from the Gaussian fitting results (Equation (5.1)).

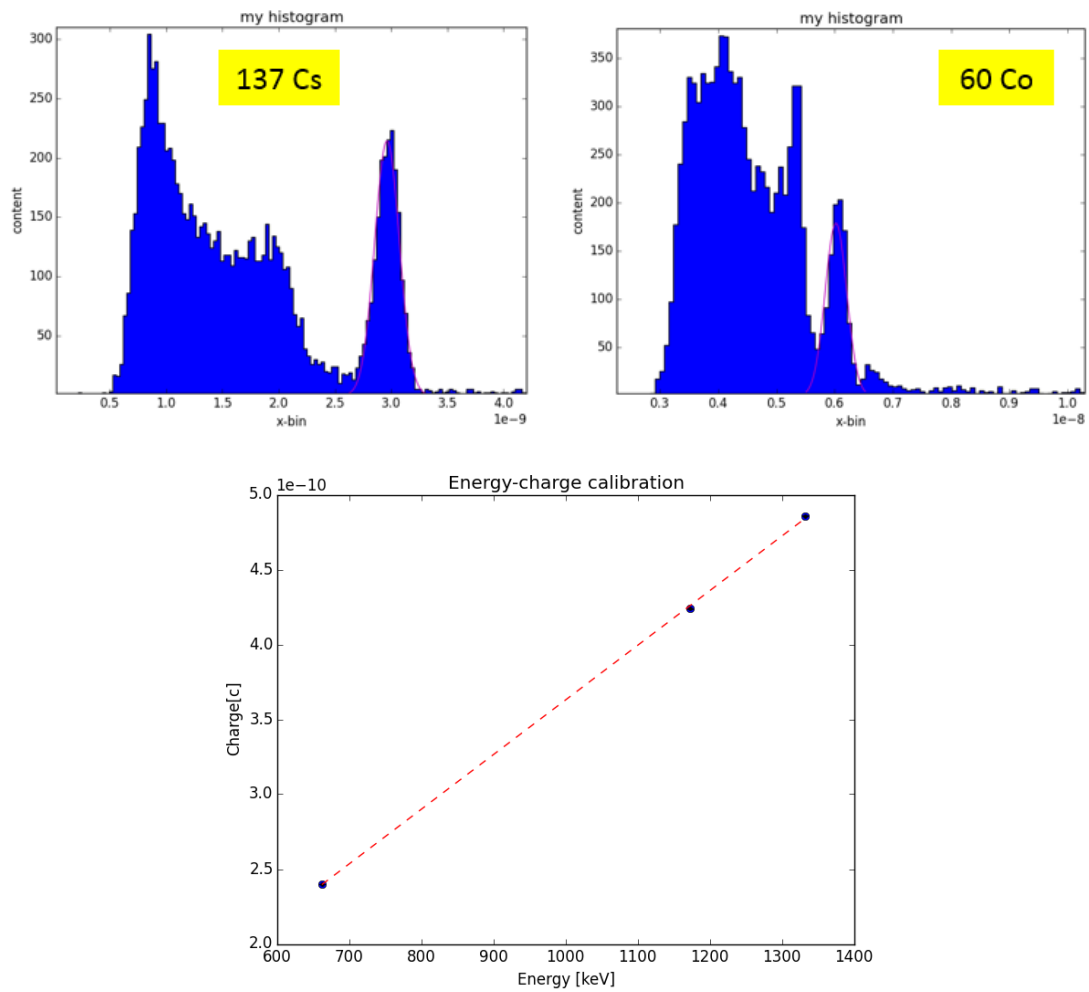


**Figure 5.1**  $^{60}\text{Co}$  and  $^{137}\text{Cs}$  spectra (upper figures) and the energy-charge calibration curve (bottom figure).

The results of the optimization of the FOM value are shown in Figure 5.4. Increasing the prompt window width, the FOM shows a fast and short increase, followed by a sharp, long decrease. Changing the delayed window width has a minimal effect on the FOM. For the CLYC crystal in this study, the best FOM we found is 2.64, with a prompt window width of 70 ns and a delayed window width of 1930 ns. Figure 5.5 shows the two dimensional PSD plot obtained when selecting the window prompt time at 70 ns. Two regions are clearly displayed: an upper band related to the neutron events and a bottom part corresponding to  $\gamma$ -rays. From the plot, we can also see that the  $\gamma$ -ray population prevails.

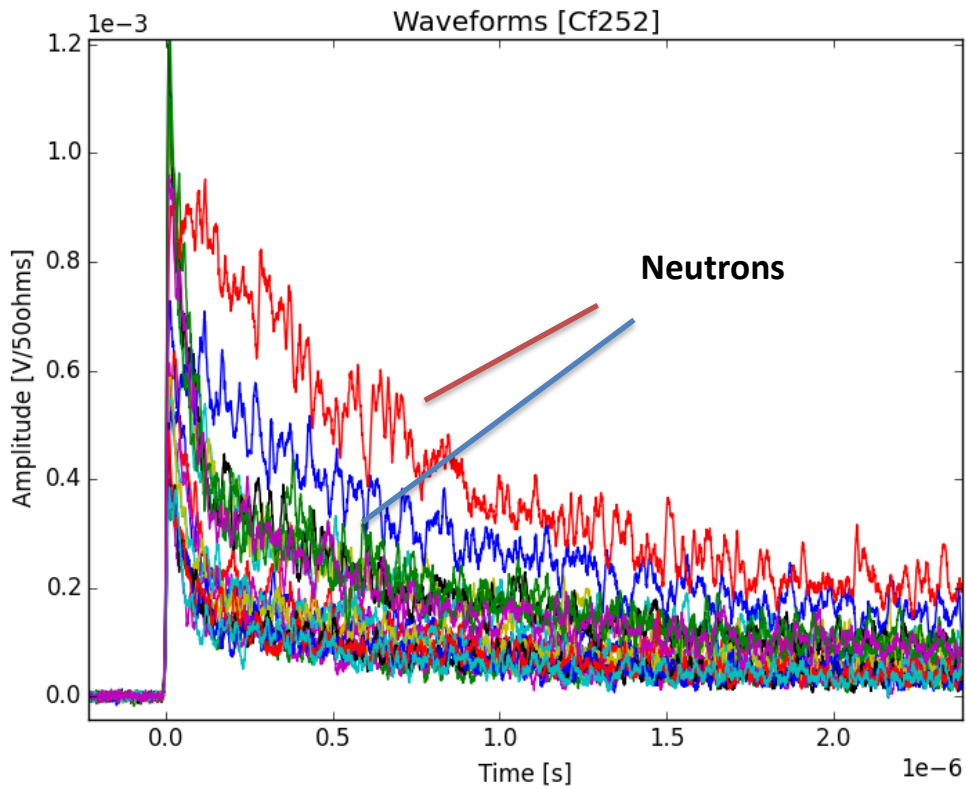


Figure 5.2 100 PMT output signals from the oscilloscope

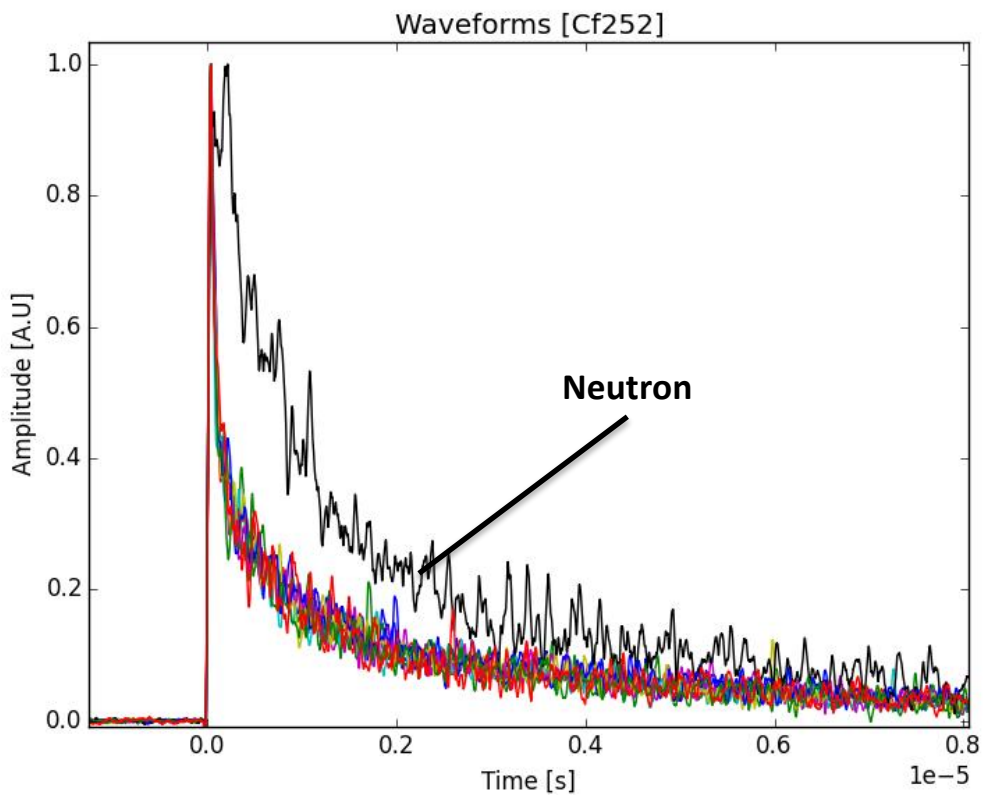


Figure 5.3 The output signals from the oscilloscope after normalization to their peak.

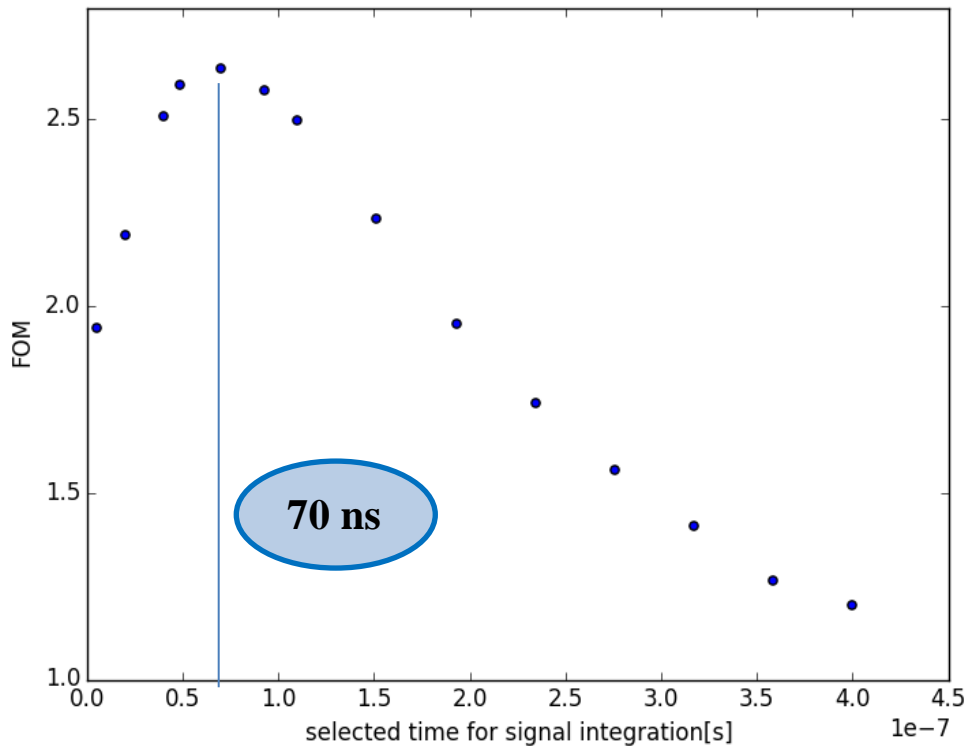


Figure 5.4 FOM versus prompt window time. The best FOM is found at 70 ns.

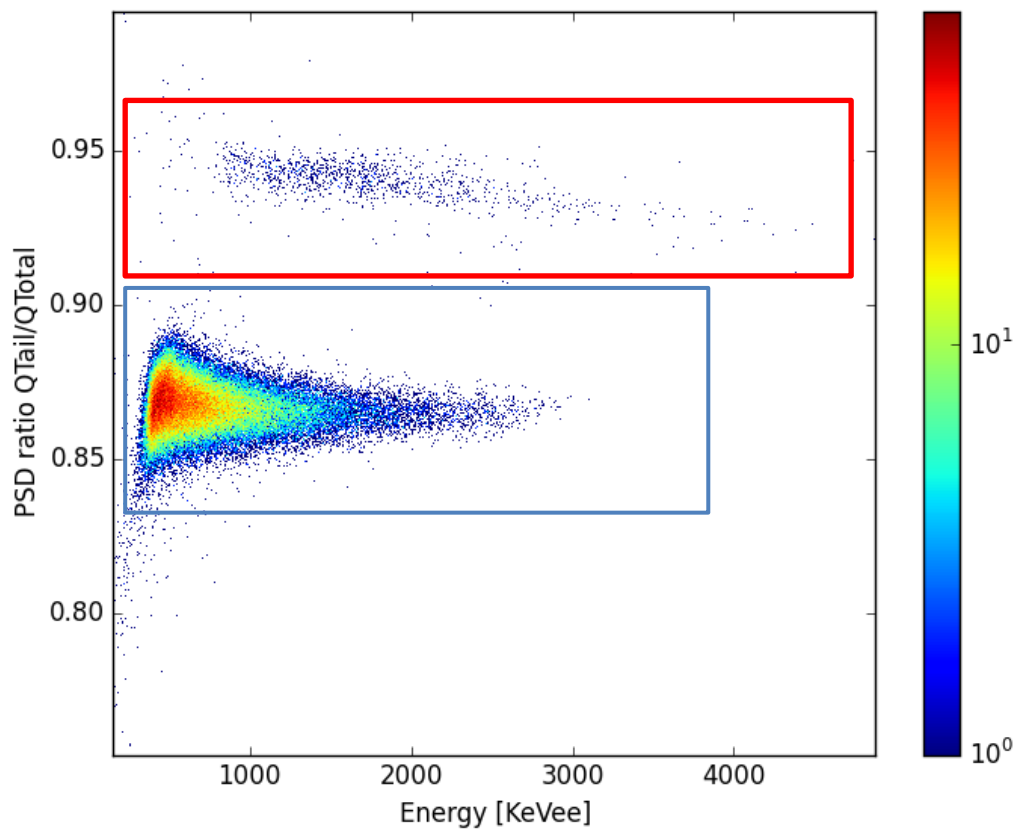


Figure 5.5 Two dimension PSD plot for the best configuration (prompt window = 70 ns). The blue box identifies gamma events while the red one corresponds to neutron events.

### 5.1.3 PSD with CLYC + SiPM Array J-30035-64P-PCB

The CLYC crystal is coupled to the SensL ArrayJ-30035-64P-PCB through an optical grease to match the refraction indexes and avoid internal reflections. The SiPM array is connected to the breakout evaluation board ArrayJ-BOB3-64P; a board was designed in order to sum up all contributions coming from each of the 64 elements and to end on a single-channel output. All this setup is enclosed inside a light-tight box with BNC panel connectors. A positive reverse bias voltage of 28.5 V is applied to the *n-type* common cathode of the array. The STD and fast output chains are extracted. The STD output is then read on a load resistor of 50 Ohms, while the fast output is obtained through an AC coupling (series capacitors) on the output and a balun transformer on the summed signal.

Measurements to evaluate the PSD performance were carried out with the standard and the fast outputs. In order to compare the results, the same procedure and sources employed with the PMT were used with the SiPM:

- $^{252}\text{Cf}$  neutron source
- $^{60}\text{Co}$  and  $^{137}\text{Cs}$   $\gamma$  sources for calibration

However, unlike in the case of the PMT signal output, a Savitzky–Golay filter [3] was applied to increase the signal-to-noise ratio without distorting the signal. Hence the alignment of each waveform at 20% of the peak amplitude was possible.

#### 5.1.3.1 SiPM Standard output

Figure 5.6 shows the output signals from the oscilloscope. No differences on the pulse shape signals are remarked between neutron and gamma events even after a smoothing filter was applied to the data.

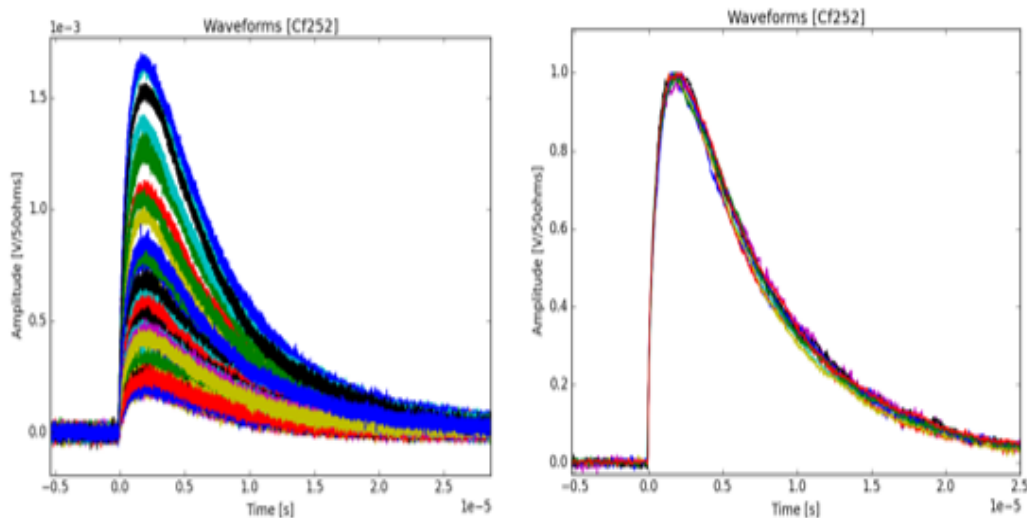


**Figure 5.6** The standard output signals from the oscilloscope on the left and the same signals after normalization to the maximal amplitude and smoothing filter on the right.

The same charge comparison method used in the previous analysis was performed giving unsuccessful results. Then another algorithm based on the ratio between the peak and the tail integral was applied varying the width and the position of the tail integral (Figure 5.7). It consist in dividing the maximum of the signal and divide it by an optimized width. Figure 5.8 shows the results from two different tail windows applied: from 10 to 15  $\mu\text{s}$  and from 15 to 20  $\mu\text{s}$ . However no successful results were obtained. A single band can be seen corresponding to both  $\gamma$  and neutron events.



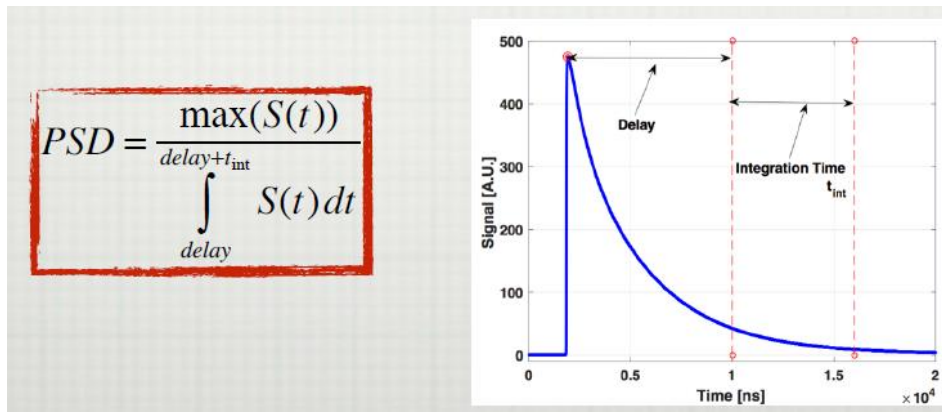


Figure 5.7: The peak to tail algorithm principle.

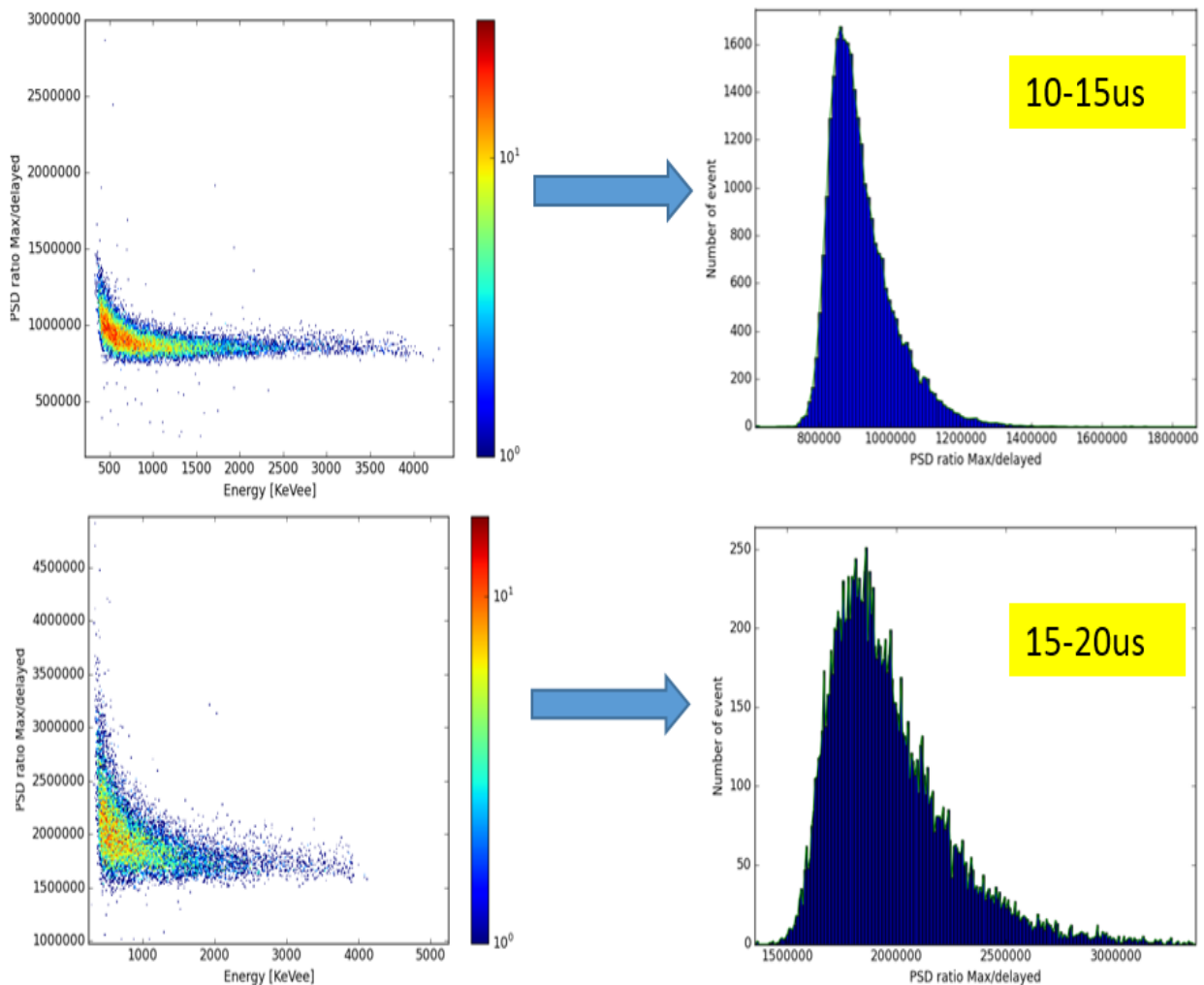
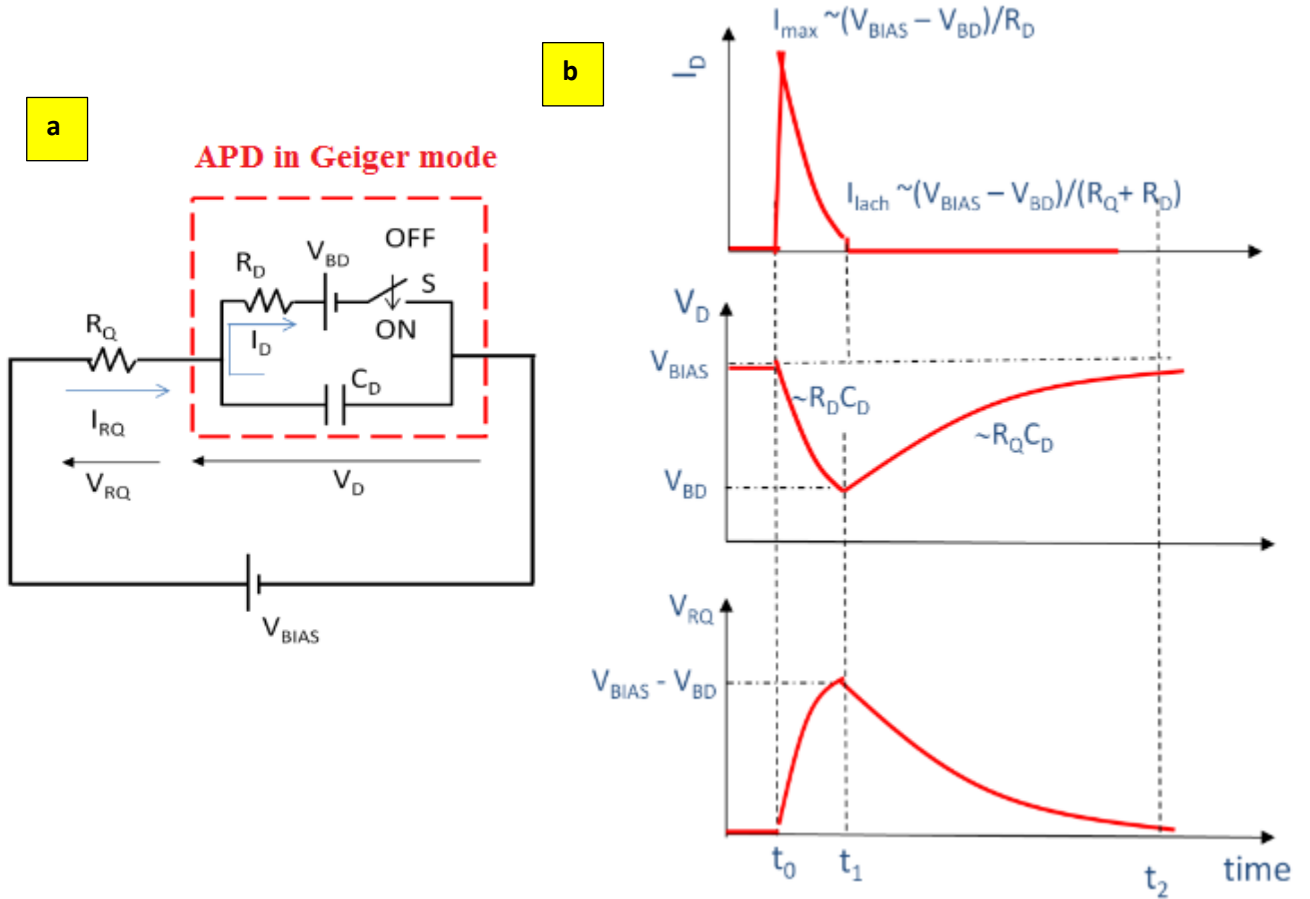


Figure 5.8 The PSD results with two different integration tails from 10-15  $\mu$ s and from 15-20  $\mu$ s.

It can be concluded that  $\gamma/n$  discrimination is not possible using the signals from the standard output. This is mainly due to the high capacitance of the total SiPM array. A SiPM is a pixelated device where each pixel (microcell) is a series combination of an avalanche photodiode (APD) and a quenching resistor ( $R_Q$ ). All of the microcells are connected in parallel. The electrical model developed by Haitz et al. [4] associated to the elementary microcell is depicted in Figure 5.9a. The time evolution of current and voltage across the APD during the avalanche process are shown in Figure 5.9b.



**Figure 5.9: (a) Equivalent circuit of a GM-APD (APD operating in Geiger mode) (b) Time evolution of the avalanche current signal and the voltage across a Geiger-mode diode.**

$V_{BD}$  is the breakdown voltage,  $R_D$  and  $C_D$  the diode resistance and capacitance,  $R_Q$  is the quenching resistor, S is a switch with OFF/ON positions, which represents the diode before and when the avalanche occurs, respectively,  $V_{BIAS}$  is the applied reverse voltage and  $V_D$  is the voltage across the diode (equal to  $V_{BIAS}$  when the switch S is in the OFF position: no avalanche) [4].

- Before the avalanche  $t < t_0$   $C_D$  is charged at  $V_D = V_{BIAS} > V_{BD}$  and no current flows through the circuit. When the microcell absorbs a photon, an electron-hole pair is formed; one of the charge carriers drifts to the avalanche region, where it can initiate an avalanche ( $t = t_0$ ).

- At  $t_0$ , the switch S closes (ON position), the current pulse reaches the maximum of  $I_D = I_{MAX} = (V_{BIAS} - V_{BD})/R_D$  and  $C_D$  starts discharging exponentially through  $R_D$  ( $R_D \ll R_Q$ ) with the time constant  $\tau_{discharge} = R_D C_D$ .  $C_D$  discharges from  $V_{BIAS}$  to  $V_{BD}$  between  $t_0$  and  $t_1$ . When the decreasing voltage  $V_D$  approaches  $V_{BD}$ , the intensity of  $I_D$  becomes low and tends to an asymptotic value of  $(V_{BIAS} - V_{BD})/(R_D + R_Q)$  because the  $V_{BIAS}$  applied crossing the  $R_Q$  and  $R_D$  causes an exponential growing current flowing through them. As the  $I_D$  decreases, the number of carriers that traverse the avalanche region becomes small. Since the avalanche process is statistical, it can happen that none of the carriers that cross the high field region drive any further ionizations. The probability of such a fluctuation to zero carrier multiplication becomes significant when the diode current  $I_D$  falls below  $<100 \mu A$  (called  $I_{latch}$ ), and rapidly increases as  $I_D$  further decreases. Thus the avalanche is self-sustaining above  $I_{latch}$  and it is self-quenching below it. Therefore, proper high value of quenching resistance is crucial to let the internal current  $I_D$  decrease to  $I_{latch}$ . The latching current determines a strict limit on the lower value of  $R_Q$  to some hundreds of k $\Omega$  [5].

- As the avalanche process is terminated, the switch S is again open (OFF position) and the circuit returns to its initial configuration. The capacitance, previously discharged at  $V_{BD}$ , starts recharging to the bias voltage with a time constant  $\tau_{recharge} = C_D R_Q$  ( $t_1 < t < t_2$ ), and the device becomes ready to

---

detect the arrival of a new photon. Since the  $R_Q$  is usually much higher than the diode series resistance, the  $\tau_{recharge}$  is much longer than the  $\tau_{discharge}$ .

The dynamic behaviour of the GM-APD was described above for a single microcell. The SiPM is composed of several microcells connected in parallel. The effect on the output signal shape of multiple microcells has been described in [6]. The signal can be divided in three parts: rising, quenching and recharging. It has been shown that when the number of cells increases ( $>200$ ), the rising time tends to a constant, while the quenching time raises up with a roughly constant slope ( $\approx$  load resistance value). In addition, the recovery time constant linearly grows with the total number of cells. Therefore, the signal obtained from the SiPM standard output (64 pixels) shows a similar rising time as we irradiated only one pixel but a much longer recovery time. The final output signal from a scintillator coupled with a SiPM is the folding of both responses. Since the response of the SiPM is much slower than the response of the CLYC, the initial differences in the decay time between  $\gamma$ -rays and neutrons are lost, so that all signals ( $\gamma$  or neutron) look very similar (Figure 5.6) and  $\gamma/n$  discrimination is not possible anymore.

### 5.1.3.2 SiPM Fast output

A photon can trigger a Geiger-mode avalanche which occurs in a very short time ( $<1$  ns), so the observed rise time in the standard output is determined only by stray capacitances and resistors. However, the fall time is determined by the quenching resistor values and the total capacitance of the microcells is typically tens of nanoseconds. Typical values of  $R_Q$  and  $C_D$  explain the long pulse tails observed in standard SiPM signals. This effect increases with the number of microcells. According to the datasheet, the total capacitance of one element is 1 nF. The SensL Array J-30035-64P-PCB is composed of 64 elements equivalent to a capacitance of 64 nF in total. However SensL has developed a proprietary [7] fast mode output in addition to the standard output available in SiPM devices. It consists in a third electrode which is coupled to individual microcells through low capacitance. As a result, the fast output (formed from the sum of all microcells) also has considerably lower capacitance and the response signal has much shorter pulse width. The third electrodes are coupled to a common “Fast Output” terminal. According to the datasheet, the capacitance of the SiPM fast output is 3.2 nF ( $50$  pF \* 64 pixels). Because the equivalent capacitance is reduced by a factor of 20, the signal collected from the fast output has a much shorter falling time than the conventional output signal. The bipolarity of the fast signal comes from the fact that the fast output signal is the derivative of the internal fast switching of the microcell in response to the detection of a single photon. Figures 5.10 and 5.11 show the signals obtained from the fast output, respectively without and with the Savitzky–Golay filter. Two trends are visible: signals with a fast rise time (peaking time  $\approx 120$  ns) and a fast decay time ( $\gamma$ ), other signals with a slightly slower rise time (peaking time  $\approx 150$  ns) and a much longer decay time (neutron).

For the PSD analysis only the positive part of each waveform was taken into account. To find the optimized windows the following parameters were applied:

- (1) the width of the prompt integration window was varied from 100 ns to 250 ns in 50 ns steps. The 120 ns point corresponding to the gamma peak was also chosen;
- (2) the delayed integration window started where the prompt window ended, so its width varied in correlation with the width of the prompt window. The end of the delayed time varied from 300 to 700 ns.

Figure 5.12 shows the FOM obtained for all configurations. With the increase of the prompt window width, the FOM shows a slow increase, followed by a sharp decrease. The best value is 1.64 when selecting a prompt window of 150 ns and a delayed time of 600 ns, equivalent to a delayed window of 450 ns. The two dimensional PSD plot for the best configuration is shown in figure 5.13. The two bands are clearly visible. Figure 5.14 is the PSD histogram where the two gaussians are well separated. A sufficient  $\gamma/n$  discrimination (FOM  $> 1.27$ ) for the SiPM Array J-30035-64P-PCB is therefore possible using the fast output.

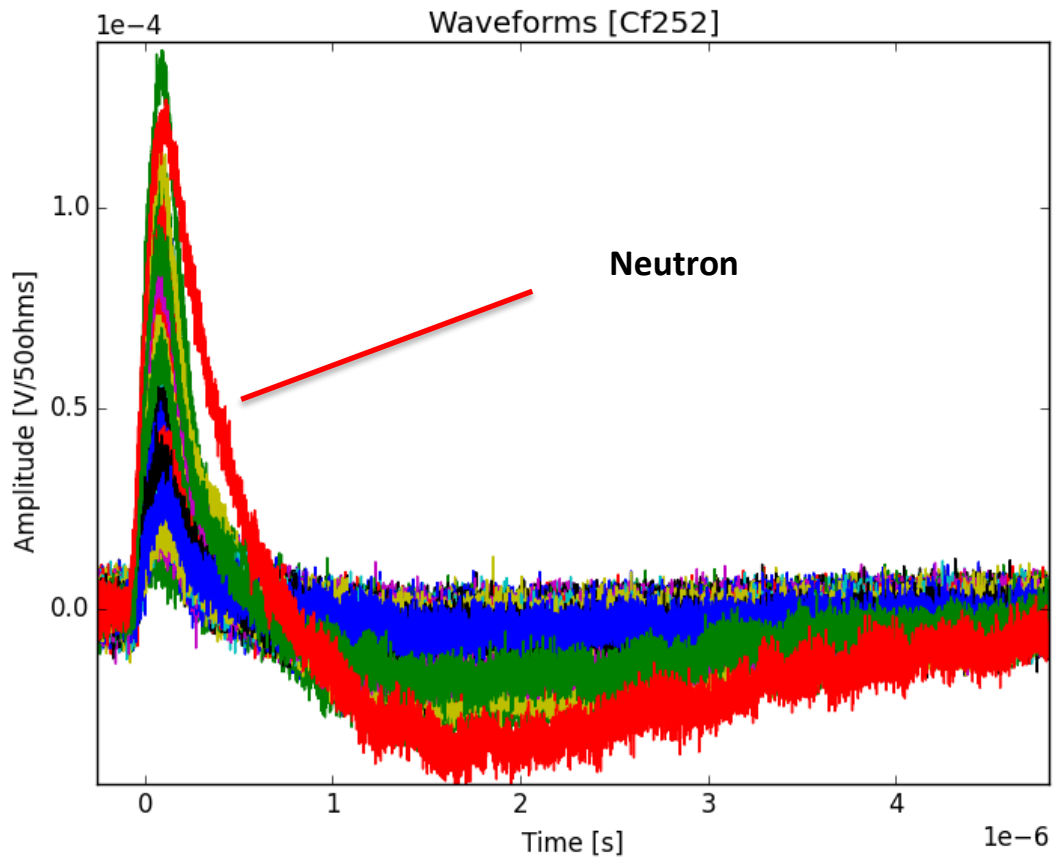


Figure 5.10 The fast output signals from the oscilloscope

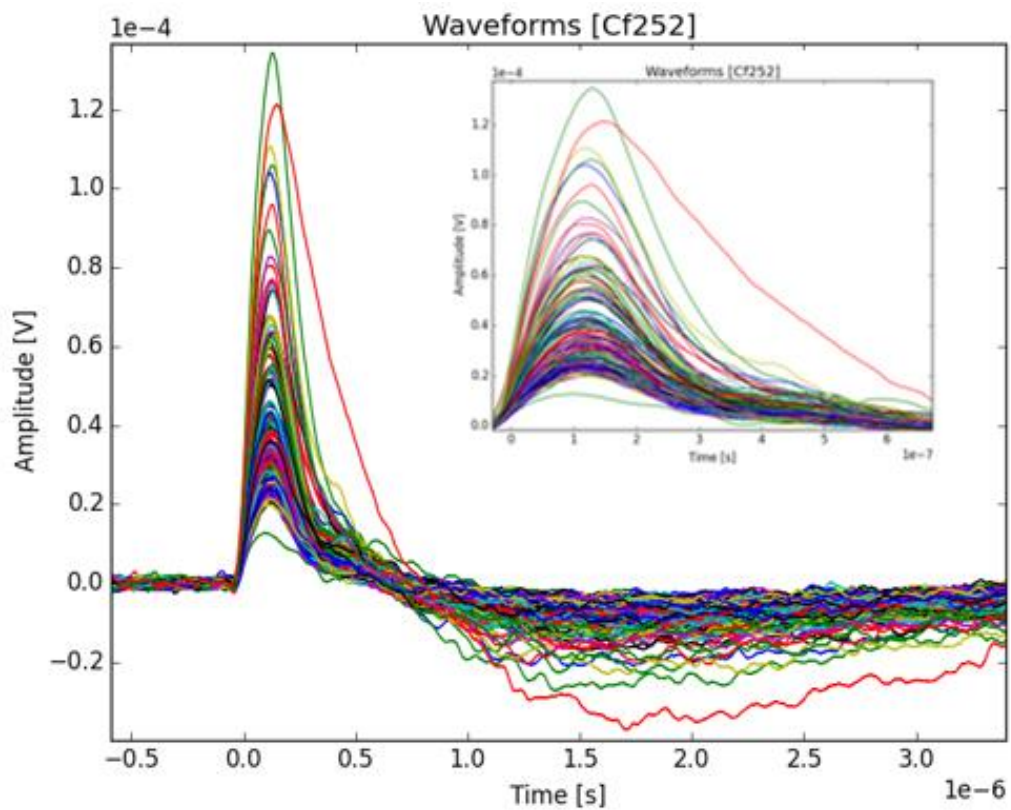


Figure 5.11 The fast output signals from the oscilloscope after the Savitzky-Golay smooth filter. The internal plot is a zoom of the first 100 ns of the plot.

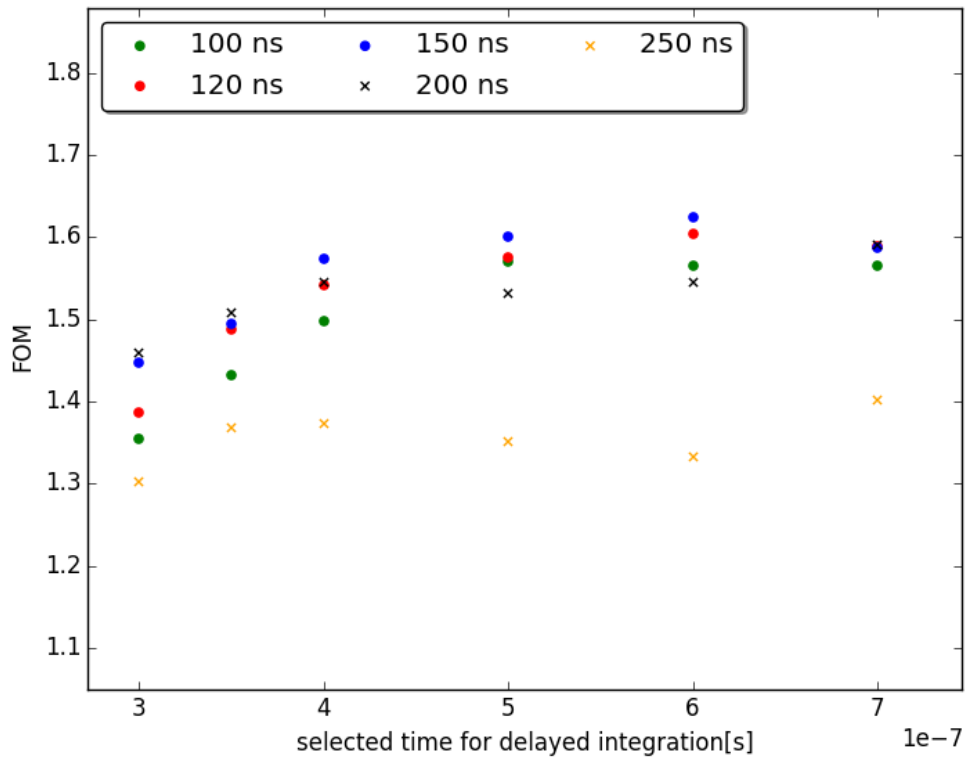


Figure 5.12 FOM versus delayed windows time for different prompt windows. The best configuration for an optimized FOM of 1.64 is 150 ns-600 ns.

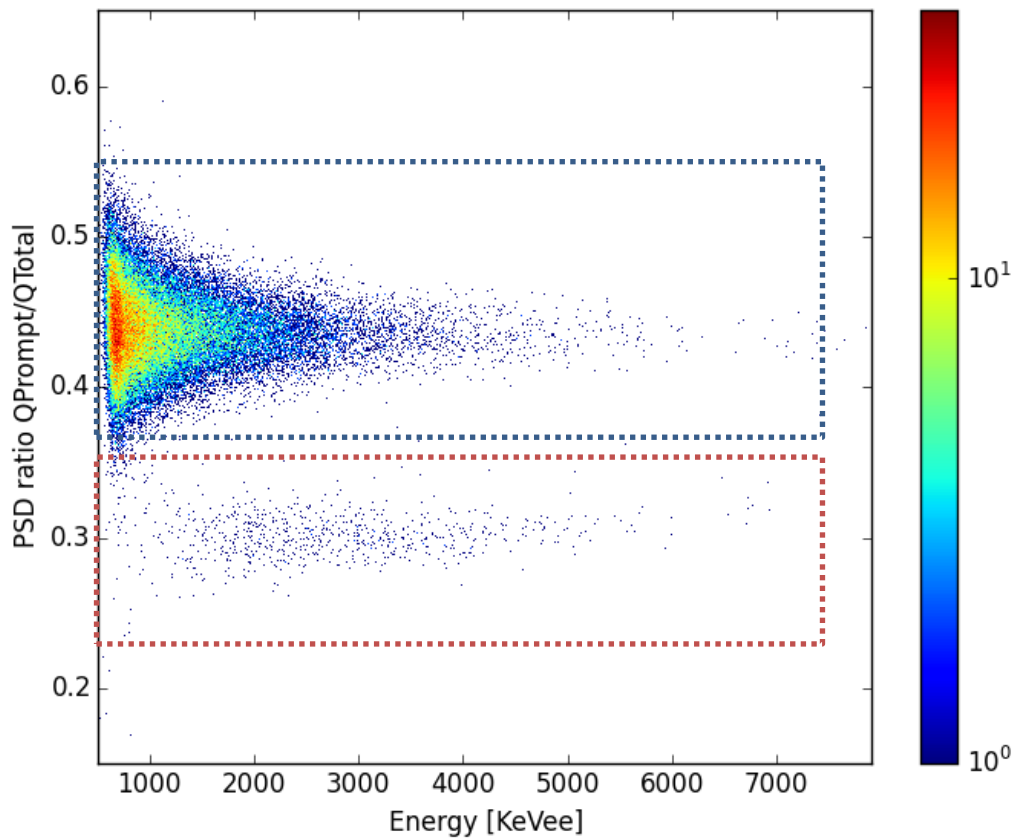
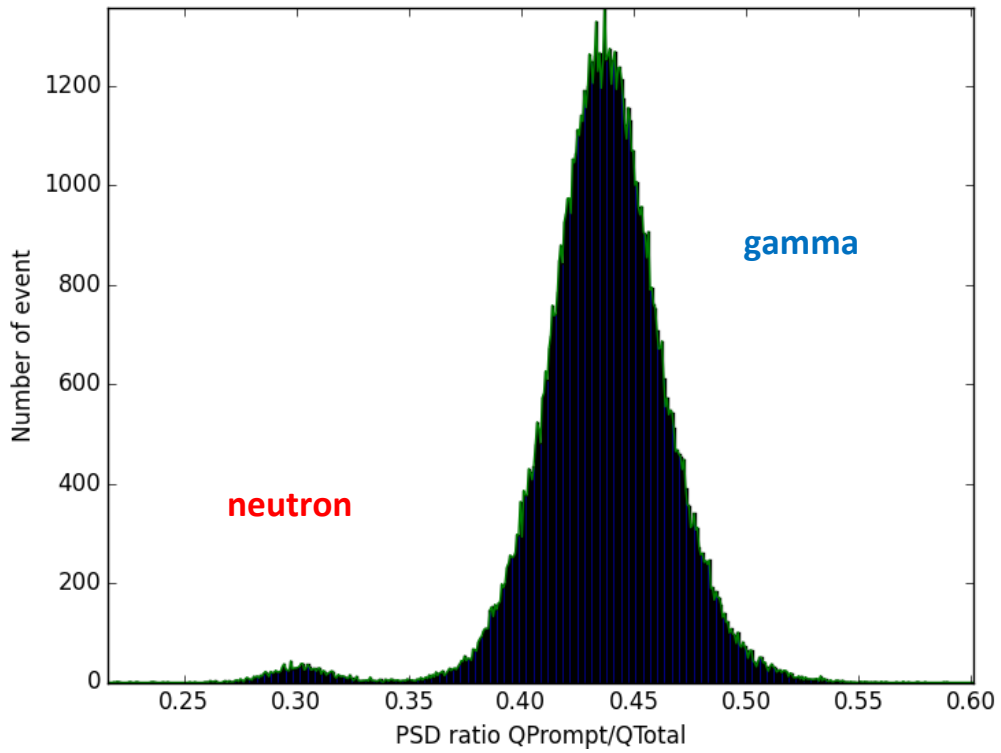


Figure 5.13 two dimension PSD plot. The blue box are gamma events while the red box corresponds to neutron events.



**Figure 5.14 Projection of PSD axis. Two Gaussians are separated.**

### 5.1.3.3 SiPM Standard output + RC compensation

To test the performance of the PCB developed (see section 4.3.2.2), the same set-up and irradiation condition were used. Figure 5.15 shows the waveforms obtained on the oscilloscope from the pole zero output with a  $50\ \Omega$  termination. A neutron signal is clearly distinguishable. The gamma peak is located at around 90 ns while the neutron peak is at 200 ns.

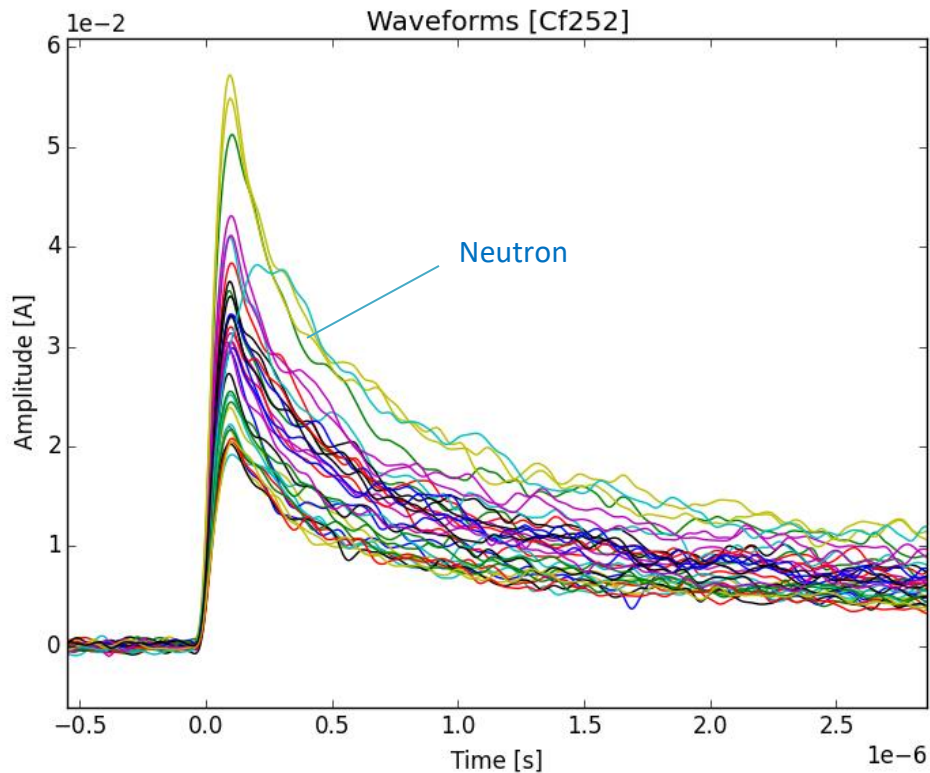


**Figure 5.15 output signals from the oscilloscope.**

With these new timing features we are able to extract and highlight the different scintillation decay times for gammas and neutrons and perform the PSD exploiting the STD output. For the PSD analysis the following parameters were implemented off-line:

- (1) the width of the prompt integration window was varied from 90 ns to 200 ns;
- (2) the delayed integration window started right after the end point of the prompt window. Its width varied according to the width of the prompt window. The end of the delayed time varied from 0.5  $\mu$ s to 2  $\mu$ s with an increment of 500 ns. One additional point at 200 ns corresponding to the neutron peak was also chosen.

Figure 5.16 shows the Figure of Merit (FOM) obtained for all configurations. A delayed time of 1  $\mu$ s appears to be the best choice for a high FOM. The optimized prompt window is 90 ns. The two dimensional PSD plot for the optimized configuration is presented in figure 5.17 where the two different populations are clearly separated. Figure 5.18 shows the projection of PSD ratios on the x-axis and leads to an excellent FOM of 2.03, compared to the one obtained with the PMT (2.6). It is important to note that this value does not include any cut in energy. With a cut at the Q value of the reaction (615 keV) the FOM is even higher: 2.97 (PMT) and 2.30 (SiPM). After trying different configurations, fast SiPM outputs and different RC circuits, the electronic board presents the highest FOM we obtained so far.

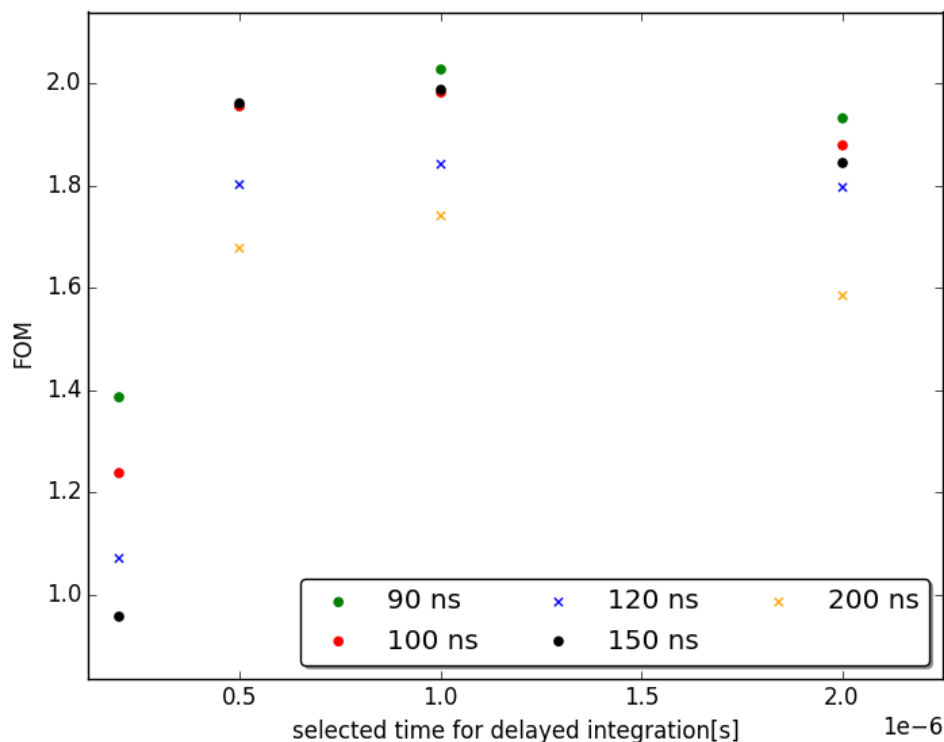


**Figure 5.16 FOM versus delayed window time for different prompt windows. The best configuration for an optimized FOM of 2.03 is 90 ns -1  $\mu$ s.**

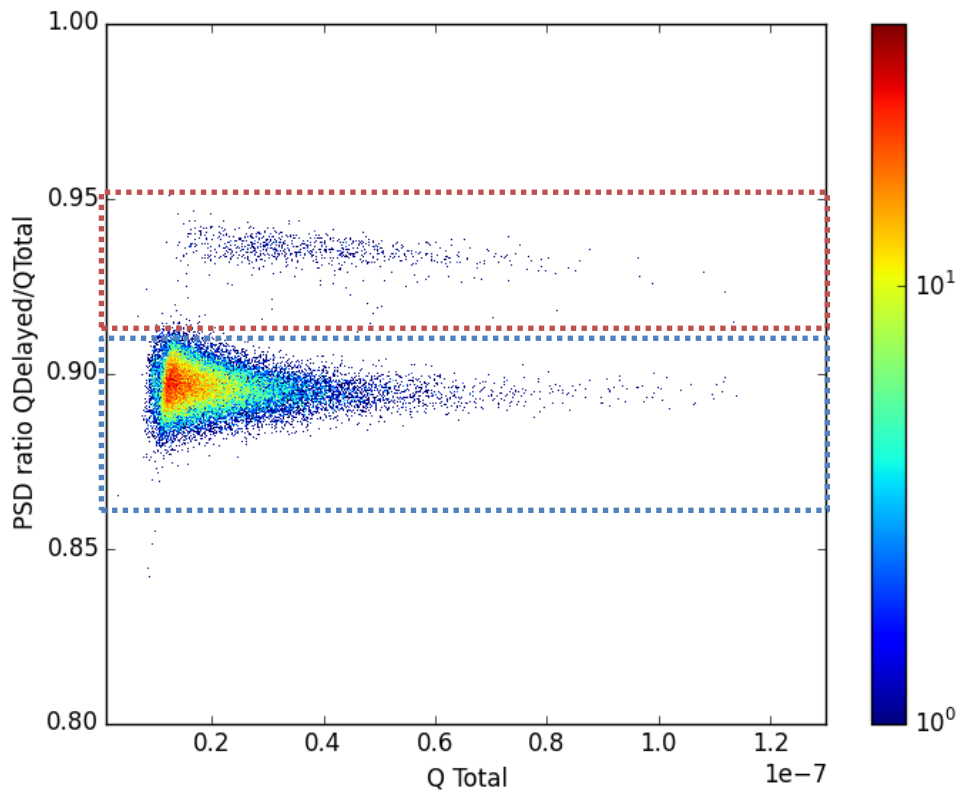


Figure 5.17 two dimension PSD plot for the best configuration (prompt window =90 ns, delayed window = 1  $\mu$ s). The blue box are gamma events while the red box corresponds to neutron events.

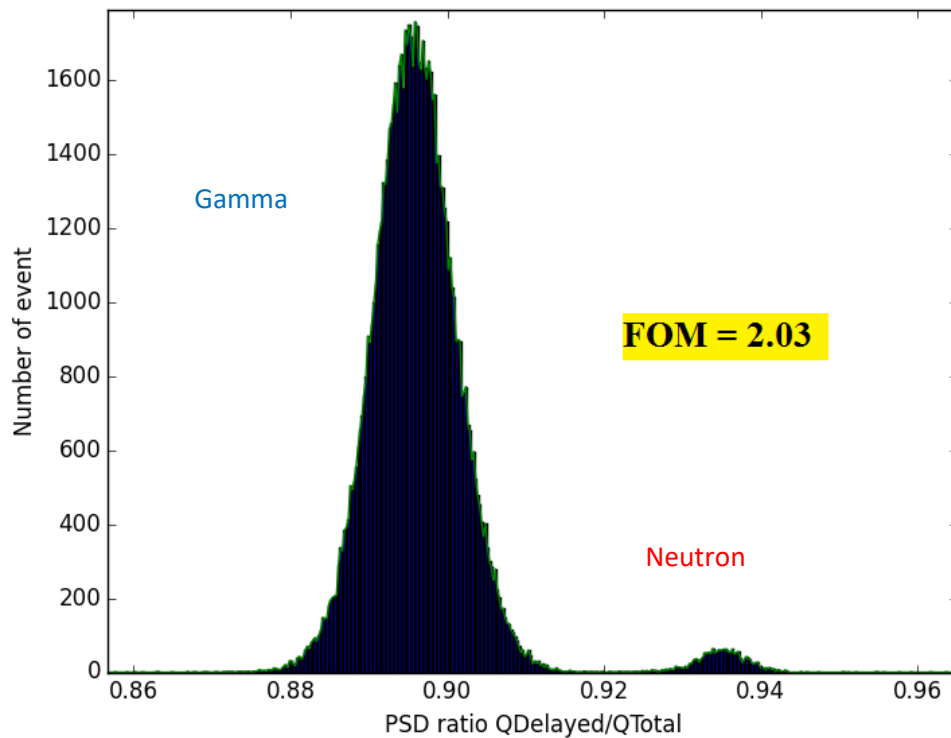


Figure 5.18 Projection of PSD ratio on the axis. The two Gaussians are well separated.

## 5.2 Scintillation decay times

According to the highest FOM the neutron and photon signals were averaged and normalized to their peak amplitude to produce a so-called standard pulse. The standard pulses contribute to eliminate the noise fluctuation in individual signals and reveal the details on the prompt and delayed shape. To study

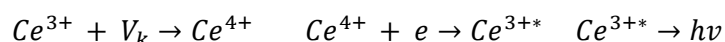


the decay time under photon and neutron irradiations, the standard pulses were fitted with exponential decay curves, each decay time constant corresponding to a specific scintillation mechanism

### 5.2.2 Scintillation mechanisms

For Ce<sup>3+</sup> doped crystals, up to four mechanisms contribute to the scintillation corresponding to four different energy transfers which occur at different timescales:

- **Direct e-/hole capture by Ce<sup>3+</sup>:** After absorbing a  $\gamma$  -ray, free electrons and holes are created in the conduction band and valence band, respectively. These free electrons and holes may be trapped within 1 ns by a Ce<sup>3+</sup> ion and the observed decay time is characteristic of the lifetime of the excited state of Ce<sup>3+</sup> leading to 4f–5d excitation and followed by 5d–4f emission with 100% efficiency. This type of fast energy transfer is desired for impurity Ce<sup>3+</sup>activated inorganic scintillator materials but other process enter in competition.
- **Binary e-/hole recombination:** Instead of being captured by the Ce<sup>3+</sup>, the hole produced initially in the valence band is not stable and will be bound between 2 anions to form a  $X_2^-$  ( $Cl_2^-$  for *CLYC*) molecular complex called :  $V_k$  center. Due to thermal activation, the  $V_k$  will move from one site to another in the crystal lattice, until it is trapped by Ce<sup>3+</sup> and creates Ce<sup>4+</sup> or an Ce<sup>3+</sup>– $V_k$  complex. Finally the free electron is captured leading to the excitation of Ce<sup>3+</sup>:



The time constant of this process depends not only on the lifetime of the 5d states of Ce<sup>3+</sup> but also on the migration time of  $V_k$  center to Ce<sup>3+</sup> and electrons to Ce<sup>4+</sup> or Ce<sup>3+</sup>– $V_k$ . Therefore this process is slower than the direct e-/hole capture by Ce<sup>3+</sup>.

- **Self-trapped exciton (STE) diffusion/emission:** If the  $V_k$  center is captured by an electron from the conduction band, before to be trapped by Ce<sup>3+</sup>, a STE is formed. STE is luminescent itself and has a lifetime of several  $\mu$ s. The STE may also transfer its energy to the Ce<sup>3+</sup> activator by two mechanism: radiative and diffusion:

-**Radiative transfer** due to absorption of STE luminescence by the Ce ions results in Ce luminescence and a dip in the STE emission band at the position of the Ce absorption band. Figure 5.19 shows the X-ray excited emission spectra, recorded at room temperature, of the pure- and Ce-doped  $Cs_2LiYCl_6$  crystals. The X-ray excited emission spectrum of pure  $Cs_2LiYCl_6$  exhibits one broad emission band between 240 and 460 nm which is attributed to STE emission. A similar structureless broad band due to STE emission has been observed in several other chlorides. An emission with peaks at 372 and 400 nm for  $Cs_2LiYCl_6$ :Ce, characteristic to cerium emission is seen [8]. The decay time of this mechanism is characteristic of the lifetime of the STE.

-**Diffusion:** contrary to the radiative transfer, the diffusion is thermally activated. The STE may migrate and give its energy to the Ce<sup>3+</sup> activator. An increase of Ce<sup>3+</sup> luminescence at the expense of STE lifetime is observed as it was studied by Combes. The decay time for this mechanism is therefore determined by both the lifetime of the STE and the rate of energy transfer to Ce<sup>3+</sup>. Providing than the migration STE time is shorter than the STE decay time, diffusion is faster than STE radiative transfer.

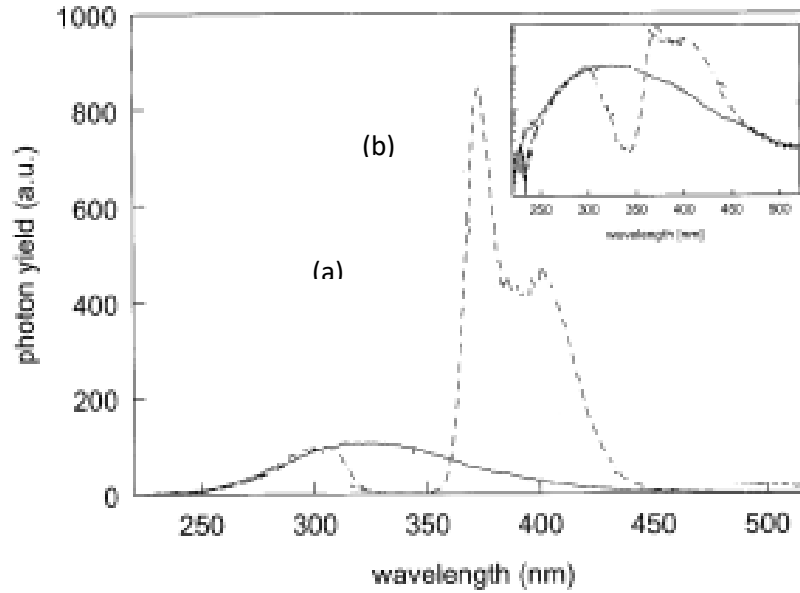


**Figure 5.19** X-ray excited emission spectra of pure  $Cs_2LiYCl_6$  (solid line),  $Cs_2LiYCl_6:Ce$  (dashed line), recorded at room temperature. The inset displays the same spectra plotted with a logarithmic axis. The emission intensity of the crystals was normalized at 300 nm [8].

- **Core-to-valence luminescence (CVL):** In case of chloro elpasolite (such as the CLYC), a fourth mechanism may occur [9]. When the incident high-energy photon excites an electron from the upper core band into the conduction band the resulting hole is short lived and will recombine with an electron from the valence band. If the process is radiative, it's a CVL. CVL is characterize by a short decay time of 0.6 to 3 ns [10].

### 5.2.3 Decay times

According to the PSD optimal results, neutron and gamma signals were averaged and normalized to their peak amplitude to produce the so-called standard pulse as shown in figure 5.20. These standard pulses contribute to eliminate the noise fluctuation in individual signals and reveal the details on the prompt and decay shape. Thereby different characteristics can be found between neutron and gamma signal shapes due to the different scintillation mechanisms.

To study the decay time under gamma and neutron excitation, the standard pulses were fitted with exponential decay curves, each decay time constant corresponding to a specific scintillation mechanism. A gamma standard pulse was fitted with a combination of four exponential decays (figure 5.21):

$$y = A_1 e^{-\frac{x}{\tau_1}} + A_2 e^{-\frac{x}{\tau_2}} + A_3 e^{-\frac{x}{\tau_3}} + A_4 e^{-\frac{x}{\tau_4}} + y_0$$

where  $A_1, A_2, A_3$  and  $A_4$  are the amplitudes of the curves,  $\tau_1, \tau_2, \tau_3$  and  $\tau_4$  are the components of the decay time (ultrafast, fast, intermediate, slow),  $y_0$  is the baseline offset originating from noise. However, the standard pulses for neutrons were only fitted by two or three exponential functions. The exponential fittings with three components for neutrons are presented in Figure 5.22. It was observed that the fitting using the three functions brought only a slightly improvement (R-squared: 0.99987 vs 0.99984) and that the two-functions fitting was adequate for the CLYC scintillator. This indicates that there might be only two major scintillation components produced in the interaction of neutrons with the CLYC detector. The decay time and fraction of each component at room temperature are shown in Table 5.1.

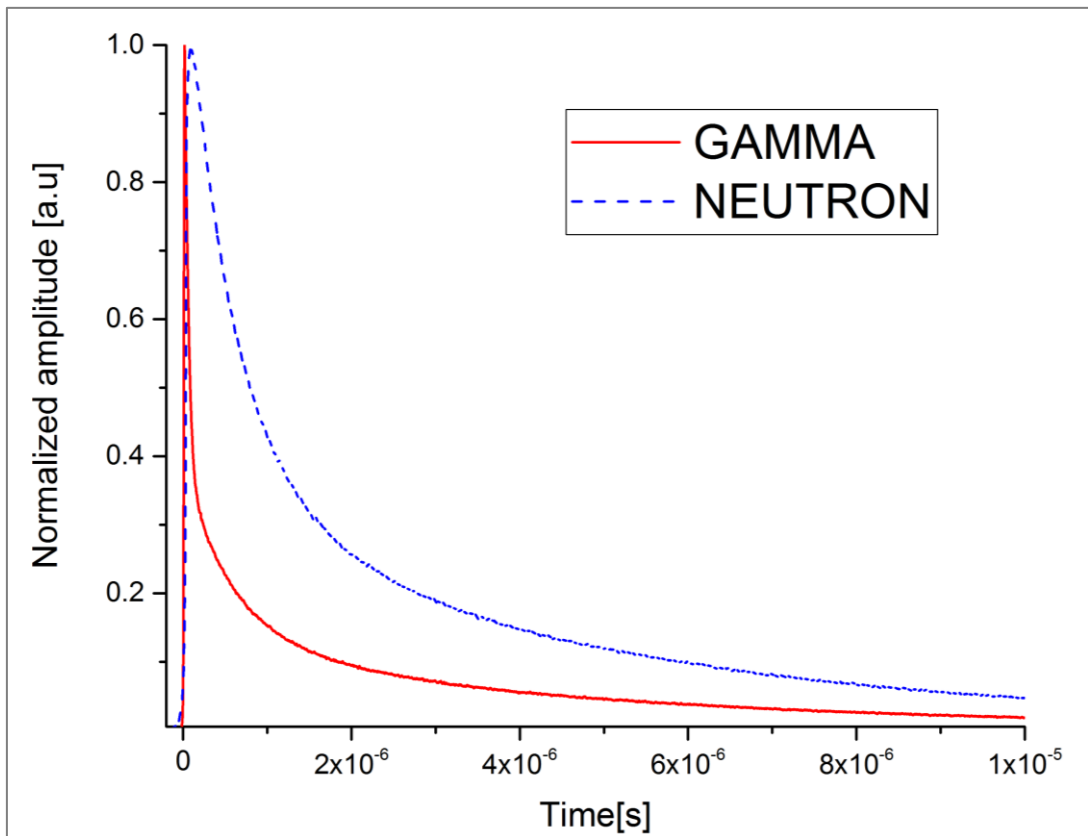


Figure 5.20 Neutron and gamma standard pulses.

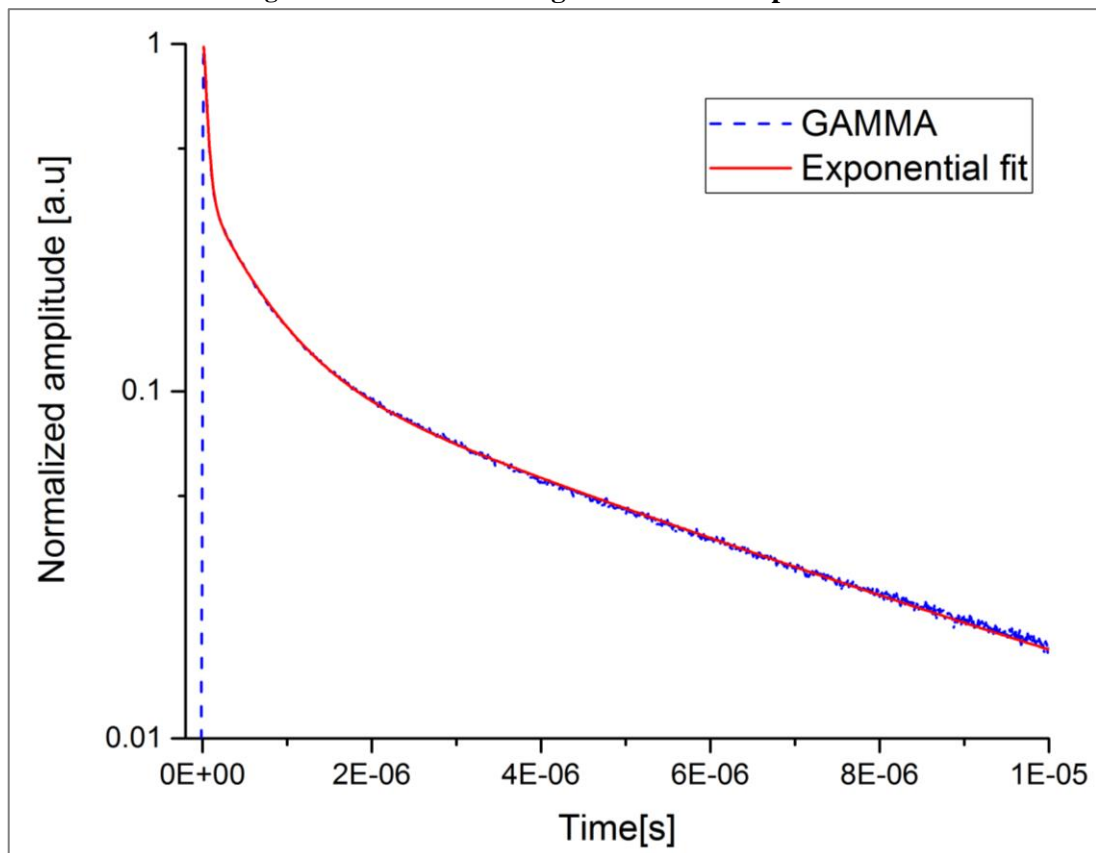


Figure 5.21 Gamma standard pulse.

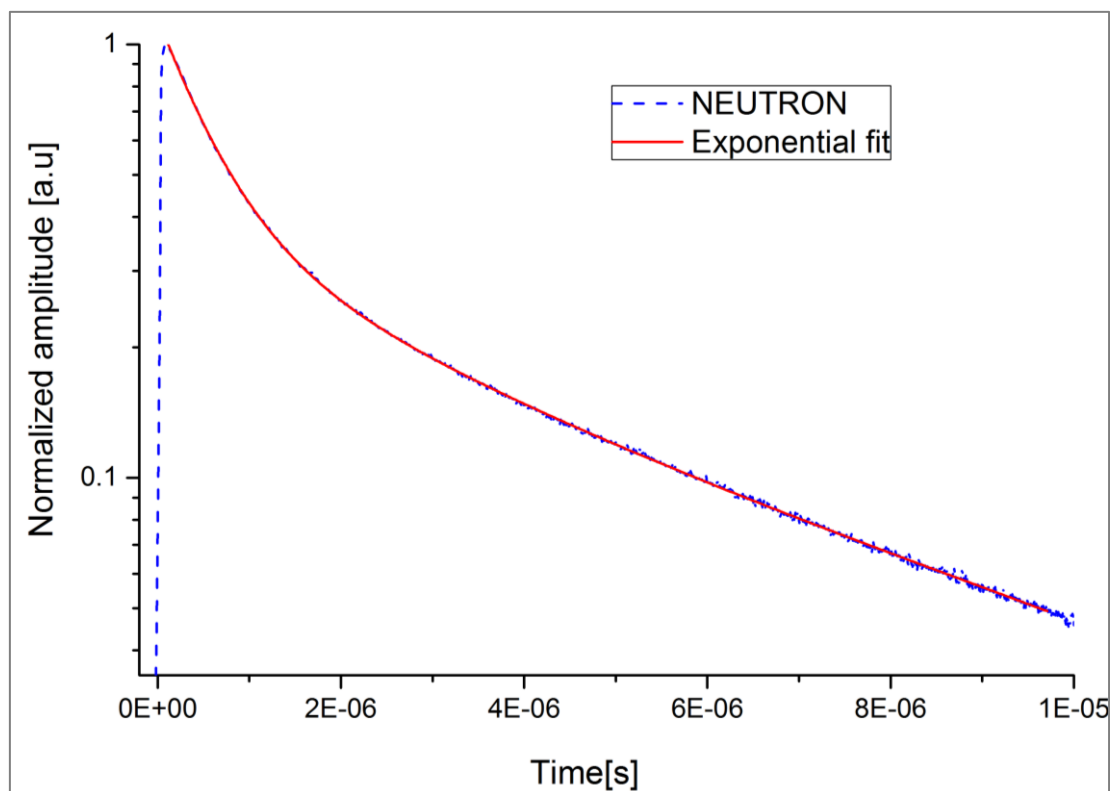


Figure 5.22 Neutron standard pulse.

The fitting results of the gamma waveform reveals four decay times: 2 ns, 48 ns, 637 ns and 4.8  $\mu$ s. Correlating these results with literature data, these mechanisms may be attributed to CVL,  $Ce^{3+}$ ,  $V_k$ , STE +  $Ce^{3+}$ . These decay times are in agreement with the results reported by different authors (table 5.2). Taking into account the two exponential decay fits, the neutron waveform at room temperature presents a component with 598 ns and 4493 ns. These times are similar to the results reported by *Xianfei Wen and al.* (Table 5.2). The decay times can be attributed to the  $V_k$  and to the STE +  $Ce^{3+}$ .

To study the influence of the photodetector response on the CLYC decay times, the CLYC was coupled with the SiPM. The same procedure of acquisition of standard pulses and fitting was applied. As with the PMT two decay times were found for the neutron waveform (517 ns and 4.2  $\mu$ s). These times are comparable to the PMT (598 ns and 4.4  $\mu$ s) and can be attributed to the same mechanism:  $V_k$  and STE +  $Ce^{3+}$ . Figure 5.23 shows the neutron standard pulse obtained with the SiPM and the PMT. Indeed, the waveforms looks quite similar.

However only three decay times were found for the gamma pulse. T3 and T4 are comparable to the PMT (Table 5.1) but the ultrafast component of the signal due to CVL is absent. Moreover the T2 component with the SiPM is slower than with the PMT (131 ns against 48 ns with the PMT). The slow recovery time of the SiPM is responsible for the disappearance of the ultrafast decay and diminishes the fast decay of the waveforms measured. Table 5.3 shows the rise time defined as the amplitude to go from 10% to 90% along with the fall time of SiPM and PMT.

Compared with the PMT, the SiPM rise times increase by approximately 20% (18% and 21% for gamma and neutron signals, respectively). While the neutron fall time is not strongly affected by the SiPM (about 10%), the gamma fall time is about 45% longer than PMT. This result emphasizes the fact that only the fast component of the signal (hundred ns) are slowing down by the SiPM response. Figure 5.24 shows the gamma standard pulse measured with the PMT and SiPM. The absence of CVL is clearly seen. The difficulty to discriminate gamma and neutron signals when coupling the CLYC with SiPM was reported by many authors [11]. However, although the fast components are affected by the SiPM

and consequently responsible for the reduction in PSD capability from a traditional PMT, the PSD is still possible with an FOM of 2.3.

**Table 5.1 Measured decay times for gamma and neutron induced CLYC emission at room temperature.**

		<b>T1</b> (ns)	<b>f1</b> (%)	<b>T2</b> (ns)	<b>f2</b> (%)	<b>T3</b> (ns)	<b>f3</b> (%)	<b>T4</b> (ns)	<b>f4</b> (%)
<b>PMT</b>	Gamma	2	0.03	48	1.6	637	13	4821	85.37
	Neutron	-	-	-	-	598	16.55	4493	83.45
<b>SIPM</b>	Gamma	-	-	131	2	494	12.59	4215	85.41
	Neutron	-	-	-	-	517	16.75	4208	83.25

**Table 5.2 CLYC emission decay times from the literature at room temperature.**

	<b>Reference</b>	<b>Ultrafast</b> (CVL)	<b>Fast</b> (Ce <sup>3+</sup> )	<b>Intermedi- ate</b> ( $V_k$ )	<b>Slow</b> (STE + Ce <sup>3+</sup> )
<i>gamma</i>	<i>B.S.Budden and al.</i>	3	72	415	3470
	<i>Xianfei Wen and al.</i>	0.09-0.38	47-55	651-692	4955-5163
	<i>Li Kui-Nian and al.</i>	2	50	420	3400
<i>neutron</i>	<i>Xianfei Wen and al.</i>	-	-	624	4566
	<i>DOlympia and al.</i>	-	-	440	1170 and 6310

**Table 5.3 Rise and fall times for CLYC**

	<b>Rise time</b> (ns)		<b>Fall time</b> (us)	
	PMT	SiPM	PMT	SiPM
<b>Gamma</b>	17	95	1.70	3.62
<b>Neutron</b>	28	128	3.68	4.13

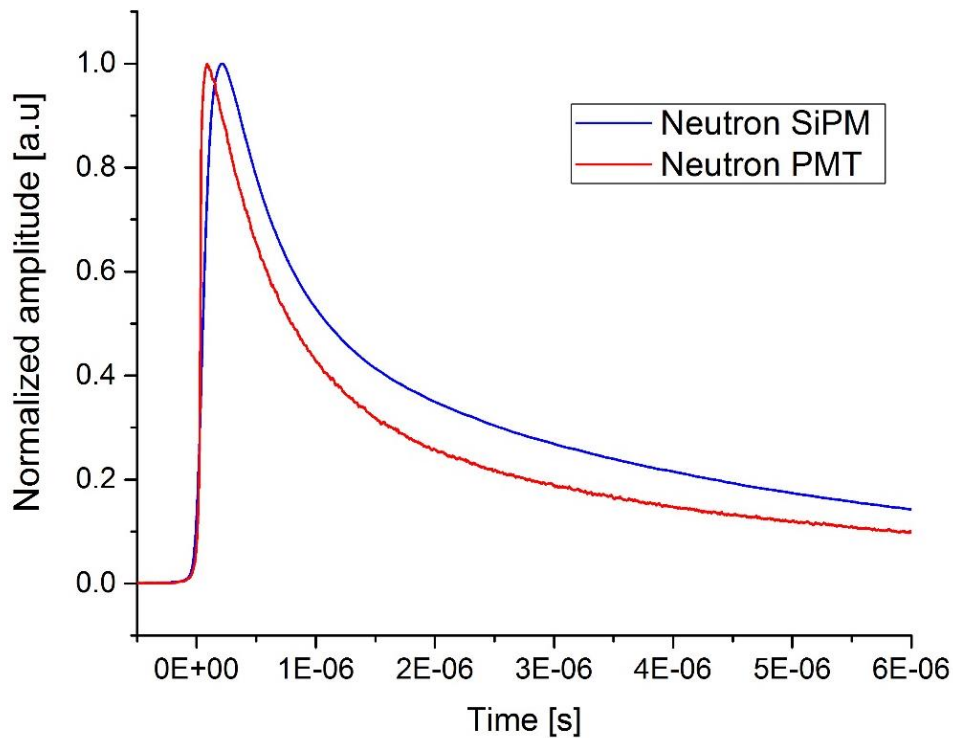


Figure 5.23 Neutron signals with PMT (red) and SiPM (blue).

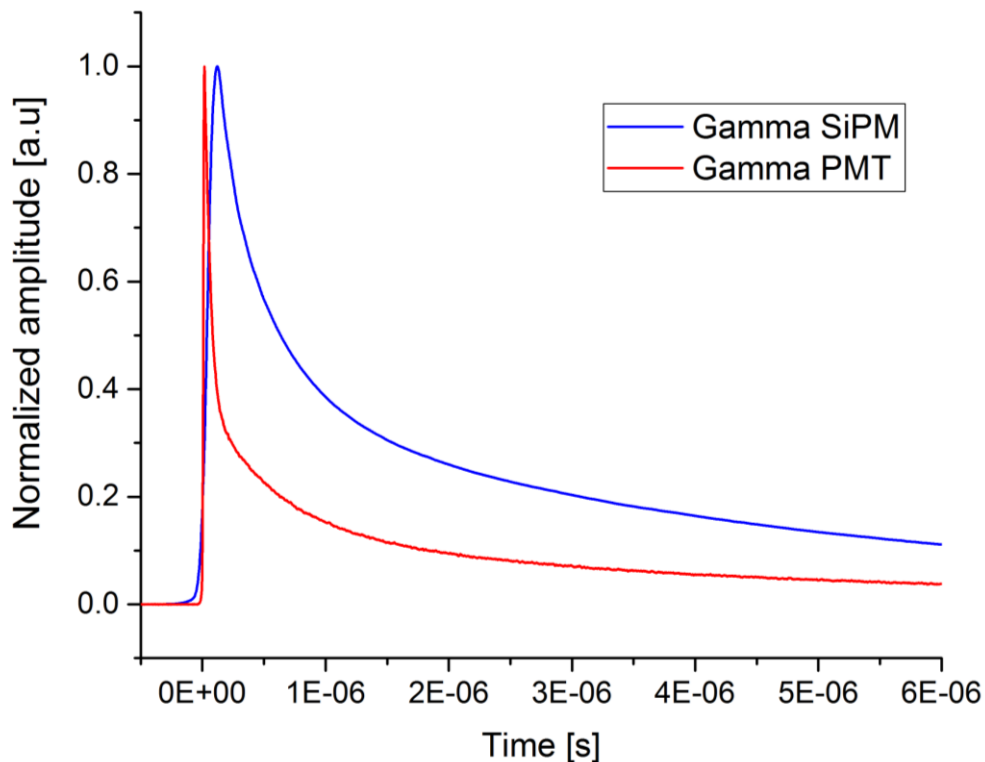


Figure 5.24 Gamma signals with PMT (red) and SiPM (blue).

### 5.3 Response linearity

Potential counting losses may arise at high-count rates from dead time of scintillation counting systems. The energy-to-light conversion efficiency is higher in inorganic scintillators than in plastic scintillators, due to their high atomic number and inherently higher photon yields. The higher light yield of inorganic scintillators creates more dependence on the time resolution characteristics of the photon detector; since

---

the count rate is higher, dead time contributions are also higher. The count rate linearity of a CLYC+photodetector system is determined by its time resolution, which is defined as the minimum time between successive scintillation pulses that the detection system can distinguish. This time interval may be limited by the decay rate of the scintillator, the frequency characteristics of the signal processing circuit, and timing characteristics of the photodetector's electronics. The decay time of the scintillation pulses from CLYC detectors is as long as a few microseconds, resulting in significant pulse pile-up at moderate input count rates.

To study the linearity range of CLYC and the effect of SiPM (instead of traditional PMT) on this range, measurements were performed with gamma sources. Indeed the main component of the output signals are from gamma interactions with the crystal, the neutron efficiency being <1%. Therefore, the saturation will occur with gamma signals. Two set-up were employed:

-CLYC+SiPM: the positive output signal from the PCB board (after the RC circuit) was first sent to a time filter amplifier to invert the signal without modifying the signal times. Therefore, the integration time was set to the smaller possible value (20 ns) and the differentiation time to the highest value ( $\mu$ s). Before the counter, the signal was sent to the discriminator where the width was fixed at 50 ns, a value sufficiently low not to saturate the electronics.

-CLYC+PMT: the set-up was the same except for the fact that the output signals were already negative so it was not necessary to invert the signal. The signals were amplified through the amplification stage of the PCB board (gain of 41).

The discriminator threshold affects the linearity range. Therefore, in order to compare the linearity range of the CLYC when coupled with the SiPM or PMT, the same discriminator threshold was fixed through an energy calibration measurement. Several waveforms from  $^{137}\text{Cs}$  and  $^{60}\text{Co}$  sources were registered with the Lecroy oscilloscope. The data were integrated with a Python script in order to obtain the spectrum of each source. A calibration was performed to find the proper threshold to set according to the energy. It was fixed at 47 mV for the SiPM and at 43 mV for the PMT that is equivalent to 330 keV. Figures 5.25 and 5.26 show the gamma spectra obtained with the PMT and the SiPM array together with the energy cut at 330 keV. Four  $^{137}\text{Cs}$  sources of different activities were used (300 MBq, 3 GBq, 30 GBq, 300 GBq). The dose rate was changed by changing the distance to the source and the activity of the source. Figure 5.27 shows the count rate as a function of dose rate for both the PMT and SiPM at the same threshold. For clarity, only the fit to the PMT data points are shown. The saturation appears at about 1 mSv/h for the SiPM while the PMT is still linear. This discrepancy may be explained by the difference in the shape of the signals. As seen in figure 5.24, the gamma signals with the PMT are thinner than the ones obtained with the SiPM. A large width of the signal increases the probably of pile up effects, thus shortening the range of linearity of the detector.

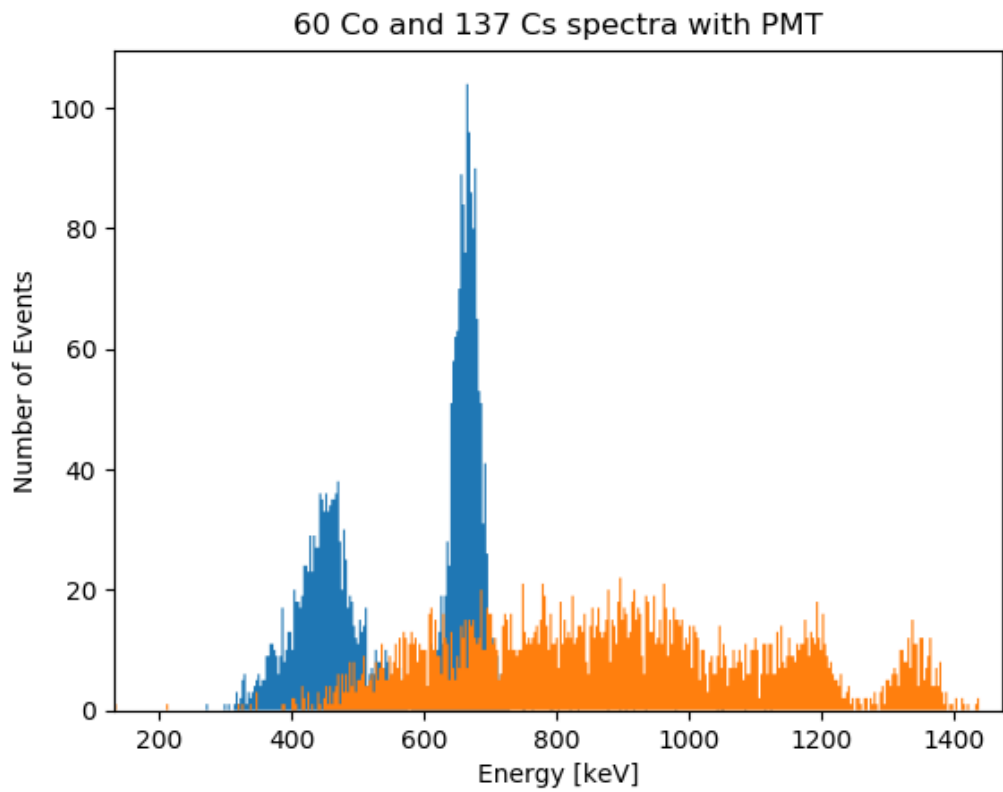


Figure 5.25  $^{137}\text{Cs}$  (blue) and  $^{60}\text{Co}$  (orange) spectra obtained with the CLYC + PMT.

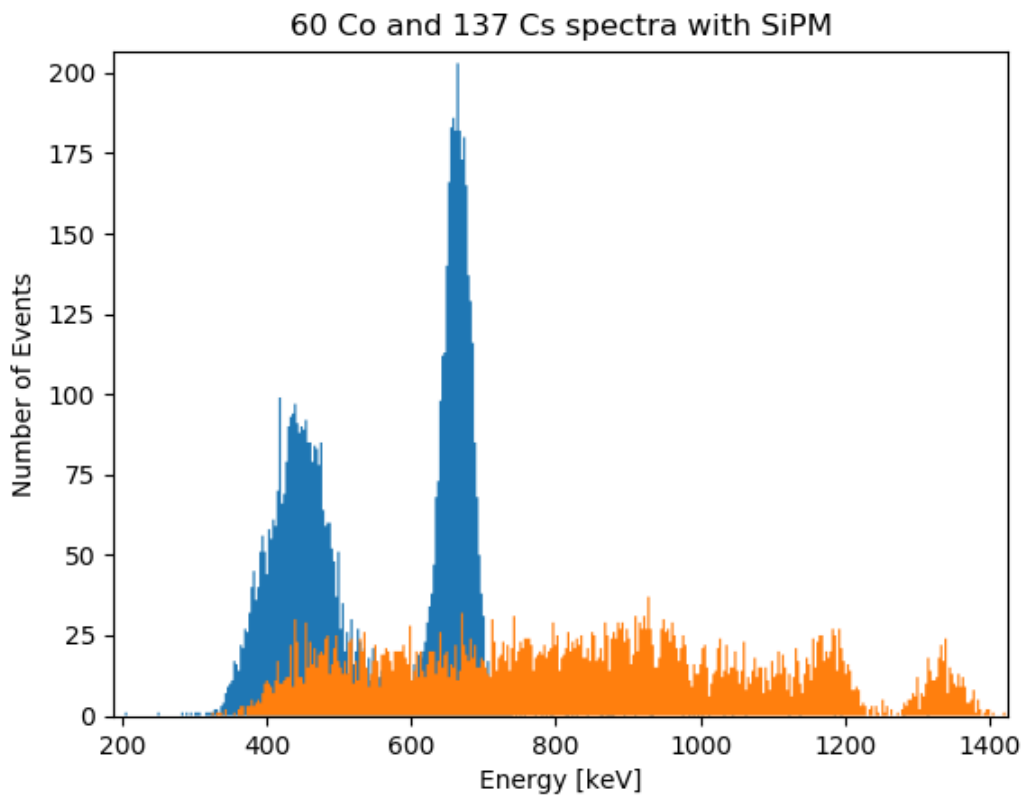


Figure 5.26  $^{137}\text{Cs}$  (blue) and  $^{60}\text{Co}$  (orange) spectra obtained with the CLYC + SiPM.



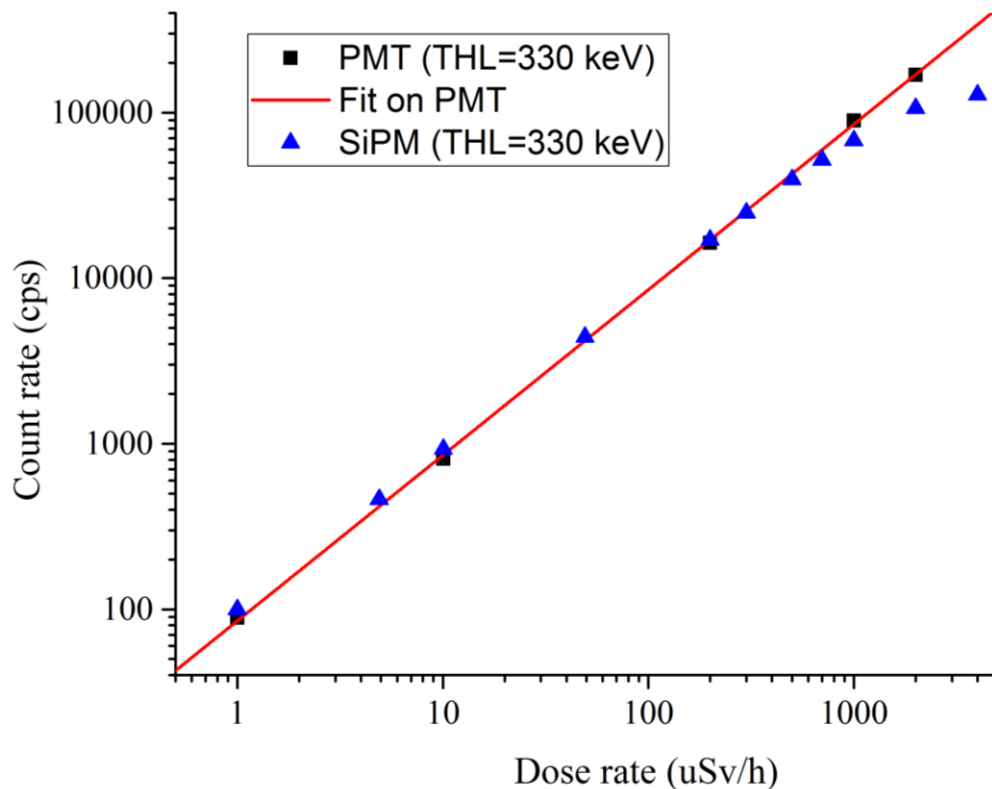


Figure 5.27 Count rate as a function of dose rate obtained with the SiPM (blue) and PMT (black) at the energy threshold of 330 keV. The red line represents the linear fit to the PMT data.

#### 5.4 Angular dependence

The energy states of molecules consist of a series of discrete levels which affect the scintillation mechanism in inorganic materials. Therefore, the mechanism is dependent of the crystal lattice, which means that the response of the scintillator can be anisotropic. To study the angular response of the detector, the CLYC was coupled with the PMT and irradiated with a pure gamma ( $^{137}\text{Cs}$ ) and a mixed gamma/neutron (AmBe) source. The system CLYC+PMT was placed at different angles from  $-90^\circ$  to  $+90^\circ$  at interval of  $30^\circ$  (see Figure 5.28).

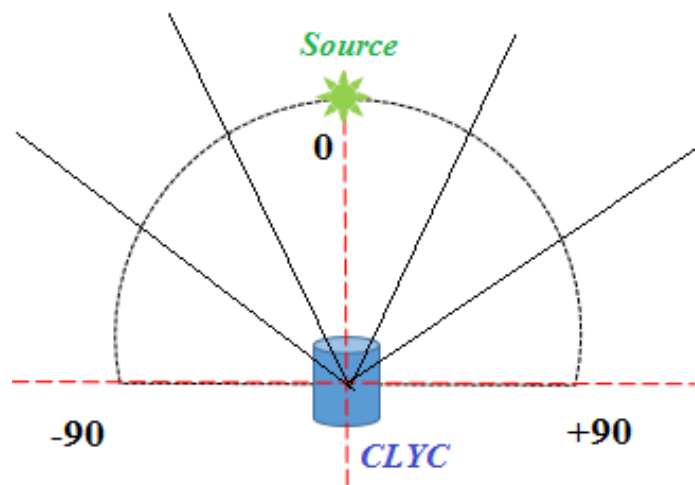


Figure 5.28 Schematic of the irradiation set-up for determining the angular response of the CLYC.

Figures 5.29 and 5.30 show the angular response of the CLYC when irradiated with  $^{137}\text{Cs}$  and AmBe sources, respectively. The first effect seen is that the response of the CLYC is symmetric around its  $0^\circ$  axis. Indeed, for example the count rates at  $-30^\circ$  and  $+30^\circ$  are very similar. Another effect is that the

count rate increases with angle (up to 17%), the minimum being at 0°. This effect can be attributed to the smaller solid angle provided by the cylindrical geometry of the sensitive volume when viewed head-on. Indeed the difference of solid angle when irradiating the CLYC head on as compared with irradiating it side on is about 20%.

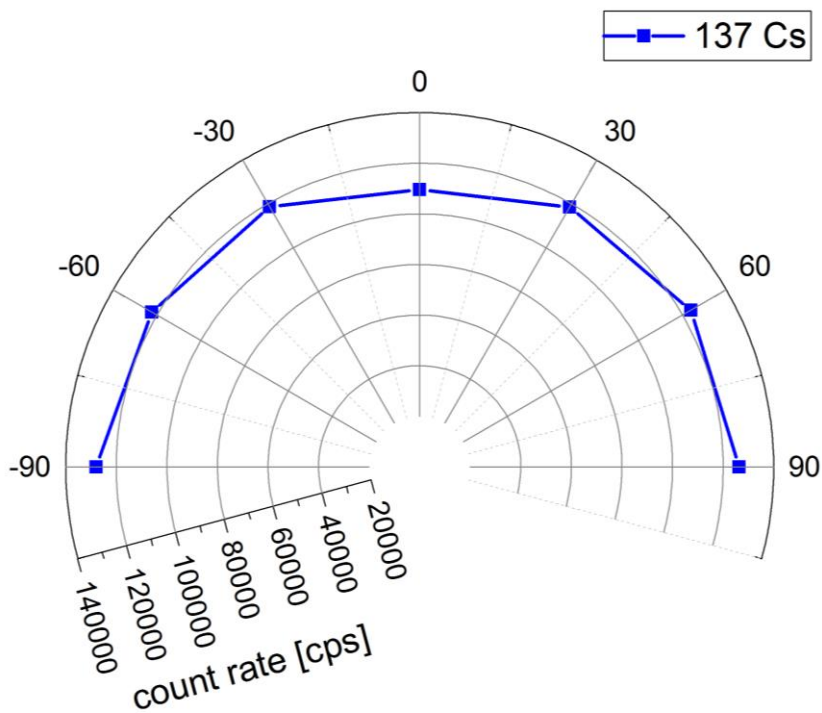


Figure 5.29 Directional response of the CLYC to a  $^{137}\text{Cs}$  source.

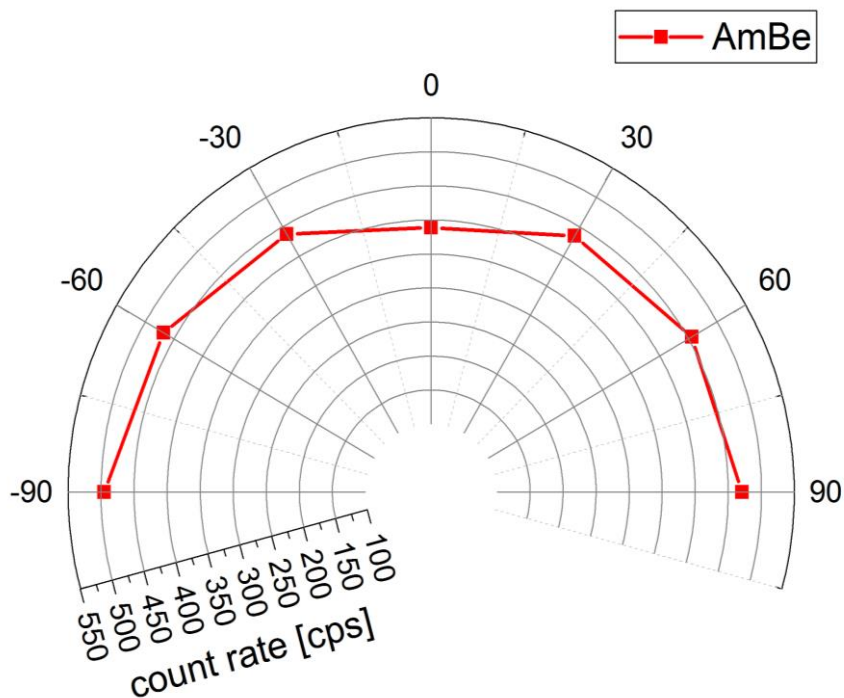


Figure 5.30 Directional response of the CLYC to an AmBe source.

## 5.5 Fast neutron efficiency

### 5.5.1 Simulated efficiency with MCNP

The Monte Carlo N-Particle 6 (MCNP6) code developed by Los Alamos National Laboratory was used to obtain a theoretical estimate of the efficiency of CLYC to fast neutrons [12]. In the input file, surface, cell and data cards were defined. A 1 inch right cylinder made of CLYC enriched with 99% of  $^7\text{Li}$ , 75% of  $^{35}\text{Cl}$  and 25% of  $^{37}\text{Cl}$  was simulated. The evaluated nuclear data file ENDF/B-VII.0 was implemented for these calculations [13]. The scintillator was placed at 135 cm from an AmBe source in a concrete room of  $13 \times 13 \times 13 \text{ m}^3$  volume that modeled the CALLAB geometry (Figure 5.31). The neutron energy spectrum was generated according to the AmBe energy binning defined in the ISO-8529-2 norm [14] (Figure 5.32). The energy spectrum of the emitted neutrons is a continuum up to around 10 MeV. The source definition was a point source. The number of source particles used in the simulation was  $10^7$ , sufficient to provide good statistics while minimizing the computing time.

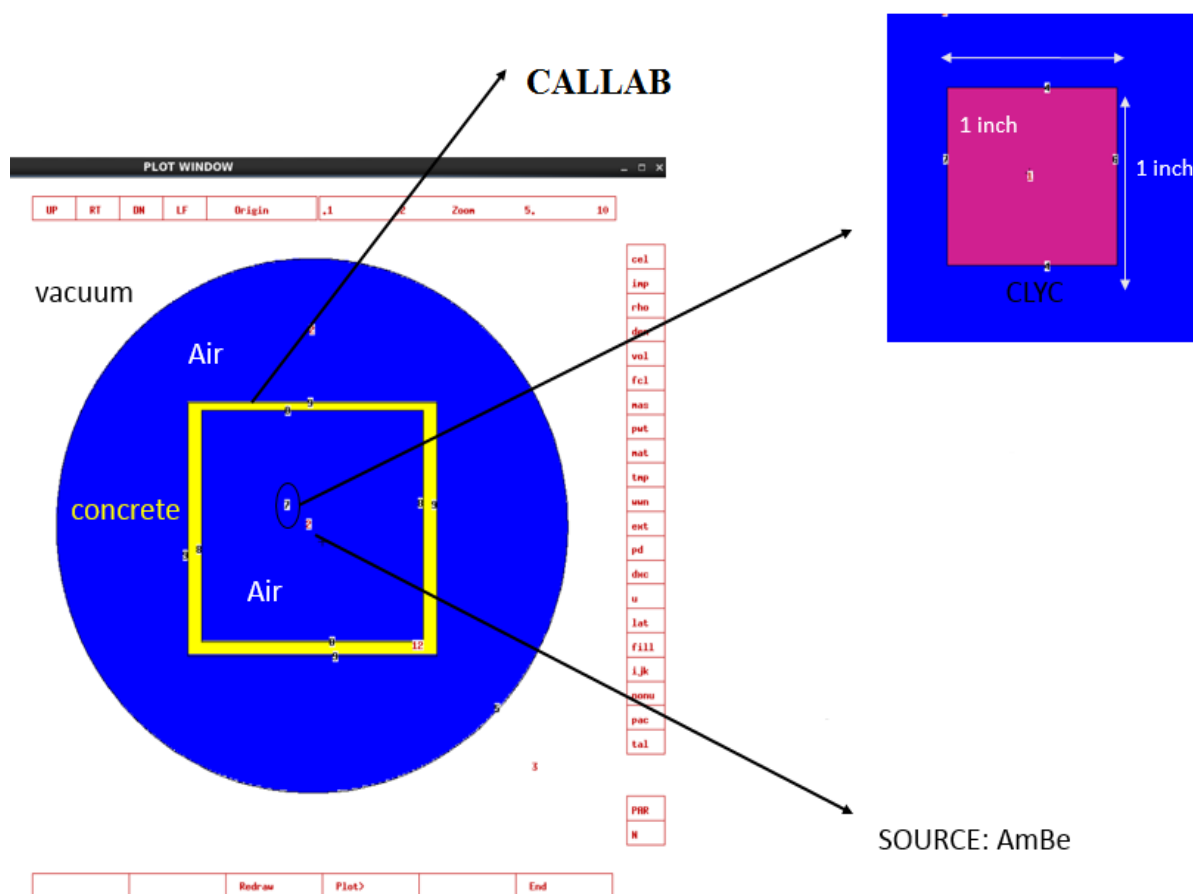


Figure 5.31 Cross-sectional view of the MCNP geometry.

Neutron interactions within CLYC-7 result in the production of protons, alpha particles and deuterons [15]. Thus, the tallying of these product particles enables evaluating the neutron interactions.

The F8 Pulse Height Tally, which records the energy deposited in a cell by each source particle and its secondary particles, was used. Contrary to the other tallies, the F8 needs, to model microscopic events realistically. However the F8:n (for neutrons) tally is unreliable because of the non analogue nature of transport that departs from microscopic realism at every step[12]. Therefore, the F8:h (for protons), F8:a (for alpha particles), and F8:d (for deuterons) tallies were employed instead. The F8 tally was

associated to pulse height light PHL treatment in order to model the pulse height energy spectrum of the CLYC detector. The PHL tally treatment allows for the conversion of the energy deposition (F6 tally) into detector pulse height (F8 tally).

The intrinsic efficiency was calculated as the ratio between the total number of particles created inside the CLYC (protons, alpha particles and deuterons) and the number of neutrons impinging on the CLYC surface. The value obtained is 0.7% corresponding to a calibration factor of 11 nSv/count.

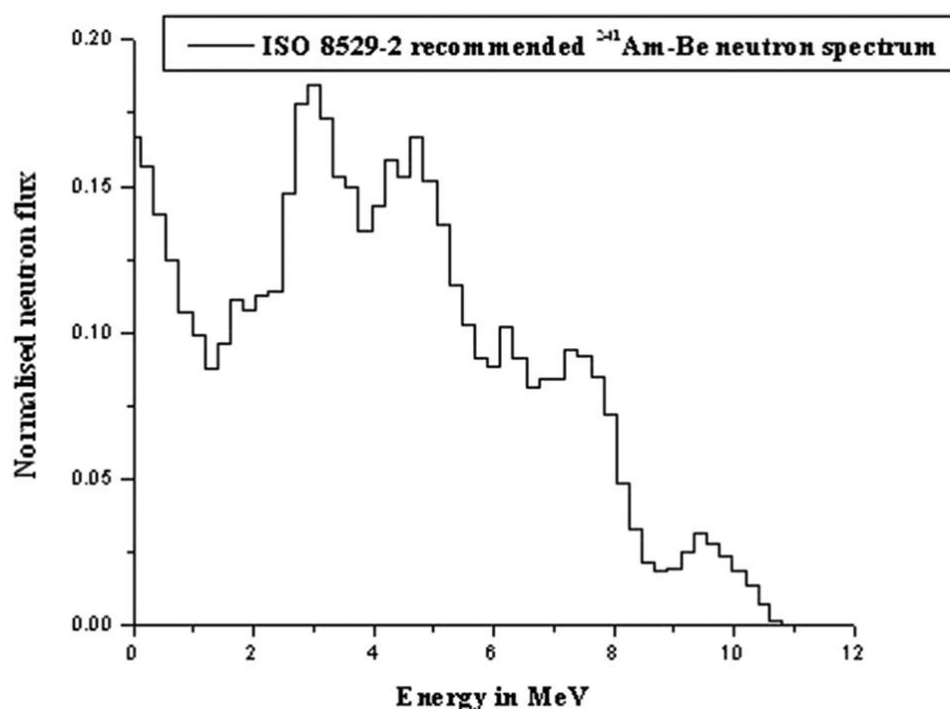
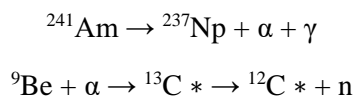


Figure 5.32 ISO 8529-2 recommended <sup>241</sup>Am-Be neutron spectrum [14].

### 5.5. 2 Validation with experimental data

To estimate the intrinsic neutron detection efficiency of the CLYC, the scintillator was irradiated with an isotropic AmBe source at the CERN Calibration Laboratory. The activity of the source was 100 GBq emitting 6.4E+06 n/s through the following reactions:



The intrinsic efficiency was defined as the ratio between the neutron fluence detected by the CLYC and the neutron fluence incident on the crystal taking into account the solid angle. The CLYC coupled with the SiPM and the electronic board was placed at 135 cm from the source. The data acquisition was set to approximately 1h30 to get the maximum number of files that can be registered by the oscilloscope (100,000) and analysed off-line. The optimal windows to optimise the FOM was applied (90 ns -1 μs). Only the neutron Gaussian peak was integrated from the projection of the PSD ratio on the x axis, giving a total number of counts of 5437 neutrons.

The neutron intrinsic efficiency was found to be 0.8% for an AmBe source (calibration factor of 12 nSv/count). This value is in excellent agreement both with the simulated efficiency and with literature data ([15] and [16]) giving 0.7% and 0.8%, respectively).

---

## References

- [1] A. Parveen I. Siddavatam, *Methods of Pulse Shape Discrimination (PSD)*, *International Journal of Application or Innovation in Engineering & Management (IJAIEEM)*, (2014)
- [2] N. Zaitseva et al., *Pulse Shape Discrimination in Impure and Mixed Single-Crystal Organic Scintillators*, *IEEE Transactions on Nuclear Science*, 58:6, p. 3411, (2011).
- [3] A. Savitzky and M. J. E. Golay, *Analytical Chemistry*, vol. 36, pp. 1627–1639 (1964).
- [4] R. H. Haitz, *Model for the electrical behaviour of the micro-plasma*, *Journal of applied physics*, vol. 35, no. 5, pp. 1370–1376, (1964).
- [5] S. Cova, M. Ghioni, A. Lacaita, C. Samori, and F. Zappa, “*Avalanche photodiodes and quenching circuits for single-photon detection*,” *Appl. Opt.*, vol. 35, no. 12, pp. 1959–1976, (1996)
- [6] D. Marano, M. Belluso, G. Bonanno and al., “*Silicon Photomultipliers Electrical Model Extensive Analytical Analysis*” *IEEE Transactions on Nuclear Science*, vol. 61, no. 1, (2014).
- [7] N. Pavlov, *Silicon Photomultiplier and Readout Method*, *USPTO Patent Application Publication*, No. US2013/0099100 A1, (2013).
- [8] C. M. Combes, P. Dorenbos, C. W. E. van Eijk, K. W. Kramer, H. U. Gudel, *Optical and scintillation properties of pure and Ce<sup>3+</sup>-doped Cs<sub>2</sub>LiYCl<sub>6</sub> and Li<sub>3</sub>YCl<sub>6</sub>:Ce<sup>3+</sup> crystals*. *J. Lumin.* 82, 299–305 (1999).
- [9] E. V. D. Van Loef, P. Dorenbos, C. W. E. van Eijk, K. W. Kramer, H. U. Gudel, *Scintillation properties of LaBr<sub>3</sub>:Ce<sup>3+</sup> crystals: fast, efficient and high-energy-resolution scintillators*. *Nucl. Instrum. Methods Phys. Res. A* 486, 254–258 (2002)
- [10] A. Piotr, *Core-valence luminescence in scintillators*, *Radiation Measurements* 38(4):343–352 (2004)
- [11] B. Budden, et al., *Analysis of Cs<sub>2</sub>LiYCl<sub>6</sub>:Ce<sup>3+</sup> (CLYC) waveforms as read out by solid state photomultipliers*, *IEEE Nuclear Science Symposium Conference Rec.*, N1-164, pp. 347–350, (2012).
- [12] D. B. Pelowitz, *MCNP6 User’s Manual*, Version 1.0. Los Alamos National Laboratory Report, LA-CP-11-00634, 2013.
- [13] M. B. Chadwick and al., *ENDF/B-VII.0: Next generation evaluated nuclear data library for nuclear science and technology, nuclear data sheets*, vol. 107, pp. 2931–3060 (2006).
- [14] *ISO International Standards. ISO 8529-1 Reference Neutron Radiations – Part 1: Characteristics and Methods of Production* (2001).
- [15] R. S. Woolf and al., *Response of the Li-7 enriched CLYC-7 scintillator to 6–60 MeV neutrons* *Nucl. Instrum. Methods Phys. Res. A* 803, 47–54 (2015)
- [15] A. Mentana et al, *Measurement of fast neutron efficiency of <sup>6</sup>Li and <sup>7</sup>Li enriched CLYC scintillators*, *J. Phys.: Conf. Ser.* 763 012006 (2016)
- [16] A. Giaz and al., *The CLYC-6 and CLYC-7 response to  $\gamma$ -rays, fast and thermal neutrons*, *Nucl. Instrum. Methods Phys. Res. A* 810 132 (2016).

---

# Chapter 6 New materials as perspective

Following the study performed with the CLYC, it was decided during the last month of the thesis to investigate other possibilities for the neutron probe that could combine an efficient PSD capability and a higher fast neutron efficiency. After an important research on the literature, two potential candidates were chosen: the EJ-276 plastic and the stilbene scintillators. The EJ-276 was purchased from Scionix [1] and the stilbene from Inrad Optics [2]. Both materials have a 1 inch right cylinder shape. This chapter is divided into two parts according to the material. The preliminary PSD and fast neutron efficiency results were evaluated for each of them and compared with the CLYC.

## 6.1 EJ-276 plastic scintillator

The EJ-276 was coupled to the SensL ArrayJ-30035-64P-PCB through an optical grease. The SiPM array is connected to a SiPM board that was designed in this study (see section 4.3.2.2). A positive reverse bias voltage of 28.5 V is applied to the *n-type* common cathode of the array. The signals were directly sent from the SiPM output (without amplification and RC compensation) to the 12 bit, 1 GHz Lecroy HDO6104 oscilloscope with a 50 Ohms termination.

A  $^{252}\text{Cf}$  source was used to study the  $\gamma/n$  discrimination. About 100,000 signal traces were recorded and analyzed off-line. The waveforms were filtered (Savitzky-Golay) and aligned to a common zero (the point where the amplitude was 20% of the maximum was chosen). Moreover, to remove the variable off-set on the y axis, the baseline mean value (estimated in the first 700 ns before the trigger) was determined and subtracted from the signal. Figure 6.1 shows the output signals from the EJ-276 after normalization to the peak amplitude. Two types of waveform are clearly identifiable: gamma rays (faster signals) and neutrons (slower signals). They exhibit similar rise times but the difference between the two signals is seen on the tail.

The charge integration method was employed to perform the PSD:

- (1) the width of the prompt integration window was varied from 60 ns, 100 ns, 200 ns, 400 ns, 700 ns to 1  $\mu\text{s}$ ;
- (2) the delayed integration window started right after the end point of the prompt window. Its width varied according to the width of the prompt window. The end of the delayed time is 1.5  $\mu\text{s}$ .

The separation between the neutron and gamma-ray regions is smaller for smaller pulses, creating the potential for gamma ray pulses to be misclassified as neutron pulses and vice versa. Increasing the measured light threshold will decrease the total amount of misclassifications. Therefore, a cut was applied to quantify a FOM value.

Figure 6.2 shows the FOM obtained for all configurations after the cut was applied. The two dimensional PSD plot for the optimized configuration (200 ns and 1.5  $\mu\text{s}$ ) is presented in figure 6.3 where the two different populations are clearly separated leading to a good FOM of 1.40.

Applying the optimized integration windows, the neutron events were selected and integrated to obtain the total number of neutrons that have interacted inside the scintillator. This value was divided by the neutron fluence on the scintillator to estimate the neutron efficiency. The intrinsic efficiency of 13% was reached. This value is 13 times higher than for the CLYC.

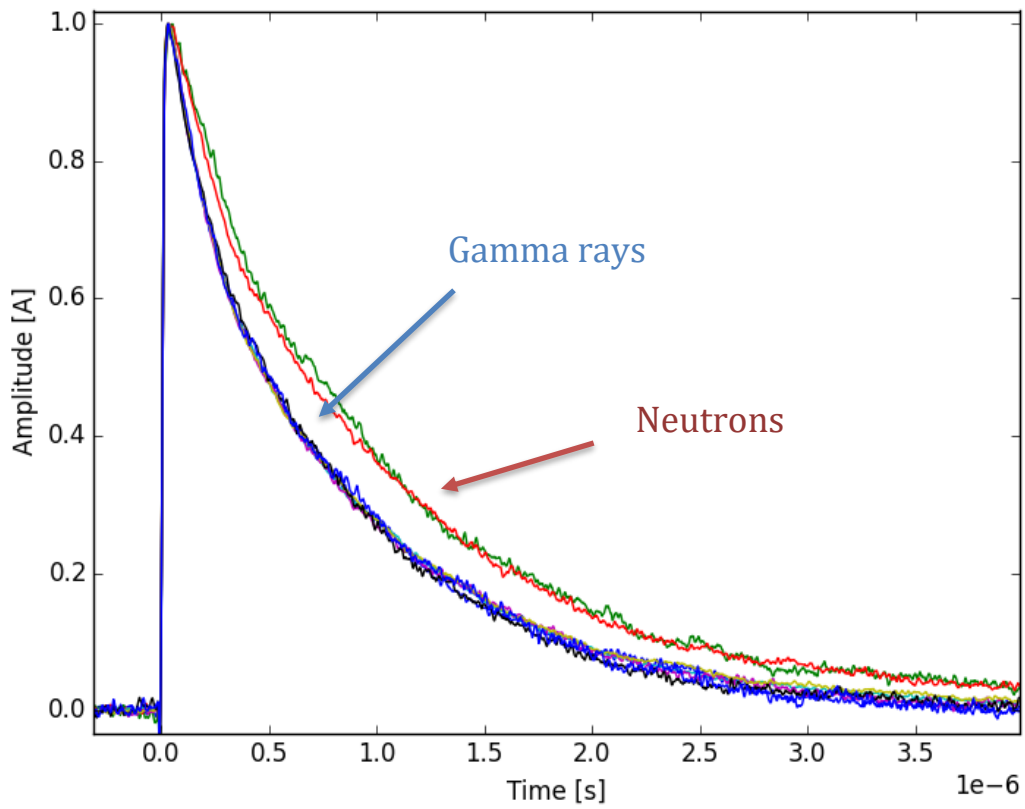


Figure 6.1 The EJ-276 output signals from the oscilloscope after normalization to their peak.

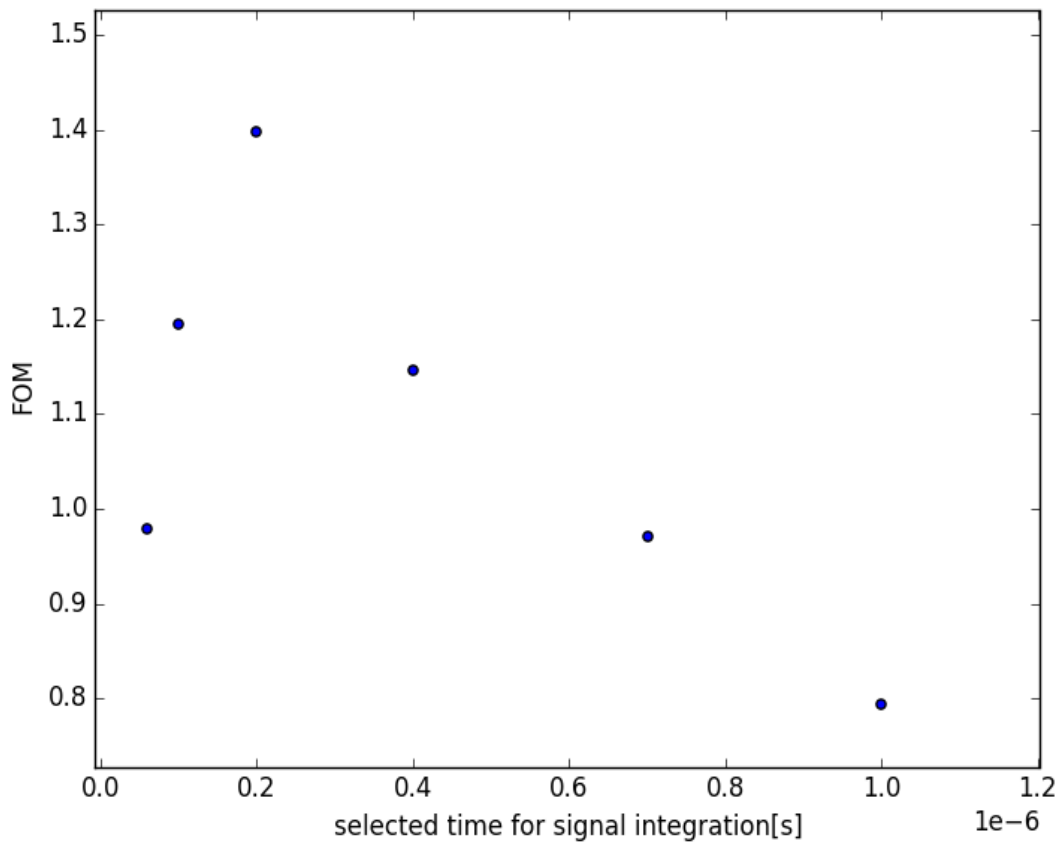
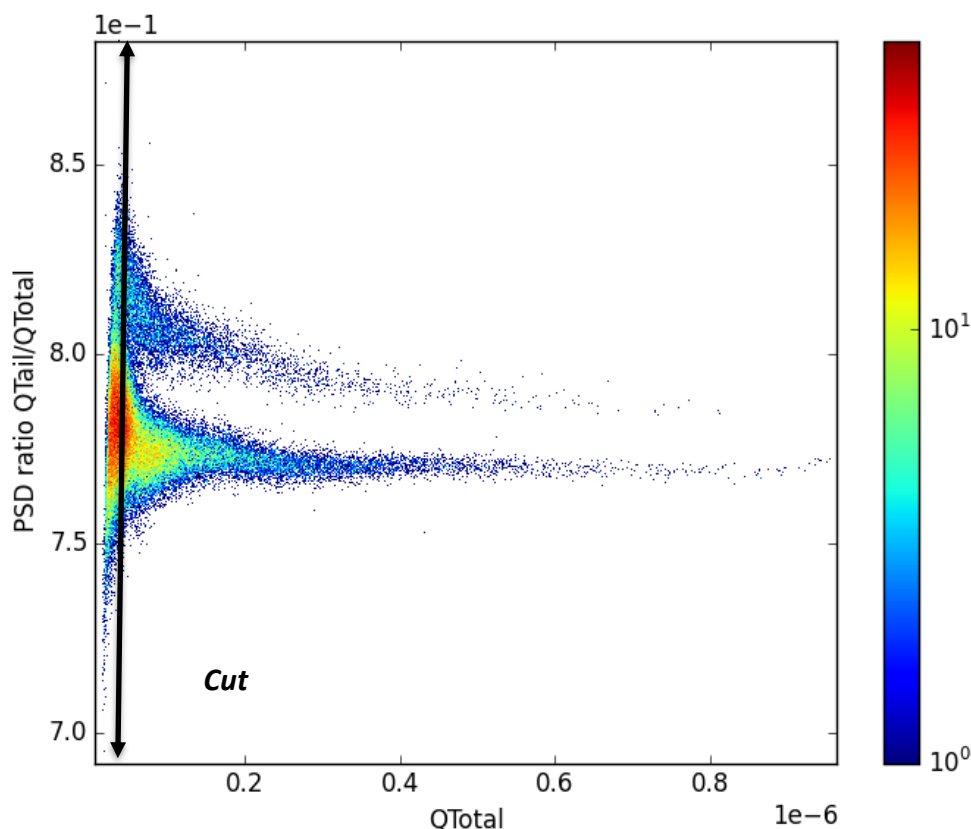


Figure 6.2 FOM versus delayed window time for different prompt windows. The best configuration for an optimized FOM of 1.40 is 200 ns -1.5  $\mu$ s.



**Figure 6.3** Two dimensional PSD plot for the best configuration (prompt window =200 ns, delayed window = 1.5  $\mu$ s). The blue box are gamma events while the red box corresponds to neutron events.

## 6.2 Stilbene scintillator

The same set-up used for the EJ-276 was employed for the stilbene. The charge integration method was also applied, leading to the ratio between the  $Q_{TAIL}$  and  $Q_{TOTAL}$ . For the PSD analysis the following parameters were implemented off-line:

- (1) the width of the prompt integration window was varied from 1  $\mu$ s to 3  $\mu$ s with a step of 0.5  $\mu$ s;
- (2) the delayed integration window started right after the end point of the prompt window. Its width varied according to the width of the prompt window. The end of the delayed window is 4  $\mu$ s.

Figure 6.4 shows the FOM obtained for all configurations. A delayed time starting at 1  $\mu$ s appears to be the best choice for a high FOM. The two dimensional PSD plot for the optimized configuration is presented in figure 6.5 where the two different populations are clearly separated leading to a good FOM of 1.51. It is important to note that this value does not include any cut in energy. As for the CLYC, the subtraction of the slow SiPm response through the same RC circuit could significantly improve the FOM value.

The intrinsic efficiency was calculated as for the CLYC (the ratio between the neutron fluence detected by the stilbene and the neutron fluence incident on the crystal taking into account the solid angle). A value of approximately 15% was reached. This value is 15 times higher than for the CLYC.



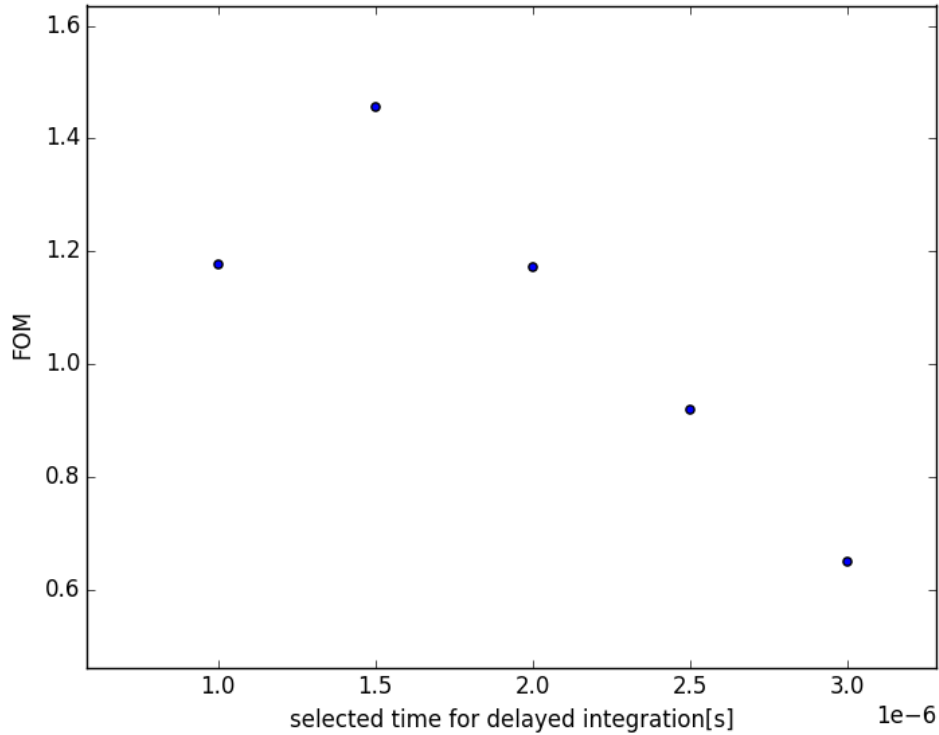


**Figure 6.4 FOM versus delayed window time for different prompt windows. The best configuration for an optimized FOM of 1.51 is 1.5  $\mu$ s -4  $\mu$ s.**

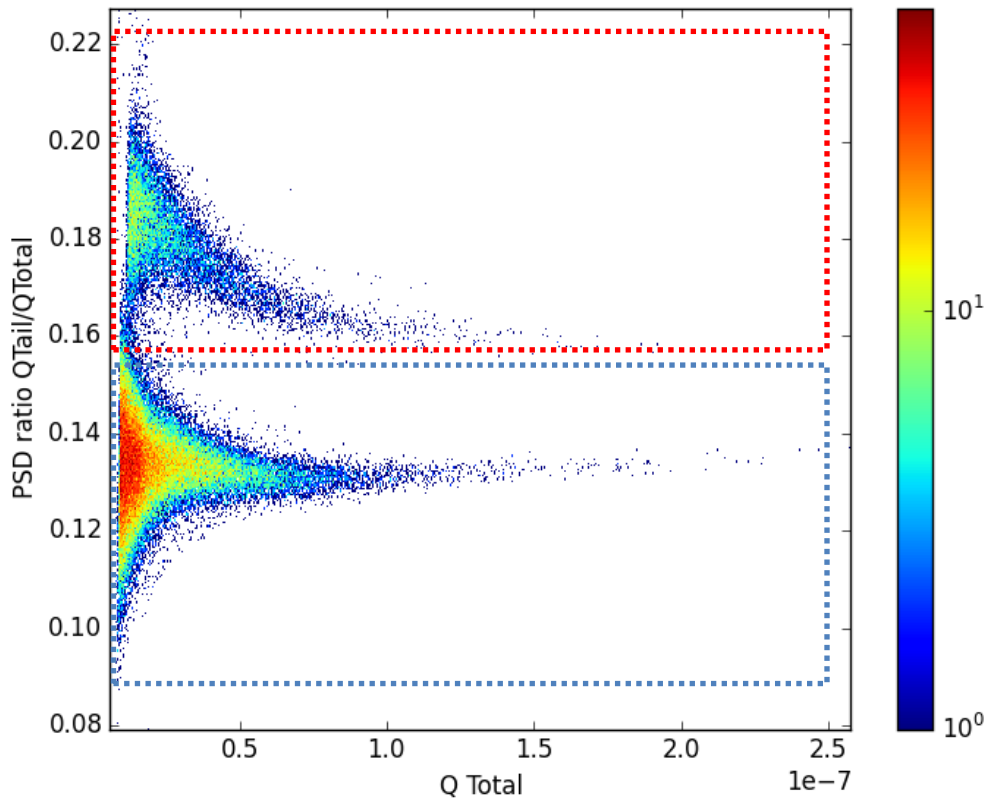


**Figure 6.5 Two dimensional PSD plot for the best configuration (prompt window =1.5  $\mu$ s, delayed window = 4  $\mu$ s). The blue box are gamma events while the red box corresponds to neutron events.**

Table 6.1 summarises the properties of the 3 materials studied in this thesis. The stilbene and the EJ-276 shows a higher efficiency for fast neutron detection while the CLYC has better gamma neutron discrimination. It is important to note that the measurements performed for the stilbene and the EJ-276 were made without the RC compensation that allows to remove the slow response component of the SiPM while keeping

the response of the scintillator. While it was not possible to discriminate gamma and neutron signals without the use of the RC for the CLYC, an efficient FOM (>1.27) is already possible for the 2 new materials taking the signal output directly. This could be explained by two factors:

- The mean wavelengths of the two materials are closer to the peak PDE wavelength of the SiPM ArrayJ-30035-64P-PCB (420 nm) than the CLYC.
- The main difference between pulses are seen on the tail with the stilbene and the EJ-276 whereas for the CLYC the important part of the pulse waveform is in the leading edge. Thus, for the CLYC, despite having a much longer tail than the plastics, the important part of the waveform is on a much shorter timescale.

CLYC is the only material to perform neutron spectroscopy without the need of an unfolding code up to 10 MeV. This is due to the excellent linearity between the proton produced by the reaction on Chlorine and the incident neutron energy. Above 10 MeV several reaction channels become possible and the spectroscopy requires an unfolding code.

Due to its higher concentration in hydrogen, stilbene is the most efficient material for fast neutron detection but it is fragile and expensive while the EJ-276 shows similar performances and it is more robust. However the stilbene is able to detect lower energy neutrons with a good PSD while an energy cut is necessary for the EJ-276. Compared to the CLYC, stilbene is more fragile but less expensive.

The neutron sensitivity for the CLYC is 12 nSv/count. In order to estimate the calibration factors for the stilbene and the EJ-276, the conversion coefficient for  $^{252}\text{Cf}$  (380 pSv.cm<sup>-2</sup> [3]) was multiplied by the neutron fluence reaching both material. The ratio between the neutron flux inside the scintillator and the previous quantities leads to a value in nSv/count. The LINUS rem counter shows a high efficiency of 1.1 nSv/count thanks to its high cross section for thermal neutrons. However, rem counters are rather slow and heavy (due to time and the amount of polyethylene required to moderate neutrons) compared to fast neutron detectors such as the stilbene and the EJ-276

**Table 6.1 Properties of the CLYC, the STILBENE and the EJ-276 plastic scintillators.**

Detector	LIGHT OUTPUT (ph/MeV)	PSD (FOM)	EFFICIENCY (%)	CALIBRATION FACTOR (nSv/count)	SPECTROSCOPY (no unfolding)	PEAK EMISSION (nm)	DECAY TIMES (ns)
<b>CLYC</b>	20000	2.03	0.8	12	Up to 10 MeV	370	2, 50, 650, 4500 ( $\gamma$ ) 620, 4000 (n)
<b>STILBENE</b>	14000	1.51	15	4.9	NO	410	5, 21, 135 ( $\gamma$ ) 5, 27, 253 (n)
<b>EJ-276</b>	8600	1.40	13	5.8	NO	425	13, 35, 270 ( $\gamma$ ) 13, 59, 460 (n)

## References

---

[1] *Scionix*, <https://scionix.nl/>

[2] *Inrad Optics*, <http://inradoptics.com/>

[3] *ISO International Standards. ISO 8529-1 Reference Neutron Radiations – Part 1: Characteristics and Methods of Production (2001).*



---

# Conclusions

The first part of this study consisted in testing performance of the several neutron detectors usually employed for radiation protection at high-energy particle accelerators. The intercomparison was made at CERF, a unique workplace field that simulates the neutron spectrum encountered in the proximity of high-energy accelerators and at commercial flight altitudes. Before being used at CERF, the detectors were characterized and calibrated in the CERN calibration laboratory. Particular attention was given to the reference detector of the CERF field, the LINUS that was tested for the first time in an aircraft campaign in Prague. The CERF intercomparison campaign allowed to understand the behaviour of the different detector and quantify their over/underestimations with respect to the reference ambient dose equivalent function.

Moreover, these experimental data were used to benchmark the new FLUKA simulation performed in 2017. CERF has been available at CERN since 1992 and the reference spectra and dose values were calculated using the 1997 version of the FLUKA code, from now-on FLUKA-1997. Since then, the code has undergone many developments, especially concerning the neutron physical models. Hence, new simulations were performed with the current FLUKA development version (FLUKA-2017) and a few geometrical changes were implemented.

This work aimed at properly characterizing the neutron radiation field in order to start the facility accreditation process as reference workplace field.

The second part of this thesis was the investigation of a fast neutron detector for a novel radiation survey meter (called B-RAD) able to operate in the presence of a strong magnetic field, to be used for radiation surveys e.g. in the LHC experimental areas. The CLYC was selected as potential candidate for neutron detection because of its promising properties, such as its capability to discriminate gamma rays from fast neutrons and its energy resolution. Small CLYC scintillators were already used but coupled with PMT. However, the choice of SiPM for the neutron probe was justified by crucial requirements: the insensitivity to external magnetic fields, extreme compactness, light and robust mechanical device. This thesis evaluated the performance of a 1-inch right CLYC cylinder coupled with a large SiPM array and compared the result with PMTs.

The uniformity of the SiPM array was investigated through measurements of the bias voltage, the gain, the photo detection efficiency by measuring each pixel response. The temperature sensitivity of the system CLYC+SiPM was tested from -10 °C to +40 °C. An overall variation 10% in the position of the peak centroid was found. The system is linear up to 1 mSv/h where it starts showing a slight saturation effect. The angulation response was measured with both gamma and neutron sources. A variation of 20% in count rate was found between front and lateral irradiation (0° and 90°).

The gamma energy resolution of the system CLYC+SiPM was 5.6% which is better than the CLYC+PMT (Bialkalide). This energy resolution is comparable to the intrinsic resolution of the LaBr crystal (4.6% with the same electronic set-up).

The capacity of the CLYC+SiPM to discriminate gamma and neutron signals was the more challenging part when dealing with such a large array since the total capacitance increases with the number of pixels. The extraction of the fastest scintillation decay time constants from the crystal and the shortening of the falling time of the signal without cutting the crystal response was made through an electronic process (RC compensation). An excellent FOM of 2.03 was found approaching the results obtained with PMT. Shortening the signals allows to increase the linearity range and the frequency of the event at which the CLYC is sensitive.

Finally, the fast neutron efficiency was simulated with MCNP and the results were validated experimentally. Similar efficiency values of approximately 0.8% were found. Such a low efficiency and the consequent long measurement time could be the limiting factor for an application as portable handheld probe (i.e.

---

about 0.2 counts per second for a dose rate of 1 uSv/h). However, the CLYC could be used as a stationary detector to monitor both the gamma and the neutron dose rates in workplaces that could lead to an undesired exposure of personnel (nuclear power plants facility, personnel monitoring for general health and safety of workers, environment...)

Another potential application for the CLYC is its use for homeland security (non-proliferation, border security...) to improve the detection of special nuclear materials (SNM). SNM are for example plutonium, uranium-233, uranium enriched in either uranium-233 or uranium-235. Spontaneous and induced fission events in SNM produce neutrons and gamma rays, which can be detected and well separated thanks to the excellent discrimination capabilities of the CLYC. The fission products have an energy between 500 keV and 10 MeV that fit the measuring range of the CLYC. These fast neutrons are largely unaffected by a few centimetres of high-Z material that would instead be sufficient to attenuate most gamma rays, while tens of centimetres of hydrogenous materials are required to achieve substantial attenuation of neutron fluxes from SNM. CLYC neutron detectors can therefore be used as dual mode to detect gamma ray and neutron in SNM search and monitoring applications.

To reduce the measurement time, a material with higher efficiency for fast neutron was investigated. Two potential scintillators were selected: the EJ-276 and the Stilbene. As preliminary results, they shown an efficiency more than 10 times higher than the CLYC but a lower capacity of gamma/neutron discrimination (1.4 and 1.51, respectively). This FOM is sufficient ( $>1.27$ ) but can probably be improved by the use of a RC circuit used for the CLYC to avoid the probability of false counts due to misclassification of gamma as a neutron.

Another important step is the need of calibration. Contrary to the CLYC, the gamma photo-peaks will not be present but only the Compton edge due to the low Z of the two materials. An energy calibration is possible using several experimental methods but also via MCNP simulations.

Several point of investigations are required, such as the response of these scintillators, the linearity range and the angular response. The temperature sensitivity of the system materials+SiPM should be also studied and eventually compensated.

On the electronic point of view, the integration of a PSD circuit in the actual PCB board is an important step to obtain an online analysis and avoid a time consuming off-line analysis of the signals. Another possibility to avoid time consuming related to the PSD off-line analysis is to select the signal according to the wavelength by placing filters between the CLYC and the SiPM. In this way, the signal due to neutron can directly be selected without performing PSD.

Titre: Développement de détecteur de neutron pour l'utilisation en radioprotection.

Mots clés : Instrumentation – neutron - détection - spectroscopie - discrimination

Résumé : La première partie de cette étude a consisté à tester les performances de plusieurs détecteurs de neutrons habituellement utilisés pour la radioprotection des accélérateurs de particules à haute énergie. La comparaison a été réalisée à la CERF, un champ unique qui simule le spectre neutronique rencontré à proximité d'accélérateurs à haute énergie et à des altitudes de vols commerciaux. La campagne a permis de comprendre le comportement des différents détecteurs et de quantifier leurs sur/sous-estimations par rapport à la fonction d'équivalent de dose ambiante de référence et de réaliser le benchmark des nouvelles simulations FLUKA réalisée en 2017.

La deuxième partie de cette thèse portait sur l'exploration d'un détecteur à neutrons rapides destiné à un nouvel appareil de mesure capable de fonctionner en présence d'un champ magnétique puissant. Le CLYC a été choisi comme candidat potentiel pour la détection neutronique en raison de ses propriétés prometteuses, telles que sa capacité à discriminer les rayons gamma des neutrons rapides et sa résolution énergétique. Cette thèse évalue les performances d'un large cylindre CLYC couplé à une matrice SiPM et compare les résultats à ceux des PMT. Les capacités spectrométriques du CLYC ont été soulignées. Pour le comptage neutronique de nouveaux matériaux ont été étudié en perspective.

Title: Development of neutron detector for use in radiation protection.

Keywords : Instrumentation - neutron detection – spectroscopy - discrimination

Abstract : The first part of this study consisted in testing performance of the several neutron detectors usually employed for radiation protection at high-energy particle accelerators. The intercomparison was made at CERF, a unique workplace field that simulates the neutron spectrum encountered in the proximity of high-energy accelerators and at commercial flight altitudes. The CERF intercomparison campaign allowed to understand the behaviour of the different detector and quantify their over/underestimations with respect to the reference ambient dose equivalent function. Moreover, these experimental data were used to benchmark the new FLUKA simulation performed in 2017. .

The second part of this thesis was the investigation of a fast neutron detector for a novel radiation survey meter (called B-RAD) able to operate in the presence of a strong magnetic field, to be used for radiation surveys e.g. in the LHC experimental areas. The CLYC was selected as potential candidate for neutron detection because of its promising properties, such as its capability to discriminate gamma rays from fast neutrons and its energy resolution. This thesis evaluated the performance of a 1-inch right CLYC cylinder coupled with a large SiPM array and compared the result with PMTs. The capacity of the CLYC+SiPm for spectroscopy was underlined. For neutron counting, new materials were investigated.

